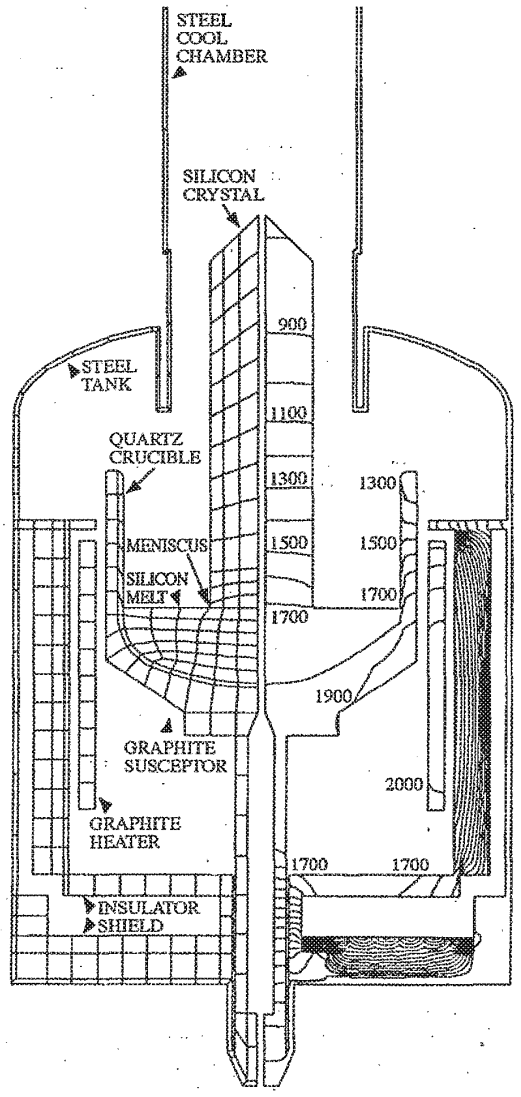

FIG. 44. Temperature distribution along the ingot and in the puller during crystal growth, obtained by computer simulation (from Ref. 165).

ing treatment (1320 °C for 3 h). To this purpose, high-temperature annealing was applied for as-grown precipitate dissolution and interstitial oxygen homogeneization, as described earlier by Shimura[167] and by Jastrzebski *et al.*[168] On the other hand, Fusegawa and Yamagishi[169] found that a low-temperature (450 °C for 2 h in O_2) preheating improves the axial uniformity of oxygen precipitation resulting after a two-step anneal treatment (800 °C for 4 h in N_2+1000 °C for 16 h in O_2).

Inoue and co-workers[129] found that there is an incubation time for the nucleation of oxygen precipitates and that the density of nuclei reaches a saturation value after some period of annealing. This incubation period depends on the thermal history of the crystals,[129] as well as on the nucleation temperature[129] and the interstitial oxygen content.[170]

Several authors[125,129,170] have shown the importance of low-temperature interval during the thermal history of the wafers. Recently, Fraundorf, Fraundorf, and Craven[171] proposed the existence of a metastable oxide precursor phase with maximum nucleation temperature of about 600 °C. Such precursors have a high surface-to-volume ratio and act as seeds for the most common platelet-type oxide precipitates, which have a maximum nucleation rate at 750 °C. The precursors form during the crystal cooling process and may also grow from the thermal donors.[171,172]

However, although a single-step preannealing at low temperature may be useful in certain thermal treatments, Fusegawa *et al.*[173] have recently shown that before specific thermal treatments during CMOS fabrication a two-step preannealing treatment is needed. In particular, they have shown that annealing at 450 °C for 2 h followed by a second step at 650 °C for 2 h is very effective in obtaining a uniform distribution of oxygen precipitates along the crystal growth axis.

Thermal history effects can also be reduced using another approach, i.e., by performing a high-temperature rapid thermal annealing (1200 °C for 2 min in Ar atmosphere) prior to a two-step annealing, as proposed by Chiou.[174]

2. Effect of single-step annealing

When studying nucleation and precipitation of oxygen in silicon single crystals it is essential to start from a standard specimen.[175]

The ideal conditions would be the following: treatment for as-grown precipitate dissolution and C_{ox} homogeneization at very high temperature (1320 °C); measurement of interstitial oxygen and substitutional carbon content; isochronal or isothermal annealing treatment.

Since ideal conditions are not met systematically, it is difficult to compare the experimental results obtained by different authors. Nevertheless, from the large amount of experimental data on oxygen behavior in silicon upon thermal annealing, some overall considerations could be made.

Generally, a thermal treatment is considered single step when the "as-received" wafer is annealed for the first time and only once. The high-temperature treatment usually performed to dissolve the as-grown precipitates is not taken into account. Oxygen agglomerates formed upon single-step thermal treatments can be divided in two major categories on the basis of their electrical activity:

(i) thermal donors;
(ii) electrically inactive precipitates.

Such a division is further supported by the fact that thermal donors are typically not directly visible by microscopic techniques and could be only revealed by electrical measurements, while the other precipitates have larger dimensions and are directly visible by means of TEM or high-resolution TEM (HREM).

Here we give only a brief overview of the electrically active structures. For general overviews on thermal donors the reader is referred to Refs. 82 and 176–179.

Downloaded 21 Apr 2008 to 146.186.238.16. Redistribution subject to AIP license or copyright; see http://jap.aip.org/jap/copyright.jsp

SIONYX1403000026.0063

SAMSUNG EX. 1002 - 2528/4148

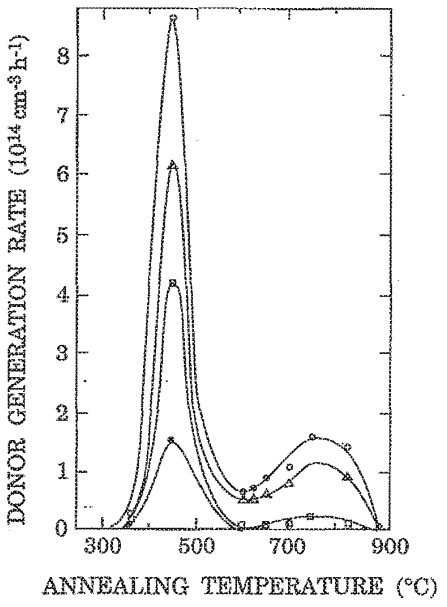

FIG. 45. Donor generation rate as a function of annealing temperature for different initial interstitial oxygen concentrations: 40 ppm (open circles), 37 ppm (triangles), 32 ppm (squares), and 24 ppm (closed circles) (from Ref. 197).

a. Thermal donors. (a) Old thermal donors: Since the early work of Fuller *et al.*[152,180] it is now well established that heat treatment of Cz-grown oxygen-rich silicon in the 350–500 °C temperature range generates microdefects which act as shallow double donor centers, called thermal donors. These centers are often referred to as old thermal donors (OTD), since they were discovered previously with respect to other types of donors. According to the original idea of Kaiser, Frisch, and Reiss[181] it has been widely accepted that OTD are small oxygen aggregates formed at the early stage of oxygen precipitation. Despite an overwhelming number of articles dealing with these donors, their atomic structure and the origin of their electrical activity are still not understood. OTD formation has been studied by a large number of experimental techniques: Resistivity measurements,[182,183] IR absorption,[154,184–186] photoluminescence,[187] Hall effect,[155,188] electron paramagnetic resonance,[189,190] electron nuclear double-beam resonance,[191,192] and deep-level transient spectroscopy (DLTS).[67,193] Since these defects are undesirable in commercial silicon wafers, they are usually eliminated by heat treatments above 500 °C for a few hours.

Several studies[154,188,193] showed that the OTD are double donors with ionization energies of about 70 and 150 meV. Eleven neutral OTD^0 and nine singly charged OTD^+ species have been observed in IR spectra.[194] The individual OTD^0 and OTD^+ species have slightly different ionization energies ranging from 69.2 to 49.9 meV and from 156.3 to 116.0 meV. Very recently Götz, Pensl, and Zulehner[195] have reported the existence of five new effective-mass-like OTD species. They are supposed to develop from the known OTD species via additional atoms. The chemical nature of these atoms is not yet identified, but it is believed that oxygen plays an important role in the formation of such nuclei.

A generation rate of the OTD proportional to the fourth power of the interstitial oxygen concentration was found.[181] Recent results of Londos *et al.*[196] show a strong deviation from the fourth power dependence for several heating temperatures, although they are in agreement with that law for annealing close to 450 °C. The increase of the number of OTD is proportional to the annealing time, the proportionality factors depending on the treatment temperature. The generation rate is maximum at 450 °C and sharply decreases for both low and high temperatures, as shown in Fig. 45.[197] The formation kinetics of the individual OTD does not follow the monomolecular law which is observed for the total OTD concentration.[198] The generation rate of each donor state is different and can be studied by IR absorption. The linear relation between the oxygen loss from the solution and the OTD formation rate shows a derivative varying from below two to nine in the temperature range 300–500 °C.[196] This indicates that oxygen dimerization controls the OTD formation kinetics, but that the dimers become increasingly unstable above 400 °C.

Activation energy for OTD formation is recently reported by Claybourn and Newman[199] to be 1.7 eV for at least six of the nine different OTD^+. Their low activation energy is the main problem for understanding the nature of the OTD.

It was found that different impurities have a significant impact on OTD generation. Some examples follow.

High carbon concentration suppresses the OTD generation.[154,200,201] The concentration of generated OTD can be lowered by up to two orders of magnitude.

Anneal in H plasma increases both the OTD concentration and the oxygen loss from the solution in the temperature range 350–450 °C.[72] Such a treatment increases the OTD density much more than do furnace annealings.

The influence of doping atoms on the OTD generation is still somewhat controversial. In some articles it is claimed that the donor concentration is increased in p-type material and unaffected by n-type doping;[154,200] in some others[132] similar results are reported for p-type material, with a reduced donor concentration observed in n-type material.

In spite of a very large number of articles published on the formation of thermal donors, there is not yet a general agreement on their exact nature. While the original models relate the thermal donors to pure oxygen complexes,[181,202–204] more recently models involving also vacancies[205,206] and silicon self-interstitials[52,69,207] have been proposed.

The current view is that oxygen is involved in the OTD cores and that the different donor states evolve sequentially by addition of oxygen or self-interstitial atoms. Nevertheless, the exact structure and composition of the OTD are still unclear.

(b) New thermal donors: Upon annealing at high temperatures a different type of oxygen-related donor states is observed.[153,155,182,200,208,209] They are known as new donors (ND) and occur in the temperature range 600–900 °C, with a maximum generation rate at about 800 °C (see Fig. 45).

Downloaded 21 Apr 2008 to 146.186.238.16. Redistribution subject to AIP license or copyright; see http://jap.aip.org/jap/copyright.jsp

SIONYX1403000026.0064

SAMSUNG EX. 1002 - 2529/4148

Their formation strongly depends on the interstitial oxygen concentration and hence they are not observed in FZ material. Ionization energy derived from Hall-effect measurements[209] varies between 30 and 120 meV.

The generation rate of ND is proportional to the 4.5th power of C_{ox}, i.e., very close to the behavior of OTD.[155] It can be increased by a preanneal at about 470–550 °C,[155,182] while for ND annihilation heating above 1000 °C is required. The ND generation is found to be higher in p-type than in n-type wafers.[182]

High carbon concentration present in the material accelerates ND formation[155,182] (while it retards OTD formation). Furthermore, Leroueille[210] found that ND formation is inhibited in crystals where the carbon concentration is below the IR detectability threshold even with high C_{ox}. This implies that carbon plays an essential role in the formation of the new donor complexes. Recently, Hahn *et al.*[211] have shown that carbon and oxygen coimplantation strongly enhances the ND formation. ND are most probably related to some kind of oxygen precipitates as they occur in a temperature range in which oxygen precipitation also takes place.[212]

Several models have been proposed to explain the ND formation. Grinshtein *et al.*[213] proposed that large oxygen precipitates upon annealing dissociate in smaller complexes which then become electrically active, while Kanamori and Kanamori[182] extended the Helmreich–Sirtl model[205] for OTD to the ND. Gaworzewski and Schmalz[155] related ND to C-O complexes formed at the initial stage of heat treatment. Pensl *et al.*[212] proposed a "SiO_x interface model" relating ND characteristics to the interface states at the precipitate/silicon interface and to bound states in the SiO_x precipitates. Qian *et al.*[214] explained their formation by the dangling bonds on the small dislocation loops formed by the oxygen precipitation.

Moreover, Wijaranakula and Matlock[215] found that the donors observed upon annealing in the temperature range 500–800 °C have a different nature in carbon-lean and carbon-rich material. They found that in carbon-rich material donor formation corresponds to the reduction of substitutional carbon, while interstitial oxygen concentration does not vary; therefore, they identify ND as carbon donors.

(c) Other oxygen-related donors: Besides OTD and ND, some other oxygen-related donor states have been reported.

In the low-temperature range where OTD are formed, the formation of a new type of shallow termal donors with significantly lower concentration has been found, where nitrogen seems to play a catalytic role.[216,217] These donors are single donors and at least seven different states have been identified with ionization energies between 34.7 and 37.4 meV.

Recently Kamiura *et al.*[218,219] reported the formation of a new type of thermal donors upon prolonged annealing at 450–470 °C in phosphorus-doped Cz silicon. They found them to be double donors with continuously varying ionization levels and broad IR-absorption bands. These donors have a lower generation rate and a higher thermal stability than OTD. Kamiura, Hashimoto, and Yoneta[220] showed that besides OTD and ND also a third and a fourth class of oxygen donor states formed at 520 °C could be distinguished.

TABLE VI. Lattice defect distribution after single- and two-step annealing treatments. An indication of the dependence of defect density on the preannealing temperature is given by the numbers from 1 (minimum) to 4 (maximum) (from Ref. 151).

T (°C)	650	700	750	800	850	900	950	1000
Low-temperature N_2 anneal:								
Rodlike	4	4	3					
Platelike	4	4	4	3	3	2	2	2
Platelike with punching					1	2	2	2
60° dipoles	4	4	4	3				
90° dipoles	3	3	3	3				
With subsequent oxidation (1150 °C):								
Frank stacking faults	3	4	4	4	4	3	1	
Elongated loops	3	4	4	4				
Prismatic loops	3	3	3	3	3	3	3	3
Octahedral prec.	1	3	4	4	4			
Platelike prec.						3	3	3
Prismatic punch.						3	3	3
Irregular loops						3	3	3

b. Large electrically inactive precipitates. Essentially four types of electrically inactive defects caused by oxygen precipitation are known to form after a single-step annealing: rodlike defects, platelike precipitates, dislocation dipoles (60° or 90° type), and prismatic dislocation loops (see Table VI).[151] Somewhat less-defined structures such as "loopites" and "blobs" were also reported.[78] These defects are considered electrically inactive in the sense that they do not provide free carriers to the conduction or valence band; however, they could have a certain impact on electrical properties of silicon, producing deep traps and therefore influencing the carrier lifetime.

(a) Rodlike defects: It is generally accepted that the rodlike (or ribbonlike) defects are formed upon annealing in the temperature range 465–750 °C,[78,151,221–224] although some disagreement still exists.[162,225]

Rodlike defects have also been observed by TEM in samples subjected to ion implantation of many different species under self- or nonself-annealing conditions[226–228] and electron irradiation of Si in the electron microscope.[229]

The rodlike defects are generally aligned with dislocation dipoles[151,221,230] and sometimes are found on dislocation cores.[151,231] They are stable for annealing below 700 °C, as found by Tempelhoff and co-workers,[223] while above this temperature they transform into elongated ⟨110⟩ narrow dislocation loops. Such behavior led the authors to conclude that rodlike defects are a preliminary state of the formation of dislocation dipoles. This idea is also worked out in the nucleation and growth model proposed by Tan.[232]

The ribbonlike defect density increases with anneal time and temperature and reaches a maximum at 650 °C, about 0.3×10^8 cm^{-2}. Similar values of defect density are reported by various authors.[77,78,151,230]

Structural characterization of these defects is performed by HREM (see Sec. IV B).[77,151,175,177,231,233] It is found that each defect consists of a different crystalline phase in the silicon lattice elongated along the ⟨110⟩ direction. The cross section of the largest defect is up to 6×1 nm^2, while the length goes up to several micrometers. The (100) silicon/

Downloaded 21 Apr 2008 to 146.186.238.16. Redistribution subject to AIP license or copyright; see http://jap.aip.org/jap/copyright.jsp

SIONYX1403000026.0065

SAMSUNG EX. 1002 - 2530/4148

precipitate interface is incoherent, and furthermore, it is not strictly, but slightly, zig-zag shaped with small portions following {411} or {311} planes[77,233] (see Fig. 58). On the other hand, the (110) interface is at least partially coherent. Precipitates introduce a dilatation in the [100] directions. (100) planes are displaced by 0.18 a [100] to 0.27 a [100] depending on the precipitate dimension, where a is the lattice constant.

Bourret and co-workers[77] showed that dislocations of the dipoles formed during the low-temperature annealing are decorated by a rodlike precipitate. On the other hand, Bender[151] found such a decoration only on a small number of dislocations.

Tempelhoff *et al.*[221,223] and Yamamoto and co-workers[230] on the basis of TEM and IR analysis attributed rodlike defects to some forms of SiO_x precipitates. In addition, Bourret[177,231] and Bender[151] have identified rodlike defects present after low-temperature annealing of Cz silicon as SiO_2 precipitates in the coesite phase.

Other arguments supporting the interpretation involving coesite are clearly outlined by Bender and Vanhellemont.[130] They are as follows.

Bergholz and co-workers[78] showed that the balance between the oxygen reduction measured in the wafer and the oxygen incorporation into rodlike defects made of coesite is very well fulfilled at 485 °C.

The compressive stress on the precipitates is higher than the minimum pressure at which the coesite is a stable SiO_2 phase. From the temperature-pressure phase diagram of coesite, Bourret and co-workers[77] derived a pressure of 3 GPa for the transformation quartz to coesite. They have also shown the existence of a critical radius of 1.2 nm, below which coesite precipitates are stable.

After a subsequent high-temperature annealing step, during which the rodlike defects annihilate, rows of octahedral precipitates along ⟨011⟩ directions are observed.[130] It has been assumed that these are nucleated on the remainders of the rodlike defects. Similar findings were also reported earlier by Gaworzewski *et al.*[234]

On the other hand, several arguments against this interpretation have been raised by Bourret,[227] Bender and Vanhellemont,[130] Reiche, Reichel, and Nitzsche,[235] and Carpenter *et al.*[236]

On those basis, Bourret[227] dropped the interpretation of the rodlike defects as coesite precipitates and proposed a new model involving hexagonal silicon.

The presence of hexagonal silicon in ion-implanted samples under self-annealing conditions was already reported on the basis of electron-diffraction data.[237,238] Hexagonal silicon is also reported to form after mechanical deformation at moderate temperatures.[237,239,240]

A good matching of the experimental images of the rodlike defects in oxygen-rich silicon with simulated images of the coesite structure along [100] direction exists;[77,151] however, as shown by Bender and Vanhellemont,[233] the simulated images of the coesite structure always look more complicated than the experimental images.

One of the major objections against the coesite nature of the defects is the required enhanced interstitial oxygen diffusion at the low temperature of defect formation. Contrary to the oxygen diffusion data, the reported values for the self-intestitial diffusion scatter over a wide range, depending on the method adopted. The silicon self-interstitial diffusion coefficient reported by Bronner and Plummer[241] and by Mayer, Mehrer, and Maier[242] is about three to four orders of magnitude larger than the oxygen diffusion coefficient in the considered temperature range. It means that the silicon interstitial diffusion is fast enough to form the rodlike defects after the long time annealings even at the lowest formation temperatures.

It was pointed out earlier that the amount of oxygen involved in the formation of coesite defects at the lowest temperatures and of coesite and platelike precipitates at higher temperatures agrees well with the decrease of the interstitial oxygen concentration, as measured by IR spectroscopy. Therefore, the assumption of hexagonal silicon implies that much more interstitial oxygen must have precipitated in platelike form than usually assumed. This is not in contradiction with the experimental findings since small precipitates (<5 nm) cannot be detected by HREM, and therefore an accurate estimate of the precipitate density and size distribution from electron microscopy observations is not possible. Since the critical radius for homogeneous precipitation at these temperatures is very small, oxygen content in platelike precipitates or in their nucleation centers are very likely to be underestimated.

Oxygen agglomeration in platelike precipitates should be a source of silicon self-interstitials due to volume difference between the SiO_x in the precipitates and in the silicon matrix. The total number of interstitials incorporated in the rodlike defects has to correspond to the number of interstitials generated by oxygen precipitation. Bender and Vanhellemont[233] calculated such numbers for annealing at 650 °C for 264 h. They found that the total number per cm^3 of generated self-interstitials is $C_I^g = 2.0\times10^{17}$ atoms/cm^3, while the number per cm^3 of interstitials incorporated in the hexagonal silicon rods is $C_I^{hs} = 1.5\times10^{16}$ atoms/cm^3; however, a large density of interstitials is incorporated also in interstitial-type dislocation dipoles, whose concentration was calculated to be $C_I^{dip} = 1.5\times10^{17}$ atoms/cm^3. This shows that the required conservation of point defects, taking into account the large uncertainty of the estimates, is fulfilled. However, it should be pointed out that the observed hexagonal silicon rods play only a minor role as a sink for self-interstitials; in fact, the self-interstitial balance is mainly obtained by the formation of dislocation dipoles, which can be seen as an evolution of the rodlike defects. A similar result for oxygen balance is found assuming that the rodlike precipitates are coesite. As shown by Bourret and co-workers[77] only ≈10% of oxygen is found in coesite precipitates.

In summary, it may be concluded that many arguments support the hexagonal silicon hypothesis, as suggested by Bender and Vanhellemont.[130]

In other words, a definitive distinction between the coesite and the hexagonal silicon model for the rodlike defects cannot be obtained, either by comparison of simulated HREM images with experimental observations,[243] or by comparison of the lattice spacings in the defects

Downloaded 21 Apr 2008 to 146.186.238.16. Redistribution subject to AIP license or copyright; see http://jap.aip.org/jap/copyright.jsp

SIONYX1403000026.0066

SAMSUNG EX. 1002 - 2531/4148

with the expected values for [100]-oriented coesite or $[2\bar{1}\bar{1}0]$-oriented hexagonal silicon, or by performing the point defect balance.

(b) Platelike SiO_x precipitates: The second type of defects observed after a single-step heat treatment are platelike, present after sample annealing in the temperature range 650–1050 °C. Tempelhoff and co-workers[221] found that these defects have {100} habit planes and ⟨110⟩ edges. The IR spectrum taken on such samples is characterized by an intense double peak with maxima at 1125 and 1222 cm^{-1}. The authors related these structures to the presence of α-cristobalite and Matsushita[162] also reported the presence of α-cristobalite in samples annealed at 800–1100 °C. On the other hand, Bender,[151] on the basis of detailed studies of the precipitate morphology as a function of the anneal time and temperature, has not revealed the presence of crystalline oxide precipitates in this temperature range.

Oxygen precipitates are usually characterized in terms of number density, size, and shape by chemical etching;[41] however, this technique fails for the samples heated at low temperatures since the etch-pit density becomes too large and individual pits cannot be resolved in the micrographs. TEM gives only snapshot views of the samples and the analyzed regions can be unrepresentative of the whole sample, although it has the advantage of showing the structure and morphology of the particles. After anneals below 800 °C, the platelike precipitates are observed as small black dots. Electron-diffraction contrast is caused by the strain field associated with these defects, although in this case only limited information concerning their morphology is obtained.

A more detailed structural characterization of platelike defects can be obtained from HREM imaging.[41,151,244,245] However, even with this technique and even after long annealing time at 650 °C, the precipitates are generally only visible by their strain field which shows up as black dots in the perfect silicon matrix. Dark "blobs" with diameters ranging from 2 to 10 nm are also reported by Bergholz and co-workers[78] in samples subjected to prolonged anneals at 485 °C. Due to the instability under the electron beam the authors interpreted these defects as aggregates of interstitial atoms; however, the similarity of these defects with those reported after annealing at higher temperatures by other authors suggests that blobs are the initial stages of the oxide precipitates. The interpretation of the blobs as precursors of oxide precipitates is also supported by the loss of interstitial oxygen during the annealing.

The composition of the precipitates is measured by electron energy-loss spectroscopy (EELS) by Carpenter *et al.*[246] as $SiO_{1.2}$ and by Skiff, Tsai, and Carpenter[247] as $SiO_{0.95}$. It has to be remarked that electron-beam-induced damage probably plays a significant role in the quantitative results and in the peak shape of EELS spectra since the measurements are performed with very high electron current densities;[130] therefore, the reported stoichiometry is likely to be a lower limit.

Though Tempelhoff and co-workers[221] suggested that the platelets are composed of α-cristobalite, recent IR studies by Borghesi *et al.*[248,249] have shown that, from the analysis of the 1230 cm^{-1} band, information on stoichiometry of the SiO_x in the platelets can be obtained (see Sec. IV C). They have shown that for samples heated at 1100 °C for 1 h the platelets consist of amorphous Si-rich oxide, mainly SiO_x with $x=1.8$. The band line shape indicated the presence of oxides with $x<1.8$, too.

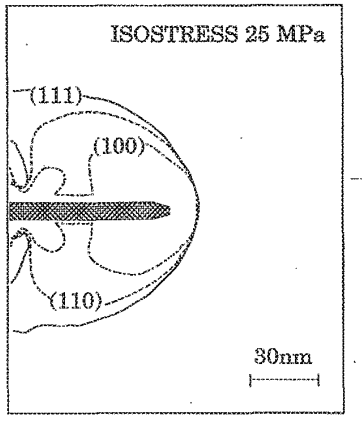

FIG. 46. Elastic isostress curves around a precipitate platelet for different platelet habit planes (from Ref. 156).

SANS studies[41,244] have shown a decrease of the precipitate density and an increase of the precipitate size with anneal time at 750 and 800 °C, and very good agreement among SANS, TEM, and IR analysis was found. Advances in SANS analysis led recently to the development of anisotropic measurements[250,251] (which do not require the comparison with either IR or HREM data), that confirmed earlier findings. By means of SANS, platelets were revealed as cushion-shaped objects[245] lying predominantly on the {100} planes, with edges along the ⟨110⟩ directions. From the comparison of the experimental and calculated scattering density in SANS, Takeda *et al.*[252] conclude that the composition of the platelike oxide precipitates must be oxygen-deficient SiO_{2-y} without further specifying the composition, i.e., their results are in agreement with the most recent IR studies.[248,249]

The tendency of oxide precipitates to develop a platelet morphology on the {100} planes is related to the possibility of total strain energy minimization. For silicon, which has anisotropic elastic properties, the {100} planes are the preferred precipitate habit planes since the Young's modulus of silicon in ⟨100⟩ directions has the minimum value. Theoretical predictions are in very good agreement with the reported data on low-doped Si samples.[253–255]

On the other hand, in an extrinsic silicon degenerately doped by means of substitutional impurities such as boron the hydrostatic compression is partially compensated by the local tensile strain introduced by the impurities. Relaxation of the lattice strain lowers the strain free energy and therefore the total free energy of the precipitate: This facilitates the precipitate growth. Wijaranakula[256] studied the morphology of the oxide precipitates in Cz-grown silicon degenerately doped with boron. In addition to square-shaped precipitate platelets having {100} habit planes, commonly observed in lightly doped silicon, he also found oxide precipitates ex-

Downloaded 21 Apr 2008 to 146.186.238.16. Redistribution subject to AIP license or copyright; see http://jap.aip.org/jap/copyright.jsp

SIONYX1403000026.0067

SAMSUNG EX. 1002 - 2532/4148

hibiting a disk-shaped morphology with both {110} and {111} habit planes. From the calculation of the elastic stress field around the precipitate platelet, as shown in Fig. 46,[256] it is evident that the precipitate grown in a lightly doped silicon is limited to the {100} planes. In silicon degenerately doped with boron the localized elastic modulus of silicon may be reduced and therefore the precipitate orientation is not restricted only to the {100} planes.

(c) Extended defects formed after low-temperature annealing: A phenomenon occurring in parallel with oxygen precipitation is the formation of extended defects which play an important role in the gettering of metallic impurities and are of great importance for device production. Here we briefly illustrate their formation upon low-temperature annealing.

The major extended defects occurring after low-temperature annealing of Cz silicon are dislocation dipoles of 60° and 90° type. They consist of two parallel dislocations along the ⟨011⟩ directions, which have opposite Burgers vectors. The habit plane of the dipoles is close to a {311} plane with a separation between the dislocations of the order of 25–35 nm. The defects are of the interstitial type, i.e., they contain extra silicon atoms.[151,257]

At low temperatures, no dissociation or decoration of the dislocation cores with precipitates is observed, while for treatments above 750 °C heavy decoration of the dislocation lines and dissociation in two partial dislocations occur. Rodlike defects are sometimes found along the dislocation lines.

The density of the 60° dipoles[230] has a similar temperature and time dependence as that of the density of rodlike defects, while the density of 90° dipoles is more than one order of magnitude lower. Several authors[222,235] reported about rodlike defect transformation into dislocation dipoles, and thus further support the self-interstitial nature of the rodlike defects.

The largest extended defects are platelike, present upon annealing above 850 °C and generated by prismatic punching.[151,258] The mechanism by which these defects form is an efficient way to release the strain on the growing precipitates.

3. Effect of two-step annealing

For most of the technological processes multistep annealing treatments are required, but only two of them are relevant for oxygen precipitation. Moreover, the two-step (for example low-high temperature) anneal is considered effective in increasing defect density: The first step leads to the generation of the nucleation centers and the second one to the defect growth. The major defects formed by such treatments[259] are octahedral or platelike precipitates, stacking faults, and different kinds of dislocation loops (see Table VI).

a. Precipitates. For Cz silicon wafers annealed in two steps both octahedral and platelike precipitates are observed. While platelike precipitates were observed even after a low-temperature second step[175] (down to 650 °C), the octahedral ones are formed only when the second step is performed at high temperature (above 1000 °C).[151,162,175,225,257,260] A detailed study of the precipitate morphology demonstrates its dependence on the conditions of the first low-temperature step.[151] If the conditions are such that the platelike precipitates remain small and thin, the lattice strain they produce is relatively small and no generation of prismatic loops takes place. Upon the subsequent high-temperature step the morphology of some precipitates changes from platelike to octahedral, so that the interface energy is minimized. On the other hand, if platelike precipitate formation is accompanied by lattice strain release through a punching mechanism, the platelike shape is stabilized during the high-temperature step and such a kind of precipitate keeps growing.

The precipitate shape is the result of the balance between different free energy contributions (as amply discussed in Sec. III C). As shown by Tiller and co-workers[150,261] thermodynamic considerations favor spherical (polyhedral) precipitate formation at higher temperatures (950–1200 °C). The expressions for the strain energy as a function of the precipitate shape for coherent and incoherent precipitation have been recently discussed by Vanhellemont and Claeys[262] and Taylor, Tan, and Gösele.[263]

Some authors[260,264] reported the presence of prismatic punching around octahedral precipitates; however, as observed by HREM, the silicon lattice around all octahedral precipitates is free from measurable strain:[151,225,259,261] The punching most probably occurs before the change of morphology from platelet to octahedron.

The octahedra have diameters ranging from 15 to 25 nm and facets along {111} and {100} silicon planes. Based upon the size and density of precipitates plus the drop in interstitial oxygen concentration, Ponce, Yamashita, and Hahn[265] concluded that these precipitates are SiO_2 particles. For larger precipitates the {100} boundary planes are absent and the precipitates are regular octahedra. HREM imaging shows that the precipitates consist of amorphous material.[150,225]

EELS has been applied to identify the composition of the octahedral precipitates. Yang and co-workers[264] report a SiO_x composition, without specifying the value of x.

b. Stacking faults. Stacking faults are the most prominent defects after a high-temperature treatment. They are extrinsic, i.e., formed by an extra plane of self-interstitials.

According to the work of Maher, Staudinger, and Patel[266] and the schematic model of Mahajan, Rozgonyi, and Brasen[267] Frank stacking faults are believed to take hexagonal shape. However, a review of TEM and x-ray topography studies of the stacking fault shape as a function of the annealing conditions[130] shows that hexagonal-like Franck defects (i.e., hexagons with rounded corners) form for anneal temperatures ≤1000 °C. At higher temperatures the bulk defects always take a circular shape, even for sizes up to several hundred micrometers.[151,268,269] As for precipitates, the stacking fault shape is determined by the minimum of the free energy required for their formation. The stacking fault energy is minimal for {111} planes.

Oxidation-induced stacking faults (OSF) are defects formed in the near-surface region under oxidizing anneal conditions and take an approximately half-elliptical shape. Their growth rate parallel to the surface is much larger than the perpendicular one. Hasebe *et al.*[270] proposed that oxide precipitates or their nuclei form around 1150 °C in the cooling sequence of the crystal and that these grown-in defects

Downloaded 21 Apr 2008 to 146.186.238.16. Redistribution subject to AIP license or copyright; see http://jap.aip.org/jap/copyright.jsp

SIONYX1403000026.0068

SAMSUNG EX. 1002 - 2533/4148

serve as nuclei for OSF during oxidation. Furthermore, it has been shown[271] that oxygen concentration affects the OSF density, but is not the main parameter in determining their distribution. Therefore, it is concluded that the temperature of the melt is the dominant factor. The experiments of Cho *et al.*[272] show that the formation of OSF nuclei during crystal growth is influenced by dopant type and concentration, pulling rate, and thermal history of the crystals. They propose that the ring distribution of the OSF is related to the presence of two different oxygen species in the melt. SiO_4 clusters directly incorporated in the ingot are proposed to be the nuclei for the OSF.

OSF nucleation mechanism is not yet completely understood. Essentially two models are proposed:[267,273] Dissociation of a perfect dislocation punched out by an oxide precipitate or direct (homogeneous) precipitation of excess self-interstitials in a {111} plane triggered by the stress of the precipitates.

c. Prismatic punching and dislocations. Upon two-step heat treatments, the first above 850 °C and the second between 900 and 1150 °C, platelike precipitates are observed together with complexes generated by prismatic punching and having the shape of loops (see Table VI). A detailed TEM investigation has shown[151,258] that the loops lie on {110} planes and consist of $\langle 1\bar{1}2\rangle$ dislocation segments.

Tan and Tice[258] found that the loops are generated by a successive cross glide of a shear loop which is initially generated in a {111} plane. On the other hand, due to the high formation energy involved, Vanhellemont, Amerlinckx, and Claeys[274] concluded that the direct nucleation of a small shear loop is unlikely and probably starts with an agglomeration of silicon interstitials. This initial nucleus further grows by climb related to the point defect supersaturation. After reaching a critical size, the growth by glide and cross glide can take over until the equilibrium shape is reached.

The loop size in complexes due to prismatic punching is uniform and corresponds to the projected size of the platelike precipitate in the ⟨110⟩ punch directions. This indicates that the precipitates do not significantly grow in the (001) plane after the strain release by punching has started. Then they further grow in a direction orthogonal to their habit plane, thus increasing the strain again. The punching stabilizes the size and platelike shape of the precipitates even at high annealing temperatures.

In the samples for which the first low-temperature treatment produces dislocation dipoles, elongated dislocation loops form during the high-temperature second step. The density of these loops is one order of magnitude lower than the density of the dipoles. The loops are elongated in the ⟨110⟩ directions and are up to 20 μm long.

Hexagonal dislocation loops are also found after the high-temperature step, and for all preanneal conditions, with {011} habit plane. The larger ones are probably generated by a transformation of 90° dipoles, while the smaller ones might be formed on oxide precipitates.[259]

4. Effect of rapid thermal annealing

Modern ULSI processing often requires rapid thermal annealing (RTA) as one of the steps. It consists of a brief ($10-10^4$ s) heat pulse, typically performed at high temperatures, characterized by extremely short (few s) ramps up and down. It is interesting to find out whether and what kind of impact RTA has on oxygen precipitation in silicon.

Hawkins and Lavine[275] have shown that only the time spent at high temperature is important and can influence precipitation, while the rapid rise or fall in temperature does not. They have further shown that for very short pulses (e.g., 2 s), precipitation is reduced by several times. As the duration of the pulse is increased to about 100 s, precipitation recovers to its initial value. For very long pulses (longer than 10^4 s), precipitation decreases to nearly zero. There are no further changes in the precipitation characteristics for pulse times up to 5×10^4 s. These results were interpreted assuming that the thermal pulses modify the initial distribution of heterogeneous nucleation sites. For short pulses, the decrease of sites accounts for the suppressed precipitation. For longer pulse times (about 100 s), the recovery of precipitation is due to a reduction of silicon self-interstitials by outdiffusion, which otherwise limit the rate of precipitation. For very long pulses (10^4 s), all nuclei are dissolved, so that negligible precipitation occurs.

5. Effect of dopant and impurity effect

The study of the influence of heavy doping on oxygen incorporation during crystal growth and on oxygen precipitation started only recently. Some authors suggested that the dopant does not influence the precipitation process directly, and that differences in the precipitation behavior between n^+, p^+, and lightly doped silicon crystals are only due to different levels of oxygen incorporation during crystal growth.[276] On the other hand, other groups found different thermally induced precipitate densities in n^+, p^+, and lightly doped wafers with the same initial oxygen concentration.[277,278] Moreover, Bains *et al.*[279] have recently shown that precipitation is independent of dopant type and concentration in the lightly doped wafers (dopant concentration $\leq 5\times10^{16}$ atoms/cm^3); however, in p^+ boron-doped wafers precipitation was found to be generally enhanced, and in n^+ antimony-doped samples it was retarded, compared with lightly doped control wafers with the same oxygen concentration. A model proposed by Wada and Inoue,[132,280] which involves free-electron effects, appears to be the most plausible explanation of these results. We illustrate now the main results for the most interesting dopants and impurities.

a. Boron. Walitzki *et al.*[276] reported that oxygen precipitation in highly B-doped crystals is only correlated to the oxygen content and is independent of doping level. On the other hand, the experiments of Barraclough[281] on heavily B-doped crystals show that although the total oxygen concentration is similar to the one in low-doped material a significant oxygen clustering takes place already during crystal cooling. He interpretes the results in terms of carrier concentration effect on the formation of termal donors, assumed to be nuclei for precipitation.

TEM studies of the influence of a heavy B doping on the precipitate morphology showed that:

Downloaded 21 Apr 2008 to 146.186.238.16. Redistribution subject to AIP license or copyright; see http://jap.aip.org/jap/copyright.jsp

SIONYX1403000026.0069

SAMSUNG EX. 1002 - 2534/4148

(i) No observable precipitates form at 650 °C, even after 128 h;
(ii) amorphous platelike precipitates form at 800 °C;
(iii) polyhedral precipitates with dislocation loops form at 1050 °C.[282,283]

The precipitate density is larger in heavily than in lightly B-doped crystals, while the growth rate of platelike precipitates is smaller.[284] Hahn *et al.*[283] explain the (i), (ii), and (iii) findings with the formation of B_2O_3 clusters which enhance the oxide precipitate nucleation. The reduced growth rate of platelike precipitates can be understood by a reduced oxygen flux due to the presence of BO_3 clusters, which also diminishes the oxygen supersaturation.

The morphology of the oxide precipitates formed after a two-step anneal in wafers degenerately doped with B was studied by Wijaranakula[256] with TEM. In addition to square-shaped precipitate platelets having {100} habit planes and commonly observed in lightly doped silicon, he found also disk-shaped precipitates both with {110} and {111} habit planes. The presence of complex dislocation loops on the polyhedral precipitates, which are not accompanied by dislocations in lightly doped material, is related to the easier dislocation nucleation and the higher dislocation mobility in heavily doped silicon, which make dislocation nucleation possible even on the stress-lean polyhedral precipitates.[283] On the other hand, it has been reported[285] that the mechanical strength increases for boron concentration above 10^{18} atoms/cm^3. This has been explained by a pinning effect of B_2O_3 or BO_3 precipitates on dislocations.

b. Phosphorus. The influence of phosphorus on the precipitation kinetics has been studied less intensively than the influence of B and Sb. Matsumoto *et al.*[284] reported that the oxygen precipitation kinetics is independent of P-doping level for anneals at 800 and 850 °C. Hahn *et al.*[283] studied the effects of heavy P doping in a wider temperature range (450–1050 °C). They found that the precipitate morphology in heavily P-doped samples is similar to that found in highly B-doped samples, while the precipitate density is lower and the size of precipitates is larger. Diffuse x-ray scattering shows that in such samples interstitial-type defects predominate, while the formation of PO_5 clusters is not favored.

c. Antimony. A high Sb-doping level reduces the amount of precipitated oxygen.[32,95,120,276,277,286,287] Some authors[120,277,287] attribute this effect to the evaporation of Sb_2O_3 from the melt during the growth process. A similar tendency was reported by Walitzki *et al.*,[276] who found that oxygen concentration in Cz-grown silicon crystals highly doped with Sb is reduced by 40% compared to low-doped crystals grown under the same conditions. Nevertheless, these authors believe that evaporation of Sb_2O_3 is thermodynamically unlikely.

Shimura *et al.*[277] supposed that the concentration of negatively charged vacancies is reduced by the Coulomb attraction between Sb^+ and the charged vacancies. They propose that the negatively charged vacancies serve as nucleation centers for oxygen precipitation, so that a high Sb concentration suppresses the precipitation.

Secco d'Aragona and Fejes[288] have reported that in highly Sb-doped wafers oxygen precipitation is reduced and eventually suppressed during high-temperature annealing (1050 °C), while it is independent of doping for low-temperature (650 °C) annealing. This finding suggests a heterogeneous precipitation mechanism for high-temperature annealing.

Barraclough[281] used IR spectroscopy and photon activation analysis to study the behavior of oxygen in electron-irradiated silicon samples heavily doped with Sb or B. He found that the amount of interstitial oxygen is lower and that the precipitation is strongly retarded in the n^+ material. Gupta *et al.*[287] obtained similar results by SANS analysis.

d. Carbon. Carbon plays a major role in oxygen precipitation in silicon at low temperatures and, hence, in device yield,[289,290] when its concentration C_C is above 3×10^{16} atoms/cm^3. It is generally observed that after single-step heat treatments a substitutional carbon to interstitial oxygen ratio as high as 0.3 completely inhibits the development of large precipitates[175] and those eventually formed are too small to be visible even by electron microscopy. Fraundorf and co-workers[134] found a high density (10^{13} cm^{-3}) of small microprecipitates which are under large elastic stress and probably have octahedral shape: No secondary defects were formed, so that interstitial emission seems to be inhibited. However, it is more likely that Si_I clusters remain undetectable because of the high density of nucleating centers (carbon related). Simultaneously, a large number of C-SiO_x complexes are formed, for example after a 750 °C treatment for 64 h.[291]

For two-step annealing treatments and over a large range of C_C/C_{ox} ratio (from 0.3 to 0.01) a "retardation" effect is reported.[292–295] This phenomenon consists of an initial decrease of C_{ox}, followed by an increase (the retardation stage) and a final decrease of interstitial oxygen content (the recovery stage) during the annealing, when the first step is performed in the range 750–850 °C,[125,292] or below 650 °C,[295] for 2–8 h. Tan and Kung[125] have shown that a high carbon concentration is not essential to observe this phenomenon, but can enhance the effect. The retardation is explained by the dissolution of oxide precipitates at the onset of the high-temperature (1050 °C) anneal (second step). Schrems *et al.*[296] applied their statistical modelling of growth and dissolution of oxide precipitates to the retardation/recovery phenomenon, obtaining a very good correspondence between the experimental data of Tan and Kung[125] and the calculated curves.

A study of oxygen precipitation in carbon-rich Cz silicon by synchrotron radiation topography has shown that the samples are strain free.[297] This indicates that coprecipitation of oxygen and carbon occurred so that the volume expansion and reduction due to either species compensate each other. This coprecipitation lowers the critical radius for precipitation and this explains the much higher density of stable precipitates.[53] Evidence for such coprecipitation was found also by Bender *et al.*[298] with HREM, Shimura *et al.*[299] with SIMS, and by Gupta *et al.*[300] by SANS. Recently, Taylor, Gösele, and Tan[301] proposed a strain relief mechanism involving carbon and self-interstitial fluxes to explain the behavior of C and O coprecipitation in silicon.

Downloaded 21 Apr 2008 to 146.186.238.16. Redistribution subject to AIP license or copyright; see http://jap.aip.org/jap/copyright.jsp

SIONYX1403000026.0070

SAMSUNG EX. 1002 - 2535/4148

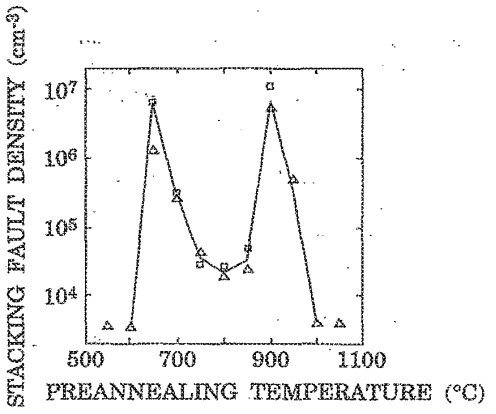

FIG. 47. Stacking fault density in C-rich Cz silicon after a two-step annealing as a function of the temperature of the first step. The second step is performed at 1050 °C for 20 h in N_2 (squares) or in wet O_2 (triangles) ambient (from Ref. 130).

A high carbon content strongly influences the oxygen precipitate morphology. It is found that at low anneal temperatures precipitates take an octahedral shape in carbon-rich more likely than in carbon-lean material.[134] A high carbon content in the precipitates reduces the strain energy so that the octahedral shape (with minimum interface energy) is favored[134,136] (see Sec. III C).

Sun *et al.*[136] found a direct correlation between the reduction of the substitutional carbon and that of interstitial oxygen for annealings at 750 °C by means of FTIR measurements. One carbon atom is transferred to a new configuration for each two oxygen atoms leaving the interstitial position. The total number of substitutional carbon atoms involved in this process is found to be independent of the initial carbon content. They suggested a direct incorporation of carbon in the oxide precipitates, therefore resulting in strain-free octahedral particles. The interaction of substitutional carbon with silicon interstitials and the strain-free precipitates is responsible for the suppression of lattice defect generation.

The number of oxygen atoms leaving interstitial positions for each displaced substitutional carbon atom is 3 at 450 °C, 4 at 750 °C, and 5 at 850 °C, as shown by Newman *et al.*[146] A ratio four to one was also determined by SANS measurements.[300] The observed differences could be attributed to the different sample thermal history.

Carbon presence in Cz silicon inhibits the rodlike defect formation,[77,214,235] but enhances the formation of small amorphous precipitates. Simultaneously, the new donor formation is enhanced, as discussed in Sec. III D 2.

Bender *et al.*[298] studied the variation of stacking fault density in carbon-rich Cz silicon after two-step low-high anneal, as a function of the temperature of the first step. A typical example[130] is shown in Fig. 47 where a strong reduction of the stacking fault density is reported between 700 and 850 °C for samples with $C_{ox}=8.5\times10^{17}$ atoms/cm^3 and $C_C=4\times10^{17}$ atoms/cm^3. The first annealing was performed in N_2 for 15 h and the second one at 1050 °C for 20 h in N_2 (squares) or in wet O_2 (triangles). In the 700–850 °C temperature range the Si-C-O clusters are formed.[134,291] It is therefore very likely that the suppression of self-interstitial supersaturation prevents the secondary defect formation.

e. Nitrogen. The widespread use of a nitrogen ambient during silicon processing and the discovery of the strong effects of nitrogen on mechanical properties of silicon[30,302] led to an increased interest in nitrogen behavior in silicon. Several authors[303,304] studied the influence of nitrogen on oxygen precipitation and it was concluded that it increases the number of nucleation sites. Recently, Sun *et al.*[305] reported the evidence of defect interactions among oxygen, carbon, and nitrogen during a three-step intrinsic gettering process. They found that nitrogen enhances nucleation in the temperature range from 750 to 1100 °C. Their results were interpreted assuming that nitrogen participates in the creation of nucleation sites for heterogeneous oxygen precipitation and also assuming that nitrogen aggregates at the strain regions surrounding the precipitates, thus retarding silicon self-interstitial migration.

f. Hydrogen. Recently the behavior of hydrogen in silicon has been the object of significant interest.[306] It is found that it passivates shallow acceptors (B,Al,Ga) and shallow donors (P,As,Sb)[307] and enhances oxygen diffusion.[72,73] It has been also shown that hydrogen presence enhances thermal donor formation in silicon,[308] suggesting that it may influence oxygen agglomeration. Indeed, Hara *et al.*[309] have shown recently that hydrogen in silicon crystal causes an enhancement of oxygen precipitation. They attributed it to an increase of the nucleation sites, related to small hydrogen aggregates.

If hydrogen affects oxygen precipitation, Hara *et al.*[309] suggested that hydrogen must exist in the form of aggregates, as the defects enhancing oxygen precipitation have high thermal stability.[304] Furthermore, it is well known that hydrogen in crystalline silicon tends to precipitate along the {111}, {113}, and {100} lattice planes.[310,311]

After Hara *et al.*[309] two mechanisms can be responsible for the enhancement of oxygen precipitation by hydrogen. One is an increase of the nucleation sites for oxygen precipitation and the other is an enhanced oxygen diffusion.

g. Intrinsic point defects. The polysilicon film deposited on the wafer back surface was found to be a good extrinsic gettering sink for its ability to generate dislocations and stacking faults at the back surface[312] (see Sec. V). It was also found that the back-surface-deposited polysilicon also enhances oxygen precipitation, therefore increasing the gettering efficiency. The precipitation enhancement effect was thought to be a nucleation effect due to polysilicon deposition thermal cycle.[313] Shirai, Yamaguchi, and Shimura[314] have shown that a polysilicon layer at the wafer backsurface causes localized oxygen precipitation near the back surface. The enhancement effect was attributed to the absorption of silicon self-interstitials by the polysilicon. This causes an increase in vacancy concentration in the nearby silicon layer where vacancies are considered to be effective nucleation sites.

Harada, Abe, and Chikawa[315] studied oxygen precipitation in Cz crystals with excess concentration of vacancies frozen in by detaching the ingot from the melt and by sub-

Downloaded 21 Apr 2008 to 146.186.238.16. Redistribution subject to AIP license or copyright; see http://jap.aip.org/jap/copyright.jsp

SIONYX1403000026.0071

SAMSUNG EX. 1002 - 2536/4148

sequent rapid cooling. They proposed a new model for the enhanced oxygen precipitation in the presence of excess vacancy concentration. Their model has two consequences: One is that the incubation time for oxygen precipitation is short and the other one is that oxygen precipitation occurs even under small supersaturation of oxygen. They also found that the excess self-interstitial atoms incorporated into the crystals during the growth suppresses oxygen precipitation and generates bulk stacking faults.

Hara *et al.*[304] studied the effect of cooling rate on oxygen precipitation in Cz silicon crystals. They found that quenching from high temperature introduces defects that enhance oxygen precipitation. These defects are related to intrinsic point defects, and they disappear upon annealing above 900 °C. Ikari *et al.*[316] obtained similar results by studying nucleation of oxide precipitates in quenched Cz silicon by means of IR spectroscopy and positron annihilation techniques. They found that oxygen clusters are introduced by quenching and that these clusters are the nuclei for the enhanced precipitation in the quenched Si crystal.

Hallberg and Lindström[317] studied the enhancement of oxygen precipitation in electron-irradiated silicon. They have shown that the effects of the presence of vacancy-oxygen (V-O) and vacancy-dioxygen (V-O_2) groups on oxygen precipitation in silicon are significant. The highest density of precipitates was found in samples with the highest initial concentration of V-O_2 defects. This suggests that the V-O_2 centers are nuclei for oxygen precipitation.

IV. TECHNIQUES FOR OXIDE PRECIPITATE CHARACTERIZATION

A. Wet chemical etching

Wet chemical etching is nowadays a very important process in semiconductor industry both for studying defects and for device processing. Although there is not a formal "theory of etching," a few general principles have been developed. Here they are reviewed and a few examples of some representative etchants and their applications described. A general standard method for detection of oxidation-induced defects by wet chemical etching in silicon wafers was developed by ASTM.[318]

1. Etch formulation and application

Whenever demands for a new etchant emerge, the main role in responding to them is played by previous experience on similar materials or systems rather than by straightforward application of chemical theory.[319]

Semiconductor etchants can be divided in two categories, i.e., into selective (often called preferential) and polishing. The ideal polishing etches have material removal rate which is independent of crystal orientation, strain, or chemical heterogeneities, and are inversely proportional to the local radius of curvature. Therefore, a specimen with rough or damaged surface, as cut for example, etched for a sufficient time in a polishing etch, develops a flat mirrorlike surface with rounded edges. This occurs irrespective of defects within the volume of the material. On the other hand, the ideal selective etch acts upon a highly defective but mirrorlike flat surface only at strain or chemical heterogeneities, such as dislocations or impurity striations. However, in practical use etchants do not achieve the ideal properties, but may come close.

TABLE VII. *Recipes for the solutions usually employed for silicon polishing (from Ref. 320).*

Solution	Purpose	Composition (volume)
CP-4A	Polishing, lapping, saw damage removal	3 HF 5 HNO_3 3 CH_3COOH
	Polishing	1 HF 4 HNO_3 2 CH_3COOH
	Slow polishing	1 HF 6 HNO_3 1 CH_3COOH
Iodine	Polishing	5 HF 10 HNO_3 11 CH_3COOH 0.3 g I_2/250 ml sol.

In principle, the chemical action of both polishing and selective etching is the same. One component of the etch solution oxidizes the surface, while another one complexes the oxidizes species to make them soluble in the etching solution. A third component, usually water or acetic acid, is added as a buffer. Insoluble reaction products may be removed mechanically, this being the principle of the chemomechanical polishing process. During the etching process care must be taken to avoid gas formation, since the bubbles can locally block the etching action. This in turn could produce false features during selective etching.

In order to obtain a continuous etching, it is necessary that fresh reactant reaches the surface while the reaction products must be permanently removed, at least as fast as they are involved in the reaction. If the reaction rates at the surface are much higher than the diffusion rate in the liquid, the process will be diffusion limited, as almost all polishing processes are.

Some useful recipes for silicon polishing[320] are given in Table VII.

2. Chrystallographic defects evidenced by selective etching

Even during selective etching, for reasonable etching times, the polished damage-free surface of a perfect crystal remains flat, provided no gas develops and the reaction products do not stick to the surface. Damaged areas, however, are etched faster and grooves or pits are formed, remaining after the initially strained material has been etched away. Once formed, upon further etching the pits become flat bottomed and continue to expand only laterally. A similar situation happens in the case of defects such as stacking faults, inclusions, and small dislocation loops.

Different features are observed in the case of line defects such as treading or slip dislocations, and "sheet" inhomogeneities such as growth striations. In that case the strain is not removed. For example, the dislocation etch pits continue to grow without changing shape and maintain their morphol-

Downloaded 21 Apr 2008 to 146.186.238.16. Redistribution subject to AIP license or copyright; see http://jap.aip.org/jap/copyright.jsp

SIONYX1403000026.0072

SAMSUNG EX. 1002 - 2537/4148

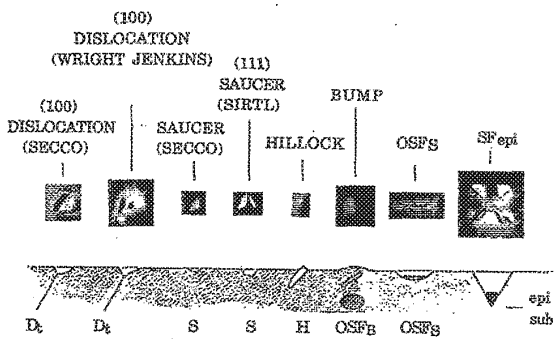

FIG. 48. Etch features found in silicon using some of the etchants listed in Table VIII: dislocation (D_t), saucer (S), hillock (H), bulk and surface oxidation stacking fault (OSF_B and OSF_S), epitaxial layer stacking fault (SF_{epi}) (from Ref. 319).

ogy. If the dislocation is not normal to the surface, the pits have a distorted morphology. Therefore, both line and localized defects may have the same morphology initially, but upon continued etching the localized defects develop pits with a flat bottom, while dislocation pits continue to deepen with a sharp bottom (see D_t and S in Fig. 48 and Fig. 49).

During selective etching etch hillocks may form, which can be easily confused with pits when observed by the optical microscope. Hillocks are usually caused by precipitates from the etch which adheres to the surface, or small unresolved oxide particles which mask the surface. Nevertheless, they can also be associated with defects, such as certain bulk precipitates or stacking faults in silicon (see *H* in Fig. 48).

The principles discussed above can be illustrated by the results obtained on silicon for which several highly refined selective etches have been developed, such as the so-called Sirtl,[322] Secco,[323] Wright,[324] Schimmel,[325] and Yang[326] etches.

Chemical recipees for silicon selective etchants are given in Table VIII.

3. Optical microscopy

The above-mentioned defects evidenced by preferential chemical etching are usually analyzed by an optical microscope or, with much higher magnification and resolution, by a scanning electron microscope (SEM). Optical microscopy limit magnification is ×2000, while SEM allows magnifications up to the order of $\times 10^5$. On the other hand, optical microscopy is a more versatile technique and is the most used for precipitate density measurements.

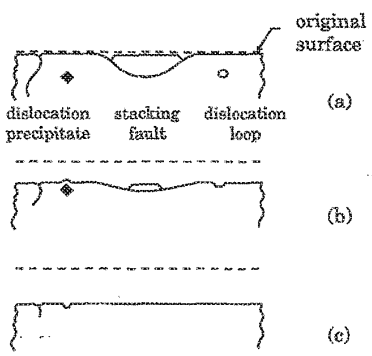

FIG. 49. (a)–(c) Scheme of three etching steps, showing the development of characteristic etch features (from Ref. 321).

TABLE VIII. Recipes for the most common selective etchants for silicon.

Etch	Composition (Volume)	Comments
Sirtl	1 HF (49%) 1 CrO_3 (5 M)	~3.5 μm/min rate good on {111} poor on {100} faceted pits
Secco	2 HF (49%) 1 $K_2Cr_2O_7$ (0.15 M)	~1.5 μm/min rate best in ultrasounds good on all planes non-cryst. pits
Wright	2 HF (49%) 2 CH_3COOH 1 HNO_3 (70%) 1 CrO_3 (4 M) 2 $Cu(NO_3)_2 \cdot 3H_2O$ (0.14 M)	~1.7 μm/min rate no ultrasounds good on all planes faceted pits good shelf life
Schimmel	2 HF (49%) 1 CrO_3 (1 M)	lightly doped Si (0.6–15 Ω cm) good on {100} no ultrasounds
Schimmel (modified)	2 HF (49%) 1 CrO_3 (1 M) 1.5 H_2O	heavily doped Si good on {100} no ultrasounds
Yang	1 HF (49%) 1 CrO_3 (1.5 M)	good on all planes no ultrasounds 1–2 μm/min rate

The resolution of optical microscope is limited by the diffraction effects, so that two points are just resolvable when they are separated by d,

$$d = \frac{0.61\lambda}{n \sin u}, \tag{87}$$

where λ is the wavelength of light, n the index of refraction of air (or immersion oil), and u is the vertical angle of divergence that the objective lens can accept. The product $n \sin u$ is called the numerical aperture (NA). Since the NA limits the resolution of the microscope, a greater magnification obtained by means of high-power oculars with lenses of low NA does not produce more details. For example, the resolution of the best microscopes is about 0.2 μm.

Although conventional optical microscopes are still widely used in reflection mode for opaque objects such as silicon wafers, a significant improvement has been made when Nomarski and Weill in 1952 proposed the interference-contrast method.[327] It has become the most important method for optical examination of semiconductor surfaces upon wet chemical etching.

The instrument based on the Nomarski interference method is essentially a two-beam microscope as illustrated in Fig. 50, showing the light beam path in the instrument. Entering from the left-hand side, the light passes through a polarizer set at 45°, being reflected downward by a half-

Downloaded 21 Apr 2008 to 146.186.238.16. Redistribution subject to AIP license or copyright; see http://jap.aip.org/jap/copyright.jsp

SIONYX1403000026.0073

SAMSUNG EX. 1002 - 2538/4148

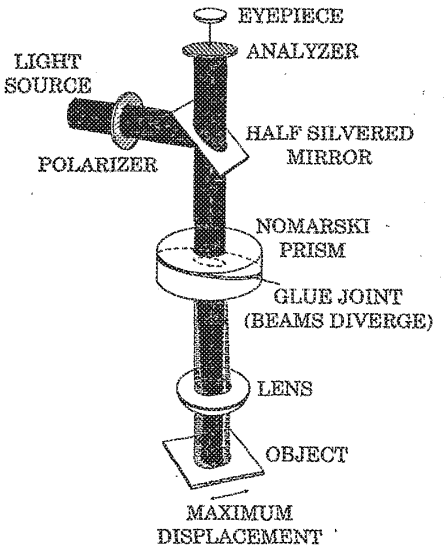

FIG. 50. Schematic diagram of the Nomarski differential interference-contrast microscope (from Ref. 319).

silvered mirror, and passes through the modified Wollaston or Nomarski prism where the light beam is split in two parts. The two beams then pass through the objective lens, are reflected from the object, and, after crossing lens, prism, mirror, and a polarizer set at 135° (analyzer), reach the eye. The Nomarski prism is made of two separate birefringent quartz prisms glued together, having perpendicular optical axes. The 45°-polarized light from the polarizer forms two components in the first birefringent prism, traveling with different speeds due to the different indices of refraction along and perpendicular to the optical axis. Then, upon striking the glue joint, they form the two divergent beams. Since the optical axis of the second prism undergoes a 90° rotation with respect to first one, the speeds are interchanged.

The thickness of the two parts of the Nomarski prism can be chosen so that the two beams come out of the prism in phase. The angle of divergence is matched up with the focal length of the objective lens so that the two beams are focused parallel onto the object. For an object having a flat surface, upon reflection the beams reach the glue joint forming a single beam that is extinguished by the analyzer set at 135°. This configuration is called the null or dark mode in the Nomarski differential interference contrast method. However, if the prism is moved to one side or the other a phase shift between beams occurs. As a result an elliptically polarized beam forms when the rays join and such a beam is not stopped by the analyzer. As a consequence, more light is transmitted.

When the prism is moved far enough, the phase shift becomes so large that the shortest visible wavelengths (dark blue) begins to interfere destructively and the resulting light becomes yellow. Additional colors appear as the prism is moved further away from the null position. It should be noted that this happens regardless of the absolute height of the flat surface observed.

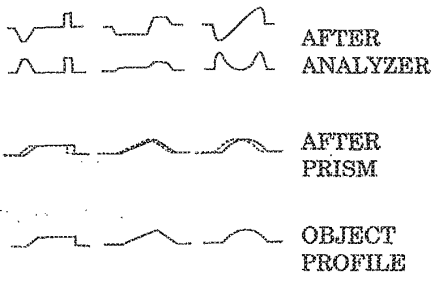

FIG. 51. Schematic illustration of object profiles, wave fronts of the displaced beams after reflection, and intensity distribution of the recombined beams after passing the analyzer for two different prism settings (from Ref. 319).

As an example, we can consider an object with a vertical relief and the beams displaced about 0.2 μm one from the other. Such a beam displacement is below the resolving power of the microscope and thus is not observed. Figure 51 illustrates an image formation for different object profiles.[319] The profiles on the bottom line represent the cross-sectional shape of three different objects. In the middle line, displacements of the wave fronts of the two beams are indicated immediately after reflection and crossing the prism. The top lines give the resulting intensity distribution after the beams have passed through the analyzer. One set of profiles (the lower one) on the top line corresponds to a null setting of the instrument which yields a black background. The other set (the upper one), which is a more common operating mode, corresponds to the prism setting slightly off null position, hence giving a grey background. The width of the displacement is magnified in the diagram and in practice it will appear just as a line. It should be pointed out that the surfaces having the same slope have the same contrast (or color), and also horizontal surfaces having different height have the same contrast. The interference contrast obtained by the microscope is proportional to the beam displacement, therefore it is maximum along the direction of displacement, and no contrast is visible in a perpendicular direction. These principles are illustrated schematically in Fig. 52. Note that only the step running parallel to the beam displacement (x direc-

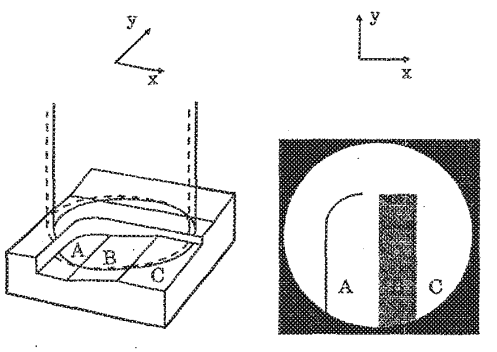

FIG. 52. Schematic illustration of an object with the two incident beams (left-hand side) and resulting images (right-hand side) (from Ref. 319).

Downloaded 21 Apr 2008 to 146.186.238.16. Redistribution subject to AIP license or copyright; see http://jap.aip.org/jap/copyright.jsp

SIONYX1403000027.0001

SAMSUNG EX. 1002 - 2539/4148

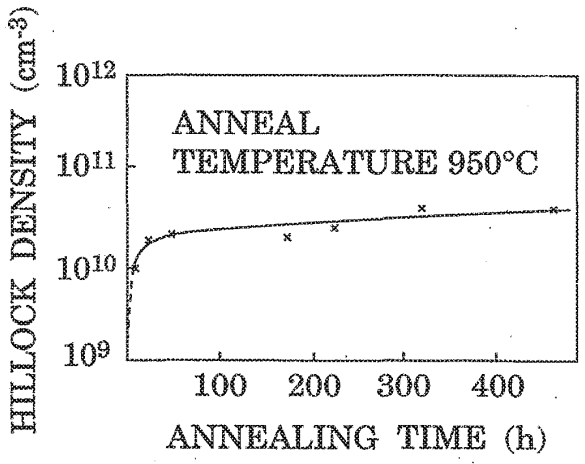

FIG. 53. Density of large etch hillocks as a function of annealing time at 950 °C (from Ref. 143).

tion) forms virtually no observable image. Step heights as low as 30 Å and the corresponding slopes (30 Å in about 0.2 μm beam separation) can be detected. Therefore, etch pits with side slopes of only a few degrees produce a sharp contrast and may appear deeper than they actually are. Absolute evaluation is possible with comparison of known features on the surface.

4. Detection of SiO_x precipitates

Wet chemical etching with optical microscopy is widely employed to measure the density per unit area of precipitates on silicon wafer surfaces, thus allowing the average density of bulk defects to be estimated. For example, Newman *et al.*[143] by analyzing silicon wafers after Wright etching and after different heating times found two types of etch features: Small pits which appeared to be present in as-grown crystals, which can be resolved after heating, and larger etch hillocks which were only observed after heat treatment. The density of the latter defects increases with the heating time up to 50 h and then remains constant (see Fig. 53). The density of small pits N (in cm^{-3}), decreasing with the annealing time, when measured after long sample annealing fits the empirical relation

$$N=0.15\ \exp(2.65/kT), \tag{88}$$

with kT expressed in eV, as shown in Fig. 32 in Sec. III B, where the results are compared with the defect density deduced from the kinetic model.

Clear evidence of the nonhomogeneous axial distribution of oxide precipitates through the seed end of a Cz silicon single crystal is reported in Fig. 54.[328] The figure shows the convex and concave layers of precipitates revealed after 1000 °C annealing. The distribution of precipitates in the same crystal as in Fig. 54 at different axial positions is reported in Figs. 55(a)–55(d).[328] This figure shows the precipitate distribution at the center of the crystal (a), and at 1/2, 3/5, and 4/5 radius [(b), (c), and (d), respectively]. At the center the precipitates are more homogeneously distributed.

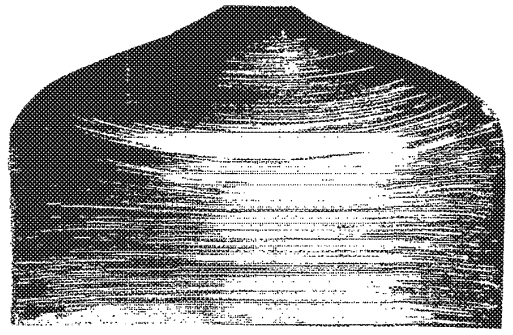

FIG. 54. Axial section of the seed end of a Cz crystal showing precipitate layers as evidenced by etching (from Ref. 328).

The layers with low precipitate density (dark stripes) are very thin, and their thickness increases with the distance from the center of the crystal [Figs. 55(b) and 55(c)]. At 4/5 radius distance [Fig. 55(d)] most of the precipitates disappeared and the residual precipitate layers are very thin.

Bains *et al.*[279] studied oxygen precipitation in p^+ and n^+ dislocation-free Cz silicon wafers. After a three-step treatment, 16 h at 1100 °C, 64 h at 650 °C, and 20 h at 1050 °C, the Sb-doped samples were etched for 30 min with Wright etch and the B-doped ones for 4 min with the modified Schimmel etch. They found that in p^+ B-doped samples precipitation is enhanced and in n^+ Sb-doped samples it is retarded with respect to lightly doped reference samples with the same oxygen concentration, where the precipitation behavior is independent of dopant type and concentration. Figure 56 shows[279] two images of the etched cross section of a p^+ ([B]=9×10^{17} atoms/cm^3) sample with 7.6–8.96×10^{17} atoms/cm^3 interstitial oxygen concentration after the three-step annealing. The figure evidences the formation of oxygen-related platelet defects. Moreover, precipitate-free regions surrounding these defects are visible, probably caused by the gettering effect of the platelets on the oxide precipitates present in the sample.

B. Transmission electron microscopy

Transmission electron microscopy is a well-known technique, particularly powerful to study defects and small aggregates where high space resolution is needed.[329] Broad range applications of electron microscopy in the high-resolution mode (HREM) have been actually devoted to study defect structures of various types (linear, planar, dislocation cores, grain boundaries, etc.). To achieve the extreme resolution limits the key parameter on which to act is the accelerating voltage of the instrument. For instance, distances and features having dimensions decreasing from 2.1 to 1.6 Å can be resolved[329] when the voltage is raised from 200 to 400 keV: Therefore, the point defects can also be directly observed by TEM.

The main sources of the noise, which represents the limiting factor for detecting small clusters, are essentially two: Thickness variation of the matrix (due, for instance, to oxide formation, as in silicon) and surface roughness. The two of

Downloaded 21 Apr 2008 to 146.186.238.16. Redistribution subject to AIP license or copyright; see http://jap.aip.org/jap/copyright.jsp

SIONYX1403000027.0002

SAMSUNG EX. 1002 - 2540/4148

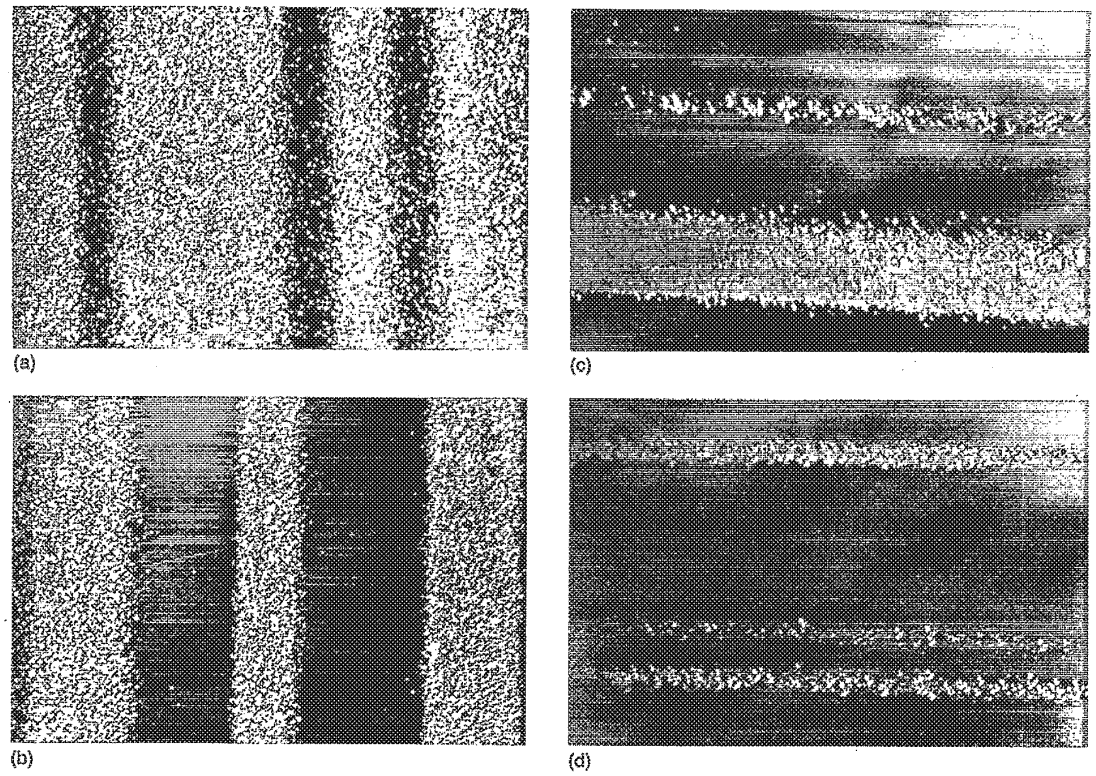

FIG. 55. Precipitate distribution (a) in the center, (b) at 1/2, (c) at 3/5, and (d) at 4/5 radius of the same crystal as in Fig. 54 (from Ref. 328).

them give a coupled contribution to statistical noise corresponding to ±4 atomic steps if one wants to investigate small aggregates with a signal-to-noise ratio S/N ~1.[329] As a consequence, 4^1, 4^2, and 4^3 impurity atoms should be included along the direction of the electron beam for observing linear, planar, or three-dimensional agglomerates, respectively. In order to detect aggregates of defects at such a low S/N ratio, a minimum density of 10^{15} defects/cm^3 is required. Also scanning transmission electron microscopy, which allows electron microdiffraction using a subnanometer probe, is affected by the same limitations.

Information from TEM on particle size and shape is direct, since a large region in reciprocal space is sampled, whereas, e.g., SANS explores only a small volume of k space. In other words, with TEM very small volumes are examined and the response is strictly an image of such a specific part of the sample, which might diverge even substantially from that of the bulk.

TEM is one of the most used techniques for the study of oxygen precipitation in silicon,[141,265,266] often combined with other analytical methods such IR absorption,[234] SANS,[244] and x-ray topography. TEM, with respect to other techniques, allows one to determine the shape of individual pre-

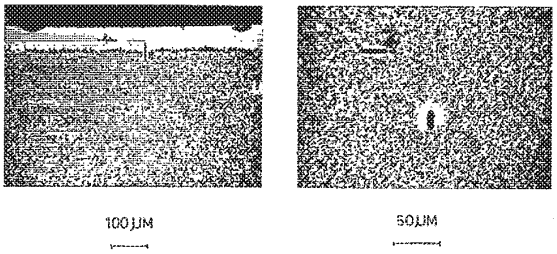

FIG. 56. Preferential etch cross sections of a p^+ wafer showing gettering of oxide precipitates by platelet defects formed after a tristep heat treatment (from Ref. 279).

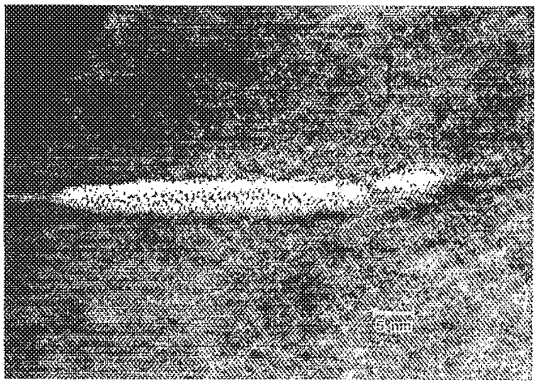

FIG. 57. HREM image of a platelet precipitate grown after annealing at 850 °C for 60 h. The image shows the amorphous structure and the orientation along {100} silicon planes (from Ref. 150).

Downloaded 21 Apr 2008 to 146.186.238.16. Redistribution subject to AIP license or copyright; see http://jap.aip.org/jap/copyright.jsp

SIONYX1403000027.0003

SAMSUNG EX. 1002 - 2541/4148

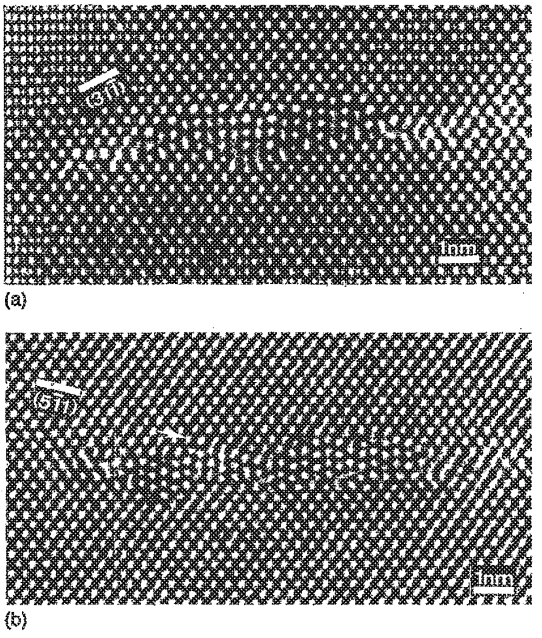

FIG. 58. High-resolution images of rodlike defects seen along their elongated axis: zig-zag shape of the defect consisting of one part along $(31\bar{1})$ plane and one along (100) plane (upper image); the arrow indicates the interface plane $(5\bar{1}1)$ (lower image) (from Ref. 233).

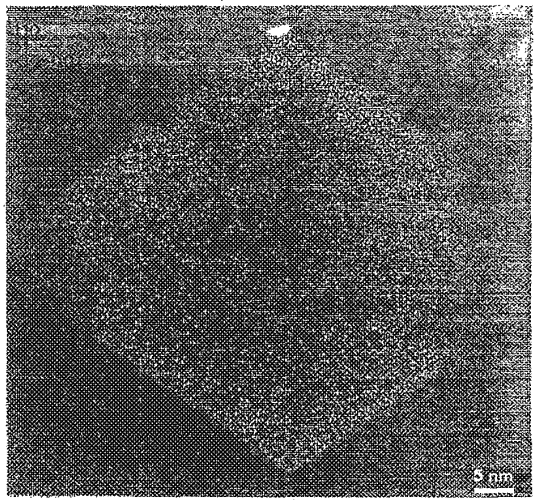

FIG. 59. High-resolution image of a truncated octahedral precipitate, showing its amorphous structure (from Ref. 151).

cipitates as well as their structure (amorphous or crystalline) and their interfaces with the host crystal. For example, TEM images are reported by Tiller and co-workers[150] to confirm the results of a model concerning the equilibrium shape for thermally induced microdefects in Cz silicon, based on thermodynamic and kinetic considerations (see Sec. III C). Figure 57 shows a HREM image of an amorphous platelet precipitate grown after intermediate-temperature annealing (850 °C for 60 h) of a Cz silicon sample. The platelet lies parallel to {100} silicon planes. The correlation between circular stacking faults in silicon and subsurface precipitates has also been demonstrated by a TEM study.[330] As for the precipitate structure and orientation in the silicon crystal, in several articles these characteristics have been studied as a function of the particular annealing conditions. Recently, a review of the results about the structure of oxygen-related lattice defects in silicon has been presented by Bender and Vanhellemont,[331] with the comparison of different techniques.

A detailed TEM study of oxygen-related lattice defects in Cz silicon samples after one- and two-step annealing at different temperatures is reported by Bender.[151] After a one-step treatment at low temperature (in the region from 550 to 1000 °C) rod-shaped coesite precipitates, platelike amorphous SiO_x precipitates, dislocation dipoles, and prismatic loops were found. After a subsequent high-temperature (1150 °C) step different types of defects such as Frank-type stacking faults, elongated dislocation and prismatic loops, octaedral amorphous SiO_x precipitates, and plateletlike SiO_x precipitates with prismatic dislocation loops were observed.

As an example of HREM images Fig. 58(a) and 58(b) shows rodlike defects seen along their elongated axis, detected in samples annealed at 650 °C for 100 and 264 h, respectively.[233] In the upper image the zig-zag shape of the defect is found, consisting of two parts along the $(31\bar{1})$ plane and one part along the (100) plane. The lower image shows a defect with lattice planes straight and parallel; partly $(5\bar{1}1)$ interface planes are visible (see the arrow). Figure 59 reports a HREM image of a truncated octaedral precipitate observed[151] after a two-step annealing (850 °C 15 h+1150 °C 1.5 h). The amorphous structure of this kind of precipitate is clearly evidenced.

Bergholz *et al.*[244] studied systematically the defects induced in Cz silicon wafers with initial $C_{ox}=10^{18}$ atoms/cm^3 by a 48, 96, and 431 h annealing at 750 °C, performing also a direct comparison with SANS data (see Sec. IV D). Their results are summarized in Table IX where defect type, size, volume, and density as obtained from TEM images in Cz silicon samples annealed at 750 °C for different times are reported. In the samples annealed for 48 h the defects were amorphous oxide platelets lying on {100} planes and extrinsic stacking-fault dislocation loops on {111} planes. The plate diameters vary from 6 to 16 nm with 1.5 nm mean thickness. The precipitate density was 1.4×10^{13} cm^{-3}. About 60% of oxide plates present a narrow "teethlike" extension at one end. These extensions, about 35 nm long, are an extremely thin oxide layer contiguous with the main plate. Sometimes precipitates made of only the teeth (without the plate) are present, attributed by the authors to early stages of the oxygen precipitation. The samples annealed for 48 h also show SiO_2 spherical particles with an amorphous structure. They have a diameter of about 3.5 nm and their density is about 10^{12} cm^{-3}.

The main defects present in the samples annealed for 96 h are amorphous oxide plates lying on {100} planes and extrinsic stacking-fault dislocation loops on {111} planes. The plates have a density of 1.5×10^{13} cm^{-3} with a diameter of

Downloaded 21 Apr 2008 to 146.186.238.16. Redistribution subject to AIP license or copyright; see http://jap.aip.org/jap/copyright.jsp

SIONYX1403000027.0004

SAMSUNG EX. 1002 - 2542/4148

TABLE IX. Defect type, size, volume, and density as obtained from TEM images in Cz silicon samples annealed at 750 °C for different times (from Ref. 244).

Anneal time (h)	Type	Size (nm or nm^2)	Volume (cm^3)	Density (cm^{-3})
48	Plate	12×1.5	2.2×10^{-19} [a]	5.6×10^{12}
48	Plate with teeth	12×1.5 plus 35×0.4	7.1×10^{-19} [b]	8.4×10^{12}
48	Sphere	~3.5	$\sim2\times10^{-20}$ [c]	$\sim10^{12}$
48	Dislocation loop	~73		
96	Plate	20×1.7	6.8×10^{-19}	1.2×10^{13}
96	Plate with fins	20×1.7 plus 8×15	1×10^{-18} [d]	3×10^{12}
96	Sphere	~4	$\sim3\times10^{-20}$ [c]	$\sim10^{12}$
96	Dislocation loop	~48		
431	Plate	26×2.5	1.7×10^{-18}	3×10^{12}
431	Plate with fins	26×2.5 plus 5×7	2.6×10^{-18}	4.5×10^{12}
431	Sphere	~4.5	$\sim5\times10^{-20}$	$\sim10^{14}$
431	Dislocation loop	~45		6×10^{12}

[a]Assumes a 12×12×1.5 nm^3 square plate.
[b]Assumes a 12×12×1.5 nm^3 square plate plus a 35×35×0.4 nm^3 square plate.
[c]Assumes a sphere of diameter 3.5 nm.
[d]Assumes a 20×20×1.7 nm square plate and calculated volume for plate multiplied by 1.5 to give volume for plate with fin.

20 nm and a thickness of 1.7 nm. The 80% of the precipitates have the plate shape, but the other 20% have in addition a "finlike" extension on one side or on both sides. Amorphous spherical particles with a mean diameter of 4 nm and density of about 10^{12} cm^{-3} are also present.

Also in the samples annealed for 431 h the main defects are amorphous oxide plates on {100} planes and extrinsic stacking-fault dislocation loops on {111} planes. The plate diameters were about 26 nm, thickness 2.5 nm, and density about 7.5×10^{12} cm^{-3}. In this case the TEM micrographs showed that about 40% of the precipitates were plates and the other 60% have the "plate with fins" shape. These finlike extensions are typically 8 nm wide at the base where they join the main plate. They extend for about 15 nm in the

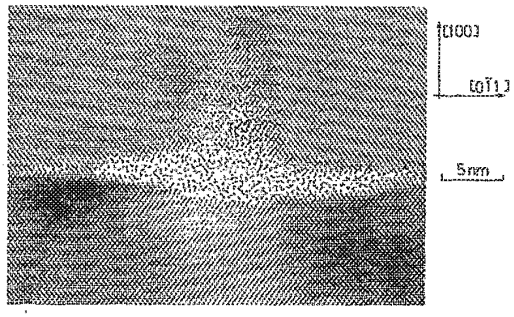

FIG. 60. HREM image of a platelike precipitate with finlike extension observed in a silicon sample annealed at 750 °C for 431 h (from Ref. 244).

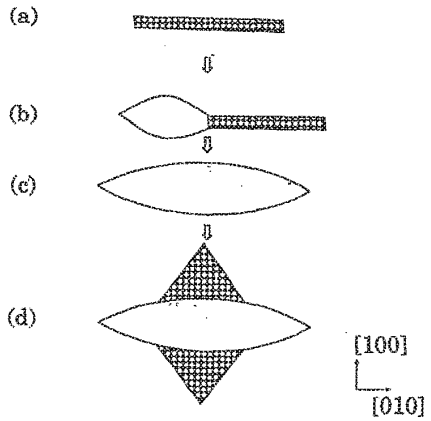

FIG. 61. Scheme of the development of a precipitate along (100) plane: (a) double-row structure; (b) double-row structure with platelet; (c) platelet; (d) platelet with fins (from Ref. 244).

directions perpendicular to the plate. This last type of precipitate is very similar to the octahedral precipitates found by several authors[123,142,265,331,332] and predicted by thermodynamic considerations.[150] Figure 60 shows a HREM image[244] of a typical platelike precipitate with a finlike extension. The main habit plane is the (100) silicon lattice plane. The TEM results just illustrated suggested to Bergholz *et al.*,[244] for Cz silicon samples annealed at 750 °C, the precipitation sequence reported in Fig. 61. Precipitation starts with the formation of a thin oxide plate on a {100} plane, formed only by few atomic layers. At one end the thickness increases, then spreads along the tooth and leads to the formation of a bigger plate. This process is partially due to the oxygen diffusion from the thin region to the thick one, proceeding until the thin portion of the precipitate dissolves. The thick plate then develops the fins, which make the precipitates assuming the octaedral shape. To accommodate the volume of the oxide plates in the silicon, interstitial silicon atoms are produced, some of which combine forming the extrinsic stacking-fault dislocation loops observed in those samples.

HREM measurements allowed investigations of precipitate shape and composition also at early stages of oxygen precipitation[77] in Cz silicon after 5 days annealing at 650 and 870 °C. Two kinds of precipitates are observed: Rodlike-shaped precipitates made of a crystalline silica phase (coesite), and dot-shaped precipitates made of an amorphous oxide phase. Both types are detected in the samples treated at 650 °C. After heat treatment at 870 °C the small dot precipitates grow in size assuming a square shape and lying on {100} planes. The thickness of all these precipitates is so small (about 1.5 nm) that they could not be detected by conventional methods.

C. Infrared absorption

Oxygen precipitation in silicon can be studied using IR spectroscopy in two ways. One of them can be defined as an indirect method for detection and quantitative evaluation of precipitated oxygen. It is based on the measurement of inter-

Downloaded 21 Apr 2008 to 146.186.238.16. Redistribution subject to AIP license or copyright; see http://jap.aip.org/jap/copyright.jsp

SIONYX1403000027.0005

SAMSUNG EX. 1002 - 2543/4148

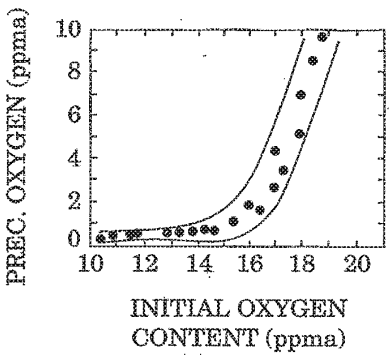

FIG. 62. Results of the statistical reduction of test A data (from Ref. 333).

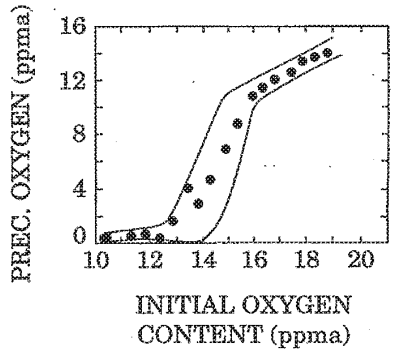

FIG. 63. Results of the statistical reduction of test B data (from Ref. 333).

stitial oxygen concentration by the intensity of the 1107 cm^{-1} band before and after the precipitation annealing. Assuming that the decrease of C_{ox} is only due to precipitation, such a decrease can be considered a measure of the concentration of precipitated oxygen. The second method, more recent and sophisticated, is a direct one and is based on the detection and analysis of precipitate-related absorption bands in the mid-IR spectral range. Although data analysis is not straightforward, this second method can provide more information about precipitates (shape, composition, orientation, local density) and can be used also for as-grown silicon, where the first method is completely ineffective due to its higher sensitivity limit. In this subsection both methods of analysis are described and the most significant experimental data available in the literature reported.

1. Indirect precipitate detection

The procedure for the evaluation of interstitial oxygen concentration C_{ox} by the IR-absorption band at 1107 cm^{-1} in the room-temperature spectrum of silicon is described in Sec. II C 1 and the conversion factors reported. Therefore, only the use of this procedure for the study of oxide precipitates is illustrated here.

The reproducibility of the results of this indirect method has been recently tested[333] to state whether it is suitable for the development of an ASTM standard test method. B- and P-doped Cz silicon samples (100) oriented and with 10–15 Ω cm resistivity (p type) and 1.5–7 Ω cm resistivity (n type) are studied. The samples from different silicon material vendors have been studied in different laboratories by measuring the difference ΔO_i of interstitial oxygen concentration before and after one of two kinds of thermal treatments, called test A and B. Test A consisted of a 16 h annealing at 1050 °C and test B was the same as test A, but with a 4 h preheating at 750 °C. All other annealing parameters (ramp up and down, push and pull rate, ambient) were the same.

The values of ΔO_i obtained for p- and n-type wafers after A and B heat treatments are determined for samples with different initial oxygen concentrations. A statistical reduction of the data was performed by evaluating, for each 0.5 parts per million atoms (ppma) interval in initial C_{ox}, the average values of C_{ox} and ΔO_i. The results obtained in a single laboratory by a FTIR instrument are reported in Figs. 62 and 63 for samples subjected to A and B tests, respectively. The solid lines around the data points in the figures represent the 2σ band in ΔO_i as calculated from the data of four laboratories. After test A no precipitation detectable as ΔO_i occurs in samples with initial C_{ox} lower than about 8×10^{17} atoms/cm^3 (15–16 ppma), then precipitated oxygen increases up to 4×10^{17} atoms/cm^3 in samples with 9×10^{17} atoms/cm^3 initial C_{ox}. A different behavior was found for the samples subjected to test B. Precipitation begins to be detectable for initial C_{ox} as low as 6.5×10^{17} atoms/cm^3 and rapidly increases (for samples with 7.5×10^{17} atoms/cm^3 initial O_i concentration precipitated oxygen reaches $5-6\times10^{17}$ atoms/cm^3); then the precipitation rate decreases ($\Delta O_i \sim 7\times10^{17}$ atoms/cm^3 for 9×10^{17} atoms/cm^3 initial O_i).

Some possible sources of error in the measurements of C_{ox} are present:

(i) the backside roughness of the wafers;
(ii) the different type of IR spectrometer (dispersive or Fourier transform);
(iii) different software package to calculate C_{ox};
(iv) after heat treatment the oxide precipitate band can overlap the interstitial oxygen peak leading to an incorrect value of C_{ox}. Nevertheless, some conclusions can be drawn:

(1) No differences are evidenced in oxygen precipitation from n- and p-type silicon at the doping level tested;
(2) the thermal treatments carried out in different laboratories give completely equivalent results;
(3) the preheating enhances oxygen precipitation (see Sec. III D).

On this basis an ASTM standard method for oxygen precipitation characterization in silicon wafers by the measurement of interstitial oxygen reduction was developed in 1989.[334] This standard illustrates a method of selection and preparation of test samples, evaluation of error sources, and calculation and interpretation of the results.

2. Direct precipitate detection

The first evidence of an effect of SiO_x precipitates on the Si optical properties was reported by Kaiser[19] who detected

Downloaded 21 Apr 2008 to 146.186.238.16. Redistribution subject to AIP license or copyright; see http://jap.aip.org/jap/copyright.jsp

SIONYX1403000027.0006

SAMSUNG EX. 1002 - 2544/4148

IR light scattering in heat-treated Cz silicon. The pioneer work by Patrick[335] showed that an IR-absorption band at about 1230 cm^{-1} rises in Cz Si samples where oxygen precipitation occurred during heat treatment for long times. Hu and Patrick[336] studied the effect of oxygen concentration on dislocation movements, correlating dislocation size and IR-absorption spectra. A series of indents was made to create dislocations in Si samples with C_{ox} ranging from 5×10^{17} to 15×10^{17} atoms/cm^3 and annealed for different times (from 20 min to 240 h) at different temperatures (from 700 to 1300 °C). The IR-absorption spectra clearly show, for long sample annealing at 1000 °C, a significant reduction of the intensity of the 1107 cm^{-1} absorption band indicating a reduction of interstitial oxygen concentration. In the same spectra a new absorption band appears at 1230 cm^{-1} due to the clustering of oxygen atoms. From then on, the behavior of the IR-absorption band at about 1230 cm^{-1} related to precipitated oxygen was extensively analyzed. For example, Rozgonyi and Pearce[337] evidenced that when oxidizing the wafers in HCl-added oxygen ambient the 1225 cm^{-1} band disappears, due to the reduction of oxygen precipitation. From IR-absorption spectra where a 1225 cm^{-1} band is present Hu[111] showed that oxidizing ambients strongly retard precipitation. The investigation of the 1225 cm^{-1} absorption band after sample annealing at different temperatures allowed Shimura *et al.*[90,260] to conclude that the precipitates are made of cristobalite and they form through heterogeneous nucleation.

Tempelhoff *et al.*[222,223] studied oxygen precipitation in dislocation-free Cz silicon subjected to annealing at temperatures ranging from 400 to 1000 °C and compared the results obtained from IR and TEM measurements on the same samples. They found that oxide precipitates present a different shape depending on the annealing temperature.

In the low-temperature range (from 400 to about 750 °C), where the spectra show a broad absorption peak growing in intensity and shifting its maximum from 1030 to 1100 cm^{-1} with increasing the temperature, the precipitates consist of amorphous SiO_x ($x<2$), which transforms into SiO_2 if the annealing temperature is raised. In this temperature range TEM images show the appearance of rodlike defects and their transformation in dislocation loops.

In the intermediate temperature range (about 750–950 °C) the appearance of two intense peaks at 1125 and 1222 cm^{-1} in the high-energy region of the spectra and at 489 cm^{-1} in the low-energy region lead the authors to the conclusion that α-cristobalite precipitates were formed. In this temperature range TEM measurements reveal the presence of dislocation loops and platelet-shaped precipitates.

After high-temperature annealing (about 950–1100 °C) a decrease in the intensity of the two high-energy peaks as well as of the low-energy peak occurs, while two peaks at 1100 and 472 cm^{-1} show up. This was interpreted by the authors as due to the conversion of α-cristobalite into amorphous SiO_2. TEM images of the same samples show the dissolution of platelet-shaped precipitates and the formation of microprecipitates.

Results of IR-absorption measurements and of high-resolution TEM investigation on oxide precipitates in Cz silicon specimens after heat treatments in the temperature range from 600 to 1275 °C were also reported by Gaworzewski *et al.*[234,338] By analyzing samples with initial interstitial oxygen concentration from 0.9 to 1.5×10^{18} atoms/cm^3 and with carbon concentration from 10^{16} to 10^{17} atoms/cm^3, they found that at least four different kinds of precipitates exist, depending on the temperature of heat treatment, on oxygen and carbon concentrations and on the thermal history of the samples. The correlation[234] between IR-absorption spectra and the corresponding TEM micrographs of the four different precipitates is shown in Fig. 64. In Fig. 64(a) the broad band centered at about 1085 cm^{-1}, obtained after annealing samples with $C_{ox}=1.4\times10^{18}$ atoms/cm^3 and $C_C=2.2\times10^{16}$ atoms/cm^3 for 240 h at 600 °C, is clearly correlated to the presence of rodlike defects. In Fig. 64(b) the broad band centered near 1100 cm^{-1}, less symmetrical than that reported above, is obtained after annealing samples with $C_{ox}=1.5\times10^{18}$ atoms/cm^3 and $C_C=10.5\times10^{16}$ atoms/cm^3 for 64 h at 900 °C. In this case TEM micrographs show the presence of a high density of globular-shaped precipitates with small size. In Fig. 64(c) the IR spectrum characterized by a double band with peaks at about 1120 and 1225 cm^{-1} obtained after annealing for 64 h at 900 °C Si samples with $C_{ox}=1.4\times10^{18}$ atoms/cm^3 and $C_C=6\times10^{16}$ atoms/cm^3 is reported. The authors do not confirm the presence in this case of α-cristobalite precipitates, as proposed by Tempelhoff *et al.*,[222,223] because some of the spectra do not show the characteristic absorption band of cristobalite at 485 cm^{-1}. Instead, they suggest that the double-peak structures observed in the absorption spectra of these samples may be due to the contemporary presence of the precipitates shown in Fig. 64(b) responsible for the absorption at 1120 cm^{-1}, and a new form of precipitate responsible for the absorption at

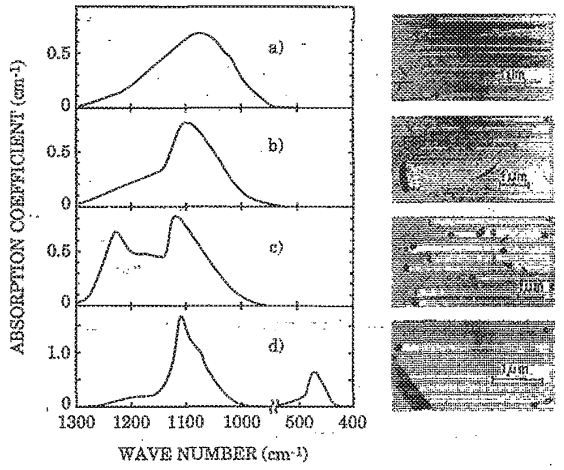

FIG. 64. Infrared-absorption spectra and high-resolution transmission electron microscopy images of different silicon samples annealed in the temperature range 600–1275 °C. The sample characteristics and annealing conditions are: (a) $C_{ox}=1.4\times10^{18}$ atoms/cm^3, $C_C=2.2\times10^{16}$ atoms/cm^3, annealed for 240 h at 600 °C; (b) $C_{ox}=1.5\times10^{18}$ atoms/cm^3, $C_C=10.5\times10^{16}$ atoms/cm^3, annealed for 64 h at 900 °C; (c) $C_{ox}=1.4\times10^{18}$ atoms/cm^3, $C_C=6\times10^{16}$ atoms/cm^3, annealed for 64 h at 900 °C; (d) $C_{ox}=1.6\times10^{18}$ atoms/cm^3, $C_C\leq10^{16}$ atoms/cm^3, annealed for 2 h at 1275 °C (from Ref. 234).

Downloaded 21 Apr 2008 to 146.186.238.16. Redistribution subject to AIP license or copyright; see http://jap.aip.org/jap/copyright.jsp

SIONYX1403000027.0007

SAMSUNG EX. 1002 - 2545/4148

1225 cm^{-1}. This last band, as also suggested by Hu,[339] can be attributed to platelet-shaped precipitates. TEM micrographs reveal the formation of irregularly shaped precipitates with a weakly decreased density with respect to those found in the samples of Fig. 64(b). The IR spectrum reported in Fig. 64(d) shows two absorption bands at 1105 and 470 cm^{-1} and refers to samples with $C_{ox}=1.6\times10^{18}$ atoms/cm^3 and an undetectable C_C, annealed for 2 h at 1275 °C. The spectrum shows the same features as the typical spectrum of amorphous bulk SiO_2 and was found only in Si wafers initially oxygen rich and carbon free (under the IR detection limit). The TEM pattern evidences faceted octahedral precipitates and do not show any defects of small size, except those induced by octahedral precipitates.

The first model to justify the absorption band at about 1230 cm^{-1} of SiO_2 precipitates in silicon was proposed by Hu.[339] He approximated the precipitates by ellipsoids with axes (a_1,a_2,a_2), obtaining in this way with continuity the different shapes from the needle $(a_1=\infty)$ to the sphere $(a_1=a_2)$ to the disk (or platelet, $a_1=0$). For small precipitates (less than 0.36-μm-long axes) the electric field E_p inside the particles can be considered uniform and is given by

$$\mathbf{E}_p=\mathbf{g}\mathbf{E}_m, \tag{89}$$

where $\mathbf{E}_m$ is the electric field in the silicon matrix and $\mathbf{g}$ is a tensor. If the complex dielectric functions ϵ_m and ϵ_p of the matrix and precipitate compounds are isotropic, for a particular choice of the axes of the ellipsoid with respect to the coordinate system $\mathbf{g}$ becomes diagonal, with elements

$$g_i=\frac{\epsilon_m}{L_i\epsilon_p+(1-L_i)\epsilon_m}, \tag{90}$$

where $i=1-3$ and L_i are geometrical parameters related to the depolarization factors along the i axis of the ellipsoid. When the precipitates are randomly oriented in the silicon lattice the net effect is obtained by averaging over all the orientations, therefore $\mathbf{g}$ is a scalar,

$$g=\tfrac{1}{3}(g_1+g_2+g_3). \tag{91}$$

According to the effective medium theory,[340,341] the average electric field of the composite medium $\mathbf{E}_{avg}$ is given by

$$\mathbf{E}_{avg}=(1-f)\mathbf{E}_m+f\mathbf{E}_p, \tag{92}$$

where f is the volume fraction occupied by the precipitates in the sample, and

$$\mathbf{P}_{avg}=(1-f)\mathbf{P}_m+f\mathbf{P}_p, \tag{93}$$

where $\mathbf{P}_{avg}$, $\mathbf{P}_m$, and $\mathbf{P}_p$ are the average polarization vectors of the composite medium, the matrix and the precipitates, respectively. From Eqs. (89), (92), and (93) the average complex dielectric function ϵ_{avg} of the composite medium is obtained as

$$\epsilon_{avg}=1+\frac{(1-f)(\epsilon_m-1)+f(\epsilon_p-1)g}{(1-f)+fg}. \tag{94}$$

Then, the absorption coefficient α can easily be calculated as

$$\alpha=\frac{\mathrm{Im}\ \epsilon_{avg}}{\mathrm{Re}\ n_{avg}}2\pi\bar{\nu}, \tag{95}$$

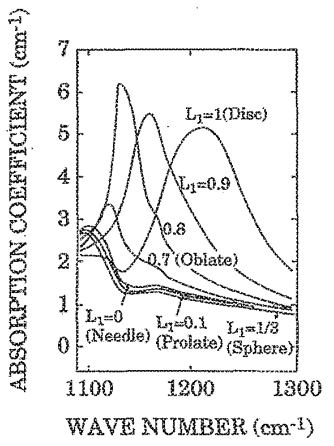

FIG. 65. Calculated infrared-absorption spectra of silicon substrates with 50 ppm volume of small SiO_2 particles of various shapes (from Ref. 339).

where n_{avg} is the average complex index of refraction calculated from ϵ_{avg} $(n=\sqrt{\epsilon})$ and $\bar{\nu}$ is the wave number.

Figure 65 shows the absorption coefficients calculated from Eq. (95) of 50 ppm of SiO_2 precipitates embedded in the silicon sample, under the hypothesis of different precipitate shapes.[339] The curves are labeled using the values of the depolarization factor L_1, i.e., with $L_1=1$ (disk), $L_1=0.9$, 0.8, 0.7, 1/3 (sphere), 0.1 and 0 (needle). The results of Fig. 65 were obtained considering the refractive index of silicon equal to 3.35 and the extinction coefficient to 2.5×10^{-5} $\bar{\nu}^{-3.13}$ ($\bar{\nu}$ in cm^{-1}) and ϵ_p taken from the literature SiO_2 optical functions.[342]

It is interesting to note that the depolarization factors $L_1=1$ and $L_2=L_3=0$ correspond to thin plates of all shapes and, in particular, to the disk shape. This last morphology is typical of oxide precipitates in silicon after sample annealing at intermediate temperatures (see Sec. III C). Moreover, the frequency of the experimentally observed absorption band at about 1230 cm^{-1} appears reasonably close to 1215 cm^{-1}, which is the one calculated for disks. Hu[339] assigned the 1230 cm^{-1} band to the longitudinal-optical (LO) mode of SiO_2 composing the precipitates, suggesting that LO mode, usually IR inactive in bulk materials, can be detected in particular system such as the disk-shaped precipitates in silicon. Figure 65 shows that the 1215 cm^{-1} band is absent in the calculated spectra of spherical SiO_2 particles embedded in silicon. In this case a less-pronounced peak at about 1095 cm^{-1} and a very weak peak at 1170 cm^{-1} show up, attributed by Hu to transverse optical (TO) mode and TO+LO mode, respectively. Finally, it is worth noting that no information comes from the reported analysis concerning the structure, crystalline or amorphous, of the precipitates.

Shimura and co-workers[291] investigated the relation between carbon atoms in substitutional positions and oxygen precipitation in Cz silicon crystals on the basis of a detailed analysis of the 1225 and 1124 cm^{-1} absorption bands related to SiO_x precipitates.

A very interesting comparison between IR spectra and

Downloaded 21 Apr 2008 to 146.186.238.16. Redistribution subject to AIP license or copyright; see http://jap.aip.org/jap/copyright.jsp

SIONYX1403000027.0008

SAMSUNG EX. 1002 - 2546/4148

microdefects in bulk Cz silicon wafers subjected to single-step isothermal, two-step (low-high and high-high), and three-step (high-low-high) annealing was performed by Kung.[343] In the absorption spectra of the single-step-annealed samples a broad peak at 1230 cm^{-1} is observed, becoming very strong in the spectra of three-step-annealed samples where also a new band at 1125 cm^{-1} is present. After the low-high two-step annealing no absorption bands in the range from 1100 to 1300 cm^{-1} were observed. After the high-high two-step annealing the spectra are very similar to those of single-step-annealed samples, but present a significantly lower peak amplitude. According to Hu[339] the appearance of a sharp peak at 1230 cm^{-1} in the spectra of samples subjected to a three-step annealing reveals the presence of tiny platelet-shaped precipitates. The band at 1125 cm^{-1} in the same spectra is attributed to thicker platelets. After the single-step annealing platelet precipitates are also present, but their density in the samples is lower with respect to the density in three-step-annealed samples. Moreover, many precipitates are tangled with dislocations and do not have exactly the platelet shape. Therefore, the 1230 cm^{-1} absorption peak detected in the spectra of the single-step-annealed samples is not as sharp and intense as in the spectra of three-step-annealed samples. In the two-step annealed samples no platelet particles are observed and this clarifies why the absorption band at 1230 cm^{-1} is absent in the corresponding spectra.

IR absorption was also successfully applied, in addition to other techniques, to investigate the effect of electron irradiation on oxygen precipitation in silicon samples annealed at 900 °C for up to 444 h, after the irradiation by a 2 MeV beam with doses ranging from 10^{15} to 10^{18} cm^{-2}.[317] Two kinds of defects were formed by irradiation in the silicon samples, i.e., vacancy-oxygen centers and vacancy-dioxygen centers. In all the samples an enhanced oxygen precipitation rate was detected; in the samples with the first kind of centers it was only a transient process related to a dose-dependent decreasing of the nucleation time (see Sec. III A). On the contrary, in the samples with vacancy-dioxygen centers the enhancement of precipitation is a more stable phenomenon, attributed to the fact that such defects act as nuclei for precipitation, although quite inefficient. The different nucleation times observed for the different IR-absorption bands confirm their origin from differently shaped precipitates.

An oxygen precipitation enhancement was also observed[344] in FZ silicon samples ($C_{ox}=1.8\times10^{17}$ atoms/cm^3) irradiated with thermal neutron doses of 2.9×10^{17} and 1.13×10^{18} neutrons/cm^2. After 30 min annealing the IR spectra of all the samples treated at temperatures higher than 600 °C evidenced the typical absorption band due to SiO_x precipitates. The neutron-irradiated silicon samples present a lot of vacancy-type defects which probably act as precipitation nuclei also when the interstitial oxygen concentration is very low, as in FZ samples.

Recently, Borghesi *et al.*[345] showed evidence of oxygen precipitation in Cz silicon samples annealed at 1100 °C for only 80 min, while the usual precipitation annealing takes several hours. This was made possible by the development of

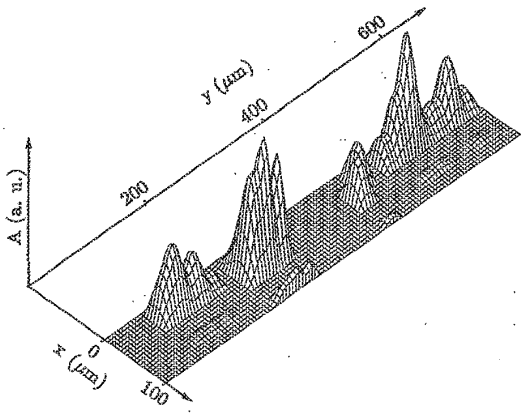

FIG. 66. Map of absorbance values at 1230 cm^{-1} as a function of the position where the spectra were taken on the sample surface (*xy* plane) (from Ref. 348).

a new high-spatial-resolution technique,[346] which allows one to perform IR-absorption measurements on sample regions as small as 20 μm in diameter. Spatial resolution is higher than that used in previous microscopic IR studies,[347] and a deeper analysis of the results can be performed, thus obtaining more information about the characteristics of SiO_x precipitates in silicon. Such a high-spatial-resolution technique applied to oxide precipitates detection gives the following two advantages. First, by performing several series of measurements on a high number of adjacent spots it is possible to draw a map of IR absorption at 1230 cm^{-1}, i.e., a map of discoidal precipitates present in the samples.[348] In this way, the inhomogeneous precipitate distribution within the samples was detected, as shown in Fig. 66, where the absorbance values at 1230 cm^{-1} are reported as a function of the spot coordinates on the sample surface where the corresponding spectra were collected. Second, a very small average concentration of discoidal SiO_x precipitates can be re-

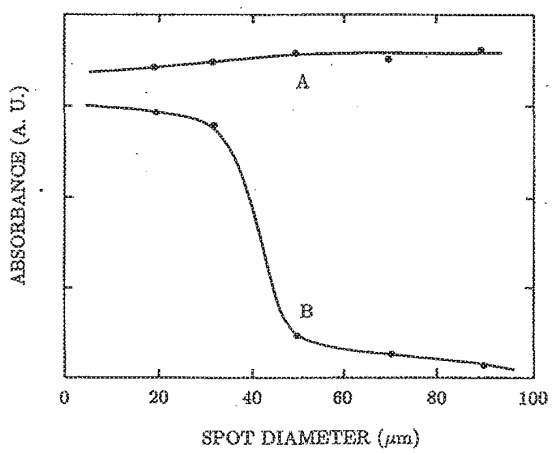

FIG. 67. Intensity of 1107 and 1230 cm^{-1} absorption bands (curve A and B, respectively) in one particular site as a function of the spot diameter used for the measurements (from Ref. 345).

Downloaded 21 Apr 2008 to 146.186.238.16. Redistribution subject to AIP license or copyright; see http://jap.aip.org/jap/copyright.jsp

SIONYX1403000027.0009

SAMSUNG EX. 1002 - 2547/4148

vealed when using spot diameters small with respect to the standard dimensions (~1 cm). This was demonstrated by collecting several IR spectra at the same position on the sample using different spot sizes. For a spot diameter from 20 to 50 μm the absorption band at 1230 cm^{-1} was detected (curve B), whereas the same band is no longer observable when the spot grows larger, as shown in Fig. 67. At the same time, the 1107 cm^{-1} band intensity (curve A) remained constant, indicating a homogeneous distribution of the interstitial oxygen atoms. This has been interpreted as due to the fact that with large spots the sample volume investigated during the measurements is so large that the concentration of precipitates over all this volume decreases below the IR detection limit. Such a behavior can be related to the inhomogeneous distribution of precipitates in as-grown samples or after short annealing treatments.

Using the same technique, evidence of oxygen precipitation occurring in epitaxial silicon layers was achieved.[349] In principle, this should not be possible, because epitaxially deposited silicon layers are oxygen free. As a matter of fact, oxygen has been shown[350] to diffuse during epitaxial deposition to about 15–20 μm from the Cz substrate into the epitaxial layer through the detection of the 1107 cm^{-1} absorption band (related to the presence of interstitial oxygen). A summary of high-spatial-resolution IR results concerning both oxygen diffusion into the epitaxial layer and formation of SiO_x precipitates was presented by Pivac *et al.*,[351] who studied differently doped substrates and epitaxial layers.

A local preferential orientation of the disk-shaped precipitates in the silicon lattice has been deduced[351,352] from IR measurements performed at different sample orientations with respect to the incident beam, which show a strong dependence of the 1230 cm^{-1} absorption band on orientation. According to the effective medium theory, in fact, only when the electric field of incident radiation is perpendicular to the diskoidal precipitates does absorption at 1230 cm^{-1} occur. Therefore, the detected anisotropy in IR absorption leads us to conclude that the SiO_x particles giving rise to the absorption within the analyzed volume are preferentially oriented.

The orientation effect of the disk-shaped precipitates in silicon on IR absorption has been investigated by some of the authors[353] by comparing effective medium theory results and IR spectra collected with polarized light. Considering the precipitates as disks lying on the (x,y) plane, which is also the plane of incidence during IR-absorption measurements, in the coordinate system of the ellipsoid principal axes the elements of the tensor g [see Eq. (90)] become

$$g_{xx}=g_{yy}=1, \tag{96}$$

and

$$g_{zz}=\frac{\epsilon_m}{\epsilon_p}. \tag{97}$$

Therefore, Eq. (89) for the cases of light polarized along the different axes leads to different electric field components inside the particles, i.e.,

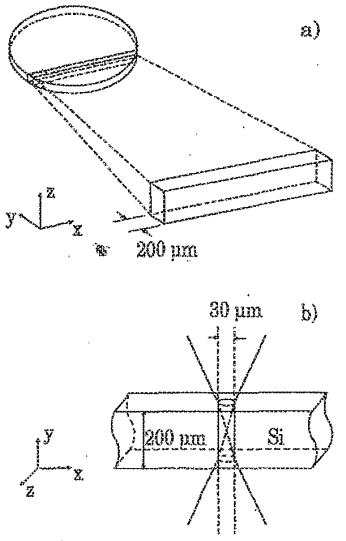

FIG. 68. (a) Picture showing the stripe cutting from the silicon wafer; (b) experimental configuration used for the absorption measurements (from Ref. 353).

$$E_p^x=\begin{pmatrix}1&0&0\\0&1&0\\0&0&\epsilon_m/\epsilon_p\end{pmatrix}\begin{pmatrix}E_m^x\\0\\0\end{pmatrix}=\begin{pmatrix}E_m^x\\0\\0\end{pmatrix}, \tag{98a}$$

$$E_p^y=\begin{pmatrix}1&0&0\\0&1&0\\0&0&\epsilon_m/\epsilon_p\end{pmatrix}\begin{pmatrix}0\\E_m^y\\0\end{pmatrix}=\begin{pmatrix}0\\E_m^y\\0\end{pmatrix}, \tag{98b}$$

and

$$E_p^z=\begin{pmatrix}1&0&0\\0&1&0\\0&0&\epsilon_m/\epsilon_p\end{pmatrix}\begin{pmatrix}0\\0\\E_m^z\end{pmatrix}=\begin{pmatrix}0\\0\\E_m^z(\epsilon_m/\epsilon_p)\end{pmatrix}. \tag{98c}$$

Then, following the same procedure as that illustrated above [see Eqs. (89), (92), and (93)], different expressions for ϵ_{avg} in the case of light polarized along the x (or y) axis or along the z axis can be obtained,

$$\epsilon_{avg}^x=(1-f)\epsilon_m+f\epsilon_p \tag{99a}$$

and

$$\epsilon_{avg}^z=\frac{\epsilon_m\epsilon_p}{(1-f)\epsilon_p+f\epsilon_m}. \tag{99b}$$

If the disks (precipitates) are randomly oriented the effective dielectric function of the samples should be an average of expressions (99a) and (99b), and no polarization-dependent IR spectra are expected. On the contrary, in the case of a preferential orientation of the precipitates, spectra collected with different light polarizations must be different, as confirmed with measurements performed on differently oriented samples. Figure 68 shows the sample cutting procedure (a) and the experimental configuration (b) corresponding to the

Downloaded 21 Apr 2008 to 146.186.238.16. Redistribution subject to AIP license or copyright; see http://jap.aip.org/jap/copyright.jsp

SIONYX1403000027.0010

SAMSUNG EX. 1002 - 2548/4148

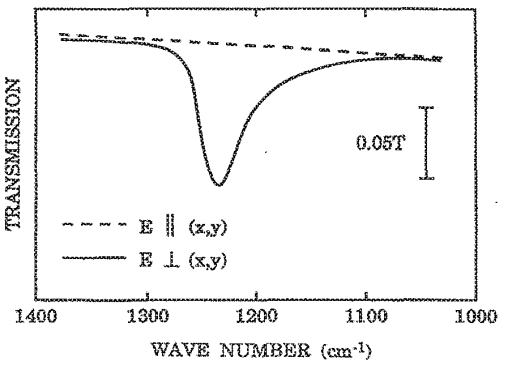

FIG. 69. Transmission spectra calculated on the basis of Eqs. (11), (95), and (99) for a 200-μm-thick sample with 5 ppm volume of oxide precipitates (from Ref. 353).

assumptions made to derive Eqs. (99a) and (99b) and used to collect the transmission spectra, while Fig. 69 shows the results of the calculations in terms of transmission of a 200-μm-thick sample with volume fraction of the precipitates $f=5$ ppm. Figure 70 reports high-spatial-resolution spectra collected with incident light unpolarized [Fig. 70(a)] or polarized [Fig. 70(b)] along the x axis (0°), along the z axis (90°), and along intermediate directions (30° and 60°). From the comparison of the results of Figs. 69 and 70 it is easy to conclude that the precipitates are strongly oriented. In particular, (x,y) plane, corresponding to the (100) crystallografic plane of silicon, is their habit plane. This conclusion is not completely equivalent to the conclusions of the kinetic

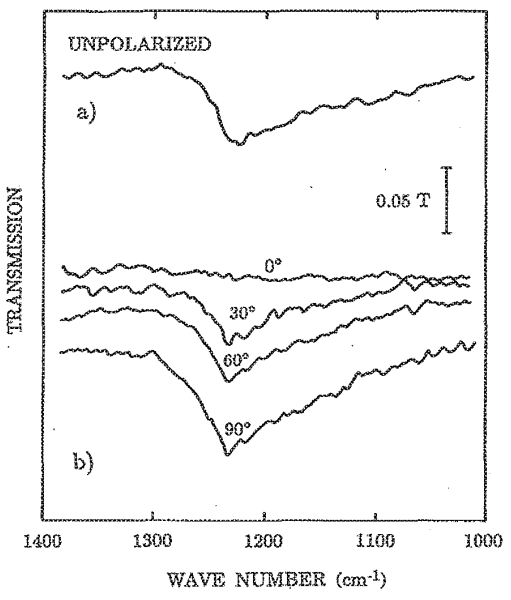

FIG. 70. (a) Relative transmission spectrum taken with unpolarized light; (b) spectra taken on the same position with light polarized along the x axis (0°), the z axis (90°), and two intermediate directions (30° and 60°) (from Ref. 353).

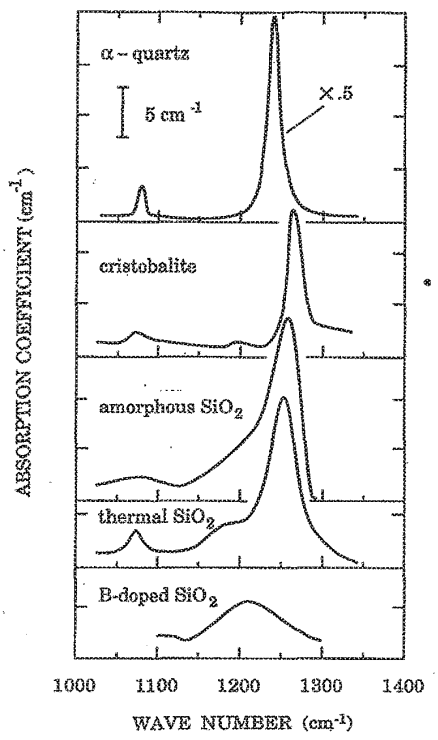

FIG. 71. Absorption coefficient calculated for silicon with 5 ppm volume of oxide precipitates made of different SiO_2 polymorphs (from Ref. 248).

model for the formation of disk-shaped SiO_x precipitates about their orientation (see Sec. III C). Also the kinetic of precipitation predicts the {100} as the habit planes, but it does not distinguish among all the equivalent {100} planes, i.e., the (100), (010), and (001). On the contrary, the IR results by Borghesi *et al.*[248,249,353] indicate that the precipitates mainly lie on (100) planes, i.e., they are parallel to the wafer surface [all Cz silicon samples were cut from (100)-oriented wafers]. Probably, being (100) planes perpendicular to the ingot growth direction, some anisotropy was introduced in the silicon crystal during Cz growth and this should have influenced precipitate orientation in the as-grown crystal. Such an anisotropy was not removed by the short annealing treatment performed.

An additional advantage due to the high-quality spectra of high-spatial-resolution technique is the possibility of studying the exact peak position and line shape.[248] From these analyses information about stoichiometry and structure of the oxide composing the precipitates can be obtained with a consequent quantitative evaluation of precipitate volume fraction more reliable than those previously obtained by standard IR spectroscopy. The absorption coefficient of silicon samples with 5 ppm volume fraction of diskoidal precipitates made of different SiO_2 polimorphs, both crystalline and amorphous, were calculated as a first step, to compare with experimental curves. As shown in Fig. 71, the peak positions found considering the precipitates as made of α-quartz, cristobalite, amorphous, and thermal SiO_2 and

Downloaded 21 Apr 2008 to 146.186.238.16. Redistribution subject to AIP license or copyright; see http://jap.aip.org/jap/copyright.jsp

SIONYX1403000027.0011

SAMSUNG EX. 1002 - 2549/4148

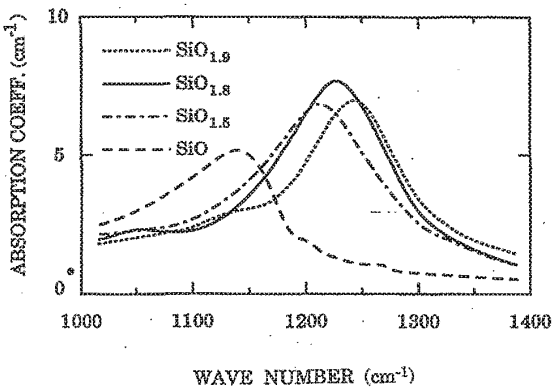

FIG. 72. Absorption coefficient calculated for silicon with 5 ppm volume of oxide precipitates made of different substoichiometric SiO_x (from Ref. 248).

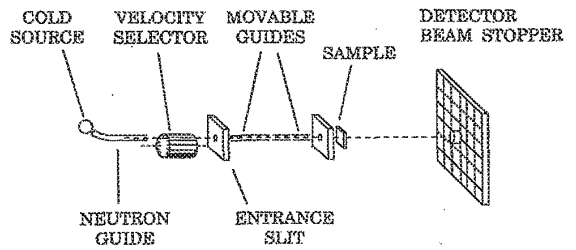

FIG. 73. Scheme of the SANS apparatus at Institute Laue Langevin in Grenoble (from Ref. 244).

B-doped SiO_2 were all different from the experimental 1230 cm^{-1}, therefore, none of these compounds is presumably the material composing the precipitates. Then, the hypothesis that this type of precipitate is composed of SiO_x with $x<2$ was checked[248,249] for the cases $x=1$, 1.5, 1.6, 1.8, and 1.9. The spectrum calculated using the optical functions of amorphous $SiO_{1.8}$ leads to a very good agreement with experimental findings, therefore showing that $x=1.8$ is the stoichiometric index corresponding to the oxide actually composing the disk-shaped precipitates. In Fig. 72 the spectra calculated for these amorphous substoichiometric oxides are reported for comparison with the experimental ones of Fig. 70(b).

From a comparative study of the line shapes of the experimental and calculated absorption bands, the first one strongly asymmetrical and the second one symmetrical, the authors concluded that probably forms of SiO_x with $x<1.8$ are also present as oxides composing the particles. In fact, from a decrease of x a decrease of the wave number of the peak position is predicted by the effective medium theory [Eqs. (99a) and (99b)], so that the broad shoulder at low wave number can be interpreted as a contribution from suboxides with $x<1.8$.

Finally, the quantitative evaluation of the actual fraction f occupied by the precipitates has been made from the intensity comparison between experimental and calculated spectra, resulting in $f=5$ ppm for the precipitates made of $SiO_{1.8}$. This very low concentration shows once again that the high-spatial-resolution technique is fundamental for detecting the precipitate absorption band in samples annealed for short times. Quantitative evaluation of precipitates made of the other oxides, responsible for the asymmetry of the absorption band, leads[354] to even lower f values, such as 2 and 3 ppm for oxides corresponding to $x=1$ and 1.5. Nevertheless, some doubts about the validity of the quantitative analysis of IR absorption at 1230 cm^{-1} are raised based on the dependence of the spectra on many parameters. First of all, spectra collected with unpolarized light do not allow any reliable evaluation; moreover, even with polarized light one has to be sure about the exact polarizer position and the SiO_x stoichiometry.

A detailed discussion of results concerning the possible habit planes for platelet-shaped precipitates as deduced from IR measurements is reported by some of the authors[138] also for as-received Cz silicon samples (i.e., samples subjected only to the thermal-donor killing treatment prior to the measurements). The hypothesis of oxygen precipitation taking place in such samples, without any annealing, was already proposed,[113,123,128,355] but this is the first experimental evidence of the presence of disk-shaped precipitates.

An alternative approach to effective medium theory has been recently proposed[356] to explain IR results on oxygen precipitation in silicon, based on the Berreman effect.[357] All the features of experimental spectra can be justified also following this interpretation. On this basis, for the case of SiO_x disks embedded in silicon the two approaches have been shown to be identical.

Recently, a low-temperature FTIR mapping of oxide precipitates in silicon has been performed.[358] While at room temperature the absorption band related to interstitial oxygen is at 1107 cm^{-1}, at low temperature it shifts to 1136 cm^{-1}, making the precipitate absorption band at 1100 cm^{-1} also detectable. Although the kind of precipitates giving rise to the 1100 cm^{-1} absorption band is still unclear, the authors believe that from the height of both 1100 and 1230 cm^{-1} absorption bands a reliable quantitative evaluation of oxide precipitate density in the samples can be performed.

D. Small-angle neutron scattering

SANS is a powerful technique for the study of clusters or precipitates in a material when the mismatch between the neutron-scattering coherence length of the grains and of the matrix is large enough that scattering at very small angles can be detected. The knowledge of size, density, shape, and crystal orientation is essential in order to give a complete and satisfactory description of phenomena such as oxygen precipitation in silicon. From the analysis of the scattered neutrons it is possible to obtain such a global information in a single experiment, with the additional advantage (with respect to other techniques) that large samples (>1 cm^2) can be used, so that the data obtained are representative of the bulk.

In Fig. 73 the spectrometer D11 at the Institute Laue Langevin in Grenoble is schematically reported.[244] From the collimated beam of monochromatic neutrons, incident on the

Downloaded 21 Apr 2008 to 146.186.238.16. Redistribution subject to AIP license or copyright; see http://jap.aip.org/jap/copyright.jsp

SIONYX1403000027.0012

SAMSUNG EX. 1002 - 2550/4148

sample, the unscattered neutrons, blocked by a beam stop, are separated from those scattered through small angles, falling on a two-dimensional detector comprising an array of 3808 1×1 cm^2 active elements. The neutron beams travel in evacuated tubes to minimize the scattering.

The scattered neutrons give rise to successive anular regions about 1 cm wide: The radius of each anular cell corresponds to a scattering vector $\mathbf{Q}$ with[41]

$$|\mathbf{Q}|=\frac{4\pi \sin\theta}{\lambda}, \tag{100}$$

where θ is half of the scattering angle and λ is the wavelength of the incident neutrons. As a general rule, λ is greater than the Bragg cutoff (which in the case of silicon is 6.26 Å, i.e., twice the largest interplanar spacing).

It should be noted that incoherent scattering as well as the contributions from randomly distributed impurity atoms would give rise to negligible or very small isotropic scattering. On such a background, measurable signals can show up due to constructive interference originated by local-density fluctuations if the properties of the material deviate from those which give rise to the just-mentioned background. This takes place for instance with the presence of clusters, microcrystallites, and small aggregates of impurities, having specific characteristics. As for the space resolution, SANS allows one to resolve spatial features in the range 1–100 nm. In other words, this technique is particularly suitable when one has to study properties of space inhomogeneities having a size of that order, and the information should be extracted from the bulk or from a relatively large size volume. Furthermore, the capability of the technique to study low concentrations of defects has been demonstrated:[359] Volume fractions down to ~10 ppm have been characterized.

The observed scattering is the Fourier transform of the geometrical shape of the precipitates and is given by[251]

$$\frac{d\sigma}{d\Omega}=\frac{n}{N}\left(\Delta\rho\int_V \exp(i\mathbf{Q}\cdot\mathbf{r})d^3\mathbf{r}\right)^2, \tag{101}$$

where σ is the scattering cross section, Ω is the solid angle, $\mathbf{r}$ is the real-space vector, n is the number of precipitates per unit volume, N is the number of atoms per unit volume of the host lattice, $\Delta\rho$ is the contrast difference between the precipitate and the matrix, and V is the volume of one precipitate. $d\sigma/d\Omega$ is usually called the absolute differential scattering cross section. After carrying out the experiments it is also possible, with the help of a computer approach to the scattering process, to derive conclusions on shape and orientation of defect aggregates from the symmetry of the scattering pattern. Details on the SANS technique as applied to the study of precipitates in silicon are given in Refs. 41, 244, and 360.

A detailed study of oxygen precipitation in silicon annealed at 750 °C for different times has been performed by Bergholz *et al.*[244] using SANS. The results are shown in Fig. 74 which reports the cross section $d\sigma/d\Omega$ as a function of $|\mathbf{Q}|$. Open circles and triangles down refer to an untreated sample and shows a low and flat cross section, denoting the absence of precipitates. As the annealing time grows, the $\mathbf{Q}$

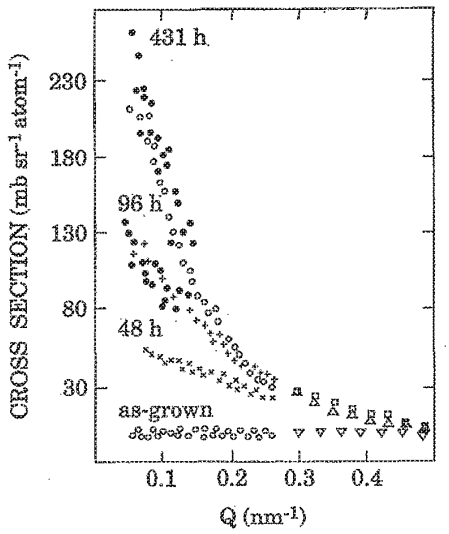

FIG. 74. Scattering cross section as a function of scattering vector for samples as-grown and annealed at 750 °C for different times. The different symbols used for each annealing time refer to different sample-detector distances during the measurements (from Ref. 244).

dependence of the cross section becomes stronger. In the same article it is also possible to find a detailed comparison among SANS, TEM, and IR-absorption results.

The orientation of the precipitates can be inferred from the anisotropy of the detected scattering pattern.[250] In principle, the size of the precipitates could be determined from the Fourier transform of the scattering pattern (we recall that the SANS pattern is the Fourier transform of the real defect), but this approach presents some difficulties related to the limited region of the reciprocal space involved.

SANS has been used[251] to study in detail platelet-shaped precipitates formed in Cz silicon samples treated at 750 °C for different times. From the fourfold symmetry of the scattering images and from the sample orientation with respect to the incident neutron beam it was deduced that the precipi-

TABLE X. Summary of SANS and IR data for the different annealing conditions. The parameter w, the radius of the precipitates r, and the number density of precipitates N are reported (from Ref. 41).

			SANS data		IR data	
T (°C)	t (h)	w	r (Å)	N (cm^{-3})	r (Å)	N^a (cm^{-3})
650	2000	[b]	32	2.5×10^{14}	30	1.3×10^{14}
700	808	4.5	93	4.3×10^{12}	59	1.8×10^{13}
750	16	[b]	29	...	31	2.4×10^{12}
750	72	[b]	54	1×10^{13}	64	2.4×10^{12}
750	208	2.0	88	3×10^{12}	95	2.4×10^{12}
750	600	4.3	143	1.2×10^{12}	113	2.4×10^{12}
750	744	6.1	133	1.5×10^{12}	114	2.4×10^{12}
800	808	6.8	146	1.1×10^{12}	196	4.6×10^{11}
800	1000	5.6	153	9.9×10^{11}	196	4.6×10^{11}
850	808	10.7	210	3.8×10^{11}	316	1.1×10^{11}

[a]Assumed to be constant.
[b]Spherical precipitates.

Downloaded 21 Apr 2008 to 146.186.238.16. Redistribution subject to AIP license or copyright; see http://jap.aip.org/jap/copyright.jsp

SIONYX1403000027.0013

SAMSUNG EX. 1002 - 2551/4148

tates have cubic symmetry and that their short edge is perpendicular to (100) planes. Moreover, the narrow streaks of the pattern indicate that the other dimension of the precipitates is much larger than that along [100] direction, confirming that after the mentioned annealing the precipitates are platelets lying on {100} planes.

Recently, SANS has been demonstrated as a suitable technique also for the study of precipitates in heavily doped crystals,[287,361] where other analytical methods such as IR-absorption spectroscopy cannot be applied.

An interesting comparison between SANS and IR-absorption results can be performed on the basis of Table X for Cz samples annealed at well specified annealing conditions.[41] The precipitate radius and the number of precipitates per unit volume as determined by the two techniques are listed and show a fairly good agreement. The radius increases and the concentration decreases as the annealing temperature and time increase. This can be related to the fact that increasing the temperature more nuclei redissolve and the others grow to larger dimensions. The parameter w is defined as the ratio between the large and the small edges of the precipitate; for example, for a cube $w=1$, while for a very thin platelet w would become large. The parameter w allows one to evaluate the shape of the precipitates for the different annealing conditions: They are initially spherical, becoming progressively more platelike as the annealing time at 750 °C increases. For long annealing time at temperatures from 700 to 850 °C the precipitates are platelets, while at 650 °C they are spherical even after 2000 h annealing.

E. Optical scattering

Optical scattering is an important aspect of the interaction of electromagnetic waves with a material. Scattering due to the presence of imperfections is detectable with standard techniques and is being used as a method of investigation.[362] In particular, when oxide precipitates (with a diameter smaller than the wavelength) are embedded in the silicon crystal lattice, they act as scattering centers and optical scattering can be detected. In this case, using an incident electromagnetic wave in the wavelength range where both silicon and silicon oxide are transparent, i.e., from about 1 to 9 μm, Rayleigh scattering is responsible for the decrease of the intensity of transmitted radiation. Such a decrease is usually described by introducing the absorption coefficient α due to the scattering. In particular, Kaiser[19] obtained the concentration N (cm^{-3}) of the scattering centers (precipitates) having a diameter of about 0.1 μm in Si wafers heat treated at 1000 °C using a radiation wavelength of 1.15 μm from the following relation

$$N=\frac{24\pi^3}{\alpha}\left(\frac{N_O M}{2\rho A}\right)^2\left(\frac{n_{ox}^2-n_{Si}^2}{n_{ox}^2+2n_{Si}^2}\right)^2\frac{n_{Si}^4}{\lambda^4}, \tag{102}$$

where N_O is the number of oxygen atoms per cm^3 present in the precipitates, M is the molar weight of the particle material ($M=60$ for SiO_2), ρ is the density of particle material ($\rho=2.3$ g cm^{-3} for SiO_2), A is Avogadro's number, and n_{ox} and n_{Si} are the refractive indexes of SiO_2 and silicon, respectively.

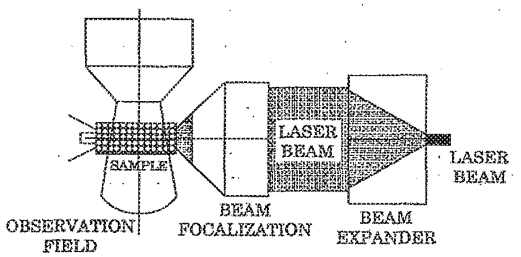

FIG. 75. Experimental setup for LST measurements (from Ref. 372).

Following the same procedure Newman *et al.*[143] obtained the behavior of N versus temperature, very similar to that obtained from etch-pit measurements. Nevertheless, the N values obtained from Eq. (102) are about three times greater than those found from etching measurements.

1. Laser scanning tomography

The analytical method just illustrated is based on bulk scattering, i.e., information is obtained by measuring the total light scattered by a given sample volume. In the 1960s a new method based on the measurement of the individual particle scattering was proposed to detect imperfections in crystals.[363] This new technique enables one to study particles, inhomogeneity clusters, and dislocations using a scanning ultramicroscope.

It has been subsequently largely improved by Moriya and Ogawa[364–366] and Ogawa and Nango,[367] particularly in the experimental setup. They use as source a 15 mW He-Ne laser ($\lambda=1.15$ μm) focused on a 40-μm-diam spot on the sample and an IR microscope with a TV camera to collect the scattered light at 90° with respect to the incident light. Successive images are digitized by a frame memory and recorded in a dedicated computer. A step-by-step acquisition allows to draw a map of scattering centers. This particular approach, called laser scanning tomography (LST), offers the opportunity to investigate structural defects in semiconductors transparent to IR radiation. In particular, impurity precipitates in silicon caused by fluctuations of growth parameters, dislocations decorated by impurities or undecorated, and lattice defects were detected and made clearly visible.

It is worth noting that the scattered light is proportional to the density N of scattering centers and to their cross section Ω. In the case of an electron trapped in an electronic center with H-like structure, Ω can be written as[365]

$$\Omega=\frac{1}{2}\frac{r_e^2\omega^4}{(\omega_0^2-\omega^2)^2+\Gamma\omega^2}(1+\cos^2 2\theta), \tag{103}$$

where r_e, ω_0 and Γ are the classical radius, the resonance frequency, and the damping constant of the electron, respectively. ω is the laser frequency and 2θ is the angle between incident and scattered light.

Although in the IR range the scattered intensity is reduced compared to visible light, the high detectivity and amplification obtained using a computer and a camera allow one to get high-quality images. A comparison between an IR tomograph and a Lang topograph (see Sec. IV F) for a sample

Downloaded 21 Apr 2008 to 146.186.238.16. Redistribution subject to AIP license or copyright; see http://jap.aip.org/jap/copyright.jsp

SIONYX1403000027.0014

SAMSUNG EX. 1002 - 2552/4148

TABLE XI. Precipitate density N obtained by LST on a Si sample after different annealing times t. The measured numbers of particles are considered distributed in a 0.213×10^6 μm^3 volume (from Ref. 374).

Sample	t (h)	No. of particles	N ($10^9/cm^3$)
a	2	1589	7
b	5	4306	20
c	10	4977	23
d	25	5861	27

treated for 160 h at 900 °C is reported in Ref. 365. The images are very similar but the deduced precipitate densities are different because IR tomography detects only the precipitates present in a slab about 40 μm thick (i.e., of the order of the laser spot dimension), while the sample thickness investigated by Lang topography is equal to the thickness of the whole sample (in this example 2 mm).

The application of LST to oxide precipitates in silicon was further developed by Gall *et al.*[368–372] Their experimental setup is reported in Fig. 75. A Nd:YAG laser ($\lambda=1.06$ μm) is focused on the lateral face of a silicon wafer and the laser beam enters the material as a nearly parallel beam, due to the high refractive index of Si. The scattered light is collected at 90° with respect to the laser beam direction by a TV camera with a PbS-PbO vidicon tube. The silicon wafer is then moved step by step and the corresponding images are stored in a computer to obtain a two-dimensional scattering pattern. In this way an image of the scattering particles lying in a "tomographic plane" parallel to the wafer surface can be obtained. The thickness of the tomographic plane depends on the size of the laser spot. The diameter of the beam, typically 30–50 μm, can be reduced down to 5–10 μm for high-resolution images. The method is powerful enough to detect very small defects, with dimensions lower than 100 Å and density up to 10^{12} cm^{-3}.[373]

From the analysis of a series of LST images the concentration N of precipitates was studied as a function of annealing time, as reported in Table XI. LST is very useful to detect small nucleation sites and can reveal precipitate densities below the etch-pit detection limit.[375]

2. Scanning infrared microscopy

A different approach to use light scattering for the study of impurities and defects is the laser scanning microscope, first developed by Wilson and Sheppard[376] using a visible laser light focused on the sample surface. The reflected light coming from the mechanically rastered-scanned specimen was collected by a photodiode detector to produce an image of the sample surface.

In the last years a scanning infrared microscope (SIRM) was developed[377–379] on the basis of the same general principles. SIRM uses an IR laser beam (Nd:YAG at 1.32 μm) which can be focused not only on the sample surface but also within the sample bulk. The light reflected or transmitted at different angles due to scattering gives dark-field (DF) or bright-field (BF) images, respectively, as shown in Fig. 76. SIRM supplies three-dimensional images of precipitates, voids, localized point defects, and microstrains, in other words of any kind of scatterers. Dislocations and particles decorating the dislocations can also be revealed.

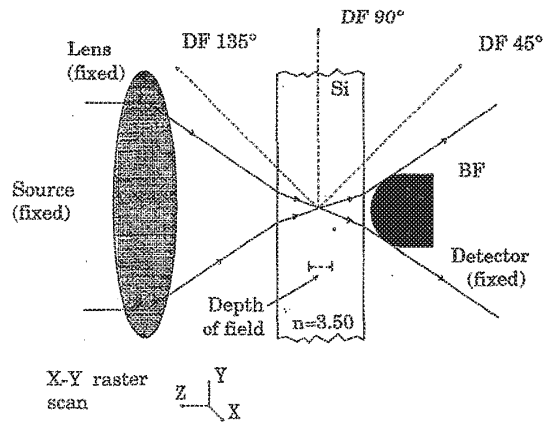

FIG. 76. Scheme of the optic geometries used during SIRM measurements (from Ref. 380).

The size of the spot, typically ranging from 1 to 3 μm, depends on the numerical aperture of the focusing system and on the refractive index of the material under study. For BF images the transmitted light is collected by a Ge photodiode. When a particle moves to the laser focus the incident light is scattered and the photodiode signal is reduced. A dark two-dimensional image of the particles can be drawn by moving the specimen with a high-precision translator along the x and y directions (with fixed z) synchronously with the position of the pixels of a screen. Three-dimensional images can then be obtained performing the same measurements at different depths z and by scanning the xz or yz planes. A similar procedure carried out after placing the photodiode at different angles (such as 45°, 90°, 135° indicated in Fig. 76) provides a three-dimensional image of the light scattered from the particles, which in this case appear bright in a DF image. The instrument is fully automated and computer elaboration is performed to improve image quality. The schematic diagram of SIRM operating in BF mode is shown in Fig. 77. The typical volume analyzed is $1.5\times1.5\times15$ μm^3 in a standard configuration. The use of a pin hole in front of the detector (confocal mode) allows to improve spatial resolution up to an analyzed volume of about $1\times1\times7$ μm^3.[380,381]

Images collected with polarized light allow one to determine the Burgers vector of dislocations present in the sample. SIRM can be used for particle densities of about 10^6–10^9 cm^{-3} and a single particle down to 30 nm in size can be detected. A summary of the SIRM operating modes and mechanisms producing the contrast and information obtainable are reported in Fig. 78.

Images in BF and DF taken from a (011) cross section of a Cz Si wafer heat treated to grow oxide particles in the bulk of the wafer and to obtain a denuded zone have been analyzed in Ref. 380 and are shown in Fig. 79. Single particles are detected in the BF image as dark spots and in the DF image as bright spots. Moreover, the presence of a denuded zone in the surface region where the density of particles is very low is observed. Quantitative data of precipitate density

Downloaded 21 Apr 2008 to 146.186.238.16. Redistribution subject to AIP license or copyright; see http://jap.aip.org/jap/copyright.jsp

SIONYX1403000027.0015

SAMSUNG EX. 1002 - 2553/4148

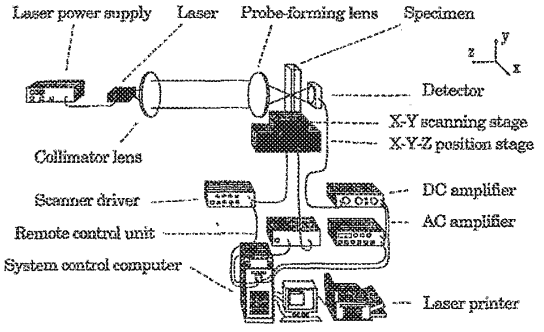

FIG. 77. Schematic diagram of a SIRM apparatus operating in BF mode (from Ref. 380).

are obtained by counting the number of spots present in the volume analyzed. The values obtained at different depths form the analysis of narrow stripes parallel to the wafer surface is reported in the lower profile of Fig. 80. This profile clearly shows the presence of the denuded zone, which is about 40 μm thick, followed by a region of about the same thickness in which particle density progressively increases from below the detection limit (about 10^6 cm^{-3}) to the bulk value (1.5×10^7 cm^{-3}). The upper profile in Fig. 80 is obtained from the analysis of a wafer subjected to the same thermal treatment, except that the time of the first annealing step at 1100 °C was reduced from 16 to 8 h. The lower annealing time of these samples produced only a region with a partially reduced density of particles (extended to about 60 μm from the surface) and the denuded zone is not completely evident.

Finally, we note that very interesting results were obtained from SIRM measurements in the study of intrinsic gettering of metal impurities such as Cu, Co, Pd, and Ni by oxide precipitates.[382,383]

F. X-ray topography

Among the techniques developed for materials characterization, x-ray diffraction is of particular interest due to its sensitivity to lattice distortions and to the ability of x rays to

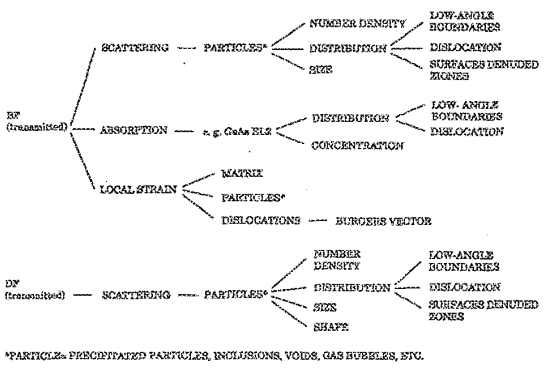

FIG. 78. Summary of SIRM operating modes and information obtainable (from Ref. 380).

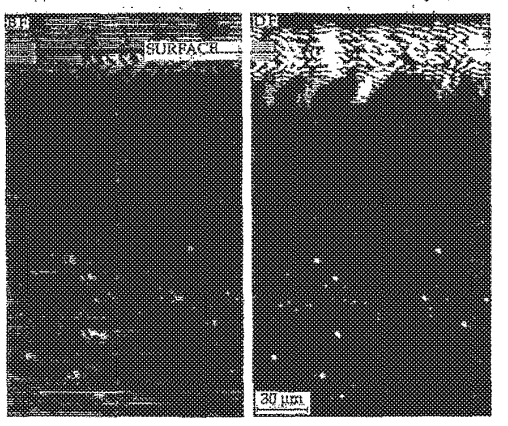

FIG. 79. BF and DF SIRM images of a (011) cross section of a silicon wafer heat treated to grow oxide precipitates in the bulk, creating a denuded zone (from Ref. 380).

penetrate into thick samples. X-ray topography,[384] based substantially on x-ray diffraction, is a nondestructive technique that gives a direct access to the nature of extended crystal lattice defects, with the drawback, however, of the relatively poor spatial resolution of about 10–20 μm.[321] Several review articles illustrate the use of x-ray topography for the study of defects in semiconductors.[319,321,385]

X-ray analytical methods are based on the interaction of incident x-rays with the crystal lattice. X-ray diffraction and absorption are influenced by imperfections or defects in the crystal lattice and their analysis gives qualitative and quantitative information about crystal imperfections (point defects, dislocations, stacking faults, grain boundaries, precipitates, voids).

It is well known that for perfect crystallographic planes the intensity of diffracted x-rays follows the Bragg equation

$$\lambda = 2d \sin \theta_B, \tag{104}$$

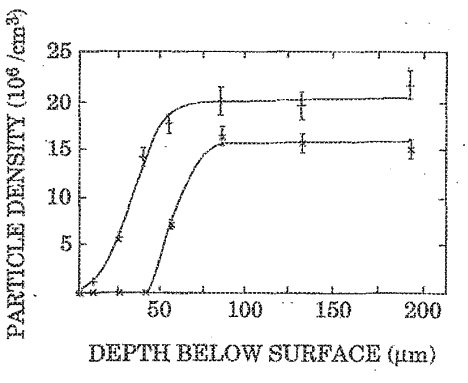

FIG. 80. Profiles of precipitate density along the thickness for a sample annealed at 1100 °C for 16 h, at 800 °C for 8 h, and at 1100 °C for 16 h (lower profile) and one subjected to the same thermal cycle, with a shorter (8 h) first step (upper profile) (from Ref. 380).

Downloaded 21 Apr 2008 to 146.186.238.16. Redistribution subject to AIP license or copyright; see http://jap.aip.org/jap/copyright.jsp

SIONYX1403000027.0016

SAMSUNG EX. 1002 - 2554/4148

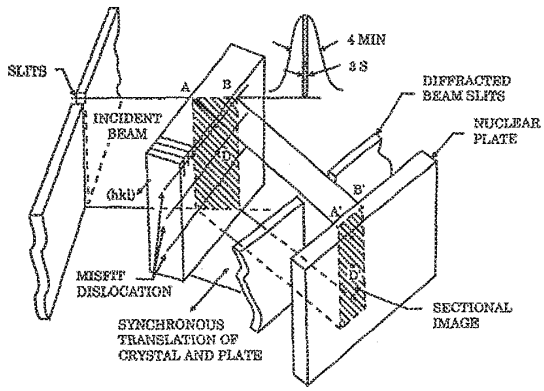

FIG. 81. Schematic representation of the defect imaging process by Lang x-ray topography (from Ref. 319).

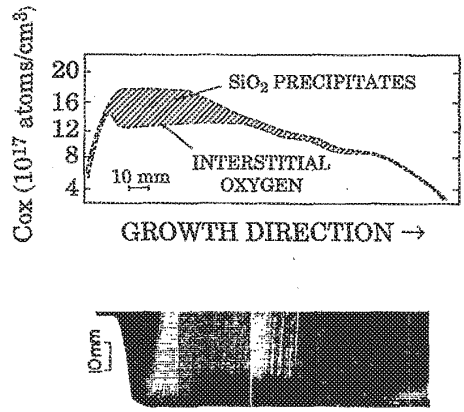

FIG. 82. Comparison between infrared determination of interstitial and precipitated oxygen (upper figure) and a sectional x-ray topograph (lower figure) of a silicon crystal (from Ref. 392).

where λ is the x-ray wavelength, d is the distance between the diffracting crystal planes and θ_B is the angle between scattered beam and diffracting planes (Bragg angle).

Basically, x-ray topography experiments can be carried out in two modes of operation, i.e., transmission and reflection.

1. Transmission topography

Transmission x-ray topography is usually performed with the instrumental setup designed by Lang in 1958.[386–388] The Lang camera is schematically represented in Fig. 81.[319] It provides the possibility to synchronously scan the crystal and the nuclear (photographic) plate using a tall narrow beam of x-rays. Diffracted x rays passing through the crystal give the transmission x-ray topograph. The very sharp incident beam typically consists of a characteristic line whose horizontal divergence is limited to about 4 min of arc by a slit at the end of the collimation tube. The vertical divergence of the incident beam is controlled by using a point source of x-rays and adjusting the divergence between source and sample. The crystal under study is usually oriented so that a set of lattice planes (hkl) fulfills the Bragg equation. In this way, as shown in Fig. 81, a sectional image of the crystal lattice is collected at the plate. The diffracted beam coming out from the back of the sample passes through a slit which prevents the transmitted beam and fluorescent radiation from influencing the photographic emulsion. As shown in Fig. 81, the emulsion is exposed to the beam A′B′ yielding an image of a cross section of the crystal at the position AB.

It is important to note that Bragg condition does not apply simultaneously to the perfect regions of the sample and to the regions where the lattice spacing or orientation locally varies due to crystal defects. Consequently, the diffracted x-ray intensity recorded on the photographic plate changes in correspondence of the points where irregularities of the crystal lattice are present. For example, any defect or strain center located at position D within the bulk creates intensity variations that are observed as a contrast at position D′ on the photographic plate. This yields a section topographic image that can be used to locate the position of the imperfection within the bulk of the crystal. By activating a scanning mechanism, an image of the entire sample can be obtained. An automatic control is generally used to maintain the Bragg condition during the scanning process. X-ray topography was also developed for *in situ* measurements[389] to follow step-by-step dynamical processes.

Due to its peculiarity, x-ray topography is widely used in the studies of oxygen precipitation after heat treatments of silicon crystals.[269,390,391] The opportunity of x-ray topography to obtain images of large sample sections is very useful in the study of oxide precipitate distribution both in wafers and in ingot sections. For example, Fig. 82 shows a comparison between oxygen precipitation in a 180-mm-long silicon single crystal produced by high-oxygen and low-growth-rate pulling, as detected by IR-absorption bands at 1107 and 1230 cm^{-1} (related to interstitial and precipitated oxygen, respectively), and a sectional x-ray topograph of the same crystal, as reported by Abe.[392] The interstitial and precipitated oxy-

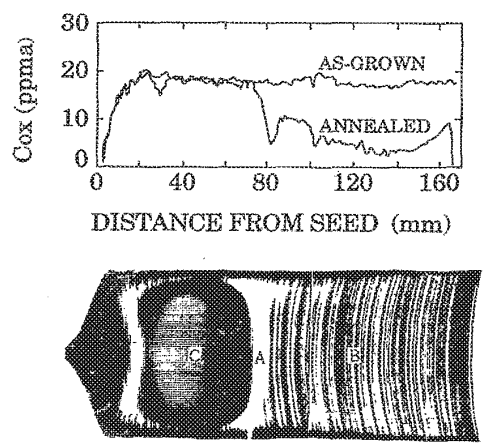

FIG. 83. Interstitial oxygen profile along a longitudinal section of a crystal detached from the melt and annealed a 1000 °C for 16 h in Ar (upper figure); x-ray topograph of the same sample (lower figure) (from Ref. 392).

Downloaded 21 Apr 2008 to 146.186.238.16. Redistribution subject to AIP license or copyright; see http://jap.aip.org/jap/copyright.jsp

SIONYX1403000027.0017

SAMSUNG EX. 1002 - 2555/4148

FIG. 84. X-ray topograph of a silicon wafer subjected to a thermal treatment for denuded zone formation (from Ref. 321).

gen concentrations in the as-grown crystal are inhomogeneously distributed along the growth direction.

Nowadays, in standard as-grown single crystals it is very difficult to evidence any defects generated during growth; however, some defects such as oxide precipitates, present in as-grown materials as nuclei or very small particles, become detectable during the heat treatments following the growth. A very interesting example[392] is shown in Fig. 83 referring to a longitudinal section of a silicon ingot detached from the melt and heat treated for 16 h at 1000 °C. The lower image in Fig. 83 shows the x-ray topograph and the upper one reports the interstitial oxygen concentration C_{ox} measured by IR spectroscopy at different distances from the seed. For comparison also the C_{ox} in the as-grown crystal is reported. While the O_i distribution in the as-grown material is uniform, after the heat treatment a reduction of interstitial oxygen concentration from point A indicates that in the end side of the crystal oxygen precipitation took place. This is due to the rapid cooling of this part of the crystal from growth temperature to room temperature (caused by the detachment) generating by thermal stress a lot of nucleation sites for oxygen precipitation. The reduction of interstitial oxygen evidenced by IR-absorption measurements corresponds to the white contrast regions in the x-ray topograph.

An x-ray topographic image of a section of a 450-μm-thick silicon wafer after denuded zone formation[321] is shown in Fig. 84, where the device (surface) region is evidenced to be precipitate free, while the central region presents a high precipitate density (black dots).

X-ray topography has been useful to Freeland *et al.*[393] to clearly evidence the effect of preheating on oxygen precipitation. They studied dislocation-free Cz crystals containing 8×10^{17} atoms/cm^3 of interstitial oxygen and annealed for 8 h at 1200 °C. One of the samples was also subjected to a preheating for 2 h at 700 °C. In the as-grown crystal with no pretreatment no defects are visible after 8 h annealing at 1200 °C, while the crystal which received such a preliminary treatment shows a large number of defects.

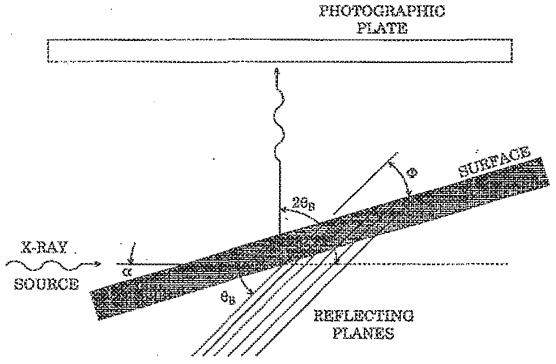

FIG. 85. Scheme of the camera for reflection-mode x-ray topography (from Ref. 319).

2. Reflection topography

Besides the transmission geometry, x-ray topographs can also be obtained by diffracting the x-rays back through the entrance sample surface. This mode is called reflection, Berg–Barrett,[394,395] or Bragg geometry. Figure 85 schematically illustrates the inherent simplicity of the camera for reflection-mode topography. Operationally, the angle of incidence α should be small for maximum illumination of the sample and minimum interference with the photographic plate, the angle between the incident and diffracted directions $2\theta_B$ should be near 90°. Also, the diffracted x-rays should be absorbed perpendicularly to the emulsion. This minimizes photoelectron track lengths and image distortion in the thick emulsions.

It is important to point out that in the reflection geometry only the first layers of a sample are investigated, typically 2–10 μm and occasionally down to a depth of 50 μm. Therefore, the reflection mode is particularly suitable for the study of epitaxial layers and of material processing problems where surface strain is important.

Reflection topography of semiconductor samples has not been so popular as the transmission mode, where the images are characterized by a better contrast. Nevertheless, there are many situations where the selective imaging of the surface defect structures by reflection topography is advantageous, e.g., when the dislocation density is such that counting dislocation sites is simpler than analyzing overlapping lines.

In the analysis of crystal surfaces by reflection topography a choice of the diffracting plane is an important issue. The penetration depth of x-rays, the magnitude of the distortions in the vicinity of the defects, and the angular range of reflection for regions of perfect crystal, called the Darwin–Prins half-width,[396] determine the ability to image dislocations and/or surface strain gradients. Other factors such as geometrical image distortions and diffracted beam intensity must be also evaluated. All these variables are coupled through the (hkl) plane which produces the image. A very useful analysis and compilation of data for all possible (hkl) planes for six semiconductor materials (Si, Ge, GaP, GaAs, InAs, and InSb) has been given by Halliwell, Childs, and O'Hara[397] for wafers with {100}, {110}, or {111} surface orientations. The use of reflection-mode topography for depth analysis is also discussed by Rozgonyi and Miller.[385]

Double- and triple-crystal reflection topography have also been developed[384,398] utilizing two (or three) successive Bragg reflections. The first crystal (or the first two) act as a monochromator, while the second one (or the third) is the sample to be studied. These configurations are very sensitive to strain (measurable $\Delta d/d\sim10^{-8}$) and this reduces the spatial resolution of the technique, since the strain field extends far from the generating crystal defects.

Recently, x-ray topography has also been used to study the distribution and size of oxide precipitates after heat treatment of MCz silicon samples.[399,400] The low density of pre-

Downloaded 21 Apr 2008 to 146.186.238.16. Redistribution subject to AIP license or copyright; see http://jap.aip.org/jap/copyright.jsp

SIONYX1403000027.0018

SAMSUNG EX. 1002 - 2556/4148

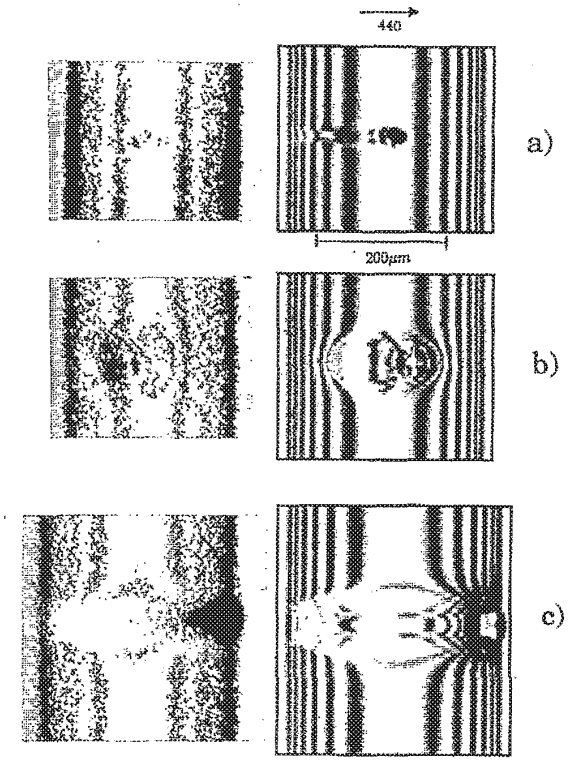

FIG. 86. Experimental (left-hand side) and simulated (right-hand side) images of oxide precipitates in a MCz sample annealed at (a) 450, (b) 650, and (c) 800 °C for 18 h (from Ref. 399).

cipitates present in these samples allows one to study the individual particles. In Ref. 399 images obtained by x-ray topography have been compared with numerical simulations. This procedure allows one to estimate the magnitude and the sense of the strain field generated by precipitation. Three MCz 430-μm-thick samples have been studied after annealing for 18 h at 450, 650, and 800 °C. In Fig. 86 the experimental (left-hand side) and simulated (right-hand side) images of precipitates for the different annealing temperatures are shown. The parameter accounting for the strain effects, determined by matching the illustrated images, increases monotonically with annealing temperature.[399]

V. TECHNOLOGICAL INTEREST OF OXYGEN PRECIPITATION

The fabrication of high-performance analog and digital integrated circuits (IC) requires rather complex processing sequences involving several high-low temperature treatments in both inert and oxidizing ambients. Each thermal treatment may result in the formation of a lot of defects in the silicon substrate and in the surface region which can have detrimental effects on the IC performances and yield.[401] For example, in the 1 Gbit electrically eraseable read-only memory the minimum linewidth is predicted to be about 0.15 μm with a defectivity lower than 1 defect/km. To significantly reduce their defectivity, the devices are generally produced on high-quality epitaxial films and not directly on the silicon wafer surface, which is sometimes damaged. The perfection of these films depends on several factors such as the cleanliness of the substrates, the deposition parameters, and, especially, the imperfections of the substrate surface.

Since one of the main sources of bulk and surface defects is oxygen precipitation, a direct correlation between device yield reduction and oxygen precipitation has been evidenced. Nevertheless, when oxide precipitates form far from the epi-substrate interface they can have a beneficial effect, acting as gettering centers for metal impurities.

Usually, to reduce the impurity content in the device regions two different gettering techniques are applied. The first one, called external or extrinsic gettering, can be provided by several processes such as HCl oxidation, back-surface implant, phosphorus back-surface diffusion, sand blasting, abrading, laser irradiation, polysilicon deposition, or film stress. The second one is called intrinsic or internal or *in situ* gettering (IG) and is provided by bulk SiO_x precipitates. In particular, for each SiO_x particle formed during precipitation, some Si self-interstitials are produced, due to volume expansion. The so-emitted self-interstitials can form dislocation loops, since a dislocation loop represents an energetically more favorable state than randomly arranged self-interstitials. Moreover, the large volume increase associated to the precipitation is not completely released by the Si self-interstitial emission and each precipitate particle is normally surrounded by a strain field. The dislocation loops, which usually contain an extrinsic stacking fault,[402] and the strain field surrounding the precipitates provide the IG.

In the surface region the situation is quite different. Indeed, during annealing oxygen diffuses out from the bulk leaving an oxygen-depleted zone close to the surface, called the denuded zone [(DZ), see Sec. V C].[49,65,401,402] This process can be explained considering that oxygen is a rather fast diffusing element (its diffusion coefficient is more than two orders of magnitude larger than that of other doping impurities in silicon). Out-diffusion reduces the interstitial oxygen concentration and then the chemical driving force for oxygen precipitation.[166,403,404] As the degree of supersaturation falls the precipitation rate is drastically reduced, reaching zero near the surface region. As a consequence, in this region the defects caused by oxygen precipitation are strongly reduced.[405]

DZ formation and IG are the main procedures used in the IC industry to increase device yield. In fact, the presence of bulk stacking faults or precipitates close to the wafer surface leads to the formation of stacking faults and dislocations, respectively, in the epitaxial layer, i.e., in the region where the devices are created. Therefore, it is very important to find the relation between the defect density in the epitaxial layer and the DZ depth, although this is not straightforward. A careful examination of the region close to the interface between epitaxial layer and substrate shows occasional precipitates also in the DZ area, sometimes extending to all the epitaxial film. This means that the DZ is not homogeneous and its width (or depth) is not constant, therefore the above-mentioned relation can be found only on a statistical basis. In this respect, Rossi *et al.*[404] suggested an interesting study of

Downloaded 21 Apr 2008 to 146.186.238.16. Redistribution subject to AIP license or copyright; see http://jap.aip.org/jap/copyright.jsp

SIONYX1403000027.0019

SAMSUNG EX. 1002 - 2557/4148

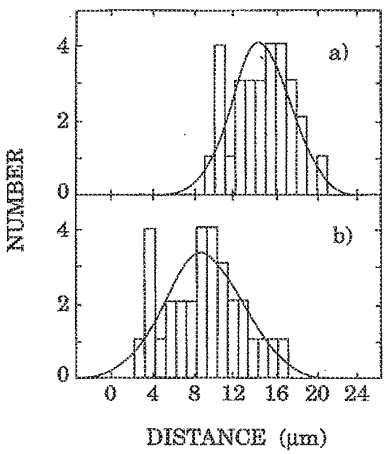

FIG. 87. Histograms of the number of precipitates as a function of distance from epilayer/substrate interface for two different samples (a and b) and normal curve best fit (solid lines) (from Ref. 404).

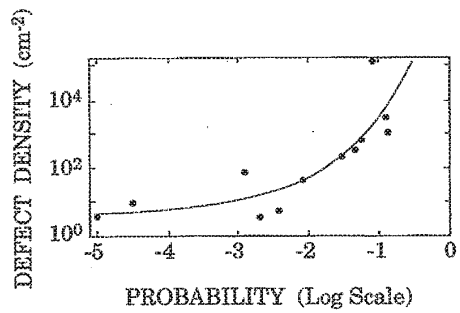

FIG. 88. Experimental data (dots) of epitaxial defect density as a function of the probability of finding a defect of at the epilayer/substrate interface. The solid line represents the best fit (from Ref. 404).

the relation between surface defects and DZ depth, based on an operational definition of the DZ depth. They proposed the following procedure:

(i) Determination of defect density on epilayer surface by wet chemical etching;
(ii) cleavage, angle polishing, and etching of the wafer cross section;
(iii) measurement of the distance of the precipitates from the epilayer/substrate interface along the entire wafer diameter, obtaining a distribution;
(iv) construction of the histogram of the number of precipitates versus distance and fitting by a normal curve;
(v) calculation of the probability of finding defects at the epilayer/substrate interface, given by the area under the normal curve extending in the epilayer region; and
(vi) plotting of the defect density in the epitaxial layer measured in step (i) versus the probability of finding a defect at the epilayer/substrate interface, deduced in step (v). Two examples of histograms obtained by Rossi *et al.*[404] are reported in Fig. 87. In the upper figure (a) the histogram and the normal curve fit (solid line) refer to a silicon wafer where the average distance of the first precipitates from the surface is about 14 μm. The standard deviation of the distribution is about 2.8 μm and the probability of finding a defect at the interface is 10^{-4}, corresponding to a measured defect density at the epilayer surface of 4 defects/cm^2. Figure 87(b) reports the same results for a different wafer, where the average distance of the first precipitates is only 8 μm (standard deviation 2.8 μm), the probability of finding a defect at the epilayer/substrate interface is 10^{-2}, and the measured defect density on the epilayer surface is 237 defects/cm^2. The empirical relation between the probability of finding defects at the epilayer/substrate interface and the defect density on the epilayer surface was deduced by Rossi *et al.*[404] for different samples and is reported in Fig. 88. The figure clearly evidences that materials having a 10% probability of finding defects at the interface show a defect density at the epilayer surface of 10^3–10^5 defects/cm^2 (right-hand side of Fig. 88) and therefore are not suitable for any device fabrication. From the analysis of the curve it is possible to deduce that in order to minimize the defect density on the epilayer surface, the probability of finding a defect at the interface with the substrate must be as small as 10^{-4}. For these probability values no substrate contribution to the epilayer surface defects is found and the defects eventually present have a different origin. Rossi *et al.*[404] suggest that the probability value 10^{-2} dotted line in Fig. 88 separates the region where the substrate contribution is significant (right-hand side) from that where different factors affect the defect density on the epilayer surface (left-hand side).

A. Influence of precipitation on the mechanical properties of silicon

During wafer heating or cooling a large temperature gradient between the center and the edge of the wafers is created which generates dislocations, when the mechanical stress exceeds the silicon elastic limit (critical shear stress). These dislocations propagate from the edge to the center of the wafer and their generation and mobility strongly depend on the temperature and on the availability of dislocation sources like oxide precipitates.[321,406] While in nonprecipitated wafers dislocations are mainly generated at the wafer edge, in precipitated wafers they are generated in the center region. Patel and Chaudhury[407] reported the first study of the critical stress as a function of oxygen precipitation, dislocation density, temperature, and strain rate. More recently an accurate study of warpage, defined as the deviation exhibited by the center line of a wafer from the planar condition, when such a deviation includes both concave and convex regions, was performed by Leroy and Plougonven.[408] They determined the temperature dependence of the critical shear stress as a function of precipitated oxygen concentration. The data of the critical stress at the center of the wafer are reported in Fig. 89. The figure clearly shows that as the precipitated oxygen increases the temperature marking the critical shear stress decreases. In other words, the higher the oxygen precipita-

Downloaded 21 Apr 2008 to 146.186.238.16. Redistribution subject to AIP license or copyright; see http://jap.aip.org/jap/copyright.jsp

SIONYX1403000027.0020

SAMSUNG EX. 1002 - 2558/4148

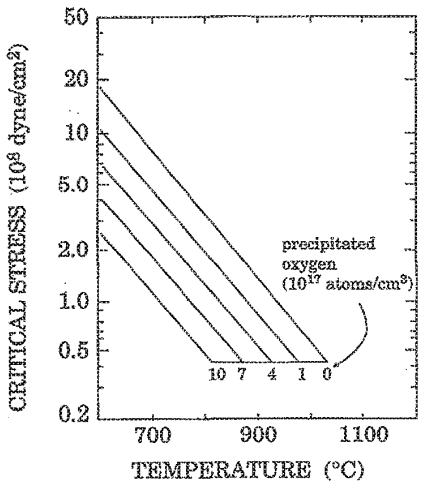

FIG. 89. Critical stress at the center of the wafer as a function of annealing temperature for different precipitated oxygen concentrations (from Ref. 408).

tion the lower the mechanical strength. An important result is that warpage increases with wafer diameter, so that the use of thicker wafers is necessary.

Dislocation generation, especially when it occurs at the center of the wafers, produces warping, therefore influencing the wafer mechanical properties. A study of the influence of oxygen precipitation and dislocations on mechanical properties of heat-treated Cz grown silicon was performed by Yasutake, Umeno, and Kawabe[409] on samples with $9-10\times10^{17}$ atoms/cm^3 interstitial oxygen content and with $8-12\times10^{16}$ atoms/cm^3 (crystal I) or undetectable (crystal II) carbon content. They evidenced that after annealing at 800 °C for 240 h the stress in crystal I does not decrease, probably due to the fact that the very small oxygen clusters (<50 Å) present in this sample do not act as dislocation sources, but as obstacles to their movement. On the other hand, the stress in crystal II is remarkably lower, probably due to the presence of glide

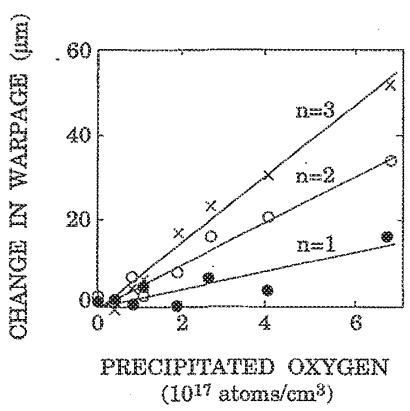

FIG. 90. Change in warpage as a function of precipitated oxygen concentration after n thermal cycles at 1000 °C (from Ref. 410).

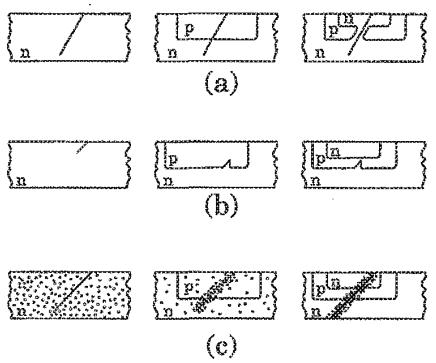

FIG. 91. Scheme of various models proposed to explain emitter-collector shorts: (a) Enhanced diffusion of emitter dopant along the crystal defect; (b) locally retarded base-dopant diffusion; (c) precipitation of fast diffusing impurities (from Ref. 415).

dislocations nucleated on platelike precipitates, present with large densities ($\sim10^9$ cm^{-3}) and dimensions. The direct influence of precipitated oxygen on wafer warpage for different sample heat treatments is illustrated in Fig. 90.[410] The figure refers to the warpage change as a function of precipitated oxygen after n thermal cycles at 1000 °C on samples preannealed at 800 °C. The change in warpage is defined as the difference in the bow along two orthogonally crossed ⟨010⟩ and ⟨001⟩ directions with respect to an untreated wafer. The warpage change increases as precipitated oxygen increases. This confirms that oxide precipitates act as sites for dislocation generation, which results in plastic wafer deformation. The wafer warpage is therefore inversely proportional to interstitial oxygen concentration.[411]

B. Influence of precipitation on the electrical properties of silicon

Electrical properties of IC devices are strongly influenced by the presence of defects like those induced by oxygen precipitation in crystalline silicon. For example, leakage currents, which increase in presence of oxide precipitates, are responsible for device degradation. In particular, they increase the current in reverse-biased p-n junctions, reduce refresh time in dynamic random access memories (RAM), and are responsible for the large collector-emitter current in bipolar transistors when the base terminal is open. The leakage current is related to different types of dislocations and to stacking faults, both intrinsic and extrinsic,[412–414] originating from oxide precipitates. These defects strongly affect the device yield being present in the active regions of the wafers (where the devices are located), both at the wafer surface and in the epitaxial layer. For example, in shallow junction transistors, emitter-collector shorts (pipes) increase the leakage current and constitute the dominant failure mechanism. Several factors have been proposed as responsible for the formation of pipes and are schematically illustrated in Fig. 91:[415]

(i) The enhanced diffusion of emitter dopant along the crystal defects [Fig. 91(a)];

Downloaded 21 Apr 2008 to 146.186.238.16. Redistribution subject to AIP license or copyright; see http://jap.aip.org/jap/copyright.jsp

SIONYX1403000027.0021

SAMSUNG EX. 1002 - 2559/4148

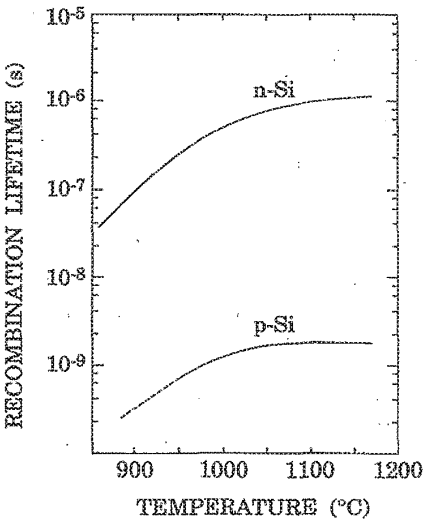

FIG. 92. Recombination lifetime as a function of the second-annealing temperature for n- and p-type silicon (from Ref. 423).

(ii) the locally retarded base-dopant diffusion [Fig. 91(b)]; and
(iii) the precipitation of fast diffusing impurities on crystal defects [Fig. 91(c)].

At the present time, the model involving factor (i) proposed by Miller[412] is accepted to a larger extent, although many questions remain still unsolved about the physical mechanisms involved.

It was found that the formation of SiO_x precipitates within the bulk of Cz wafers affects both the recombination and the generation lifetimes.[416] This has been found by using various techniques, such as the pulsed MOS capacitor method,[417–419] the diode recovery method,[420] the photoconductive method,[421] the surface photovoltage method,[418] and the measurement of the diode leakage current.[422] Nevertheless, it is not yet clearly established what causes the lifetime degradation, and questions on the following points are still open: The dominant source for lifetime degradation (precipitates, secondary defects such as dislocation loops or stacking faults, point defects); the relation of the carrier lifetime to the density and the size of precipitates and to the Si/precipitate interface; the differences and similarities between the known Si/SiO_2 interface and the Si/precipitate interface.

Variation of the recombination lifetime in Cz silicon with the temperature of the second annealing in a two-step anneal sequence as determined experimentally[423] for both p- and n-type bulk silicon is given in Fig. 92. Data concerning samples subjected to different heat treatments fit well on the curves. From DLTS measurements Hwang and Schroder[423] concluded that Si/precipitate interface states are the dominant recombination centers, responsible for the lifetime degradation. They developed a model to explain the difference between p- and n-type materials, based on the existence of fixed positive charges in the oxide near the Si/precipitate interface.

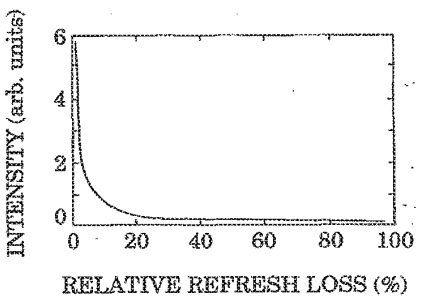

FIG. 93. Relative diffracted x-ray intensity as a function of relative refresh loss in a MOS dynamic RAM cell (from Ref. 164).

Kim, Kim, and Min[424] also studied the effects of electron traps on generation lifetime in heat-treated n-type Cz wafers by DLTS. They found that the volume defects induced by oxygen precipitation are related to the formation of deep traps. Furthermore, they found a relation between the increase of generation lifetime in MOS devices caused by Dz formation and the decrease of defects due to the aggregation of the deep traps created by oxygen, vacancies, and dislocation loops in the region where oxygen precipitates.

It has been reported[425] that in MCz crystals with 10 ppm of interstitial oxygen smaller amounts of oxide precipitates, dislocation loops, and stacking faults are produced after heat treatments as compared to conventional Cz crystals. Furthermore, it has been also shown[426] that MCz crystals have a higher minority-carrier generation lifetime than FZ and Cz crystals. Most of the earlier studies[426,427] showing that oxygen influences recombination lifetime were performed on processed material, the process conditions, process-induced impurities, and defects being possible causes of erroneous conclusions about the role of oxygen. To eliminate these problems, Pang and Rohatgi[428] measured the lifetime before and after processing on wafers cut from different sections of the same MCz-grown ingot, therefore having different oxygen concentrations. They found that oxygen-related defects formed during crystal growth, such as microprecipitates, lower the lifetime at a moderate injection level. On the contrary, these defects do not affect the lifetime associated with defect-related extrinsic recombination mechanisms in high-quality MCz with oxygen concentration <10 ppm.

Carrier lifetime in oxidized samples was found to decrease with oxygen concentration at lower as well as at moderate injection levels, while this is not true for as-grown material. The lifetime degradation at lower injection level is attributed to the interaction between process-induced impurities and oxygen.

Bipolar devices containing dislocations and stacking faults in the p-n junction region exhibit an enhanced reverse current,[429] which may reach values up to five orders of magnitude higher with respect to a p-n junction without defects. An increase of the forward voltage drop[430] and a reduced breakdown voltage[431] were also reported. The minority-carrier lifetime, defined as the mean time spent by excess charge carriers before they recombine to reestablish the ther-

Downloaded 21 Apr 2008 to 146.186.238.16. Redistribution subject to AIP license or copyright; see http://jap.aip.org/jap/copyright.jsp

SIONYX1403000027.0022

SAMSUNG EX. 1002 - 2560/4148

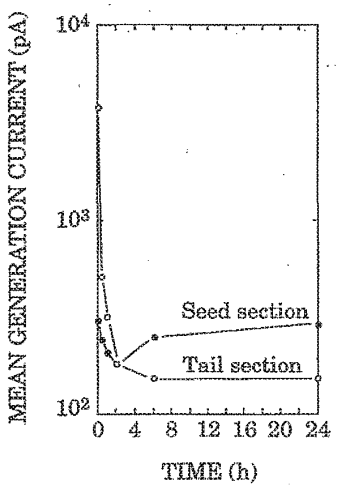

FIG. 94. Mean generation current as a function of 1000 °C annealing time for MOS devices created on wafers cut from the seed-end and the tail-end parts of a Cz silicon crystal (from Ref. 434).

mal equilibrium carrier concentration, is reduced when oxygen precipitation increases[432] and electrical characteristics of n^+-p junctions on wafers with high oxygen content (and then high precipitated oxygen content) strongly depends on preheating treatment conditions.[433]

The beneficial effects of precipitated oxygen on MOS devices was extensively studied from different points of view. Huff *et al.*,[164] by analyzing the performances of n-channel MOS dynamic RAM, were able to correlate the refresh time to the MOS minority-carrier generation lifetime and to the amount of oxygen precipitated in the bulk of the wafer, as determined by x-ray topography. From the data reported in Fig. 93, where the relative diffracted x-ray intensity versus the relative refresh loss is illustrated, the authors clearly demonstrate that an increased oxygen precipitation in the bulk can be related to a reduced wafer refresh loss, also for wafers supplied by different vendors. The absence of data in the upper right-hand side of the figure is significant and shows that high refresh losses are associated with minimum oxygen precipitation in the bulk. Patrick, Hu, and Westdorp[434] reported the beneficial effect of oxide precipitates in reducing the generation currents in MOS capacitors, where they act as gettering sites. The value of the generation current, measured by the method of capacitance relaxation of a pulse-depleted MOS capacitor, strongly depends on the heat treatment of the wafers, i.e., on the oxide precipitate concentration. The value of the mean generation current in wafers obtained from the seed-end and tail-end parts of a silicon crystal as a function of 1000 °C annealing time is reported in Fig. 94, demonstrating that the generation current in MOS capacitors is strongly reduced by the increase of the wafer annealing time, i.e., by the increase of oxygen precipitation. On the contrary, when the precipitation-induced defects lie within the active region, large generation currents result.

Beyer *et al.*[435] studied the effect of a preannealing treatment on wafers supplied by different vendors subjected to the MOS thermal process sequence on oxygen precipitation and on MOS leakage current. Small variations of the MOS leakage current were detected in the different wafers after an initial 30 min 1150 °C heat treatment in O_2 and HCl. Without preannealing the MOS leakage current is significantly higher as shown in Table XII. During the simulation of MOS process the oxide precipitate concentration is significantly different in wafers supplied by different vendors and, within a given set of wafers coming from the same vendor, also from wafer to wafer. The reduction of MOS leakage current is correlated by Beyer *et al.*[435] to the presence of different defect distributions in annealed with respect to unannealed samples, mainly due to the oxygen outdiffusion from the surface and consequently to the formation of a DZ.

TABLE XII. Average precipitated oxygen and average MOS leakage current for different vendor wafers after MOS process simulation (from Ref. 435).

Vendor	Anneal process (°C)	Average precipitated oxygen (ppm)	MOS leakage current (pA)
I	1150+900	1.4±0.8	73±48
I	1150	1.6±0.9	43±53
I	900	4.5±2.0	176±126
I	none	4.6±2.5	212±122
II	1150	8.3±2.2	29±45
II	1150	23.4±1.5	35±59
III	1150+900	4.5±1.8	38±50
III	1150	25.2±1.9	38±57

C. Denuded zone

As illustrated before, the oxygen presence in silicon can play a positive or a negative role on the devices grown directly on the wafers or on epitaxial layers. Defects induced by oxygen precipitation in the device area during device processing, in particular those decorated by heavy metals, strongly reduce the yield. However, defects present in the bulk of the silicon wafers have a beneficial effect on device performances by acting as gettering sites for contaminating atoms, which otherwise would reach the active regions leading to the reduction of device yield. To be able to successfully use IG in production lines it is necessary to balance the amount of oxygen in different states during the circuit fabrication process. In particular, the amount of precipitated oxygen and the morphology of precipitates and their distribution, related to the depth of the DZ, have a strong influence on the gettering efficiency and therefore on the device yield. The conditions for effective intrinsic gettering by oxide precipitates were studied by Tice, Tan, and Gardner.[436,437] They found that after wafer annealing at 1150 °C the SiO_x precipitates and the related dislocations are mainly concentrated in the middle of the wafer section, leaving a defect-free region many micrometers thick near the section edges (wafer surface). The effect of this defect distribution is the reduction of the leakage current in p-n junctions.

A new IG technique based on the use of a two-step annealing was proposed by Nagasawa, Matsushita, and

Downloaded 21 Apr 2008 to 146.186.238.16. Redistribution subject to AIP license or copyright; see http://jap.aip.org/jap/copyright.jsp

SIONYX1403000027.0023

SAMSUNG EX. 1002 - 2561/4148

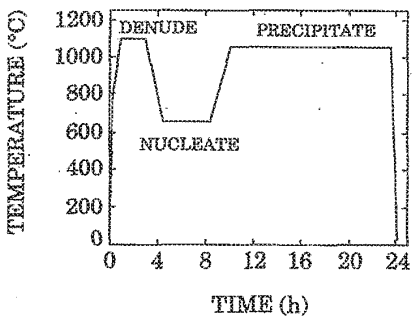

FIG. 95. Typical tristep thermal cycle.

Kishino.[438] The first step, at high temperature (~1000 °C), is carried out in order to out diffuse interstitial oxygen present near the wafer surface. The second step, at low temperature (~650 °C), introduces a high density of microdefects in the inner part of the wafer. This produces a wafer having both a defect-free DZ near the surface and a region rich in gettering sites in the bulk. More recently, the tristep thermal cycle shown in Fig. 95 has been recommended for IG applications[439] and is usually applied. The steps are as follows.

The first is a high-temperature step where the oxygen concentration near the surface is lowered due to out-diffusion and where precipitation does not occur. During this step the grown-in nuclei are dissolved. The width of the DZ can be well controlled by the duration and the temperature of this step.[440]

The second is a low-temperature (or preannealing) step, where the nuclei for precipitation form. The duration of this step determines the oxygen precipitation rate observed in the wafers. No measurable precipitation nor diffusion take place during this step.

The third is a precipitation step, frequently corresponding to the fabrication process.

The first step performed at high temperature is the most important one for DZ formation. The simplest model to calculate the out-diffusion of oxygen from the wafer is based on the solution of the one-dimensional diffusion equation,[441]

$$\frac{\partial C_{ox}(x,t)}{\partial t} = D\,\frac{\partial^2 C_{ox}(x,t)}{\partial x^2}, \tag{105}$$

where $C_{ox}(x,t)$ is the interstitial oxygen concentration and D the diffusion coefficient. Considering the following boundary conditions, C_0 being the initial interstitial oxygen concentration and C_s the solid solubility concentration of oxygen at the wafer surface, Eq. (105) gives the solution[441]

$$C_{ox}(x,t) = C_s + (C_0 - C_s)\,\mathrm{erf}\left(\frac{x}{2\sqrt{Dt}}\right), \tag{106}$$

expressing $C_{ox}(x,t)$ as a function of the position x with respect to the wafer surface and of time t. Using for C_s and D the values suggested by Andrews,[441] i.e.,

$$C_{ox}(x,t) = 1.63\times10^{21}\,\exp(-11\,973/T)\ \ (\mathrm{cm}^{-3}), \tag{107}$$

and

$$D = 0.17\,\exp(-29449/T)\ \ (\mathrm{cm}^2\,\mathrm{s}^{-1}), \tag{108}$$

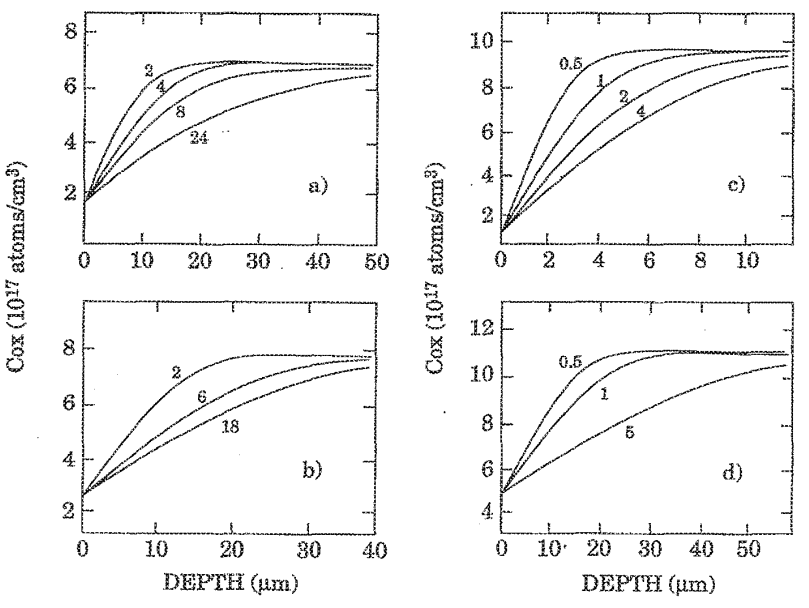

FIG. 96. Interstitial oxygen profiles as a function of depth for different first-step annealing times (marked on the curves in hour units): (a) $C_0 = 7\times10^{17}$ atoms/cm^3, $T = 1050$ °C; (b) $C_0 = 8\times10^{17}$ atoms/cm^3, $T = 1100$ °C; (c) $C_0 = 10\times10^{17}$ atoms/cm^3, $T = 1000$ °C; (d) $C_0 = 11\times10^{17}$ atoms/cm^3, $T = 1200$ °C (from Ref. 442).

Downloaded 21 Apr 2008 to 146.186.238.16. Redistribution subject to AIP license or copyright; see http://jap.aip.org/jap/copyright.jsp

SIONYX1403000027.0024

SAMSUNG EX. 1002 - 2562/4148

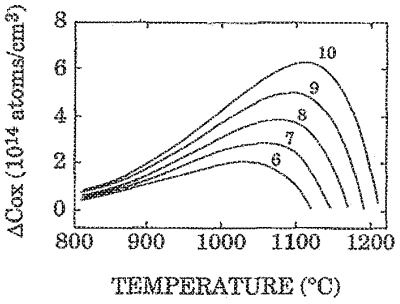

FIG. 97. Total interstitial oxygen removed per cm^2 area from a silicon wafer ΔC_{ox} as a function of temperature of the 5 h first-step annealing for various initial oxygen contents (marked on the curves in 10^{17} atoms/cm^3 units) (from Ref. 442).

it is possible to obtain a family of different interstitial oxygen concentration profiles for various times of the high-temperature first annealing step. Figures 96(a)–96(d) report the families of interstitial oxygen profiles as a function of the depth x for initial oxygen content of 7, 8, 10, and 11×10^{17} atoms/cm^3, respectively, and for different temperatures.[442] To optimize the first step of the annealing cycle it is necessary to find, for a given initial oxygen concentration, the temperature and annealing time corresponding to the maximum quantity of interstitial oxygen removed from the silicon wafer by out-diffusion. The total quantity Q of oxygen removed from 1 cm^2 of surface area of the wafer can be calculated by integrating the difference between the initial oxygen content C_0 and the oxygen concentration $C_{ox}(x,t)$ given in Eq. (106),

$$Q=\int_0^\infty [C_0-C_{ox}(x,t)]dx$$

$$=(C_0-C_s)\int_0^\infty \operatorname{erfc}\left(\frac{x}{2\sqrt{Dt}}\right)dx, \tag{109}$$

obtaining

$$Q=2\left(\frac{Dt}{\pi}\right)^{1/2}(C_0-C_s)\ \ (\mathrm{cm}^{-2}). \tag{110}$$

A plot of Q as a function of the annealing temperature for 5 h denuding time, calculated from Eq. (110) by Villa and Paciaroni,[442] is shown in Fig. 97 for various initial interstitial oxygen concentrations. The competition effect between oxygen diffusivity and solubility at different temperatures causes a maximum in Q. From the figure the best temperature for oxygen removal can be easily found for the different values of initial oxygen content.

Temperature and duration of the first-step annealing determine the DZ width (DZW). From experimental data fitting the following general analytical expression for DZW dependence on the duration of the first annealing has been found:[440,441,443]

$$\mathrm{DZW}=A+B\sqrt{t}, \tag{111}$$

TABLE XIII. Summary of experimental data of denuded zone width (DZW) as a function of first annealing temperature T and time t, nucleation annealing conditions N, precipitation annealing conditions P, and initial interstitial oxygen content C_{ox}.

T (°C)	t (h)	N	P	C_{ox} ($\times10^{17}$ atoms/cm^3)	DZW (μm)	Ref.
1100	1	700 °C	1050 °C	11	11	441
	2	24 h	2 h		16	
	4				23	
	8				25	
1100	2	750 °C	1000 °C	8	10	443
	6	6–24 h	8–48 h		17	
	10				24	
1000	0.5	650 °C	1050 °C	10	3	49
	1	4 h	16 h		5	
	2				7	
	4				8	
1100	0.5	650 °C	1050 °C	10	7	49
	1	4 h	16 h		10	
	2				12	
	4				15	
950	2	750 °C	1000 °C	7	8	405
	4	10–20 h	24 h		10	
	8				14	
	24				18	
1000	2	750 °C	1000 °C	7	11	405
	4	10–20 h	24 h		14	
	8				18	
	24				29	
1050	2	750 °C	1000 °C	7	15	405
	4	10–20 h	24 h		22	
	8				31	
	24				44	
1200	0.5	700 °C	1000 °C	11	12	440
	1	16 h	6 h		17	
	5				31	
1180	1	730 °C	1000 °C	9	16	444
	3	8 h	10 h		27	
	5				35	
1180	3	650 °C	1000 °C	9	22	444
		8 h	10 h			
1180	3	800 °C	1000 °C	9	~28	444
		8 h	10 h			
1180	5	730 °C	1000 °C	8	36	444
		8 h	10 h			
1000	5	730 °C	1000 °C	8	25	444
		2–16 h	~5 h			

where A and B are constants. A summary of experimental data of DZW as a function of different thermal treatments is reported in Table XIII.[444]

The second step is the most important one for the IG and has to be performed at low temperature (650–950 °C) before device fabrication. The high efficiency of this low-temperature annealing in generating the precipitation nuclei is clearly evident from the dependence of the nucleation rate J on the degree of supersaturation σ.[445] Considering the mole fraction of interstitial oxygen in the silicon crystal $X_{ox}=N_{ox}/(N_{ox}+N_{Si})$, where N_{ox} is the number of oxygen moles dissolved in a silicon wafer of N_{Si} moles, and the mole fraction corresponding to saturation X_{ox}^*, σ is defined as

$$\sigma=\frac{X_{ox}}{X_{ox}^*}-1. \tag{112}$$

Downloaded 21 Apr 2008 to 146.186.238.16. Redistribution subject to AIP license or copyright; see http://jap.aip.org/jap/copyright.jsp

SIONYX1403000027.0025

SAMSUNG EX. 1002 - 2563/4148

As proposed by Ataka and Ogawa,[445]

$$J = K\sigma^{\gamma}, \tag{113}$$

where K is a constant depending on the thermodynamic conditions of the silicon crystal and γ is a constant related to the number of oxygen atoms included in the nuclei. σ being inversely proportional to the temperature, J becomes higher if the temperature is decreased. At the low temperatures that are adequate for nucleation, no significant oxygen diffusion occurs, since the oxygen diffusion coefficient D is very small. On the contrary, at high temperatures the nucleation rate is negligible ($\sigma \simeq 0$), while oxygen diffusion is favored so that the growth of the nuclei previously formed can take place.

A more detailed description of nucleation can be given considering that the nucleation annealing is usually performed for such times that Eq. (30) holds, i.e., the saturation regime has not yet been reached (see Sec. III A and Figs. 19–22 therein). On the basis of this equation and looking at Fig. 19(c), the existence of an optimum temperature range for nucleation can be evidenced. If the interstitial oxygen concentration is varied from 6 to 20×10^{17} atoms/cm^3 the optimum nucleation temperature ranges from 650 to 950 °C. In particular, for the C_{ox} of the wafers used for technological applications, typically from 6 to 8.5×10^{17} atoms/cm^3, the annealing temperature corresponding to the maximum nucleation rate is between 650 and 800 °C. At lower and higher temperatures the number of generated nuclei is almost negligible.

The third annealing step at high temperature (precipitation annealing) is responsible for the precipitate growth. The nuclei formed during the previous step increase their size with the concomitane growth of oxide precipitates, thus reducing the interstitial oxygen concentration in the surrounding regions of the crystal. The radius of the precipitates strongly depends on the annealing temperature (D is a function of temperature), on the interstitial oxygen content, on the annealing time, and on the precipitation rate $1/\tau$, as discussed above [see Sec. III B and Eq. (76)]. Since the interstitial oxygen concentration C_{ox} is not constant along the wafer depth due to the first out-diffusion step, the distribution of precipitates is also expected to vary as a function of depth. In particular the region near the surface is expected to be precipitate free, while the bulk region is precipitate rich. The separation between surface and bulk regions is not sharp, but a wide transition layer forms.

The profile of the precipitated oxygen distribution in the silicon wafer as a function of depth can be evaluated on the basis of the interstitial oxygen depth profile $C_{ox}(x)$ obtained during the outdiffusion annealing (first step) and taking into account the results illustrated in Sec. III B. Considering Eq. (62) and assuming $Z=0$, Eq. (65) can be rewritten as

$$K = DN^{2/3}\left[\left(\frac{4}{3}\pi\right)^2 \frac{C_0 - C'}{C_P - C'}\right]^{1/3}. \tag{114}$$

Given the conditions of the precipitation annealing, all parameters entering Eq. (114) are determined, and N can be evaluated from the relation $N = Jt_{nucl}$. The nucleation rate J is a function of temperature and interstitial oxygen concentration, as discussed in Sec. III A, and its value for the nucleation temperature and the C_{ox} of interest can be found from Fig. 19(c). Therefore, from the $C_{ox}(x)$ profile a $K(x)$ profile is obtained. Then, through Eq. (64), the quantity $K(x)t_{prec}$, where t_{prec} is the duration of the precipitation annealing, can be related to the precipitated oxygen concentration $\Delta C_{ox} = 1 - [(C_m - C')/(C_0 - C')]$ [see Fig. 31(b)]. The depth distribution of precipitated oxygen $\Delta C_{ox}(x)$ is therefore determined. As an example, Fig. 98 shows such profiles for silicon crystals subjected to a 10 h precipitation annealing performed at 1000 °C after an 8 h nucleation annealing at 650, 730, or 800 °C. From this figure the importance of the nucleation annealing for the final profile of precipitated oxygen is evident.

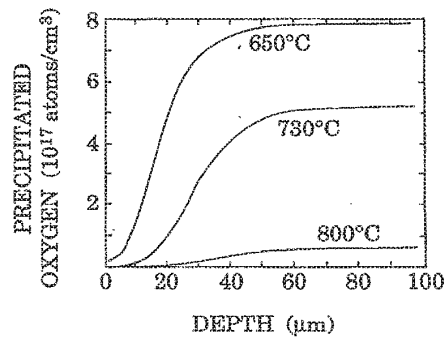

FIG. 98. Precipitated oxygen profiles as a function of depth for different temperatures of the 8 h nucleation annealing. Precipitation annealing is performed at 1000 °C for 10 h (from Ref. 444).

D. Influence of precipitation on device yield: Some examples

A detailed study of the yield of bipolar, CMOS, and charge-coupled-device (CCD) devices as a function of oxygen precipitation was performed by Jastrzebski *et al.*[158] Their work clearly shows that IG obtained during typical bipolar, CMOS, and CCD processes can be successfully used to improve the device yield. The best gettering efficiency is achieved for a certain amount of precipitated oxygen. Figure 99 shows the efficiency of internal gettering during the bipo-

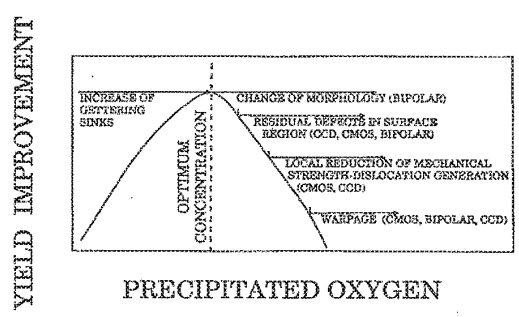

FIG. 99. Efficiency of IG as a function of the amount of precipitated oxygen. The contributions of various mechanisms are indicated (from Ref. 158).

Downloaded 21 Apr 2008 to 146.186.238.16. Redistribution subject to AIP license or copyright; see http://jap.aip.org/jap/copyright.jsp

SIONYX1403000027.0026

SAMSUNG EX. 1002 - 2564/4148

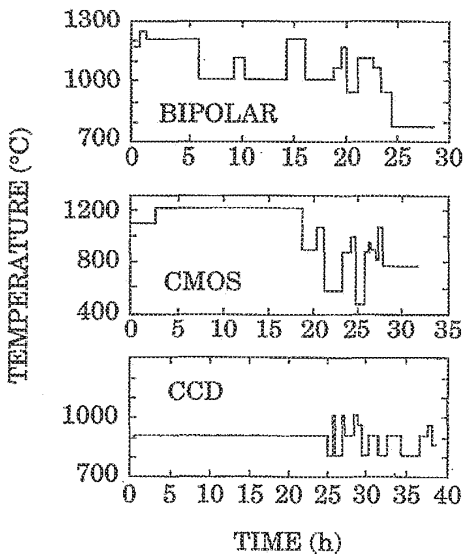

FIG. 100. Thermal cycles used to simulate bipolar, CMOS, and CCD process (from Ref. 158).

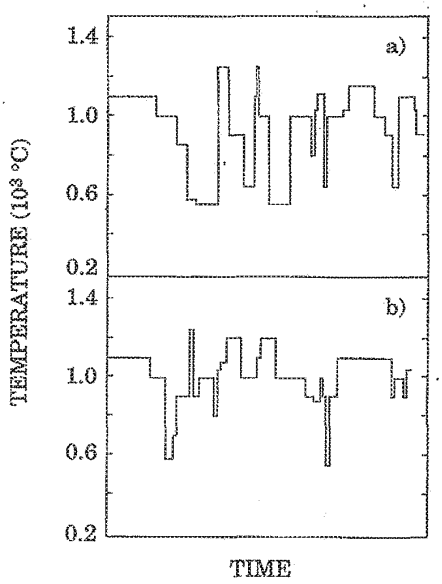

FIG. 101. Thermal cycles used to fabricate the (a) bipolar and (b) DMOS devices studied in Ref. 444.

lar, CMOS, and CCD processes (simulated by the thermal cycles illustrated in Fig. 100), expressed through the normalized yield as a function of the amount of precipitated oxygen. Initially, the gettering efficiency increases with the amount of precipitated oxygen. This is related to the increase of the number of gettering sites; the decrease of gettering efficiency found for higher amounts of precipitated oxygen is due instead to different phenomena, shown in Fig. 99. In the wafers subjected to the simulated bipolar process the maximum gettering efficiency is reached for 10 ppm of precipitated oxygen, while a decrease of the gettering efficiency is found for higher concentrations, mostly due to the precipitate morphology. In fact, in the case of low oxygen precipitation a low density of large stacking faults (which have been found to be the most efficient gettering centers for bipolar process) was observed. When the precipitated oxygen is more than 10 ppm high densities of small precipitates and stacking faults are usually observed (thus reducing the gettering efficiency).

The CMOS devices are less sensitive to contaminations than bipolar circuits. The optimum concentration of precipitated oxygen for internal gettering is 16 ppm, induced by the high-temperature treatment during CMOS process. Any attempt to increase the concentration of oxide precipitates by wafer preannealing prior to CMOS process results in a yield reduction. The reduction is mainly caused by the increase of residual defects close to the surface, which worsen the device performances. The best yield results are obtained with 28–32 ppm of initial interstitial oxygen concentration. The authors found that wafers with the same initial oxygen content supplied by different vendors show large differences in the amount of precipitated oxygen and attributed this effect to differences in the number of nucleation centers for oxide precipitates.

The performances of CCD are more affected by crystallographic defects than those of bipolar circuits and CMOS. Defects producing a recombination current of a few tenths of pA are observable as white or black spots in the display. The concentration of precipitated oxygen which gives the maximum yield after a CCD process is about 14 ppm. An additional three-step preheating is necessary (1100 °C for 3 h, 650 °C for 10 h, and 1100 °C for 4 h). The wafers that give the best results contain 28–31 ppm of initial interstitial oxygen. The increase of the amount of precipitated oxygen does not improve the yield, due to the presence of residual defects in the surface region, to the local reduction of mechanical strength, to the generation of dislocations, to the wafer warpage, and to slip formation.

Interesting results regarding the correlation between oxygen precipitation in silicon wafer substrates and device yield [for smart power bipolar and double diffused MOS (DMOS) devices] are illustrated by Villa and Paciaroni.[442] The devices were fabricated on 15-μm-thick epitaxial layers grown on substrates with interstitial oxygen concentration ranging from 6 to 8.5×10^{17} atoms/cm^3. The wafers were grouped in five sets, each one covering approximatively a 0.5×10^{17} atoms/cm^3 C_{ox} range. The thermal cycles used to produce the bipolar and DMOS devices are reported in Figs. 101(a) and 101(b), respectively. The parameters used to evaluate the device yield were I_{CE_0} (i.e., the current circulating between collector and emitter with open basis) for bipolar transistors and I_{DSS} (i.e., the current circulating between drain and short-circuited gate and source) for DMOS devices. I_{CE_0} is required to be less than 10 μA when a 20 V voltage is applied between emitter and collector, while I_{DSS} is required to be less than 10 μA when a 60 V voltage is applied between the drain and the short-circuited gate and

Downloaded 21 Apr 2008 to 146.186.238.16. Redistribution subject to AIP license or copyright; see http://jap.aip.org/jap/copyright.jsp

SIONYX1403000027.0027

SAMSUNG EX. 1002 - 2565/4148

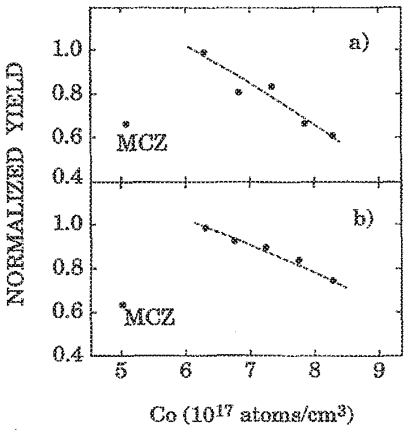

FIG. 102. Normalized yield of (a) bipolar and (b) DMOS devices as a function of initial oxygen content in the substrates. The data labeled MCz refer to devices created on MCz substrates (from Ref. 444).

source. The normalized yield for bipolar and DMOS devices fabricated on each group of wafers without any DZ treatment is reported in Figs. 102(a) and 102(b) respectively, as a function of initial C_{ox}. The decrease of the device yield by increasing the interstitial oxygen content of the wafers is clearly evidenced for both types of device. This effect is probably due to the increase of defects such as stacking faults which are generated in the bulk of oxygen-rich wafers and reach the epitaxial layer. There they originate pipes causing device failure.

Using wafers obtained from MCz ingots as substrates (i.e., wafers with a very low oxygen content, $3-5\times10^{17}$ atoms/cm^3), the device yield is strongly reduced (see Fig. 102).[444] This means that a particular C_{ox} value corresponding to the maximum device yield exists (in this case it is about 6.5×10^{17} atoms/cm^3). The reduction of yield for devices fabricated on MCz wafers is probably due to the large warpage observed in such wafers, related to their low C_{ox} [see Sec. V A]. In fact, warpage is extremely critical in processes requiring a lot of masking and alignment procedures.

ACKNOWLEDGMENTS

This work is dedicated to Professor A. Gigli Berzolari on the occasion of his 74th birthday. We would like to thank R. Falster, J. Vanhellemont, and F. F. Villa for helpful discussions and suggestions, and F. Capasso for encouragement. Many colleagues gave important contributions in different ways to our work and we would especially like to mention T. Abe, S. K. Bains, K. G. Barraclough, A. Bourret, A. J. R. de Kock, P. Gall, P. Gaworzewski, B. O. Kolbesen, Z. J. Laczik, R. C. Newman, S. Pahlke, M. Pedrotti, M. L. Polignano, F. A. Ponce, M. Porrini, P. Rossetto, G. A. Rozgonyi, R. J. Stewart, B. K. Tanner, W. A. Tiller, P. Wagner, W. Wijaranakula, and W. Zulehner for their kind collaboration. The technical assistance of M. Moscardini was particularly appreciated. This work was partially supported by the Progetto finalizzato "Materiali e Dispositivi per Elettronica a Stato Solido" of Consiglio Nazionale delle Ricerche.

[1] J. Czochralski, Z. Phys. Chem. **92**, 219 (1917).
[2] G. K. Teal and J. B. Little, Phys. Rev. **78**, 647 (1950).
[3] G. K. Teal and E. Bühler, Phys. Rev. **87**, 190 (1952).
[4] W. C. Dash, J. Appl. Phys. **30**, 459 (1959).
[5] W. Zulehner, in *Semiconductor Silicon 1989*, edited by G. Harbeke and M. J. Schulz (Springer, Heidelberg, 1989), p. 2.
[6] A. Murgai, in *Semiconductor Silicon 1981*, edited by H. R. Huff and R. J. Kriegler (The Electrochemical Society, Pennington, NJ, 1981), p. 113.
[7] K. Hoshikawa, H. Hirata, H. Nakanishi, and K. Ikuta, in *Semiconductor Silicon 1981*, edited by H. R. Huff and R. J. Kriegler (The Electrochemical Society, Pennington, NJ, 1981), p. 101.
[8] T. Carlberf, T. B. King, and A. F. Witt, J. Electrochem. Soc. **129**, 189 (1982).
[9] J. W. Moody, in *Semiconductor Silicon 1986*, edited by H. R. Huff, T. Abe, and B. Kolbesen (The Electrochemical Society, Pennington, NJ, 1986), p. 100.
[10] A. M. J. G. van Run, U.S. Patent No. 4,474,641 (1984).
[11] G. Fiegl, Solid State Technol. August, 121 (1983).
[12] H. A. Chedzey and D. T. J. Hurle, Nature **210**, 933 (1966).
[13] H. P. Utech and M. C. Flemings, J. Appl. Phys. **37**, 2021 (1970).
[14] A. F. Witt, C. J. Herman, and H. C. Gatos, J. Mater. Sci. **5**, 822 (1970).
[15] T. Suzuki, N. Isawa, Y. Okubo, and K. Hoshi, in *Semiconductor Silicon 1981*, edited by H. R. Huff and R. J. Kriegler (The Electrochemical Society, Pennington, NJ, 1981), p. 90.
[16] M. Ohwa, T. Higuchi, E. Toji, M. Watanabe, K. Homma, and S. Takasu, in *Semiconductor Silicon 1986*, edited by H. R. Huff, T. Abe, and B. Kolbesen (The Electrochemical Society, Pennington, NJ, 1986), p. 117.
[17] M. Porrini and P. Rossetto, in *Symposium on Materials and Devices for Power Electronics*, edited by F. Ferraris (GEDA, Torino, 1991), p. 90.
[18] W. Kaiser, P. H. Keck, and C. F. Lange, Phys. Rev. **101**, 1264 (1956).
[19] W. Kaiser, Phys. Rev. **105**, 1751 (1957).
[20] W. L. Bond and W. Kaiser, J. Phys. Chem. Solids **16**, 44 (1960).
[21] J. W. Corbett, R. S. McDonald, and G. D. Watkins, J. Phys. Chem. Solids **25**, 873 (1964).
[22] M. Stavola, Appl. Phys. Lett. **44**, 514 (1984).
[23] W. C. O'Mara, in *Defects in Silicon*, edited by W. M. Bullis and L. C. Kimerling (The Electrochemical Society, Pennington, NJ, 1983), p. 120.
[24] D. R. Bosomworth, W. Hayes, A. R. L. Spray, and G. D. Watkins, Proc. R. Soc. London Ser. A **317**, 133 (1970).
[25] Y. Yatsurugi, N. Akiyama, Y. Endo, and T. Nozaki, J. Electrochem. Soc. **120**, 975 (1973).
[26] C. S. Chen, F. Q. Zeng, Y. X. Huang, H. J. Ye, C. M. Hu, and D. K. Schroder, Appl. Phys. A **55**, 317 (1992).
[27] J. A. Burton, P. C. Prim, and W. P. Slichter, J. Chem. Phys. **21**, 1987 (1953).
[28] J. A. Burton, P. C. Prim, and W. P. Slichter, J. Chem. Phys. **21**, 1991 (1953).
[29] H. Kodera, Jpn. J. Appl. Phys. **2**, 212 (1963).
[30] T. Abe, K. Kikuchi, S. Shirai, and S. Muraoka, in *Semiconductor Silicon 1981*, edited by H. R. Huff and R. J. Kriegler (The Electrochemical Society, Pennington, NJ, 1981), p. 54.
[31] R. W. Series and K. G. Barraclough, in *Extended Abstracts Electrochemical Society Fall Meeting* (The Electrochemical Society, Pennington, NJ, 1987), p. 1009.
[32] H. Harada, T. Itoh, N. Ozawa, and T. Abe, in *VLSI Science and Technology 1985*, edited by W. M. Bullis and S. Broydo (The Electrochemical Society, Pennington, NJ, 1985), p. 526.
[33] L. Jastrzebski, IEEE Trans. Electron Devices **ED-29**, 475 (1982).
[34] R. J. Jaccodine and C. W. Pearce, in *Defects in Silicon*, edited by W. M. Bullis and L. C. Kimerling (The Electrochemical Society, Pennington, NJ, 1983), p. 115.
[35] F. A. Trumbore, Bell. Syst. Tech. J. **39**, 205 (1960).
[36] W. Lin and M. Stavola, J. Electrochem. Soc. **132**, 1412 (1985).
[37] W. Lin and D. W. Hill, J. Appl. Phys. **54**, 1082 (1983).
[38] R. B. Sosman, Trans. J. Br. Ceram. Soc. **54**, 655 (1955).
[39] K. M. Kim and W. E. Langlois, in *Semiconductor Silicon 1990*, edited by H. R. Huff, K. G. Barraclough, and J. Chikawa (The Electrochemical Society, Pennington, NJ, 1990), p. 81.
[40] J. C. Mikkelsen, Jr., in *Oxygen, Carbon, Hydrogen, and Nitrogen in Sili-*

Downloaded 21 Apr 2008 to 146.186.238.16. Redistribution subject to AIP license or copyright; see http://jap.aip.org/jap/copyright.jsp

SIONYX1403000027.0028

SAMSUNG EX. 1002 - 2566/4148

con, edited by J. C. Mikkelsen, Jr., S. J. Pearton, J. W. Corbett, and S. J. Pennycook (Materials Research Society, Princeton, NJ, 1986), p. 19.
[41] F. M. Livingston, S. Messoloras, R. C. Newman, B. C. Pike, R. J. Stewart, N. J. Binns, W. P. Brown, and J. G. Wilkes, J. Phys. C 17, 6253 (1984).
[42] S. T. Lee and D. Nichols, Appl. Phys. Lett. 47, 1001 (1985).
[43] S. T. Lee and D. Nichols, in *Oxygen, Carbon, Hydrogen, and Nitrogen in Silicon*, edited by J. C. Mikkelsen, Jr., S. J. Pearton, J. W. Corbett, and S. J. Pennycook (Materials Research Society, Princeton, NJ, 1986), p. 31.
[44] R. A. Logan and A. J. Peters, J. Appl. Phys. 30, 1627 (1959).
[45] A. R. Bean and R. C. Newman, J. Phys. Chem. Solids 32, 1211 (1971).
[46] Y. Itoh and T. Nozaki, Jpn. J. Appl. Phys. 24, 279 (1985).
[47] Y. Takano and M. Maki, in *Semiconductor Silicon 1973*, edited by H. R. Huff and R. R. Burgers (The Electrochemical Society, Princeton, NJ, 1973), p. 469.
[48] J. Gass, H. H. Müller, H. Stüssi, and S. Schweitzer, J. Appl. Phys. 51, 2030 (1980).
[49] R. A. Craven, in *Semiconductor Silicon 1981*, edited by H. R. Huff and R. J. Kriegler (The Electrochemical Society, Pennington, NJ, 1981), p. 254.
[50] H. J. Hrostowski and R. H. Kaiser, J. Phys. Chem. Solids 9, 214 (1959).
[51] W. Wijaranakula, Appl. Phys. Lett. 59, 1185 (1991).
[52] S. Messoloras, R. C. Newman, R. J. Stewart, and J. H. Tucker, Semicond. Sci. Technol. 2, 14 (1987).
[53] J. Vanhellemont and C. Claeys, Mater. Sci. Forum 38-41, 171 (1989).
[54] J. C. Mikkelsen, Jr., Appl. Phys. Lett. 41, 871 (1982).
[55] J. C. Mikkelsen, Jr., in *Defects in Silicon*, edited by W. M. Bullis and L. C. Kimerling (The Electrochemical Society, Pennington, NJ, 1983), p. 95.
[56] D. Heck, R. B. Tressler, and J. Monkowski, J. Appl. Phys. 54, 5739 (1983).
[57] M. Stavola, J. R. Patel, L. C. Kimerling, and P. E. Freeland, Appl. Phys. Lett. 42, 73 (1983).
[58] R. C. Newman, A. S. Oates, and F. M. Livingston, J. Phys. C 16, L667 (1983).
[59] J. C. Mikkelsen, Jr., in *Impurity Diffusion and Gettering in Silicon*, edited by R. B. Fair, C. W. Pearce, and J. Washburn (Materials Research Society, Pittsburgh, PA, 1985), p. 205.
[60] W. Wijaranakula, J. H. Matlock, and H. Mollenkopf, Appl. Phys. Lett. 53, 1068 (1988).
[61] A. S. Oates and W. Lin, Appl. Phys. Lett. 53, 2659 (1988).
[62] M. Pagani, J. Appl. Phys. 68, 3726 (1990).
[63] G. D. Watkins, J. W. Corbett, and R. S. McDonald, J. Appl. Phys. 53, 7097 (1982).
[64] R. C. Newman, A. R. Brown, R. Murray, A. Tipping, and J. H. Tucker, in *Semiconductor Silicon 1990*, edited by H. R. Huff, K. G. Barraclough, and J. Chikawa (The Electrochemical Society, Pennington, NJ, 1990), p. 734.
[65] J. C. Mikkelsen, Appl. Phys. Lett. 40, 336 (1982).
[66] A. S. Oates, M. J. Binns, R. C. Newman, J. H. Tucker, J. G. Wilkes, and A. Wilkinson, J. Phys. C 17, 5695 (1984).
[67] J. L. Benton, L. C. Kimerling, and M. Stavola, Physica B 116, 271 (1983).
[68] R. C. Newman, J. Phys. C 18, L967 (1985).
[69] R. C. Newman, A. K. Tipping, and J. H. Tucker, J. Phys. C 18, L861 (1985).
[70] F. Shimura, T. Higuchi, and R. S. Hockett, Appl. Phys. Lett. 53, 69 (1988).
[71] W. Wijaranakula, J. Appl. Phys. 68, 6538 (1990).
[72] R. C. Newman, J. H. Tucker, A. R. Brown, and S. A. McQuaid, J. Appl. Phys. 70, 3061 (1991).
[73] L. Zhong and F. Shimura, J. Appl. Phys. 73, 707 (1993).
[74] R. C. Newman, in *Defects in Electronic Materials*, edited by M. Stavola, S. J. Pearton, and G. Davies (Materials Research Society, Pittsburgh, PA, 1988), p. 25.
[75] M. Stavola and L. C. Snyder, in *Defects in Silicon*, edited by W. M. Bullis and L. C. Kimerling (The Electrochemical Society, Pennington, NJ, 1983), p. 61.
[76] S. T. Lee and P. Fellinger, Appl. Phys. Lett. 49, 1793 (1986).
[77] A. Bourret, J. Thibault-Desseaux, and D. N. Seidman, J. Appl. Phys. 55, 825 (1984).
[78] W. Bergholz, J. C. Hutchison, and P. Pirouz, J. Appl. Phys. 58, 3419 (1985).
[79] A. Bourret, in *Microscopy of Semiconducting Materials 1986*, Inst. Phys. Conf. Ser., Vol. 87 (ICP, Bristol, 1987), p. 39.
[80] U. Gösele and T. Y. Tan, Appl. Phys. A 317, 79 (1982).
[81] M. Needels, J. D. Joannopoulos, Y. Bar-Yam, and S. T. Pantelides, Phys. Rev. B 43, 4208 (1991).
[82] G. S. Oehrlein and J. W. Corbett, in *Defects in Semiconductors II*, edited by S. Mahajan and J. W. Corbett (North-Holland, New York, 1983), p. 107.
[83] L. C. Snyder and J. W. Corbett, in *Oxygen, Carbon, Hydrogen, and Nitrogen in Silicon*, edited by J. C. Mikkelsen, Jr., S. J. Pearton, J. W. Corbett, and S. J. Pennycook (Materials Research Society, Princeton, NJ, 1986), p. 207.
[84] L. C. Snyder, J. W. Corbett, P. Deak, and R. Wu, in *Defects in Electronic Materials*, edited by M. Stavola, S. J. Pearton, and G. Davies (Materials Research Society, Pittsburgh, PA, 1988), p. 179.
[85] A. Ourmazd, W. Schröter, and A. Bourret, J. Appl. Phys. 56, 1670 (1984).
[86] S. K. Estreicher, Phys. Rev. B 41, 9886 (1990).
[87] B. Pajot, Solid-State Electron. 12, 923 (1969).
[88] H. J. Hrostowski and R. H. Kaiser, Phys. Rev. 107, 966 (1957).
[89] R. C. Newman, *Infrared Studies of Crystal Defects* (Taylor and Francis, London, 1973).
[90] F. Shimura, Y. Ohnishi, and H. Tsuya, Appl. Phys. Lett. 38, 867 (1981).
[91] P. E. Freeland, J. Electrochem. Soc. 127, 754 (1980).
[92] B. Pajot, Analusis 5, 293 (1977).
[93] A. Baghdadi, W. M. Bullis, M. C. Croarkin, Y.-Z. Li, R. I. Scace, R. W. Series, P. Stallhofer, and M. Watanabe, J. Electrochem. Soc. 136, 2015 (1989).
[94] F. Schomann and K. Graff, J. Electrochem. Soc. 136, 2025 (1989).
[95] T. Tsuya, M. Kanamori, M. Takeda, and K. Yasuda, in *VLSI Science and Technology 1985*, edited by W. B. Bullis and S. Broydo (The Electrochemical Society, Pennington, NJ, 1985), p. 517.
[96] A. S. Oates and W. Lin, J. Cryst. Growth 89, 117 (1988).
[97] A. Borghesi, M. Geddo, G. Guizzetti, and P. Geranzani, J. Appl. Phys. 68, 1655 (1990).
[98] T. Iizuki, S. Takasu, M. Tajima, T. Arai, M. Nozaki, N. Inoue, and M. Watanabe, in *Defects in Silicon*, edited by W. M. Bullis and L. C. Kimerling (The Electrochemical Society, Pennington, NJ, 1983), p. 265.
[99] H. Shirai, J. Electrochem. Soc. 138, 1784 (1991).
[100] P. Wagner, Appl. Phys. A 53, 20 (1991).
[101] J. A. Baker, Solid-State Electron. 13, 1431 (1970).
[102] H. J. Rath, P. Stallhofer, D. Huber, and B. F. Schmitt, J. Electrochem. Soc. 131, 1920 (1984).
[103] G. Stingeder, S. Gara, S. Pahlke, H. Schwenk, E. Guerrero, and M. Grasserbauer, Fresenius Z. Anal. Chem. 333, 576 (1989).
[104] R. W. Shaw, R. Bredeweg, and P. Rossetto, J. Electrochem. Soc. 138, 582 (1991).
[105] S. Pahlke and W. Hauer, in *Technical Proceedings of SEMICON/EUROPA '90* (SEMI, Zürich, 1990), p. 64.
[106] P. Williams, R. K. Lewis, C. A. Evans, Jr., and P. R. Hanley, Anal. Chem. 49, 1399 (1977).
[107] K. Wittmaack, Nucl. Instrum. Methods 218, 327 (1983).
[108] R. J. Bleiler, R. S. Hockett, P. Chu, and E. Strathman, in *Oxygen, Carbon, Hydrogen, and Nitrogen in Crystalline Silicon*, edited by J. C. Mikkelsen, Jr., S. J. Pearton, J. W. Corbett, and S. J. Pennycook (Materials Research Society, Princeton, NJ, 1986), p. 73.
[109] V. R. Deline, W. Katz, C. A. Evans, Jr., and P. Williams, Appl. Phys. Lett. 33, 578 (1978).
[110] M. Goldstein, P. K. Chu, and R. J. Bleider, J. Vac. Sci. Technol. B 11, 92 (1993).
[111] S. M. Hu, Appl. Phys. Lett. 36, 561 (1980).
[112] S. M. Hu, J. Appl. Phys. 52, 3974 (1981).
[113] N. Inoue, J. Osaka, and K. Wada, J. Electrochem. Soc. 129, 2780 (1982).
[114] S. M. Hu, Materials Research Society Symp. 59, 249 (1986).
[115] N. Inoue, K. Watanabe, K. Wada, and J. Osaka, J. Cryst. Growth 84, 21 (1987).
[116] J. Vanhellemont and C. Claeys, J. Appl. Phys. 62, 3960 (1987).
[117] J. Vanhellemont and C. Claeys, J. Appl. Phys. 71, 1073 (1992).
[118] J. Burke, in *The Kinetics of Phase Transformations in Metals* (Pergamon, London, 1965), Chaps. 6 and 7.
[119] K. V. Ravi, J. Electrochem. Soc. 121, 1090 (1974).
[120] A. J. R. de Kock and W. M. Van de Wijgert, Appl. Phys. Lett. 38, 888 (1981).
[121] A. J. R. de Kock, in Proceedings of the ECS Satellite Symposium on Aggregation Phenomena of Point Defects in Silicon, Münich, 1982, p. 1.
[122] G. S. Oehrlein, J. L. Lindstrom, and J. W. Corbett, Appl. Phys. Lett. 40, 241 (1982).
[123] K. Wada, H. Nakanishi, H. Takaoka, and N. Inoue, J. Cryst. Growth 57, 535 (1982).
[124] R. A. Craven, Materials Research Society Symp. 36, 159 (1985).
[125] T. Y. Tan and C. Y. Kung, J. Appl. Phys. 59, 917 (1986).

Downloaded 21 Apr 2008 to 146.186.238.16. Redistribution subject to AIP license or copyright; see http://jap.aip.org/jap/copyright.jsp

SIONYX1403000027.0029

SAMSUNG EX. 1002 - 2567/4148

[126] N. Inoue, K. Wada, and J. Osaka, in *Defects and Properties of Semiconductors: Defect Engineering*, edited by J. Chikawa, K. Sumino, and K. Wada (KTK Scientific, Tokyo, 1987), p. 197.
[127] W. Zulehner, in Proceedings of the STEP Europe Conference 1988, p. 68.
[128] H. Furuya, I. Suzuki, Y. Shimanuki, and K. Murai, J. Electrochem. Soc. **135**, 677 (1988).
[129] N. Inoue, K. Wada, and J. Osaka, in *Semiconductor Silicon, 1981*, edited by H. R. Huff, R. J. Kriegel, and Y. Takeishi (The Electrochemical Society, Princeton, NJ, 1981), p. 282.
[130] H. Bender and J. Vanhellemont, in *Handbook on Semiconductors*, 2nd ed., edited by S. Mahajan (North-Holland, Amsterdam, 1994), Vol. 3, p. 1637
[131] N. I. Puzanov and A. M. Eidenzan, Semicond. Sci. Technol. **7**, 406 (1992).
[132] K. Wada and N. Inoue, in *Semiconductor Silicon 1986*, edited by H. R. Huff, T. Abe, and B. Kolbesen (The Electrochemical Society, Pennington, NJ, 1986), p. 778.
[133] S. Kishino, Y. Matsushita, and M. Kanamori, Appl. Phys. Lett. **35**, 213 (1979).
[134] P. Fraundorf, G. K. Fraundorf, and F. Shimura, J. Appl. Phys. **58**, 4049 (1985).
[135] F. Shimura, J. Appl. Phys. **59**, 3251 (1986).
[136] Q. Sun, K. H. Yao, J. Lagowski, and H. C. Gatos, J. Appl. Phys. **67**, 4313 (1990).
[137] E. W. Hart, Acta Metallogr. **6**, 553 (1958).
[138] A. Borghesi, B. Pivac, and A. Sassella, J. Cryst. Growth **126**, 63 (1993).
[139] J. Osaka, N. Inoue, and K. Kohra, Appl. Phys. Lett. **34**, 288 (1980).
[140] F. S. Ham, J. Phys. Chem. Solids **6**, 335 (1958).
[141] W. Patrick, E. Hearn, W. Westdorp, and A. Bohg, J. Appl. Phys. **50**, 7156 (1979).
[142] K. Wada, N. Inoue, and K. Kohra, J. Cryst. Growth **49**, 749 (1980).
[143] R. C. Newman, M. J. Binns, W. P. Brown, F. M. Livingston, S. Messoloras, R. J. Stewart, and J. G. Wilkes, Physica B **116**, 264 (1982).
[144] M. J. Binns, W. P. Brown, J. G. Wilkes, R. C. Newman, F. M. Livingston, S. Messoloras, and R. J. Stewart, Appl. Phys. Lett. **42**, 525 (1983).
[145] J. C. Wilkes, J. Cryst. Growth **65**, 214 (1983).
[146] R. C. Newman, M. Claybourn, S. H. Kinder, S. Messoloras, A. S. Oates, and R. J. Stewart, in *Semiconductor Silicon 1986*, edited by H. R. Huff, T. Abe, and B. Kolbesen (The Electrochemical Society, Pennington, NJ, 1986), p. 766.
[147] S. M. Hu, Appl. Phys. Lett. **48**, 115 (1986).
[148] Y. Matsushita, J. Cryst. Growth **54**, 588 (1981).
[149] F. A. Ponce and S. Hahn, Materials Research Society Symp. Proc. **31**, 153 (1984).
[150] W. A. Tiller, S. Hahn, and F. A. Ponce, J. Appl. Phys. **59**, 3255 (1986).
[151] H. Bender, Phys. Status Solidi A **86**, 245 (1984).
[152] C. S. Fuller and R. A. Logan, J. Appl. Phys. **28**, 1427 (1957).
[153] P. Capper, A. W. Jones, B. J. Wallhouse, and J. G. Wilkes, J. Appl. Phys. **48**, 1646 (1977).
[154] A. R. Bean and R. C. Newman, J. Phys. Chem. Solids **33**, 255 (1972).
[155] P. Gaworzewski and K. Schmalz, Phys. Status Solidi A **77**, 571 (1983).
[156] B. Goldsmith, L. Jastrzebski, and R. Soyden, in *Defects in Silicon*, edited by W. M. Bullis and L. C. Kimerling (The Electrochemical Society, Pennington, NJ, 1983), p. 142.
[157] H. D. Chiou and L. W. Shive, in *VLSI Science and Technology 1985*, edited by W. M. Bullis and S. Broydo (The Electrochemical Society, Pennington, NJ, 1985), p. 429.
[158] L. Jastrzebski, R. Soydan, J. Mc Ginn, R. Kleppinger, M. Blumenfeld, G. Gillespie, N. Armour, B. Goldsmith, W. Henry, and S. Vecrumba, J. Electrochem. Soc. **134**, 1018 (1987).
[159] Y. Shimanuki, H. Furuya, I. Suzuki, and K. Murai, Jpn. J. Appl. Phys. **24**, 1594 (1980).
[160] G. Fraundorf, P. Fraundorf, R. A. Craven, R. A. Frederick, J. Moody, and R. W. Shaw, J. Electrochem. Soc. **132**, 1701 (1985).
[161] F. Shimura and H. Tsuya, J. Electrochem. Soc. **129**, 1062 (1982).
[162] Y. Matsushita, J. Cryst. Growth **56**, 516 (1982).
[163] C. J. Varker, J. D. Whitfield, and L. Fejes, in *Silicon Processing*, ASTM STP 804 (ASTM, Philadelphia, PA, 1983), p. 369.
[164] H. R. Huff, H. F. Schaake, J. T. Robinson, S. C. Baber, and D. Wong, J. Electrochem. Soc. **130**, 1551 (1983).
[165] A. Virzi and M. Porrini, Mater. Sci. Eng. B **17**, 196 (1993).
[166] H. D. Chiou, Solid State Technol. March, 77 (1987).
[167] F. Shimura, Appl. Phys. Lett. **39**, 987 (1981).
[168] L. Jastrzebski, P. Zanzucchi, D. Thebault, and J. Lagowski, J. Electrochem. Soc. **129**, 1638 (1982).
[169] I. Fusegawa and H. Yamagishi, in *Proceedings of the 37th Symposium on Semiconductors and Integrated Circuits Technology* (The Electrochemical Society Japan, Tokyo, 1989), p. 31.
[170] K. Yang, J. Carle, and R. Kleinhenz, J. Appl. Phys. **62**, 4890 (1987).
[171] P. Fraundorf, G. K. Fraundorf, and R. A. Craven, in *VLSI Science and Technology 1985*, edited by W. M. Bullis and S. Broydo (The Electrochemical Society, Pennington, NJ, 1985), p. 436.
[172] H. F. Schaake, S. C. Baber, and R. F. Pinizzoto, in *Semiconductor Silicon 1981*, edited by H. R. Huff, R. J. Kriegler, and Y. Takeishi (The Electrochemical Society, Pennington, NJ, 1981), p. 273.
[173] I. Fusegawa, E. Iino, T. Hirohata, and H. Yamagishi, in *Defect Engineering in Semiconductor Growth, Processing and Device Technology*, edited by S. Ashok, J. Chevallier, K. Sumino, and E. Weber (Materials Research Society, Pittsburgh, PA, 1992), p. 683.
[174] H. D. Chiou, J. Electrochem. Soc. **139**, 1680 (1992).
[175] A. Bourret, in *Oxygen, Carbon, Hydrogen, and Nitrogen in Crystalline Silicon*, edited by J. C. Mikkelsen, Jr., S. J. Pearton, J. W. Corbett, and S. J. Pennycook (Materials Research Society, Princeton, NJ, 1986), p. 223.
[176] P. Wagner, C. Holm, E. Sirtl, R. Oeder, and W. Zulehner, Adv. Solid State Phys. **24**, 191 (1984).
[177] A. Bourret, in *Proceedings of the 13th International Conference on Defects in Semiconductors*, edited by L. C. Kimerling and J. M. Parsey, Jr. (The Metallurgical Soc. of AIME, Warrendale, PA, 1985), p. 129.
[178] L. C. Kimerling, in *Oxygen, Carbon, Hydrogen, and Nitrogen in Silicon*, edited by J. C. Mikkelsen, Jr., S. J. Pearton, J. W. Corbett, and S. J. Pennycook (Materials Research Society, Pittsburgh, PA, 1986), p. 83.
[179] R. C. Newman, in *Defects in Electronic Materials*, edited by M. Stavola, S. J. Pearton, and G. Davies (Materials Research Society, Pittsburgh, PA, 1988), p. 25.
[180] C. S. Fuller, J. W. Dietzenberger, N. B. Hannay, and E. Buehler, Phys. Rev. **96**, 833 (1954).
[181] W. Kaiser, H. L. Frisch, and H. Reiss, Phys. Rev. **112**, 1546 (1958).
[182] A. Kanamori and M. Kanamori, J. Appl. Phys. **50**, 8095 (1979).
[183] Y. Kamiura, F. Hashimoto, and K. Endo, J. Appl. Phys. **61**, 2478 (1987).
[184] J. L. Lindström, H. Weman, and G. S. Oehrlein, Phys. Status Solidi A **99**, 581 (1987).
[185] P. Wagner and J. Hage, Appl. Phys. A **49**, 123 (1989).
[186] M. Stavola and K. M. Lee, in *Oxygen, Carbon, Hydrogen, and Nitrogen in Crystalline Silicon*, edited by J. C. Mikkelsen, Jr., S. J. Pearton, J. W. Corbett, and S. J. Pennycook (Materials Research Society, Pittsburgh, PA, 1986), p. 95.
[187] M. Tajima, U. Gösele, J. Weber, and R. Sauer, Appl. Phys. Lett. **43**, 270 (1983).
[188] D. Wruck and P. Gaworzewski, Phys. Status Solidi A **56**, 557 (1979).
[189] S. Muller, M. Sprenger, E. G. Sieverts, and C. A. J. Ammerlaan, Solid State Commun. **25**, 987 (1978).
[190] J. Michel, J. R. Niklas, and J. M. Spaeth, in *Oxygen, Carbon, Hydrogen, and Nitrogen in Crystalline Silicon*, edited by J. C. Mikkelsen, Jr., S. J. Pearton, J. W. Corbett, and S. J. Pennycook (Materials Research Society, Pittsburgh, PA, 1986), p. 111.
[191] H. H. P. T. Bekman, T. Gregorkiewicz, and C. A. J. Ammerlaan, Mater. Sci. Forum **38-41**, 601 (1989).
[192] D. A. van Wezep, T. Gregorkiewicz, H. H. P. T. Bekman, and C. A. J. Ammerlaan, Mater. Sci. Forum **10-12**, 1009 (1986).
[193] L. C. Kimerling and J. L. Benton, Appl. Phys. Lett. **39**, 410 (1981).
[194] B. Pajot, H. Compain, J. Leroueille, and B. Clerjaud, Physica **117-118**, 110 (1983).
[195] W. Götz, G. Pensl, and W. Zulehner, Phys. Rev. B **46**, 4312 (1992).
[196] C. A. Londos, M. J. Binns, A. R. Brown, S. A. McQuaid, and R. C. Newman, Appl. Phys. Lett. **62**, 1525 (1993).
[197] V. Cazcarra and P. Zunino, J. Appl. Phys. **51**, 4206 (1980).
[198] P. Wagner, in *Oxygen, Carbon, Hydrogen, and Nitrogen in Crystalline Silicon*, edited by J. C. Mikkelsen, Jr., S. J. Pearton, J. W. Corbett, and S. J. Pennycook (Materials Research Society, Pittsburgh, PA, 1986), p. 125.
[199] M. Claybourn and R. C. Newman, Appl. Phys. Lett. **52**, 2139 (1988).
[200] J. W. Cleland, J. Electrochem. Soc. **129**, 2127 (1982).
[201] W. Wijaranakula, J. Appl. Phys. **69**, 2737 (1991).
[202] A. Ourmazd and W. Schröter, Appl. Phys. Lett. **45**, 781 (1984).
[203] M. Suezawa and K. Sumino, Phys. Status Solidi A **83**, 235 (1984).
[204] J. T. Borenstein, D. Peak, and J. W. Corbett, J. Mater. Res. **1**, 527 (1986).
[205] D. Helmreich and E. Sirtl, in *Semiconductor Silicon 1977*, edited by H.

Downloaded 21 Apr 2008 to 146.186.238.16. Redistribution subject to AIP license or copyright; see http://jap.aip.org/jap/copyright.jsp

SIONYX1403000027.0030

SAMSUNG EX. 1002 - 2568/4148

R. Huff and E. Sirtl (The Electrochemical Society, Princeton, NJ, 1977), p. 157.
[206] G. G. DeLeo, C. S. Milsted, and J. C. Kralik, Phys. Rev. B **31**, 3588 (1985).
[207] D. Mathiot, Appl. Phys. Lett. **51**, 904 (1987).
[208] H. M. Liaw and C. J. Varker, in *Semiconductor Silicon 1977*, edited by H. R. Huff and E. Sirtl (The Electrochemical Society, Princeton, NJ, 1977), p. 116.
[209] K. Schmalz and P. Gaworzewski, Phys. Status Solidi A **64**, 151 (1981).
[210] J. Leroueille, Phys. Status Solidi A **67**, 177 (1981).
[211] S. Hahn, H. J. Stein, S. C. Shatas, and F. A. Ponce, in *Defect Control in Semiconductors*, edited by K. Sumino (North-Holland, Amsterdam, 1990), p. 227.
[212] G. Pensl, M. Schulz, K. Hölzlein, W. Bergholz, and J. L. Hutchison, Appl. Phys. A **48**, 49 (1989).
[213] P. M. Grinshtein, G. V. Lazareva, E. V. Orlova, Z. A. Sal'nik, and V. I. Fistul, Sov. Phys. Semicond. **12**, 68 (1978).
[214] J. J. Qian, Z. G. Wang, S. K. Wan, and L. Y. Lin, J. Appl. Phys. **68**, 954 (1990).
[215] W. Wijaranakula and J. H. Matlock, J. Electrochem. Soc. **137**, 1964 (1990).
[216] J. A. Griffin, H. Navarro, J. Weber, L. Genzel, J. T. Borenstein, J. W. Corbett, and L. C. Snyder, J. Phys. C **19**, L579 (1986).
[217] J. A. Griffin, J. Hartung, and J. Weber, Mater. Sci. Forum **38-41**, 619 (1989).
[218] Y. Kamiura, F. Hashimoto, and M. Yoneta, J. Appl. Phys. **65**, 600 (1989).
[219] Y. Kamiura, M. Suezawa, K. Sumino, and F. Hashimoto, Jpn. J. Appl. Phys. **29**, L1937 (1990).
[220] Y. Kamiura, F. Hashimoto, and M. Yoneta, J. Appl. Phys. **66**, 3926 (1989).
[221] K. Tempelhoff, F. Spiegelberg, and R. Gleichmann, in *Semiconductor Silicon 1977*, edited by H. R. Huff and E. Sirtl (The Electrochemical Society, Princeton, NJ, 1977), p. 585.
[222] K. Tempelhoff, F. Spiegelberg, R. Gleichmann, and D. Wruck, Phys. Status Solidi A **56**, 213 (1979).
[223] K. Tempelhoff, B. Hahn, and R. Gleichmann, in *Semiconductor Silicon 1981*, edited by H. R. Huff, R. J. Kriegler, and Y. Takeishi (The Electrochemical Society, Pennington, NJ, 1981), p. 244.
[224] M. Reiche and O. Breitenstein, Phys. Status Solidi A **101**, K97 (1987).
[225] F. A. Ponce, T. Yamashita, and S. Hahn, in *Defects in Silicon*, edited by W. M. Bullis and L. C. Kimerling (The Electrochemical Society, Pennington, NJ, 1983), p. 105.
[226] C. Prunier, E. Ligeon, A. Bourret, A. C. Chami, and J. C. Oberlin, Nucl. Instrum. Methods B **17**, 227 (1986).
[227] A. Bourret, Inst. Phys. Conf. Ser. **87**, 39 (1987).
[228] J. A. Lambert and P. S. Dobson, Philos. Mag. A **44**, 1043 (1981).
[229] I. G. Salisbury and M. H. Loretto, Philos. Mag. A **39**, 317 (1979).
[230] N. Yamamoto, P. M. Petroff, and J. R. Patel, J. Appl. Phys. **54**, 3475 (1983).
[231] A. Bourret, J. Phys. (Paris) Colloq. **44**, 227 (1983).
[232] T. Y. Tan, Philos. Mag. A **44**, 101 (1981).
[233] H. Bender and J. Vanhellemont, Phys. Status Solidi A **107**, 455 (1988).
[234] P. Gaworzewski, E. Hild, F. G. Kirscht, and L. Vecsernyés, Phys. Status Solidi A **85**, 133 (1984).
[235] M. Reiche, J. Reichel, and W. Nitzsche, Phys. Status Solidi A **107**, 851 (1988).
[236] R. W. Carpenter, Y. L. Chen, M. J. Kim, and J. C. Barry, Inst. Phys. Conf. Ser. **100**, 543 (1989).
[237] T. Y. Tan and U. Gösele, Appl. Phys. Lett. **39**, 86 (1981).
[238] M. Servidori, S. Cannavo, G. Ferla, A. La Ferla, S. U. Campisano, and E. Rimini, Nucl. Instrum. Methods B **19/20**, 317 (1987).
[239] V. G. Eremenko and V. I. Nikitenko, Phys. Status Solidi A **14**, 317 (1972).
[240] P. Pirouz, R. Chaim, and J. Samuels, in *Proceedings of the 5th International Conference on Structure and Properties of Dislocations in Semiconductors* (Bulletin of the Academy of Sciences of the USSR, Moscow, 1986).
[241] G. B. Bronner and J. D. Plummer, J. Appl. Phys. **61**, 5286 (1987).
[242] H. J. Mayer, H. Mehrer, and K. Maier, Inst. Phys. Conf. Ser. **31**, 186 (1977).
[243] A. Parisini and A. Bourret, Philos. Mag. A **67**, 605 (1993).
[244] W. Bergholz, M. J. Binns, G. R. Booker, J. C. Hutchison, S. H. Kinder, S. Messoloras, R. C. Newman, R. J. Stewart, and J. G. Wilkes, Philos. Mag. B **59**, 499 (1989).
[245] F. A. Ponce and S. Hahn, Mater. Sci. Eng. B **4**, 11 (1989).
[246] R. W. Carpenter, I. Chan, H. L. Tsai, C. Varker, and L. J. Demer, in *Defects in Semiconductors II*, edited by S. Mahajan and J. W. Corbett (North-Holland, Amsterdam, 1983), p. 195.
[247] W. M. Skiff, H. L. Tsai, and R. W. Carpenter, in *Oxygen, Carbon, Hydrogen, and Nitrogen in Crystalline Silicon*, edited by J. C. Mikkelsen, Jr., S. J. Pearton, J. W. Corbett, and S. J. Pennycook (Materials Research Society, Princeton, NJ, 1986), p. 241.
[248] A. Borghesi, A. Piaggi, A. Sassella, A. Stella, and B. Pivac, Phys. Rev. B **46**, 4123 (1992).
[249] B. Pivac, A. Borghesi, M. Geddo, A. Sassella, and A. Stella, Appl. Surf. Sci. **63**, 245 (1993).
[250] S. Gupta, S. Messoloras, J. R. Schneider, R. J. Stewart, and W. Zulehner, Semicond. Sci. Technol. **5**, 783 (1990).
[251] S. Messoloras, J. R. Schneider, R. J. Stewart, and W. Zulehner, Semicond. Sci. Technol. **4**, 340 (1989).
[252] T. Takeda, S. Komura, A. Ohsawa, and K. Honda, Jpn. J. Appl. Phys. **26**, 106 (1987).
[253] J. J. Wortman and R. A. Evans, J. Appl. Phys. **36**, 153 (1965).
[254] W. A. Brantley, J. Appl. Phys. **44**, 534 (1973).
[255] H. Liang, Y. Pan, S. Zhao, G. Qin, and K. Chin, J. Appl. Phys. **71**, 2863 (1992).
[256] W. Wijaranakula, J. Appl. Phys. **72**, 4026 (1992).
[257] Y. Matsushita, S. Kishino, and M. Kanamori, Jpn. J. Appl. Phys. **19**, L101 (1980).
[258] T. Y. Tan and W. K. Tice, Philos. Mag. **34**, 615 (1976).
[259] H. Bender and J. Vanhellemont, in *Defect Engineering in Semiconductor Growth, Processing and Device Technology*, edited by S. Ashok, J. Chevallier, K. Sumino, and E. Weber (Materials Research Society, Pittsburgh, PA, 1992), p. 15
[260] F. Shimura, H. Tsuya, and T. Kawamura, Appl. Phys. Lett. **37**, 483 (1980).
[261] W. A. Tiller, J. Electrochem. Soc. **127**, 619 (1980).
[262] J. Vanhellemont and C. Claeys, in *Defects in Silicon II*, edited by W. M. Bullis, U. Gösele, and F. Shimura (The Electrochemical Society, Pennington, NJ, 1991), p. 263.
[263] W. J. Taylor, T. Y. Tan, and U. Gösele, in *Defects in Silicon II*, edited by W. M. Bullis, U. Gösele, and F. Shimura (The Electrochemical Society, Pennington, NJ, 1991), p. 255.
[264] K. H. Yang, R. Anderson, and H. F. Kappert, Appl. Phys. Lett. **33**, 225 (1978).
[265] F. A. Ponce, T. Yamashita, and S. Hahn, Appl. Phys. Lett. **43**, 1051 (1983).
[266] D. M. Maher, A. Staudinger, and J. R. Patel, J. Appl. Phys. **47**, 3813 (1976).
[267] S. Mahajan, G. A. Rozgonyi, and D. Brasen, Appl. Phys. Lett. **30**, 73 (1977).
[268] K. Wada, N. Inoue, and J. Osaka, in *Defects in Semiconductors II*, edited by S. Mahajan and J. W. Corbett (North-Holland, Amsterdam, 1983), p. 125.
[269] J. R. Patel and A. Authier, J. Appl. Phys. **46**, 118 (1975).
[270] M. Hasebe, Y. Takeoka, S. Shioyama, and S. Naito, in *Defect Control in Semiconductors*, edited by K. Sumino (North-Holland, Amsterdam, 1990), p. 157.
[271] M. S. Bawa, W. J. Bell, H. M. Grimes, and T. J. Shaffner, J. Cryst. Growth **94**, 803 (1989).
[272] H. S. Cho, H. W. Lee, Y. K. Kim, D. Buck, J. Rigotti, J. Yeh, S. Hahn, and W. A. Tiller, in *Defects in Silicon II*, edited by W. M. Bullis, U. Gösele, and F. Shimura (The Electrochemical Society, Pennington, NJ, 1991), p. 189.
[273] J. R. Patel, in *Semiconductor Silicon 1977*, edited by H. R. Huff and E. Sirtl (The Electrochemical Society, Princeton, NJ, 1977), p. 521.
[274] J. Vanhellemont, S. Amerlinckx, and C. Claeys, J. Appl. Phys. **61**, 2170 (1987).
[275] G. A. Hawkins and J. P. Lavine, J. Appl. Phys. **65**, 3644 (1989).
[276] H. Walitzki, H. J. Rath, J. Reffle, S. Pahlke, and M. Blatte, in *Semiconductor Silicon 1986*, edited by H. R. Huff, T. Abe, and B. Kolbesen (The Electrochemical Society, Pennington, NJ, 1986), p. 86.
[277] F. Shimura, W. Dyson, J. W. Moody, and R. S. Hocket, in *VLSI Science and Technology 1985*, edited by W. M. Bullis and S. Broydo (The Electrochemical Society, Pennington, NJ, 1985), p. 507.
[278] C. W. Pearce, T. Kook, and R. J. Jaccodine, in *Impurity Diffusion and Gettering in Silicon*, edited by R. B. Fair, C. W. Pearce, and J. Washburn (Materials Research Society, Pittsburgh, PA, 1983), p. 231.

Downloaded 21 Apr 2008 to 146.186.238.16. Redistribution subject to AIP license or copyright; see http://jap.aip.org/jap/copyright.jsp

SIONYX1403000027.0031

SAMSUNG EX. 1002 - 2569/4148

[279] S. K. Bains, D. P. Griffiths, J. G. Wilkes, R. W. Series, and K. G. Barraclough, J. Electrochem. Soc. **137**, 647 (1990).
[280] K. Wada, Phys. Rev. B **30**, 5884 (1984).
[281] K. G. Barraclough, J. Cryst. Growth **99**, 654 (1990).
[282] S. Hahn, F. A. Ponce, W. A. Tiller, V. Stojanoff, D. A. P. Bulla, and W. E. Castro, Jr., J. Appl. Phys. **64**, 4454 (1988).
[283] S. Hahn, F. A. Ponce, P. Masher, S. Dannefaer, D. Kerr, W. Puff, V. Stojanoff, W. W. Furtado, D. A. P. Bulla, P. B. S. Santos, S. Ishigami, and W. A. Tiller, in *Defects in Silicon II*, edited by W. M. Bullis, U. Gösele, and F. Shimura (The Electrochemical Society, Pennington, NJ, 1991), p. 297.
[284] S. Matsumoto, I. Ishihara, H. Kaneko, H. Harada, and T. Abe, Appl. Phys. Lett. **46**, 957 (1985).
[285] T. Fukuda and A. Ohsawa, Appl. Phys. Lett. **58**, 2634 (1991).
[286] T. Nozaki and Y. Itoh, J. Appl. Phys. **59**, 2562 (1986).
[287] S. Gupta, S. Messoloras, J. R. Schneider, R. J. Stewart, and W. Zulehner, Semicond. Sci. Technol. **7**, 443 (1992).
[288] F. Secco d'Aragona and P. L. Fejes, Appl. Phys. Lett. **48**, 665 (1986).
[289] K. G. Barraclough and J. G. Wilkes, in *Semiconductor Silicon 1986*, edited by H. R. Huff, T. Abe, and B. Kolbesen (The Electrochemical Society, Pennington, NJ, 1986), p. 889.
[290] B. O. Kolbesen and A. Mühlbauer, Solid-State Electron. **25**, 759 (1982).
[291] F. Shimura, J. P. Baiardo, and P. Fraundorf, Appl. Phys. Lett. **46**, 941 (1985).
[292] M. Ogino, Appl. Phys. Lett. **41**, 847 (1982).
[293] W. E. Bailey, R. A. Bowling, and K. E. Bean, J. Electrochem. Soc. **132**, 1721 (1985).
[294] M. Kanamori and H. Tsuya, Jpn. J. Appl. Phys. **24**, 557 (1985).
[295] C. Y. Kung, in *VLSI Science and Technology 1985*, edited by W. B. Bullis and S. Broydo (The Electrochemical Society, Pennington, NJ, 1985), p. 446.
[296] M. Schrems, P. Pongratz, M. Budil, H. W. Pötzl, J. Hage, E. Guerrero, and D. Huber, in *Semiconductor Silicon 1990*, edited by H. R. Huff, K. G. Barraclough, and J. Chikawa (The Electrochemical Society, Pennington, NJ, 1990), p. 144.
[297] S. Hahn, M. Arst, K. N. Ritz, S. Shatas, H. J. Stein, Z. U. Rek, and W. A. Tiller, in *Defects in Electronic Materials*, edited by M. Stavola, S. J. Pearton, and G. Davies (Materials Research Society, Pittsburgh, PA, 1988), p. 201.
[298] H. Bender, C. Claeys, J. Van Landuyt, G. Declerck, S. Amerlinckx, and R. Van Overstraeten, in *Proceedings of the 13th International Conference on Defects in Semiconductors*, edited by L. C. Kimerling and J. M. Parsey (The Metallurgical Soc. of AIME, Warrendale, PA, 1984), p. 587.
[299] F. Shimura, R. S. Hockett, D. A. Reed, and D. H. Wayne, Appl. Phys. Lett. **47**, 794 (1985).
[300] S. Gupta, S. Messoloras, J. R. Schneider, R. J. Stewart, and W. Zulehner, Semicond. Sci. Technol. **7**, 6 (1992).
[301] W. J. Taylor, U. M. Gösele, and T. Y. Tan, Jpn. J. Appl. Phys. **32**, 4857 (1993).
[302] T. Abe, H. Harada, N. Ozawa, and K. Adomi, in *Oxygen, Carbon, Hydrogen, and Nitrogen in Crystalline Silicon*, edited by J. C. Mikkelsen, Jr., S. J. Pearton, J. W. Corbett, and S. J. Pennycook (Materials Research Society, Pittsburgh, PA, 1986), p. 537.
[303] F. Shimura and R. S. Hockett, Appl. Phys. Lett. **48**, 224 (1986).
[304] A. Hara, T. Fukuda, T. Miyabo, and L. Hirai, Appl. Phys. Lett. **54**, 626 (1989).
[305] Q. Sun, K. H. Yao, H. C. Gatos, and J. Lagowski, J. Appl. Phys. **71**, 3760 (1992).
[306] R. C. Newman, in *Defects in Silicon II*, edited by W. M. Bullis, U. Gösele, and F. Shimura (The Electrochemical Society, Pennington, NJ, 1991), p. 271.
[307] E. E. Haller, Semicond. Sci. Technol. **6**, 73 (1991).
[308] C. D. Lamp and D. J. James II, Appl. Phys. Lett. **62**, 2081 (1993).
[309] A. Hara, M. Aoki, T. Fukuda, and A. Ohsawa, J. Appl. Phys. **74**, 913 (1993).
[310] J. S. Pearton, W. Corbett, and M. Stavola, *Hydrogen in Crystalline Semiconductors* (Springer, Berlin, 1992).
[311] S. Muto, S. Tukada, M. Hirata, and T. Tanabe, J. Appl. Phys. **70**, 3505 (1991).
[312] W. T. Stacy, M. C. Arst, K. N. Ritz, J. G. de Groot, and M. H. Norcott, in *Defects in Silicon*, edited by W. M. Bullis and L. C. Kimerling (The Electrochemical Society, Pennington, NJ, 1983), p. 423.
[313] M. C. Arst and J. G. de Groot, J. Electron. Mater. **13**, 763 (1984).
[314] H. Shirai, A. Yamaguchi, and F. Shimura, Appl. Phys. Lett. **54**, 1748 (1989).
[315] H. Harada, T. Abe, and J. Chikawa, in *Semiconductor Silicon 1986*, edited by H. R. Huff, T. Abe, and B. Kolbesen (The Electrochemical Society, Pennington, NJ, 1986), p. 76.
[316] A. Ikari, H. Haga, O. Yoda, A. Uedono, and Y. Ujihira, in *Defect Engineering in Semiconductor Growth, Processing and Device Technology*, edited by S. Ashok, J. Chevallier, K. Sumino, and E. Weber (Materials Research Society, Pittsburgh, PA, 1992), p. 69.
[317] T. Hallberg and J. L. Lindström, J. Appl. Phys. **72**, 5130 (1992).
[318] 1990 Annual Book of ASTM Standards, Vol. 10.05, F 416; F 47.
[319] D. C. Miller and G. A. Rozgonyi, in *Handbook of Semiconductors*, edited by S. P. Keller (North-Holland, Amsterdam, 1982), Vol. 3, p. 217.
[320] *Quick Reference Manual for Silicon Integrated Circuit Technology*, edited by W. E. Beadle, J. C. C. Tsai, and R. D. Plummer (Wiley, New York, 1985).
[321] B. O. Kolbesen and H. P. Strunk, in *VLSI Electronics*, edited by N. G. Einspruch and H. Huff (Academic, Orlando, FL, 1985), p. 143.
[322] E. Sirtl and A. Adler, Z. Mettalkem. **52**, 529 (1961).
[323] F. Secco d'Aragona, J. Electrochem. Soc. **119**, 948 (1972).
[324] M. Wright Jenkins, J. Electrochem. Soc. **124**, 757 (1977).
[325] D. G. Schimmel, J. Electrochem. Soc. **126**, 479 (1979).
[326] K. H. Yang, in *Semiconductor Processing*, edited by D. C. Gupta (ASTM, Philadelphia, PA, 1984), p. 309.
[327] G. Nomarski and A. R. Weill, Bull. Soc. Franc. Miner. Cryst. **77**, 840 (1954).
[328] W. Zulehner, in *Landolt-Börnstein—Numerical Data and Functional Relationships in Science and Technology*, edited by O. Madelung (Springer, Berlin, 1989), Vol. 22, Subvol. b, p. 391.
[329] A. Bourret, Materials Research Society Symp. Proc. **59**, 223 (1986).
[330] W. K. Tice and T. C. Huang, Appl. Phys. Lett. **24**, 157 (1974).
[331] H. Bender and J. Vanhellemont, Materials Research Society Symp. Proc. **262**, 15 (1992).
[332] H. Bender and J. Vanhellemont, in *Encyclopedia of Advanced Materials*, edited by D. Bloor, R. J. Brook, M. C. Flemings, and S. Mahajan (Pergamon, Oxford, 1994), p. 1906.
[333] R. Swaroop, N. Kim, W. Lin, M. Bullis, L. Shive, A. Rice, E. Castel, and M. Christ, Solid State Technol. March, 85 (1987).
[334] Annual Book of ASTM Standards, F 1239-89.
[335] W. J. Patrick, in *Silicon Device Processing*, National Bureau of Standards Special Publication No. 337 (U.S. GPO, Washington DC, 1970).
[336] S. M. Hu and W. J. Patrick, J. Appl. Phys. **46**, 1869 (1975).
[337] G. A. Rozgonyi and C. W. Pearce, Appl. Phys. Lett. **31**, 343 (1977).
[338] P. Gaworzewski, E. Hild, and K. Schmalz, Phys. Status Solidi A **90**, K151 (1985).
[339] S. M. Hu, J. Appl. Phys. **51**, 5945 (1980).
[340] L. Genzel and T. P. Martin, Phys. Status Solidi B **51**, 91 (1972).
[341] L. Genzel and T. P. Martin, Surf. Sci. **34**, 33 (1973).
[342] G. Hoffmann, A. Nagy, and L. Puskás, J. Phys. D **8**, 1044 (1975).
[343] C. Y. Kung, J. Appl. Phys. **65**, 4654 (1989).
[344] X.-T. Meng, Phys. Status Solidi A **129**, K131 (1992).
[345] A. Borghesi, M. Geddo, B. Pivac, A. Sassella, and A. Stella, Appl. Phys. Lett. **58**, 2099 (1991).
[346] A. Borghesi, M. Geddo, and B. Pivac, J. Appl. Phys. **60**, 7251 (1991).
[347] Q. Sun, J. Lagowski, and H. C. Gatos, Mater. Res. Symp. Proc. **104**, 205 (1988).
[348] B. Pivac, A. Borghesi, M. Geddo, A. Sassella, and A. Stella, Mater. Sci. Forum **83-87**, 1069 (1992).
[349] A. Borghesi, M. Geddo, B. Pivac, A. Stella, and P. Lupano, Appl. Phys. Lett. **58**, 2657 (1991).
[350] M. Geddo, B. Pivac, A. Borghesi, A. Stella, and M. Pedrotti, Appl. Phys. Lett. **57**, 1511 (1990).
[351] B. Pivac, A. Borghesi, M. Geddo, and A. Stella, Phys. Scr. T **39**, 265 (1991).
[352] A. Sassella and A. Borghesi, SPIE **1575**, 562 (1992).
[353] A. Borghesi, B. Pivac, and A. Sassella, Appl. Phys. Lett. **60**, 871 (1992).
[354] A. Borghesi, M. Geddo, B. Pivac, A. Sassella, and A. Stella, in *The Physics of Semiconductors*, edited by P. Jiang and H.-Z.Zheng (World Scientific, Singapore, 1992), Vol. 1, p. 1649.
[355] Y. Shimanuki, H. Furuya, and I. Suzuki, J. Electrochem. Soc. **136**, 2058 (1989).
[356] A. Sassella, Ph.D. thesis, Università degli Studi di Pavia, 1993.
[357] D. W. Berreman, Phys. Rev. B **130**, 2193 (1963).
[358] H. Ono and T. Ikarashi, Appl. Phys. Lett. **63**, 3303 (1993).

Downloaded 21 Apr 2008 to 146.186.238.16. Redistribution subject to AIP license or copyright; see http://jap.aip.org/jap/copyright.jsp

SIONYX1403000027.0032

SAMSUNG EX. 1002 - 2570/4148

[359] S. Messoloras, J. R. Schneider, R. J. Stewart, and W. Zulehner, Nature **336**, 364 (1988).
[360] S. Messoloras, B. C. Pike, R. J. Stewart, and C. G. Windsor, Metal. Sci. **18**, 311 (1984).
[361] S. Gupta, S. Messoloras, J. R. Schneider, R. J. Stewart, and W. Zulehner, J. Appl. Cryst. **24**, 576 (1991).
[362] C. F. Bohren and D. R. Huffman, *Absorption and Scattering of Light by Small Particles* (Wiley, New York, 1983).
[363] V. Vaud, K. Vedam, and R. Stein, J. Appl. Phys. **37**, 2551 (1966).
[364] K. Moriya and T. Ogawa, Philos. Mag. A **44**, 1085 (1981).
[365] K. Moriya and T. Ogawa, Jpn. J. Appl. Phys. **22**, L207 (1983).
[366] K. Moriya, Jpn. J. Appl. Phys. **55**, 6 (1986).
[367] T. Ogawa and N. Nango, Rev. Sci. Instrum. **57**, 1135 (1986).
[368] M. Castagné, J. P. Fillard, and J. Bonnafé, Solid State Commun. **54**, 653 (1985).
[369] P. Gall, J. P. Fillard, J. Bonnafé, M. Castagné, J. Weyher, and A. George, in *Proceedings of the DRIP II Symposium*, edited by E. Weber, Mater. Sci. Monographs No. 44 (Elsevier, Amsterdam, 1987), p. 215.
[370] P. Gall, J. P. Fillard, M. Castagné, J. L. Weyher, and J. Bonnafé, J. Appl. Phys. **64**, 5161 (1988).
[371] J. P. Fillard, P. Gall, M. Castagné, and J. Bonnafé, Solid State Phenom. **687**, 403 (1989).
[372] J. P. Fillard, P. Gall, J. Bonnafé, M. Castagné, and T. Ogawa, Semicond. Sci. Technol. **7**, 283 (1992).
[373] J. P. Fillard, P. C. Montgomery, P. Gall, M. Castagné, and J. Bonnafé, J. Cryst. Growth **103**, 109 (1990).
[374] T. Rakatomavo, Ph.D. thesis, Université de Montpellier, 1991.
[375] P. Gall, J. P. Joly, V. Robert, J. P. Fillard, M. Castagné, and J. Bonnafé, Electron. Lett. **25**, 429 (1989).
[376] T. Wilson and C. Sheppard, *Theory and Practice of Scanning Optical Microscopy*, (Academic, London, 1984).
[377] P. Kidd, G. R. Booker, and D. J. Sirtland, Appl. Phys. Lett. **51**, 1331 (1987).
[378] Z. Laczik, G. R. Booker, R. Falster, and W. Bergholz, Appl. Phys. Lett. **55**, 2625 (1989).
[379] Z. Laczik, G. R. Booker, R. Falster, and N. Shaw, in *Proceedings of the Conference on Microscopy of Semiconducting Materials* (Oxford University Press, Oxford, 1989), p. 807.
[380] G. R. Booker, Z. Laczik, and P. Kidd, Semicond. Sci. Technol. A **7**, 110 (1992).
[381] Z. Laczik, P. Török, G. R. Booker, and R. Falster, in *Proceedings of the Conference on Microscopy of Semiconducting Materials* (Oxford University Press, Oxford, 1989), p. 785.
[382] Z. Laczik, G. R. Booker, R. Falster, and P. Török, Mater. Sci. Forum **83-87**, 1496 (1992).
[383] R. Falster, Z. Laczik, G. R. Booker, A. R. Bhatti, and P. Török, in *Defect Engineering in Semiconductor Growth*, edited by S. Ashok, J. Chevallier, K. Sumino, and E. Weber (Materials Research Society, Pittsburgh, PA, 1992), p. 945.
[384] B. K. Tanner, *X-ray Diffraction Topography* (Pergamon, Oxford, 1976).
[385] G. A. Rozgonyi and D. C. Miller, Thin Solid Films **31**, 185 (1976).
[386] A. R. Lang, Acta Metall. **5**, 358 (1957).
[387] A. R. Lang, J. Appl. Phys. **29**, 597 (1958).
[388] A. R. Lang, J. Appl. Phys. **30**, 1748 (1959).
[389] W. Hartmann, in *X-ray Optics*, edited by H. J. Queisser, Topics in Applied Physics (Springer, Berlin, 1977), Vol. 22, p. 191.
[390] J. R. Patel and B. W. Batterman, J. Appl. Phys. **34**, 2716 (1963).
[391] J. R. Patel, J. Appl. Phys. **44**, 3903 (1973).
[392] T. Abe, in *VLSI Electronics*, edited by N. G. Einspruch and H. Huff (Academic, London, 1983), p. 3.
[393] P. E. Freeland, K. A. Jackson, C. N. Lowe, and J. R. Patel, Appl. Phys. Lett. **30**, 31 (1977).
[394] W. F. Berg, Naturwissenschaften **19**, 391 (1931).
[395] C. S. Barrett, Trans. Metall. Soc. AIME **161**, 15 (1945).
[396] R. W. James, *The Optical Properties of the Diffraction of X rays* (Cornell University Press, Ithaca, New York, 1965).
[397] M. A. G. Halliwell, J. B. Childs, and S. O'Hara, in *Proceedings of the 1972 Symposium on GaAs* (Inst. of Phys., London, 1973), p. 98.
[398] B. K. Tanner and D. K. Bowen, *Characterization of Growth Defects by X-ray Methods* (Plenum, New York, 1979).
[399] A. J. Holland, G. S. Green, B. K. Tanner, and M. Zhenhong, Materials Research Society Symp. **209**, 475 (1991).
[400] E. P. Bochkarev, S. N. Gorin, G. N. Petrov, and T. M. Tkacheva, Mater. Sci. Forum **83-87**, 1075 (1992).
[401] C.-O. Lee and P. J. Tobin, J. Electrochem. Soc. **133**, 2147 (1986).
[402] J. R. Patel, K. A. Jackson, and H. Reiss, J. Appl. Phys. **48**, 5279 (1978).
[403] P. Wang, L. Chang, L. J. Demer, and C. J. Varker, J. Electrochem. Soc. **131**, 1948 (1984).
[404] J. A. Rossi, W. Dyson, L. G. Hellwig, and T. M. Hauley, J. Appl. Phys. **58**, 1798 (1985).
[405] D. Huber and J. Reffle, Solid State Technol. **August**, 137 (1983).
[406] S. M. Hu, J. Appl. Phys. **70**, R53 (1991).
[407] J. R. Patel and A. R. Chaudhury, J. Appl. Phys. **34**, 2788 (1963).
[408] B. Leroy and C. Plougonven, J. Electrochem. Soc. **127**, 961 (1980).
[409] K. Yasutake, M. Umeno, and H. Kawabe, Appl. Phys. Lett. **37**, 789 (1980).
[410] S. Takasu, H. Otsuka, N. Yoshihiro, and T. Oxu, Jpn. J. Appl. Phys. **20**, 25 (1981).
[411] N. Yoshihiro, H. Otsuka, T. Oxu, and S. Takasu, J. Electrochem. Soc. **126**, 693 (1979).
[412] L. E. Miller, in *Properties of Elemental and Compound Semiconductors*, edited by H. C. Gatos (Wiley, New York, 1960), p. 303.
[413] P. C. Parekh, Solid-State Electron. **14**, 273 (1971).
[414] F. Barson, M. S. Hess, and M. M. Roy, J. Electrochem. Soc. **116**, 304 (1969).
[415] J. E. Lawrence, in *Semiconductor Silicon 1973*, edited by H. R. Huff and R. R. Burgess (The Electrochemical Society, Pennington, NJ, 1973), p. 17.
[416] D. K. Schroder, in *Gettering and Defect Engineering in the Semiconductor Technology*, edited by M. Kittler (Sci-Tech, Vaduz, 1989), p. 383.
[417] D. K. Schroder, J. D. Whitefield, and C. J. Varker, IEEE Trans. Electron Devices **ED-31**, 463 (1984).
[418] D. K. Schroder, J. M. Hwang, J. S. Kang, A. M. Goodman, and B. L. Sopori, in *VLSI Science and Technology 1985*, edited by W. M. Bullis and S. Broydo (The Electrochemical Society, Pennington, NJ, 1985), p. 419.
[419] K. H. Yang, H. F. Kappet, and G. H. Schwuttke, Phys. Status Solidi A **50**, 221 (1984).
[420] C. J. Varker, J. D. Whitfield, and P. Fejes, in *Defects in Semiconductors II*, edited by S. Mahajan and J. W. Corbett (North-Holland, New York, 1983), p. 187.
[421] M. Miyagi, K. Wada, J. Osaka, and N. Inoue, Appl. Phys. Lett. **40**, 719 (1982).
[422] S. N. Chakravarti, P. L. Gabarino, and K. Murty, Appl. Phys. Lett. **40**, 581 (1982).
[423] J. M. Hwang and D. K. Schroder, J. Appl. Phys. **59**, 2476 (1986).
[424] H. S. Kim, E. K. Kim, and S.-K. Min, J. Appl. Phys. **69**, 6979 (1991).
[425] S. Kawado, T. Maruyama, T. Suzuki, N. Isawa, and K. Hoshi, J. Electrochem. Soc. **133**, 171 (1986).
[426] T. Higuchi, E. Gaylord, G. A. Rozgonyi, and F. Shimura, Appl. Phys. Lett. **53**, 1850 (1988).
[427] K. Hoshi, N. Isawa, T. Suzuki, and Y. Ohkubo, J. Electrochem. Soc. **132**, 693 (1985).
[428] S. K. Pang and A. Rohatgi, J. Electrochem. Soc. **138**, 523 (1991).
[429] C. J. Varker and K. V. Ravi, J. Appl. Phys. **45**, 272 (1974).
[430] A. Y. Liang and C. J. Varker, in *Lifetime Factors in Silicon* (ASTM, Philadelphia, PA, 1980), p. 73.
[431] H. J. Queisser and A. Goetzberger, Philos. Mag. **8**, 1063 (1963).
[432] E. Simoen, J. Vanhellemont, A. Kaniava, and C. Claeys, The Electrochemical Society Extended Abstracts **93-2** 1993, p. 420.
[433] J. Vanhellemont, E. Simoen, C. Claeys, A. Kaniava, E. Ganbas, A. Blondeel, and P. Clauws, in Seventh International Symposium on Silicon Materials Science and Technology, The Electrochemical Society Spring Meeting, San Francisco, CA, 1994.
[434] W. J. Patrick, S. M. Hu, and W. A. Westdorp, J. Appl. Phys. **50**, 1399 (1979).
[435] K. D. Beyer, S. Chakravarti, P. L. Garbarino, and K. Yang, J. Electrochem. Soc. **134**, 1753 (1987).
[436] K. W. Tice and T. Y. Tan, Appl. Phys. Lett. **28**, 564 (1976).
[437] T. Y. Tan, E. E. Gardner, and W. K. Tice, Appl. Phys. Lett. **30**, 175 (1977).
[438] K. Nagasawa, Y. Matsushita, and S. Kishino, Appl. Phys. Lett. **37**, 622 (1980).
[439] J. M. Andrews, C. A. Clark, S. Muller, and G. A. Rozgonyi, in *First International Symposium on VLSI Science and Technology Proceedings*, edited by C. J. Dell'Oca and W. M. Bullis (The Electrochemical Society, Pennington, NJ, 1982), p. 43.
[440] K. Kugimiga, S. Akiyama, and S. Nakamura, in *Semiconductor Silicon*

Downloaded 21 Apr 2008 to 146.186.238.16. Redistribution subject to AIP license or copyright; see http://jap.aip.org/jap/copyright.jsp

SIONYX1403000027.0033

SAMSUNG EX. 1002 - 2571/4148

1981, edited by H. R. Huff, R. J. Kriegler, and Y. Takeishi (The Electrochemical Society, Pennington, NJ, 1981), p. 294.
[441] J. Andrews, in *Defects in Silicon*, edited by W. Murray Bullis and L. C. Kimerling (The Electrochemical Society, Pennington, NJ, 1993), p. 133.
[442] F. F. Villa and L. Paciaroni, in *Symposium on High Voltage and Smart Power ICs*, edited by M. Ayman Shibib (The Electrochemical Society, Pennington, NJ, 1989), p. 228.
[443] C. Weigel, J. Reffle, and D. Huber, in Seminar Data for Wacker's Tutorial Program on Silicon Materials Technology, 1986, p. B 20.
[444] M. A. Palmieri, Tesi di Laurea, Politecnico di Milano, 1989.
[445] M. Ataka and T. Ogawa, J. Mater. Res. 8, 2889 (1993).

Downloaded 21 Apr 2008 to 146.186.238.16. Redistribution subject to AIP license or copyright; see http://jap.aip.org/jap/copyright.jsp

SIONYX1403000027.0034

SAMSUNG EX. 1002 - 2572/4148

Principles of optics

Electromagnetic theory of propagation, interference and diffraction of light

MAX BORN
MA, Dr Phil, FRS
Nobel Laureate
Formerly Professor at the Universities of Göttingen and Edinburgh

and

EMIL WOLF
PhD, DSc
Wilson Professor of Optical Physics, University of Rochester, NY

with contributions by

A.B.BHATIA, P.C.CLEMMOW, D.GABOR, A.R.STOKES,
A.M.TAYLOR, P.A.WAYMAN AND W.L.WILCOCK

SEVENTH (EXPANDED) EDITION

SIONYX1403000027.0035

SAMSUNG EX. 1002 - 2573/4148

PUBLISHED BY THE PRESS SYNDICATE OF THE UNIVERSITY OF CAMBRIDGE
The Pitt Building, Trumpington Street, Cambridge, United Kingdom

CAMBRIDGE UNIVERSITY PRESS
The Edinburgh Building, Cambridge CB2 2RU, UK www.cup.cam.ac.uk
40 West 20th Street, New York, NY 10011-4211, USA www.cup.org
10 Stamford Road, Oakleigh, Melbourne 3166, Australia
Ruiz de Alarcón 13, 28014 Madrid, Spain

Seventh (expanded) edition © Margaret Farley-Born and Emil Wolf 1999

First published 1959 by Pergamon Press Ltd, London
Sixth edition 1980
Reprinted (with corrections) 1983, 1984, 1986, 1987, 1989, 1991, 1993
Reissued by Cambridge University Press 1997
Seventh (expanded) edition 1999

Printed in the United Kingdom at the University Press, Cambridge

A catalogue record for this book is available from the British Library

Library of Congress Cataloguing in Publication data

Born, Max
Principles of Optics–7th ed.
1. Optics
I. Title II. Wolf Emil
535 QC351 80-41470

ISBN 0 521 642221 hardback

SIONYX1403000027.0036

SAMSUNG EX. 1002 - 2574/4148

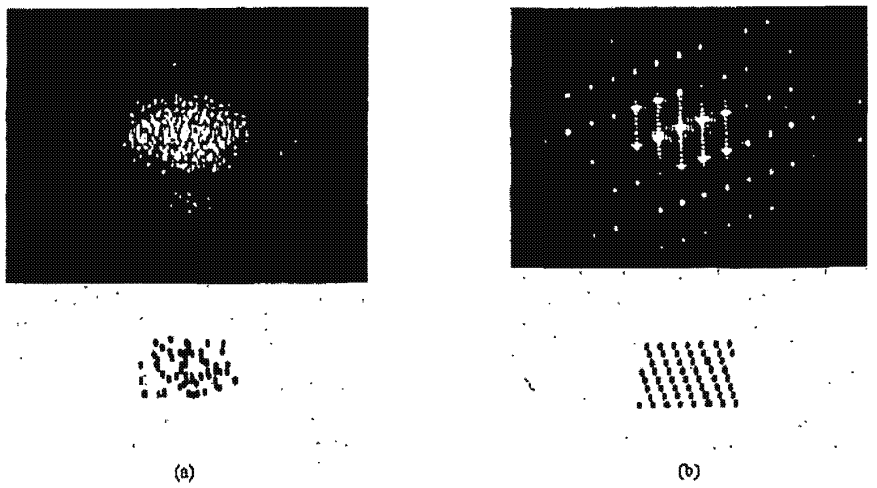

Fig. 8.15 Fraunhofer diffraction pattern from an irregular distribution (a), and a regular distribution (b), of 56 identical and similarly situated apertures in a plane screen. The form and distribution of the apertures is shown in the lower portions of the figures. Light: mercury yellow, $\lambda = 5790$ Å. (Photograph courtesy of H. Lipson, C. A. Taylor, and B. J. Thompson.)

held in the path of light from a distant source. A piece of tin-foil pierced indiscriminately by a pin will also act as a diffracting screen of the type just considered.

The results are quite different when the openings are distributed regularly, for the terms with $m \neq n$ may now give appreciable contributions for certain values of p and q. For example, if the points O_n are so situated that for certain values of p and q the phases of all the terms for which $m \neq n$ are exact multiple of 2π their sum will be equal to $N(N-1)$ and so for large N will be of the order of N^2. This enormous increase in intensity for particular directions, clearly illustrated in Fig. 8.15, is, as we shall see in the next section, of great importance in practice.

8.6 Fraunhofer diffraction in optical instruments

8.6.1 Diffraction gratings

(a) The principle of the diffraction grating

A diffraction grating may be defined as any arrangement which imposes on an incident wave a periodic variation of amplitude or phase, or both. We may characterize any particular grating by its *transmission function*, defined as follows:

Let a transparent or semitransparent object (not necessarily periodic) cover a portion of a fictitious reference plane $\xi\eta$, and let it be illuminated by a plane monochromatic wave incident in a direction specified by the direction cosines l_0, m_0. Fig. 8.16 illustrates the arrangement, the η-axis being perpendicular to the plane of the drawing. If no object were present, the disturbance in the ξ, η-plane would be represented by the

SIONYX1403000027.0037

SAMSUNG EX. 1002 - 2575/4148

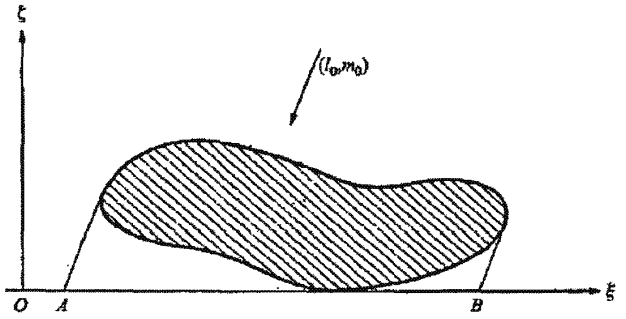

Fig. 8.16 Definition of the transmission function.

function $V_0(\xi, \eta) = A\exp[ik(l_0\xi + m_0\eta)]$, the factor $\exp(-i\omega t)$ being, as usual, omitted. Because of the presence of the object the disturbance will be modified and may be represented by some other function, which we denote by $V(\xi, \eta)$. The *transmission function* of the object is then defined as

$$F(\xi, \eta) = \frac{V(\xi, \eta)}{V_0(\xi, \eta)}. \tag{1}$$

In general F depends, of course, not only on ξ and η but also on the direction (l_0, m_0) of illumination. The transmission function is in general complex, since both the amplitude and the phase of the light may be altered on passing through the object. In the special case when the object alters the amplitude but not the phase of the incident wave (i.e. if $\arg F \equiv 0$), we speak of an *amplitude object*; if it alters the phase but not the amplitude (i.e. $|F| = 1$) we speak of a *phase object*.

If we are concerned with reflected light rather than with light that is transmitted by an object, it is more appropriate to speak of a *reflection function*, defined in a similar way, the only difference being that the reference plane is on the same side of the object as the incident light.

The ratio $|V/V_0|$ is practically unity for points outside the geometrical shadow (whose boundary is represented by points A and B in Fig. 8.16) cast by the object. If the portion outside the shadow region is covered by an opaque screen, the arrangements act as a diffracting aperture $\mathcal{A}$ with a nonuniform pupil function (see §8.3 (39)). If the linear dimensions of $\mathcal{A}$ are large compared to the wavelength and if F remains sensibly constant over regions whose dimensions are of the same order as the wavelength, the diffraction formula §8.3 (23) remains valid under the same conditions as before, provided that the integrand of the diffraction integral is multiplied by F.

Let us now consider a one-dimensional grating consisting of N parallel grooves of arbitrary profile, ruled on one surface of a plane-parallel glass plate. Let the ξ, η-plane coincide with the plane face of the plate, η being the direction of the grooves and let d be the period in the ξ direction (see Fig. 8.17).

Assume that the direction of propagation of the wave incident upon the grating is in the plane of the figure, making an angle θ_0 with $O\zeta$, and let θ denote the angle which $O\zeta$ makes with the line joining a very distant point of observation P with the grating.

SIONYX1403000027.0038

SAMSUNG EX. 1002 - 2576/4148

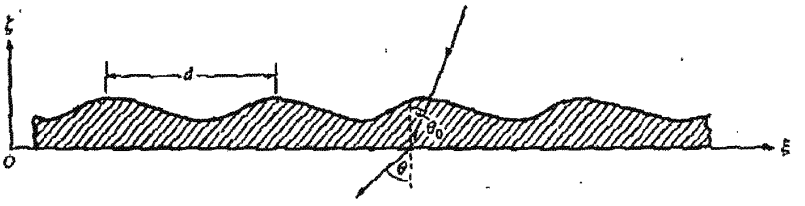

Fig. 8.17 Illustrating the theory of the diffraction grating.

As before we set $l_0 = \sin\theta_0$, $l = \sin\theta$, $p = l - l_0 = \sin\theta - \sin\theta_0$. The complex amplitude at P is then immediately obtained from §8.5 (23), where the integrand must be multiplied by the transmission function F of one periodic element. We may set $q = 0$ and

$$\xi_n = nd, \qquad \eta_n = 0 \qquad (n = 0, 1, \ldots N-1). \tag{2}$$

We then obtain

$$U(p) = U^{(0)}(p)\sum_{n=0}^{N-1} e^{-ikndp} = U^{(0)}(p)\frac{1 - e^{-iNkdp}}{1 - e^{-ikdp}}, \tag{3}$$

where*

$$U^{(0)}(p) = C\int_A F(\xi)e^{-ikp\xi}\,d\xi. \tag{4}$$

Hence

$$I(p) = |U(p)|^2 = \frac{(1 - e^{-iNkdp})}{(1 - e^{-ikdp})}\cdot\frac{(1 - e^{iNkdp})}{(1 - e^{ikdp})}|U^{(0)}(p)|^2$$

$$= \frac{1 - \cos Nkdp}{1 - \cos kdp}I^{(0)}(p), \tag{5}$$

where $I^{(0)}(p) = |U^{(0)}(p)|^2$. If we introduce the function

$$H(N, x) = \left(\frac{\sin Nx}{\sin x}\right)^2, \tag{6}$$

the formula (5) for the intensity may be written as

$$I(p) = H\left(N, \frac{kdp}{2}\right)I^{(0)}(p). \tag{5a}$$

Before discussing the implications of this basic formula we note that according to (3) the light distribution is the same as that due to a set of coherent secondary sources each characterized by the same amplitude function $|U^{(0)}(p)|$ and with phases that differ from each other by integral multiples of kdp. To see the significance of this phase difference consider two corresponding points A and B in neighbouring grooves

* Since F depends on l_0, the quantities $U^{(0)}$ and $I^{(0)}$ now depend on both l and l_0 and not on the difference $l - l_0$ only. As we are only interested in effects for a fixed direction of incidence, we may regard l_0 as constant and retain the previous notation.

SIONYX1403000027.0039

SAMSUNG EX. 1002 - 2577/4148

of the grating (Fig. 8.18). Since the effect of the grating is to impress a periodic variation onto the incident wave, it follows that the path difference between the light arriving at A and at B is the same as in the absence of the grating, i.e. it is equal to $AK = d \sin\theta_0$, K denoting the foot of the perpendicular from B on to the ray incident at A. Further, the light path from B in the direction θ exceeds the light path from A by $BL = d \sin\theta$, L being the foot of the perpendicular from A on to the ray diffracted at B in the direction θ. Hence the total path difference between light arriving at the distant point of observation from corresponding points in two neighbouring grooves is

$$BL - AK = d(\sin\theta - \sin\theta_0) = dp, \tag{7}$$

and the corresponding phase difference is $2\pi dp/\lambda = kdp$.

Formula (5a) expresses $I(p)$ as the product of two functions: one of them, $I^{(0)}$, represents the effect of a single period of the grating; the other, H, represents the effect of interference of light from different periods. The function $H(N, x)$ has maxima, each of height N^2, at all points where the denominator $\sin^2 x$ vanishes, i.e. where x is zero or an integral multiple of π. Hence $H(N, kdp/2)$ has maxima of height N^2 when

$$p \equiv \sin\theta - \sin\theta_0 = \frac{m\lambda}{d} \qquad (m = 0, \pm 1, \pm 2, \ldots). \tag{8}$$

The integer m represents, according to (7), the path difference in wavelengths between light diffracted in the direction of the maximum, from corresponding points in two neighbouring grooves. In agreement with our earlier definition (§7.3.1), we call m the *order of interference*. Between these principal maxima there are weak secondary maxima (see Fig. 8.19(a)), the first secondary maximum being only a few per cent of the principal maximum when N is large. The maxima are separated by points of zero intensity at $x = kdp/2 = \pm n\pi/N$, i.e. in directions given by

$$p \equiv \sin\theta - \sin\theta_0 = \frac{n\lambda}{Nd} \qquad (n = \pm 1, \pm 2, \ldots), \tag{9}$$

the case where n/N is an integer being excluded.

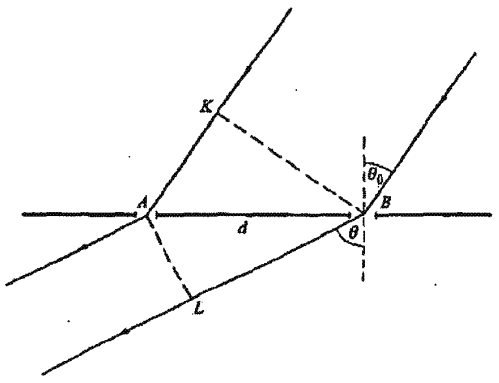

Fig. 8.18 Illustrating the theory of the diffraction grating.

SIONYX1403000027.0040

SAMSUNG EX. 1002 - 2578/4148

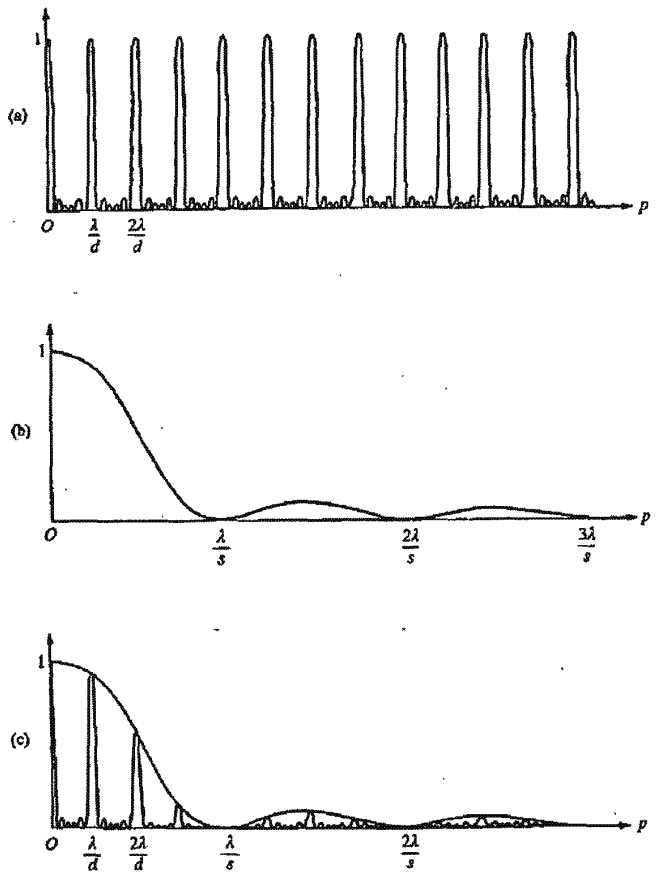

Fig. 8.19 (a) The normalized interference function

$$\frac{1}{N^2} H(N,\ kdp/2) = \left[\frac{\sin(Nkdp/2)}{N\sin(kdp/2)}\right]^2.$$

(b) The normalized intensity function of a slit

$$I^{(0)}(p) = \left[\frac{\sin ksp/2}{ksp/2}\right]^2.$$

(c) The normalized intensity function of a grating consisting of N similar equidistant parallel slits

$$\frac{1}{N^2} I(p) = \left[\frac{\sin(Nkdp/2)}{N\sin(kdp/2)}\right]^2 \left[\frac{\sin ksp/2}{ksp/2}\right]^2.$$

Only the range $p \geq 0$ is shown, all the curves being symmetrical about the vertical axis $p = 0$.

SIONYX1403000027.0041

SAMSUNG EX. 1002 - 2579/4148

The function $I^{(0)}(p)$ depends on the form of the grooves. Suppose that it has a principal maximum for some direction $p = p'$ and that on both sides of the maximum it falls off slowly in comparison with H. Then $I(p)$ will have the general form of the interference function H, but will be 'modulated' by $I^{(0)}$. Thus $I(p)$ will still have fairly sharp maxima near the directions $p = m\lambda/d$. Since these directions (except for $m = 0$) depend on the wavelength, we see that the grating will decompose a beam of nonmonochromatic light into *spectral orders*.

To illustrate these remarks let us consider a grating consisting of a succession of long equidistant slits (Fig. 8.20), each of width s and length L, in an opaque screen. If the grating is illuminated from a very distant line source parallel to the slits, the intensity $I^{(0)}$ is given by the expression §8.5 (4) (with $2a = s$, $2b = L$) and we obtain

$$I(p) = \frac{sE}{\lambda R^2}\left(\frac{\sin\dfrac{Nkdp}{2}}{\sin\dfrac{kdp}{2}}\right)^2\left(\frac{\sin\dfrac{ksp}{2}}{\dfrac{ksp}{2}}\right)^2. \tag{10}$$

Curves representing the two factors in (10) and their product are shown in Fig. 8.19. The last factor in (10), which represents the effect of a single slit, has a principal maximum at $p = 0$ and minima given by $ksp/2 = n\pi$, i.e. at

$$p = \frac{n\lambda}{s}, \qquad (n = \pm 1, \pm 2, \ldots) \tag{11}$$

separated by weak secondary maxima. We see that if $\lambda/s \gg \lambda/d$, i.e. if the width of each slit is small compared to d, the intensity $I(p)$ has in addition to a principal maximum at $p = 0$ a series of sharp, but progressively decreasing, maxima on either side of it, near directions given by (8).

Returning to the general case, it is evident that if the width of each groove is very small, of the order of a wavelength (as is often the case in practice) the formula (4), derived on the basis of Kirchhoff's approximation, can evidently no longer be expected to hold. In such cases more refined considerations must be made to determine the detailed distribution of the intensity. We may, however, expect that the main qualitative features indicated by our elementary theory, namely the existence of sharp maxima whose positions are substantially determined by the interference function H, remain even when the grooves are very narrow, provided, of course, that the intensity function of a single period varies slowly in an interval of the order $\Delta p = \lambda/d$.

Let us now consider the resolution that may be attained with a grating. The separation between a primary maximum of order m and a neighbouring minimum is, according to (9), given by

$$\Delta p = \frac{\lambda}{Nd}. \tag{12}$$

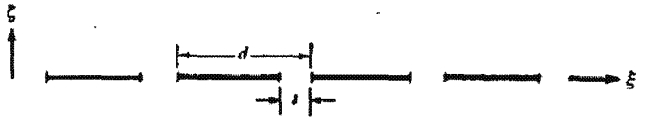

Fig. 8.20 Profile of a simple line grating.

SIONYX1403000027.0042

SAMSUNG EX. 1002 - 2580/4148

Best Available Copy

If the wavelength is changed by an amount $\Delta\lambda$, the mth-order maximum is, according to (8), displaced by an amount

$$\Delta' p = \frac{|m|}{d}\Delta\lambda. \tag{13}$$

Assuming that the lines of wavelength $\lambda \pm \frac{1}{2}\Delta\lambda$ will just be resolved when the maximum of the one wavelength coincides with the first minimum of the other (see p. 371) we have on the limit of resolution in the mth order, $\Delta p = \Delta' p$, i.e.

$$\frac{\lambda}{\Delta\lambda} = |m|N. \tag{14}$$

Thus, *the resolving power is equal to the product of the order number m and the number N of the grooves.* For the mth order we have, according to (8), that $d(\sin\theta - \sin\theta_0) = m\lambda$, so that we may also express the resolving power in the form

$$\frac{\lambda}{\Delta\lambda} = \frac{Nd|\sin\theta - \sin\theta_0|}{\lambda}. \tag{14a}$$

Because of (7) this implies that *the resolving power is equal to the number of wavelengths in the path difference between rays that are diffracted in the direction θ from the two extreme ends (separated by distance Nd) of the grating.* It is to be noted that since $|\sin\theta - \sin\theta_0|$ cannot exceed 2, the resolving power that can be attained with a grating of overall width w can never exceed the value $2w/\lambda$.

Let us illustrate the formula (14) by determining the number of grooves that a grating must have, in order to separate two lines which are a tenth of an ångström unit apart, near the centre of the visible region of the spectrum. In this case $\lambda \sim 5500$ Å, $\Delta\lambda = 10^{-1}$ Å, and if we observe in the second order ($m = 2$), we must have, according to (14) $N \geqslant 5.5 \times 10^3/2 \times 10^{-1} = 27,500$, i.e. the grating must have at least 27,500 grooves.

For comparison let us consider the resolving power of a prism, in the position of minimum deviation, with a line source that is parallel to the edge A of the prism (slit of the spectrograph). A pencil of parallel rays will be incident upon the prism and will be diffracted at a rectangle of width $l_1 = l_2$ (see Fig. 4.28). According to §8.5 (2), the first minimum of the intensity is at an angular distance (assumed to be small)

$$p = \frac{\lambda}{l_1} \tag{15}$$

from the geometrical image of the slit. The change in the angular dispersion corresponding to a change of wavelength by amount $\Delta\lambda$ is, according to §4.7 (36),

$$\Delta\varepsilon = \frac{t}{l_1}\frac{dn}{d\lambda}\Delta\lambda, \tag{16}$$

where t is the greatest thickness of the glass through which one of the extreme rays has passed, and n is the refractive index of the material of the prism. Since at the limit of resolution $p \sim \Delta\varepsilon$ the resolving power is given by

$$\frac{\lambda}{\Delta\lambda} = t\left|\frac{dn}{d\lambda}\right|. \tag{17}$$

Thus the resolving power of a prism depends only

SIONYX1403000027.0043

SAMSUNG EX. 1002 - 2581/4148

on the greatest thickness of the glass traversed by the rays; in particular the resolving power is independent of the angle of the prism. As an example, suppose that the length of the base of the prism is equal to 5 cm and that it is made of heavy flint glass, for which $dn/d\lambda \sim 1000\ \text{cm}^{-1}$ at wavelength $\lambda = 5500$ Å. If the prism is completely filled with light, then according to (17) it will resolve lines near the centre of the visible region which are not less than $\Delta\lambda$ apart, where $\Delta\lambda \sim 5.5 \times 10^{-5}\ \text{cm}/5 \times 10^3 = 1.1$ Å. Thus a prism of this considerable size has a resolving power 10 times smaller than the grating of 27,500 grooves discussed before.

We have so far considered one-dimensional gratings only, but the analysis may easily be extended to two- and three-dimensional periodic arrangements of diffracting bodies. Two-dimensional gratings (sometimes called cross gratings) find no practical applications, though their effects can often be observed, for example when looking at a bright source through a finely woven material (e.g. a handkerchief). The theory of three-dimensional gratings (sometimes called space gratings) is, on the other hand, of great importance, such gratings being formed by a regular arrangement of atoms in a crystal. The lattice distances (distances between neighbouring atoms) are of the order of an ångström unit (10^{-8} cm), this being also the order of magnitude of the wavelengths of X-rays. Hence, by sending a beam of X-rays through a crystal, diffraction patterns are produced, and from their analysis information about the structure of the crystal may be deduced. We will briefly discuss this subject in §13.1.3.

Another example of a grating-like structure is presented by ultra-sonic waves in liquids. These are elastic waves produced by a piezo-electric oscillator, differing from ordinary sound waves only in having a frequency well above the upper limit of audibility. Such waves give rise to rarefactions and condensations in the liquid which then act on the incident light like a grating. The theory of this phenomenon is discussed in Chapter XII. For the rest of this section we shall restrict our attention to one-dimensional gratings as used in spectroscopic work.

*(b) Types of grating**

The principle of the diffraction grating was discovered by Rittenhouse in 1785,† but this discovery attracted practically no attention. The principle was re-discovered by Fraunhofer‡ in 1819. Fraunhofer's first gratings were made by winding very fine wire round two parallel screws. Because of the relative ease with which wire gratings may be constructed these are occasionally used even today, particularly in the long-wavelength (infra-red) range. Later Fraunhofer made gratings with the help of a machine, by ruling through gold films deposited on a glass plate; also, using a diamond as a ruling point, he ruled the grooves directly on to the surface of glass.

Great advances in the technique of production of gratings were made by Rowland§ who constructed several excellent ruling machines and also invented the so-called

* For a fuller account of methods of production of gratings and their development, see G. R. Harrison, *J. Opt. Soc. Amer.*, 39 (1949), 413.

† D. Rittenhouse, *Trans. Amer. Phil. Soc.*, 2 (1786), 201. See also article by T. D. Cope in *Journ. Franklin Inst.*, 214 (1932), 99.

‡ J. Fraunhofer, *Denkschr. Akad. Wiss. München*, 8 (1821–1822), 1. *Ann. d. Physik*, 74 (1823), 337. Reprinted in his collected works (Munich, 1888), pp. 51, 117.

§ H. A. Rowland, *Phil. Mag.* (5), 13 (1882), 469. *Nature*, 26 (1882), 211. *Phil. Mag.*, 16 (1883), 297.

SIONYX1403000027.0044

SAMSUNG EX. 1002 - 2582/4148

INSTITUTE OF PHYSICS PUBLISHING NANOTECHNOLOGY
Nanotechnology 17 (2006) 4991–4994 doi:10.1088/0957-4484/17/19/036

An approach for the fabrication of hexagonally ordered arrays of cylindrical nanoholes in crystalline and amorphous silicon based on the self-organization of polymer micelles

Sabrina Brieger, Oliver Dubbers, Sebastian Fricker, Achim Manzke, Christian Pfahler, Alfred Plettl and Paul Ziemann

Abteilung Festkörperphysik, Universität Ulm, Albert-Einstein-Allee 11, D-89069 Ulm, Germany

E-mail: alfred.plettl@uni-ulm.de

Received 26 June 2006, in final form 29 August 2006
Published 15 September 2006
Online at stacks.iop.org/Nano/17/4991

Abstract
A nanolithographic process is introduced based on the self-organization of gold salt loaded inverse micelles formed by poly(styrene)-*block*-poly(2-vinylpyridine) di-block-copolymers in toluene. The developed procedure allows the fabrication of hexagonally arranged cylindrical nanoholes (diameters $\geqslant$ 20 nm, aspect ratios $\sim$ 7) in crystalline as well as in amorphous Si. In the latter case, applying the concept to amorphous Si layers evaporated onto any substrate results in nanomasks allowing the transfer of the hole pattern into the substrate.

1. Introduction

Although the worldwide activities in nanoscience have led to an increased understanding of nanostructures, their fabrication technology is still lagging behind. This is related to the challenge to prepare nanostructures on a sub-100 nm scale in a reproducible and cheap way. The latter demand practically excludes all the time consuming techniques based on sequential steps such as single atom/molecule manipulation by scanning probe methods such as scanning tunnelling (STM) or atomic force microscopy (AFM) [1] or, on a slightly larger scale but still within the sub-100 nm limit, electron beam lithography (EBL) [2]. More promising techniques in this respect are the various contact printing approaches [3] or those based on the self-organization of colloids [4, 5] or larger molecules [6]. Among them, the self-organized structure formation of di-block-copolymers on the nanoscale plays a special role. This is partly related to their chemical relationship to standard EBL resists such as PMMA [7, 8] or to their ability to form spherical micelles, the cores of which can be treated as nanoreactors for selectively ligating metal salts [9]. Following this latter route, arrays of hexagonally arranged Au nanoparticles can be obtained on top of practically any sufficiently flat substrate, which then serve as masks in a subsequent etching process [10, 11]. In this way, the hexagonal pattern of the mask is transferred into the substrate resulting in correspondingly arranged nanopillars. In the present contribution, this approach is significantly extended aiming at an inversion of the starting pattern, i.e. instead of nanopillars, hexagonally arranged cylindrical nanoholes are at the focus of a nanopatterning process to be introduced in the following. In this way, the aspect ratio is improved ($\sim$7) as compared to ($\sim$1) using solvent switchable di-block-copolymer templates [12].

Such nanopores offer a series of applications such as contact holes in semiconductors, which, according to the present Semiconductor Technology Roadmap, should exhibit diameters well below 80 nm for the '65 nm node generation' [13]. Similarly, applications in nanooptics appear attractive and based on colloid masks [14] nanopores were fabricated into Si with a diameter of 60 nm. Smaller diameters of the order of 30 nm in Si were obtained by manipulating

SIONYX1403000027.0045

SAMSUNG EX. 1002 - 2583/4148

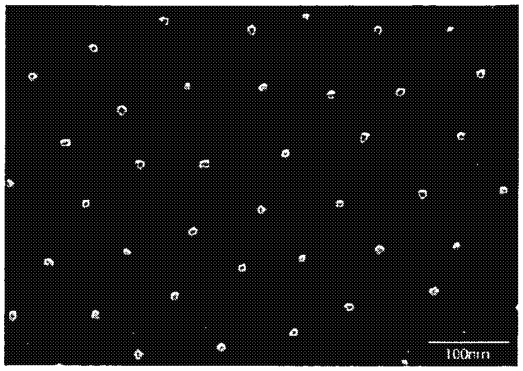

Figure 1. Hexagonally ordered gold nanoparticles (average diameter 14 nm, average interparticle distance 90 nm) prepared by the micellar route described in the text on top of an amorphous Si layer as imaged by SEM (sample tilted by 30°).

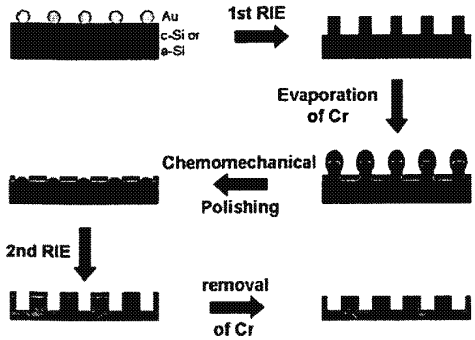

Figure 2. Sketch of the essential steps to fabricate nanopores in Si starting from ordered arrays of Au nanoparticles.
(This figure is in colour only in the electronic version)

PMMA resist with an AFM [15], thereby accepting the disadvantage of a non-parallel process. Also, the recently developed process of forming nanopores into ultrathin Si/SiO_2 membranes based on the electron beam induced viscosity of SiO_2 and applied to prepatterned and SiO_2 coated nanoholes, though highly *in situ* controlled within an electron microscope, is still a non-parallel procedure [16]. Another approach to prepare nanoholes in Si is based on self-organized porous alumina masks in combination with anisotropic Cl_2 reactive ion etching (RIE) [17]. In this way, holes with diameters >13 nm with an aspect ratio of 3 could be obtained. As will be demonstrated below, similar diameters are delivered in Si by our micellar technique adding the possibility of a significantly enhanced aspect ratio. Besides allowing the fabrication of nanoholes at a high aspect ratio directly into Si, the micellar approach is applicable to produce masks made of amorphous Si with hexagonally arranged nanoholes. These masks can be deposited on any support, opening the possibility to transfer the hole pattern into the underlying substrate.

2. Micellar mask and preparation concept

Based on the self-organization of $HAuCl_4$ loaded inverse micelles formed by poly(styrene)-*block*-poly(2-vinylpyridine) (PS-*b*-P2VP) di-block-copolymers in toluene, hexagonally ordered arrays of Au nanoparticles can be prepared on top of various substrates including Si wafers. Experimental details on the preparation of such Au nanoparticles including the control of the size and interparticle distance are reviewed in [9]. Now, hexagonally ordered Au nanoparticles (diameter 14 ± 1 nm) with an average separation of 90 nm are either deposited onto (001)-oriented crystalline (c-) Si wafers or onto amorphous (a-) Si layers prepared by evaporation at ambient temperature. In both cases, the surfaces are covered by thin oxide layers, either native or, in case of a-Si, grown by exposure to an oxygen plasma. An example of such an arrangement of Au nanoparticles is presented in figure 1 showing a high resolution secondary electron microscopy (SEM, Hitachi S 5200) image.

Using these particles as an etching mask, a first anisotropic RIE process forms the starting point of fabricating an inverse mask as schematically shown in figure 2. In short, after obtaining Si nanopillars with a very small diameter distribution by the first RIE step, an intermediate Cr layer is evaporated with its thickness adjusted to avoid a complete covering of the pillar sidewalls. Thus, the Si pillars still jut out from the Cr and they are levelled off by chemomechanically polishing in the next step. The remaining stumps are then selectively removed by a second anisotropic RIE step resulting in the desired cylindrical nanoholes. In the following, the results of the various steps are demonstrated and related experimental details are given.

The micelles used as carriers for the Au precursor ($HAuCl_4$) were formed by the di-block-copolymer PS(1850)-*b*-P2VP(730) in toluene. Here, the monomer numbers given in parentheses are a measure of each block length. After deposition of these micelles onto (001) n-Si ($\rho > 1\ \Omega$ cm) by dip coating, the polymer matrix is completely removed in a microwave etcher by exposing the sample to a hydrogen plasma (120 W) for approximately 90 min. In this way, hexagonally ordered Au nanoparticles are obtained like those presented in figure 1. A critical step is the first RIE etching delivering the Si nanopillars (cf figure 2). It turned out that standard etchants such as SF_6 or CF_4 exhibit a much too fast etching rate leading to an immediate underetching and removal of the Au nanoparticles. Consequently, similar to in the well-known Bosch process [18], a fluorocarbon layer close to the contact point of the almost spherical Au nanoparticles is needed to avoid excessive underetching. Empirical optimization revealed that an RIE process (Oxford Plasma Lab 80 plus ICP-RIE) with a mixture of CF_4–CHF_3 (flow rates: 2 sccm:20 sccm) at a total pressure of 10 mTorr and power of 30 W gives a well controlled etching rate of 4 nm min^{-1} for Si. The Au particles with a diameter of 14 nm serving as masks during this etching, safely allow the preparation of Si nanopillars of 60 nm height.

The next two steps described in the scheme of figure 2 allow inversion of the pattern defined by the previously etched Si nanopillars. For this purpose, first a 3 nm thick Cr layer is thermally evaporated at ambient temperature and a total pressure of $<5 \times 10^{-7}$ mbar from a W-crucible at a rate of approximately 0.1 nm s^{-1}. The sample's condition after this step is analysed again by high resolution SEM and the

SIONYX1403000027.0046

SAMSUNG EX. 1002 - 2584/4148

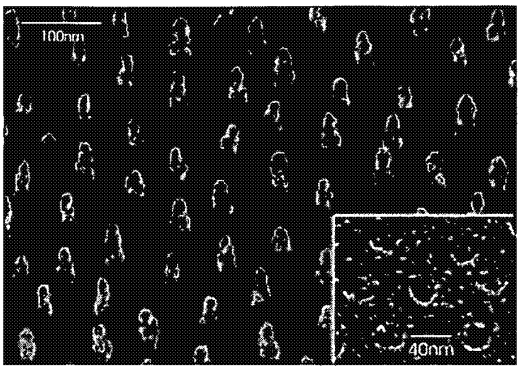

Figure 3. SEM image (sample tilted by 30°) of Si pillars (diameter <20 nm, height 60 nm) covered by 3 nm of evaporated Cr. The inset (lower right) shows the same surface after chemomechanical polishing revealing 18–20 nm broad Si stumps within the circular openings (diameter 22 nm) in the Cr layer.

corresponding image is presented in the inset of figure 3. Here, the Cr-coated Si nanopillars are clearly visible, also demonstrating that the original hexagonal order of the Au nanoparticles is still conserved. Next, the pillars jutting out from the closed Cr layer are removed by chemomechanical polishing for approximately 1 min with a commercial cloth (CONTEC C1) containing 30% KOH. After rinsing with ultrapure water (18 MΩ), the SEM image presented in the inset of figure 3 is obtained revealing the smooth Cr layer with the embedded Si stumps on the same level. This polishing process is superior to wet etching procedures in delivering excellent homogeneous starting conditions for the next step. There, these Si stumps are selectively etched by the anisotropic RIE process based on CF_4–CHF_3 under identical conditions as described above for obtaining the Si nanopillars.

3. Results

As a result, hexagonally arranged cylindrical nanopores are produced in Si. It is worth noting that the related etch rates depend on the pore diameter since its size influences the transport of etched material out the pore. In crystalline Si, the smallest pore diameters obtained so far range between 20 and 25 nm with a pore depth of 100 nm. In that case, the observed etch rate was 1.6 nm min^{-1}. The etching procedure is completed by removing the Cr top layer with a commercial Cr etchant (Rohm and Haas, MICROPOSIT Chrome Etch 1, a mixture of ammonium–cerium–nitrate and perchloric acid) and a final rinse in ultrapure water.

Since it turned out that the complete process to prepare nanoholes in crystalline Si works equally well on amorphous Si layers fabricated by evaporation at ambient temperatures, the presentation of the nanopores in c-Si by SEM images is left out here in favour of corresponding results on a-Si layers. This approach based on a-Si layers even adds significant flexibility to the overall procedure given here, since it offers the possibility to prepare masks containing hexagonally arranged nanoholes on top of practically any sufficiently flat substrate.

SEM images of the result in a-Si are presented in figure 4. In this case, commercial Si wafers covered by a 300 nm thick SiO_2 layer were used as substrates. Next, a 3 nm thick Cr film is evaporated followed by the evaporation of 120 nm a-Si, which forms the base material for the mask. After going through all the steps described above, the array of nano-openings shown as the SEM top view in panel (a) is obtained. Additional information is delivered by the SEM cross-sectional view given in panel (b), proving that almost perfect cylindrical pores with vertical walls are fabricated in the a-Si layer, and that the intermediate Cr layer acted as a stop for the Si etching. Since the Cr layer is just a representative for any other metallic substrate, the present results open the prospect of applying our approach to fabricate versatile nanomasks.

Additionally, the fabrication concept enables the thickness of the Cr-etching mask to be increased. For example, the results presented in figure 5 demonstrating an array of 140 nm deep holes with a diameter of about 20 nm, were obtained with an 8 nm thick evaporated Cr layer. In this case, a slight overetching was applied to optimize the shape of the nanoholes for a subsequent filling.

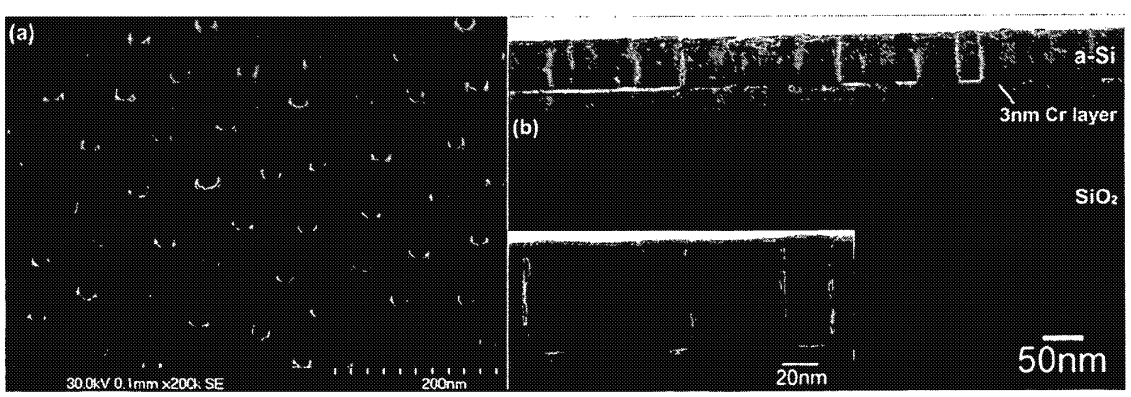

Figure 4. Hexagonally ordered cylindrical nanoholes (diameter 25 nm, interpore distance 90 nm) within an amorphous Si layer evaporated on top of 3 nm Cr as imaged by SEM. (a) Top view (sample tilted by 30°), (b) side view revealing the Si/SiO_2 substrate with the intermediate Cr layer and the a-Si top layer containing the nanoholes. The inset (lower left) provides a magnified view of the pores proving their cylindrical shape.

SIONYX1403000027.0047

SAMSUNG EX. 1002 - 2585/4148

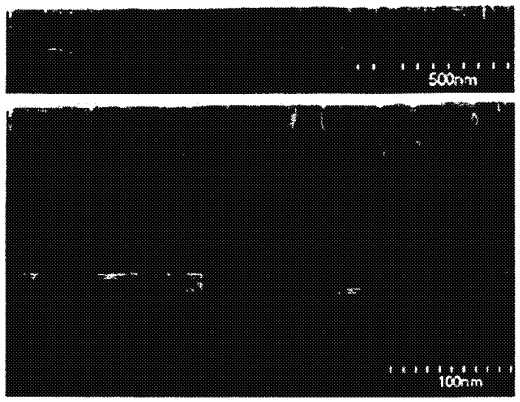

Figure 5. SEM image (side view) of deep holes (diameter 20 nm, depth 140 nm) in a-Si over 12 nm Cr on a SiO_2–Si-wafer substrate.

4. Conclusion

In summary, the described nanolithographic approach allows the preparation of ordered arrays of cylindrical nanoholes either in crystalline Si wafers or in amorphous Si layers evaporated onto any other substrate. In the latter case, the arrays can be applied as nanomasks for subsequent further additive or subtractive patterning or as a stopping mask for irradiation experiments.

Acknowledgments

We thank Dr G Kästle for helpful discussions during the early stage of this work, and Professor P Walther (ZE Electron Microscopy, Ulm) for advising us in the use of HRSEM. The support by Deutsche Forschungsgemeinschaft (DFG) within the Cooperative Research Center SFB 569 as well as by Landesstiftung Baden-Württemberg is gratefully acknowledged.

References

[1] Ebert P, Szot K and Roelofs A 2003 *Nanoelectronics and Information Technology* ed R Waser (Weinheim: Wiley–VCH) p 299
[2] Okazaki S and Moers J 2003 *Nanoelectronica and Information Technology* ed R Waser (Weinheim: Wiley–VCH) p 225
[3] Wilbur J L and Whitesides G 1998 *Nanotechnology* ed G Timp (New York: Springer) p 331
[4] Burmeister F, Badowsky W, Braun T, Wieprich S, Boneberg J and Leiderer P 1999 *Appl. Surf. Sci.* **144/145** 461
[5] Bale M, Turner A J and Palmer R E 2002 *J. Phys. D: Appl. Phys.* **35** L11
[6] Zharnikov M and Grunze M 2002 *J. Vac. Sci. Technol.* B **20** 1793
[7] Hamley I W 2003 *Nanotechnology* **14** R39
[8] Thurn-Albrecht T, Schotter J, Kästle G, Emley N, Shibauchi T, Krusin-Elbaum L, Guarini K, Black C T, Russel T M T and Russel T P 2001 *Science* **290** 2126
[9] Kästle G *et al* 2003 *Adv. Funct. Mater.* **13** 853
[10] Koslowski B, Strobel S, Herzog T, Heinz B, Boyen H-G, Notz R, Ziemann P, Spatz J P and Möller M 2000 *J. Appl. Phys.* **87** 7533
[11] Cheng J Y, Ross C A, Thomas E L, Smith H I and Vancso G 2002 *J. Appl. Phys. Lett.* **81** 3657
[12] Krishnamoorthy S, Pugin R, Brugger J, Heinzelmann H, Hoogerwerf A C and Hinderling V 2006 *Langmuir* **22** 3450
[13] Kim H-W, Yoon J-Y, Hah J-H, Woo S-G, Cho H-K and Moon J-T 2004 *J. Vac. Sci. Technol.* B **22** L38
[14] Rindzevicius T, Alaverdyan Y, Dahlin A, Höök F, Sutherland D S and Käll M 2005 *Nano Lett.* **5** 2335
[15] Hsu J-H, Lin C-Y and Lin H-N 2004 *J. Vac. Sci. Technol.* B **22** 2768
[16] Storm A J, Chen J H, Ling X S, Zandbergen H W and Dekker C 2003 *Nat. Mater.* **2** 537
[17] Shingubara S, Okino O, Murakami Y, Sakaue H and Takahagi T 2001 *J. Vac. Sci. Technol.* B **19** 1901
[18] Laermer F, Schilp A, Funk K and Offenberg M 1999 *Proc. 12th IEEE Annual Int. Conf. on Microelectromechanical Systems (New York)* (Piscataway, NJ: IEEE) p 211

SIONYX1403000027.0048

SAMSUNG EX. 1002 - 2586/4148

Demodulation Pixel Based on Static Drift Fields

Bernhard Büttgen, Felix Lustenberger, *Senior Member, IEEE*, and Peter Seitz, *Member, IEEE*

***Abstract*—A novel pixel architecture for two-dimensional pixel parallel demodulation of modulated light waves is introduced, enabling real-time three-dimensional (3-D) imaging. Applications for such methods can be found in the field of surveillance, robotics, automotive, and industry security applications. The pixel architecture is based on large areas of static drift fields and relatively small demodulation regions. The large area of static drift field forms the basic photodetection region. The constant drift field enables the very fast transport of photo-generated charges to the sampling region where demodulation of the light signal is performed. The main advantages compared to recently used demodulation pixels are lower power consumption and higher optical fill factor or sensitivity. The first implementation is a pixel of 40 × 40 μm^2 size with 25% optical fill factor. Measurements prove the concept of transporting photo-generated charges within less than 1 ns to the demodulation node. The applicability of the pixel in 3-D imaging applications is highlighted by distance measurements achieving millimeter distance resolution.**

***Index Terms*—Charge transfer devices, demodulation, demodulation pixel, distance measurement, electric field, smart pixels, three-dimensional (3-D) imaging, time-of-flight (TOF).**

I. Introduction

THREE techniques of optical contactless distance measurement, namely: 1) triangulation; 2) interferometry; and 3) time-of-flight (TOF), are known [1], [2]. The new demodulation pixel described in this paper is of particular relevance to the TOF technique. That kind of distance measurement is very suitable for the acquisition of distances of a few centimeters up to some hundreds of meters. Based on standard chip process technologies, photosensitive sensors that allow for the acquisition of the three-dimensional (3-D) information of complete scenes without the use of mechanical scanning components can be designed. 3-D imaging in real time becomes possible.

The new pixel represents an improved structure of the lock-in pixels currently used in TOF cameras [3]–[8]. While the lateral charge transport from the light receiving area to the charge detection area is dominated by thermal diffusion in the original lock-in pixels, the new structure exploits a faster and more efficient transport by lateral electric drift fields. Consequently, the charge transfer time can be reduced significantly, and the basic limitations with respect to the pixel's fill factor, optical sensitivity, and demodulation speed are overcome with the new design.

Section II presents the underlying theory of TOF distance measurement by continuously modulated light signals. In Section III, the motivation for the development of an improved pixel structure is explained on the basis of the design limitations of current lock-in pixels. The concept of the new demodulation pixel is detailed. Theoretical speed limitations are derived in Section IV. Before a conclusion is given, the pixel's operational reliability is demonstrated in Section V by presenting measurements of distances and of the pixel's charge transport speed.

Manuscript received May 15, 2006; revised August 3, 2006. This work was supported by the IEEE. The review of this paper was arranged by Editor J. Hynecek.

The authors are with Centre Suisse d'Electronique et de Microtechnique, 8048 Zurich, Switzerland.

Digital Object Identifier 10.1109/TED.2006.883669

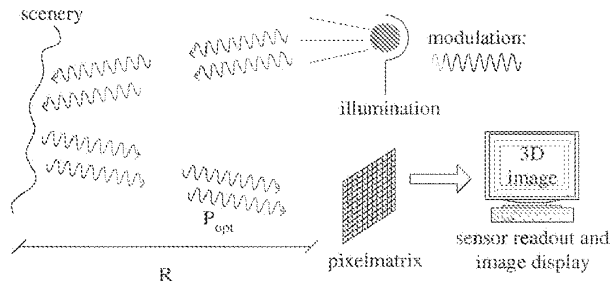

Fig. 1. Principle of the TOF measurement for real-time 3-D imaging.

II. TOF Distance Measurement

The basic concept of TOF 3-D imaging is illustrated in Fig. 1. The time that the light needs to travel from an illumination source to the object and back to the sensor is measured. It is proportionally related to the object's distance according to

$$R = \frac{c \cdot \tau}{2} \tag{1}$$

where c is the light velocity of about 3×10^8 m/s, and τ describes the TOF.

Different schemes for optical intensity modulation are imaginable, e.g., pulse, chirp, rectangular, sinusoidal, etc. For simplicity reasons with regard to the practical generation of the optically modulated signal and the extraction of the TOF, sinusoidal continuous-wave modulation is preferentially used. In particular, compared to pulse or rectangular modulation, the required bandwidth in a sinusoidal modulation is clearly restricted to just one frequency moderating the requirements to the electronic components.

A. Distance Measurement With Sinusoidal Modulation

For the case of sinusoidally modulated light signals, Fig. 2 illustrates the emitted and received signals affected by the object's distance and reflectivity, any attenuation within the optical path and the background light. The received signal is phase shifted due to the round trip of the light signal, and the additional offset is due to background illumination. Mathematically, the emitted optical signal is described by

$$P_e = P_A \cdot [1 + \cos(2\pi f_m \cdot t)] \tag{2}$$

0018-9383/$20.00 © 2006 IEEE

SIONYX1403000027.0049

SAMSUNG EX. 1002 - 2587/4148

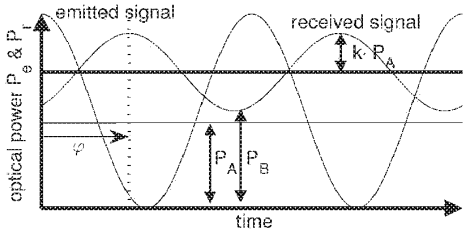

Fig. 2. Emitted and received sinusoidally modulated signal.

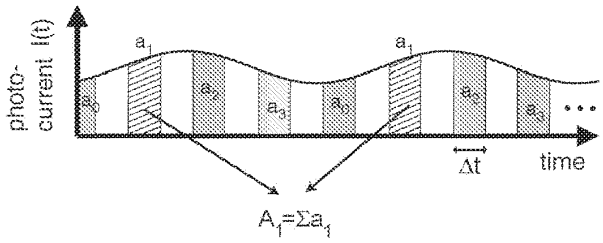

Fig. 3. Sampling procedure of the photocurrent.

where P_e is the emitted optical power, P_A is the amplitude of the modulated signal, f_m describes the modulation frequency, and t is the time parameter. The received signal is expressed as

$$P_r = P_B + k \cdot P_A \cdot [1 + \cos(2\pi f_m \cdot t - \varphi)] \tag{3}$$

where k describes the attenuation factor including any attenuation due to optical losses and absorptions at the target or within the measurement path. φ describes the phase shift of the received modulation signal and corresponds to the TOF according to $\varphi = 2\pi f_m \tau$. With regard to (1), the phase φ is used for the calculation of the distance as

$$R = \frac{c}{4\pi f_m} \cdot \varphi. \tag{4}$$

B. Demodulation of the Sine Wave

The received optical signal is converted into a photocurrent $I(t)$. The time behavior of the current is proportional to the optical signal and is described by

$$I(t) = R_{\text{ph}} \cdot P_r(t) \tag{5}$$

where R_{ph} is the optical responsivity of the pixel [9]. Four equally spaced samples A_0, A_1, A_2, and A_3 within one modulation period are sufficient for the unambiguous extraction of the signal offset B, amplitude A, and phase φ according to [7], [8]

$$A = \frac{\sqrt{(A_0 - A_2)^2 + (A_1 - A_3)^2}}{2} \tag{6}$$

$$B = \frac{A_0 + A_1 + A_2 + A_3}{4} \tag{7}$$

$$\varphi = \text{atan}\left(\frac{A_1 - A_3}{A_0 - A_2}\right). \tag{8}$$

The sampling process, which is depicted in Fig. 3, is assumed to begin with A_0 each time the emitted modulation signal has its maximum. The samples are the result of the integration of the photocurrent for a duration of $\Delta t < 1/f_m$, and hence, the samples, the offset, and the amplitude are given in number of electrons. In order to increase the signal-to-noise ratio of one sampling process, the samples A_k with $k \in [0;3]$ are the result of the summation over several up to many thousands of modulation periods. By combining (4) and (8), the distance is computed as

$$R = \frac{c}{4\pi f_m} \cdot \text{atan}\left(\frac{A_1 - A_3}{A_0 - A_2}\right). \tag{9}$$

Finite integration over Δt has a direct impact on amplitude extraction. While the amplitude is expected to equal the offset component when no background light is present, the low-pass effect due to the integration process reduces the amplitude by the so-called demodulation contrast c_d. In practice, additional nonidealities of the demodulation process, for example, inclined optical incidence, reduce the demodulation contrast even more, for which the signal theory provides an upper bound [8], [10], i.e.,

$$c_d \leq \frac{\sin(\pi f_m \Delta t)}{\pi f_m \Delta t}. \tag{10}$$

C. Distance Accuracy

The ultimate physical limitation of accuracy in distance measurement is given by photon shot noise. Exploiting the fact that the samples in number of electrons will show a Poisson distribution under the influence of photon shot noise [9] and applying the rules of Gaussian error propagation [11] to (9), the ultimate achievable resolution of the distance measurement is derived as

$$\sigma_R = \frac{c}{4\pi f_m \sqrt{2}} \cdot \frac{\sqrt{B}}{A} \tag{11}$$

where B is the sum of the number of electrons generated by the signal A/c_d, the background light BG, and by the dark current BD. A subsequent modeling of additional noise sources like analog-to-digital conversion noise, reset noise, thermal noise, etc., is introduced by a generalized parameter N [8] so that B can be rewritten as

$$B = \frac{A}{c_d} + \text{BG} + \text{BD} + N. \tag{12}$$

It is obvious that for higher modulation frequencies, the accuracy of the distance measurement gets better without the need of detecting more optical power.

III. Demodulation Pixel

We can distinguish between different structures of demodulation pixel depending on the number of samples that are delivered after one acquisition cycle. One-, two-, or four-tap pixels are mostly used in recent 3-D TOF cameras [6], [12] acquiring one, two, or four samples at the same time, respectively. While one- and two-tap structures support lower frame rates because they require several consecutive acquisitions to obtain all four samples, these pixel structures are advantageous to be used with

SIONYX1403000027.0050

SAMSUNG EX. 1002 - 2588/4148

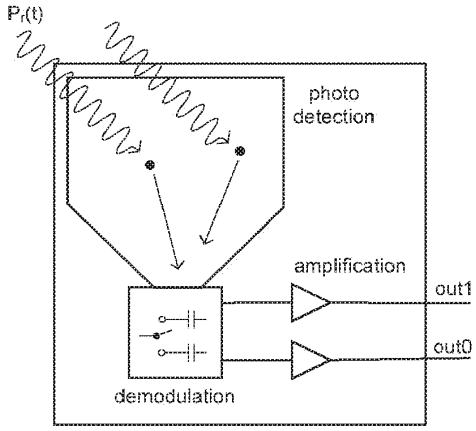

Fig. 4. Block diagram of the static drift field pixel.

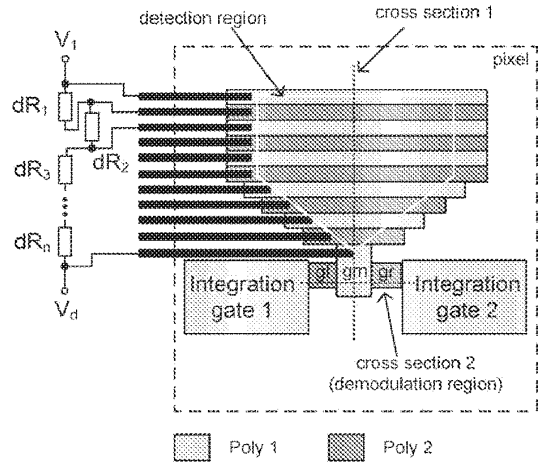

Fig. 5. Illustration of the CCD gate arrangement.

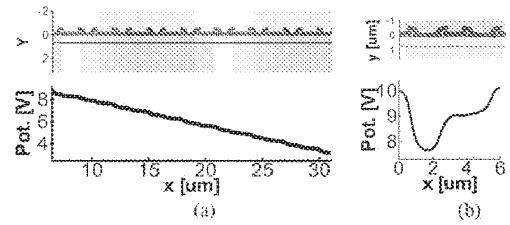

Fig. 6. Process and device simulations. (a) Part of cross section 1 through the detection region. (b) Cross section 2 through the demodulation region. (Color version available online at http://ieeexplore.ieee.org.)

regard to the mitigation of asymmetry effects in the sampling process [13].

Common to most published demodulation pixels is the utilization of the same semiconductor region for both photoelectrical conversion and signal demodulation. This double functionality restricts the pixel to be used at high modulation frequencies as long as the charge transport processes within the semiconductor are dominated by relatively slow diffusion processes. Also, high optical fill factors for increasing the pixel sensitivity are difficult to realize. The new demodulation pixel overcomes these problems by separating the detection region from the signal processing region and by employing fast charge transport methods within the semiconductor material based on lateral electrical drift fields. Compared to current demodulation pixel whose charge transport is based on modulated drift fields [10], the new structure even avoids the drawback of high in-pixel power consumption.

Fig. 4 shows a block diagram of the pixel consisting of a large detection region and a small demodulation region. Electrons and holes are generated in the detection region by the incident optical power $P_r(t)$. If the semiconductor bulk material is weakly p-doped, the holes will be drained to the substrate. The electrons are kept in the buried channel and will drift along the lateral electric field into the direction of the demodulation region. The electron flux arriving in the demodulation region is integrated on two capacitors each corresponding to one sample of the sinusoidal modulation signal. The two samples are amplified in the pixel for read-out purposes.

The whole pixel architecture is based on a combination of CMOS and charge-coupled device (CCD) processes. The detection and demodulation are performed by CCD elements. The employment of buried-channel CCDs [14] and the low number of charge transport processes in one pixel until the charge is stored ensure an almost noise-free signal processing. The readout electronics is realized by standard source follower circuits in CMOS technology, allowing such flexibility as random pixel access.

The CCD gate arrangement of the pixel is shown in Fig. 5. On the basis of this figure, the detection stage and the demodulation stage are briefly discussed in the following two subsections.

A. Detection Stage

The detection stage is responsible for the conversion of the impinging photons into electron–hole pairs in the silicon substrate. The transportation of the photo-generated electrons to the demodulation region has to be accomplished as fast as possible in order to minimize the response time and hence to increase the pixel's demodulation performance. For that reason, slow diffusion processes are avoided, and instead, lateral electric drift fields are exploited for the charge transport.

The lateral electric drift field in the semiconductor channel is generated by 18 adjacent photo-transparent poly-silicon gates of minimal width. As indicated in Fig. 5, the gates are set to constant voltages that are linearly increasing from 0 V to $V_d = 7$ V. The generation of these voltages is done outside the pixel by a resistor line. According to the CCD principle, the potential characteristics on the gates are reflected to the buried channel in the semiconductor substrate due to the capacitive coupling between the gates and the bulk [15]. A numerical simulation of the potential distribution in the buried channel along the vertical dashed line in Fig. 5 is shown in Fig. 6(a). Thanks to the small widths of the gates, an almost constant lateral electrical drift field is built up.

B. Demodulation Stage

The demodulation stage acquires two samples of the photo-generated current coming from the detection region. A second

SIONYX1403000027.0051

SAMSUNG EX. 1002 - 2589/4148

acquisition has to be performed to obtain the samples that are shifted by 90°.

The demodulation stage consists of three adjacent gates of widths as small as allowed by the process design rules for the minimization of additional transport delays. The process simulation of the CCD arrangement is shown in Fig. 6(b) as well as the device simulation for an exemplary case of static voltage settings. The photo-generated electrons are injected from the detection region into the buried channel beneath the middle gate (gm) of the demodulation region. Depending on the voltage settings on the left and right gate (gl, gr), the electrons are transferred to the left or right direction, respectively, and stored under the particular integration gate. The two charge packets correspond to two samples of the signal in the case that the left and right gate voltages are toggled between 6 and 8 V synchronously with the modulation frequency.

C. Discussion of Design Aspects of the Novel Pixel Structure

In the following, some important design aspects are summarized, exhibiting the advantages and disadvantages of the new demodulation pixel.

1) Gate Capacitances: The gate capacitances that have to be charged and discharged with the speed of the modulation frequency are minimized thanks to the small sizes. Compared to standard lock-in pixels, a factor of 10 or more can be saved. This means less power consumption within the driver electronics or higher modulation frequencies can be achieved.

2) Transit Time: The fast charge transport through the detection region by lateral electric drift fields and the short paths through the demodulation region enable the utilization of the pixel in high-speed applications, leading to increased distance accuracies. A detailed analysis of the demodulation speed is performed in the following section of this paper.

3) Optical Fill Factor: Due to the decoupling of the high-speed demodulation site from the detection site, the photon-collection region can be designed with a large area. This enables the design of TOF pixels that have high optical fill factors and support high modulation frequencies at the same time.

4) Microlenses: The geometry of the pixel is more appropriate for the utilization of microlenses than a stripe-like structure as it is present in standard lock-in pixel [4].

5) Noise: The pixel operates entirely in the charge domain, which can be considered as almost noise free. Therefore, the pixel is basically limited by photon shot noise for a wide range of optical input power levels.

6) Low Power Consumption: The application of linearly increasing but constant voltages to the successive arrangement of the gates in the detection region ensures low power consumption in this nondissipative arrangement.

7) Pixel Complexity: The density of the design has been increased compared to standard lock-in pixel.

8) Enhancement to n-Tap Structures: Since the demodulation region has to be designed as small as possible, enhancement to real n-tap structures is difficult to be accomplished. The wiring and mismatch between the n channels are important issues in this context.

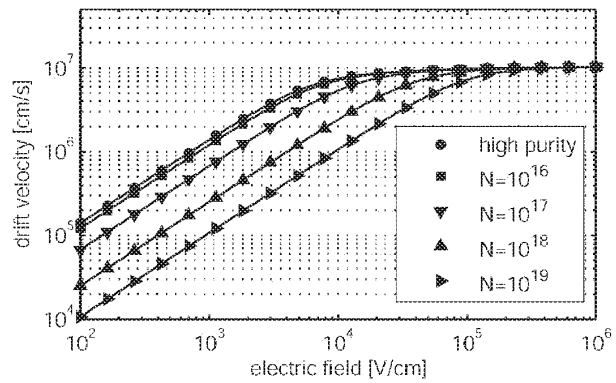

Fig. 7. Drift velocity of electrons in silicon material with different doping concentrations. Room temperature is assumed, and the silicon has a crystal orientation of ⟨111⟩.

IV. Demodulation Speed

Demodulation speed is determined by the cutoff frequency of the pixel. An assessment of the transit time of the electrons through the detection and demodulation regions becomes necessary. This is done in the first subsection. The model for the cutoff frequency is discussed in the second subsection.

A. Transit Time

The buried-channel implant needs to have a doping concentration of less or equal to $N = 10^{16}/\mathrm{cm}^3$ in order to avoid any decrease of the charge's drift velocity, as indicated in Fig. 7. The graphs are based on the phenomenological expression in [16]. The drift velocity for weakly doped silicon can be expressed by the phenomenological expression

$$v\left(E(s)\right) = \frac{\mu_0 \cdot E(s)}{1 + \frac{\mu_0 E(s)}{v_{\max}}} \tag{13}$$

where mobility μ_0 is defined as the ratio between the maximum drift velocity $v_{\max}$ and the electric field E_c at which 3 dB of the maximum drift velocity is reached. As shown in Fig. 7, for pure silicon material at a temperature of 300 K, μ_0 is about 1400 $\mathrm{cm}^2/(\mathrm{Vs})$ and E_c is about $7 \cdot 10^3$ V/cm.

Assuming that a constant drift field is the dominating transport phenomenon, the maximum drift time of the photo-generated electrons through the detection region is estimated to be

$$t_{\mathrm{drift}} = \int_0^{s_{\max}} \frac{1}{v\left(E(s)\right)} ds = \int_0^{s_{\max}} \frac{v_{\max} + \mu_0 E(s)}{v_{\max}\mu_0 E(s)} ds \tag{14}$$

where $s_{\max}$ defines the longest possible drift path. With regard to the geometrical relations of the detection region as shown in Fig. 8, the electric drift field is divided into an upper drift region of constant electric field $E_0 = V_d/(b+c)$ and a bottom drift region having an electric field that depends on the particular angle α. Drift time can be expressed as

$$t_{\mathrm{drift}} = \frac{b(b+c)}{\mu_0 V_d} + \frac{b}{v_{\max}} + \frac{c(b+c)}{\mu_0 V_d \sin^2(\alpha)} + \frac{c}{v_{\max}\sin(\alpha)}. \tag{15}$$

SIONYX1403000027.0052

SAMSUNG EX. 1002 - 2590/4148

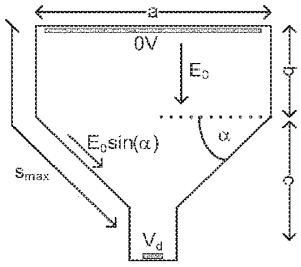

Fig. 8. Geometrical relations of the detection region.

The first implementation of the pixel has been realized with a pixel geometry of $b = 7.3$ μm, $c = 9.6$ μm, and $\alpha = 30°$. Applying a total voltage drop of 7 V over the 18 gates of the detection region, the maximal drift time is estimated to be $t_{\text{drift}} = 1.17$ ns.

The total maximum transit time of an electron through the detection and demodulation regions corresponds to the sum of the drift time plus the additional diffusion time through the demodulation region, i.e.,

$$t_{\text{tr}} = t_{\text{drift}} + t_{\text{diff}}. \tag{16}$$

If a diffusion time of about 3 ns is assumed, the maximum transit time is estimated to be about 4.17 ns.

B. Cutoff Frequency

The model for the assessment of the 3 dB cutoff frequency is based on the finite maximum transit time of the photogenerated electrons through the pixel. The impulse response function $h(t)$ describes the reaction of the pixel to an ideal infinite delta function (Dirac pulse) of optical energy and is modeled as an ideal rectangular function expressed as

$$h(t) = \frac{1}{t_{\text{tr}}} \cdot \text{rect}\left(\frac{t - t_{\text{tr}}/2}{t_{\text{tr}}}\right) = \begin{cases} 1/t_{\text{tr}}, & \text{if } 0 \le t \le t_{\text{tr}} \\ 0, & \text{if } t < 0 \vee t > t_{\text{tr}} \end{cases}.$$

The resulting photocurrent corresponds to the convolution of the optical power signal with the response function and a subsequent multiplication by the responsivity R_{ph} of the pixel, i.e.,

$$I(t) = R_{\text{ph}} P_r(t) * h(t). \tag{17}$$

The convolution in the time domain means a multiplication in the frequency domain so that

$$I(f) = R_{\text{ph}} P_r(f) \cdot H(f). \tag{18}$$

The frequency spectrum of the response function is expressed by the complex sinc function according to

$$H(f) = \text{sinc}\,(\pi f t_{\text{tr}}) \cdot e^{-j\pi f t_{\text{tr}}} \tag{19}$$

where the exponential term describes the phase shift. By defining a 3 dB cutoff frequency f_c with the utilization of the transit time t_{tr}, the relationship that can be derived from (19) is

$$\text{sinc}\,(\pi f_c t_{\text{tr}}) \approx 0.71 \quad \Longleftrightarrow \quad f_c \approx \frac{7}{16 t_{\text{tr}}}. \tag{20}$$

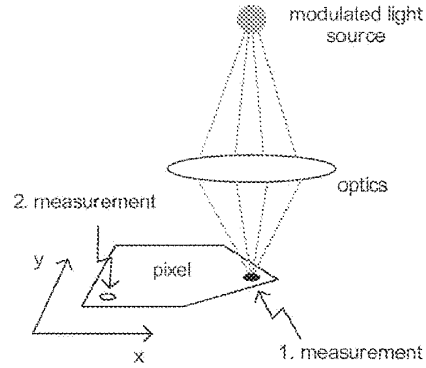

Fig. 9. Simplified depiction of the setup for measuring the transit time through the detection region. (Color version available online at http://ieeexplore.ieee.org.)

Based on a totally estimated transit time of about $t_{\text{tr}} \approx 4.17$ ns, a 3 dB cutoff frequency of about 105 MHz is expected.

V. Verification of the Pixel Concept

The first design of the pixel structure has been realized in a 0.6-μm technology of a CMOS process that offers an additional CCD option. The size of the pixel is quadratic with a side length of 40 μm. The detection area of triangular shape covers a total area of 399 μm^2, leading to a fill factor of more than 25%. Compared to standard lock-in pixels [4], [6] having the same pixel size and fill factor, the gate capacitances, which have to be charged and discharged with the modulation frequency, have been reduced by a factor of at least 3. The output diffusion capacities have been designed for storing a total amount of about 800 000 electrons. According to (11), this allows for measuring distances with an accuracy in the millimeter range when applying modulation frequencies of 20 MHz or higher. The corresponding estimation assumes no background light (BG = 0) and a negligibly small dark current in the pixel (BD $\approx$ 0). The general noise parameter N is neglected as well since the photon shot noise is expected to be the dominating noise source under strong light conditions. The following measurement results have been obtained with a sensor that has incorporated 176 $\times$ 144 of these demodulation pixels.

Two kinds of experiments have been performed to verify the pixel concept and its functionality. The first measurement results provide evidence that the charge transport through the detection region is performed at high speed thanks to lateral drift processes. The second experiment is a distance measurement exhibiting the capability of the pixel to be utilized in a real-time 3-D TOF imaging system.

The longest transit time through the detection region has been theoretically estimated to be about 1.17 ns (see Section IV-A). This transit time has been measured by illuminating a small region of the detection region with a small-sized laser spot once at the top side and once at the bottom side of the detection area. The measurement setup is schematically depicted in Fig. 9. By demodulating the photocurrent, the phase difference between the two spatially separated spots gives an approximate measure

SIONYX1403000027.0053

SAMSUNG EX. 1002 - 2591/4148

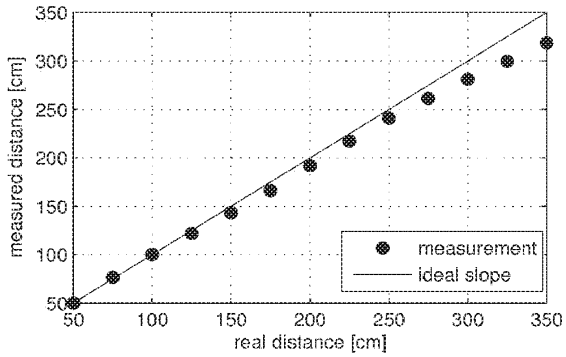

Fig. 10. Distance measurement.

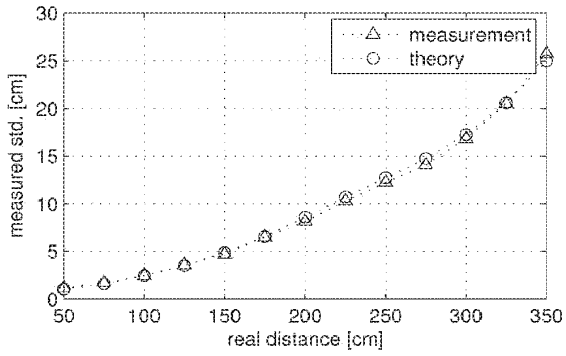

Fig. 11. Measured standard deviation versus the real distance compared to the theory.

of the transit time. We measured time differences of about 0.5 ns, which is below the theoretical worst case estimation. In practice, the transport of charge carriers is even slightly accelerated by self-induced drift effects.

The pixel's capability of measuring the TOF corresponding to the distance is shown in Fig. 10. The measured distance is depicted versus the real distance of a black target that has a reflectivity of approximately 10%. The slight deviation from the ideal slope mainly results from the harmonic distortions of the sinusoidal optical modulation signal. The corresponding standard deviation is depicted in Fig. 11, where the theoretically expected values according to (11) have been included. The measurement was accomplished without any background light (BG = 0). The modulation frequency of the signal was $f_m = 20$ MHz. Theoretical calculation neglects the dark current (BD = 0). Since less optical power is reflected from the target at longer distances, the standard deviation shows a quadratic behavior as a function of distance.

VI. Conclusion

A demodulation pixel architecture based on a combined CCD/CMOS process with very high-speed demodulation capability has been presented. It is based on lateral drift fields in an architecture separating the photodetection and demodulation regions from each other. Its functionality has been demonstrated by real distance measurements. Although the layout complexity has been increased compared to competing and currently utilized lock-in pixels, many advantages such as low power consumption, fast charge transportation, and high optical fill factor make the pixel very attractive for future 3-D TOF imaging systems.

Acknowledgment

The authors would like to thank all members of the CSEM's image sensing group for their assistance in the implementation of the test equipment and the characterization of the 3-D imager chip.

References

[1] P. Seitz, "Unified analysis of the performance and physical limitations of optical range-imaging techniques," in *Proc. Range Imag. Res. Day*, Zurich, Switzerland, 2005, pp. 9–19.

[2] R. Schwarte, G. Häusler, and R. W. Malz, *Three-Dimensional Imaging Techniques in Handbook of Computer Vision and Applications*. New York: Academic, 2000.

[3] B. Büttgen, T. Oggier, M. Lehmann, R. Kaufmann, S. Neukom, M. Richter, M. Schweizer, D. Beyeler, R. Cook, C. Gimkiewicz, C. Urban, P. Metzler, P. Seitz, and F. Lustenberger, "High-speed and high-sensitive demodulation pixel for 3-D-imaging," *Proc. SPIE*, vol. 6056, 2006. San Jose.

[4] B. Büttgen, T. Oggier, M. Lehmann, R. Kaufmann, and F. Lustenberger, "CCD/CMOS lock-in pixel for range imaging: Challenges, limitations and state-of-the-art," in *Proc. Range Imag. Res. Day*. Zurich, Switzerland, 2005, pp. 21–32.

[5] M. Lehmann, T. Oggier, B. Büttgen, C. Gimkiewicz, M. Schweizer, R. Kaufmann, F. Lustenberger, and N. Blanc, "Smart pixels for future 3-D-TOF sensors," presented at the IEEE Workshop CCD and Advanced Image Sensors, Japan, 2005.

[6] R. Lange and P. Seitz, "Solid-state time-of-flight range camera," *IEEE J. Quantum Electron.*, vol. 37, no. 3, pp. 390–397, Mar. 2001.

[7] T. Spirig, "Smart CCD/CMOS based image sensors with programmable, real-time, temporal and spatial convolution capabilities for applications in machine vision and optical metrology," Ph.D. dissertation, Eidgenössische Technische Hochschule (ETH), Zurich, Switzerland, 1997.

[8] R. Lange, "3-D time-of-flight distance measurement with custom solid-state image sensors in CMOS/CCD-technology," Ph.D. dissertation, Univ. Siegen, Siegen, Germany, 2000.

[9] B. E. A. Saleh and M. C. Teich, *Fundamentals of Photonics*. New York: Wiley, 1991.

[10] B. Büttgen, T. Oggier, R. Kaufmann, P. Seitz, and N. Blanc, "Demonstration of a novel drift field pixel structure for the demodulation of modulated light waves with application in three-dimensional image capture," *Proc. SPIE*, vol. 5302, 2004. San Jose.

[11] I. N. Bronstein, K. A. Semendjajew, G. Musiol, and H. Mülig, *Taschenbuch der Mathematik*. Thun, Frankfurt am Main: Verlag Harri Deutsch, 1997.

[12] T. Oggier, B. Büttgen, F. Lustenberger, G. Becker, B. Rüegg, and A. Hodac, "SwissRanger SR3000 and first experiences based on miniaturized 3-D-TOF cameras," in *Proc. Range Imag. Res. Day*, Zurich, Germany, 2005, pp. 97–108.

[13] R. Kaufmann, M. Lehmann, M. Schweizer, M. Richter, P. Metzler, G. Lang, T. Oggier, N. Blanc, P. Seitz, G. Gruener, and U. Zbinden, "A time-of-flight line sensor—Development and application," *Proc. SPIE*, vol. 5459, pp. 192–199, 2004.

[14] L. J. M. Esser and A. J. P. Theuwissen, "Charge coupled devices: Physics, technology and imaging," in *Handbook on Semiconductor*, vol. 4. Amsterdam, The Netherlands: North-Holland, 1993.

[15] M. J. Van Der Tol and S. G. Chamberlain, "Potential and electron distribution model for the buried-channel MOSFET," *IEEE Trans. Electron Devices*, vol. 36, no. 4, pp. 670–689, Apr. 1989.

[16] C. Jacoboni, C. Canali, G. Ottaviani, and A. Alberigi Quaranta, "A review of some charge transport properties of silicon," *Solid State Electron.*, vol. 20, no. 2, pp. 77–89, Feb. 1977.

SIONYX1403000027.0054

SAMSUNG EX. 1002 - 2592/4148

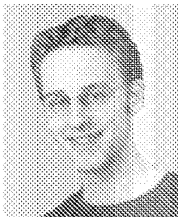

Bernhard Büttgen received the degree in electrical engineering from the University of Siegen, Siegen, Germany, in 2002. He is currently working toward the Ph.D. degree with the Swiss Center for Electronics and Microtechnology, Zurich, Switzerland.

He was with Leica Geosystems AG, Heerbrugg, Switzerland, where he worked on the characterization of smart CMOS sensors used for fast optical distance measurement. His research focus lies on the real-time acquisition of three-dimensional images. He participated in the development of new sensors capable of acquiring distance images with high resolution under different complex operation conditions.

Mr. Büttgen was awarded with the VDI Deutscher Förderpreis in 2003.

Felix Lustenberger (S'95–M'01–SM'06) received the M.Sc. degree in microengineering from the Swiss Federal Institute of Technology, Lausanne, Switzerland, in 1995, and the Ph.D. degree in electrical engineering from the Swiss Federal Institute of Technology (ETHZ), Zurich, Switzerland, in 2000.

After completing his doctoral research, he was a part-time Senior Research Assistant with the Signal and Information Processing Laboratory, ETHZ, Switzerland, leading the analog decoder research group until 2002. From 2001 to 2002, he was with Snowbush Microelectronics, Toronto, ON, Canada, where he developed cutting-edge mixed-signal circuits for high-speed data communications. Since 2002, he has been with the Photonics Division, Centre Suisse d'Electronique et de Microtechnique SA (CSEM), Zurich, where he is responsible for the image-sensor IC-design activities. Since 2004, he has been heading the image sensing group of CSEM, dealing with all aspects of high-performance imaging starting at the semiconductor level and going up to the system-design level for metrology systems of ultimate performance. His current main research interests include general analog, mixed-signal, and bio-inspired very large scale integration (VLSI) design, solid-state image sensing and image processing, microsystems design, system-oriented VLSI design, and analog design automation.

Dr. Lustenberger is a Senior Member of several IEEE societies. He has been the Secretary of the Analog Signal Processing Technical Committee (ASPTC) of the IEEE Circuits and Systems Society since 2005. He also acts as a Reviewer for several international journals and conferences.

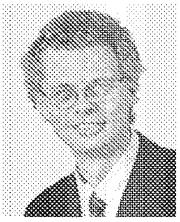

Peter Seitz (M'88) received the Ph.D. degree in physics from the Swiss Federal Institute of Technology (ETH), Zurich, Switzerland, in 1984.

From 1984 to 1987, he was a Staff Member with the RCA Research Laboratories, Princeton, NJ, and Zurich, Switzerland. In 1987, he was with the Paul Scherrer Institute, Zurich, where he formed the image sensing research group. Since 1997, he has been with Centre Suisse d'Electronique et de Microtechnique (CSEM), Zurich, Switzerland, as a Group Leader, as Head of CSEM's Photonics Division, and the Creator of CSEM's outpost on the U.S. West Coast in San Francisco. He is an extraordinary Professor of optoelectronics with the Institute of Microtechnology, University of Neuchatel, Neuchatel, Switzerland. He is the Vice President of Academic Relations with CSEM. He has authored more than 170 publications in the fields of applied optics, semiconductor image sensing, machine vision, and optical microsystems engineering. He holds 30 patents.

Dr. Seitz has been the Secretary General of the European Optical Society (EOS) from 1998 to 2004 and still serves as an EOS Board Member. He has won numerous awards together with his teams.

SIONYX1403000027.0055

SAMSUNG EX. 1002 - 2593/4148

C2

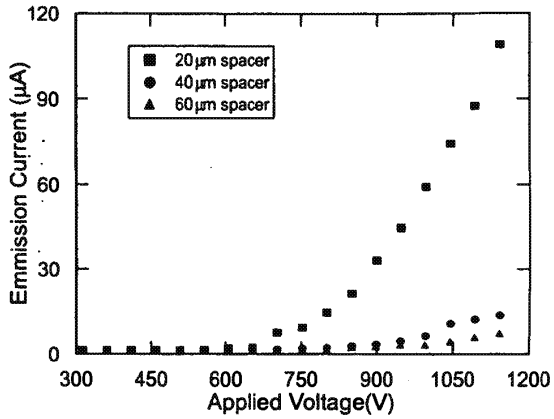

CFC2 Fig. 2. Current-voltage characteristics of the microstructure arrays at different anode-cathode separations.

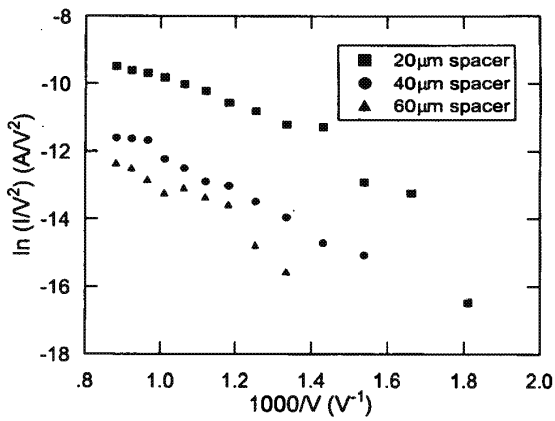

CFC2 Fig. 3. Fowler-Norheim plots of the microstructure arrays at different anode-cathode separations. The linearity of a Fowler-Nordheim plot shows that field emission is responsible for the current.

CFC2 **8:15 am**

Field Emission from Silicon Microstructures Formed by Femtosecond Laser Assisted Etching

J.E. Carey, L. Zhao,* C. Wu, and E. Mazur, *Harvard University, Division of Engineering and Applied Sciences and Department of Physics, 9 Oxford St, Cambridge, MA 02138, USA; Email: jcarey@fas.harvard.edu; *Fudan University, China*

Field-emission arrays have been extensively investigated for device applications such as flat panel displays, electron multipliers and microelectronics.[1,2] The use of silicon structures as emitters is especially attractive due to the low cost and availability of silicon. Previously, our group reported the formation of sharp, micron-sized conical structures in quasi-ordered arrays after irradiating a silicon surface with hundreds of femtosecond-laser pulses in an atmosphere of SF_6.[3,4] Figure 1 shows an SEM image of an array of spikes formed in this manner. These conical microstructures exhibit sharp tips with a radius of curvature ~0.25 μm and a subtended angle of less than 20°. Because of the potential for field emission, many fabrication techniques have been reported for making micron-sized silicon-tip arrays but they typically involve intricate processing and preparation such as multiple photolithography, etching, and oxidation steps.[5,6] Emission currents suitable for applications and comparable with current standards are achieved with no further processing beyond the laser irradiation required to form our microstructures. We report on the field emission properties of these conical microstructures through analysis of the current-voltage characteristics and the Fowler-Nordheim plots obtained for various anode-cathode separations.[7]

By raster scanning 100-fs laser pulses with fluence 10.9 kJ/m² at a speed of 100 μm/s, we formed microstructures over a 3 × 3 mm² area of an n-type silicon (800–1200 Ω · cm) wafer. The microstructures are 10–14 μm tall and have a tip-to-tip separations of 6–10 μm. Measurements were made for anode-cathode separation of 20 μm, 40 μm, and 60 μm, and an applied voltage ranging from 300 to 1150 volts. *I–V* characteristics were obtained for each spacing and are shown in Figure 2. The turn-on field, defined in our case as the field required to produce an emission current density of 1 μA/cm², is estimated to be about 12 V/μm. Emission current can be as high as 200 μA/cm² for an applied field of 55 V/μm. The Fowler-Nordheim plot in Figure 3 shows linearity over several orders of magnitude, indicating that the measured current is indeed from field emission. Lifetime testing of emission for a sample at an anode-cathode spacing of 40 μm for 6 hours showed an drop of emission current to 65% in the first half hour, with a steady emission current thereafter.

This novel method of creating silicon field emitters produced stable emitters with high emission currents without any further processing beyond laser irradiation. We plan to examine the effect of varying parameters such as microstructure height and substrate thickness in order to

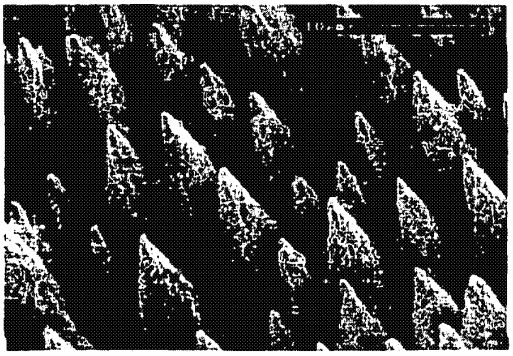

CFC2 Fig. 1. Scanning electron micrograph (SEM) of a microstructured silicon surface.

achieve lower turn-on fields and even higher emission currents. In addition, we are investigating to what degree the impurities and defects introduced during the spike formation are responsible for the high field emission observed.

References

1. M. Takai, M. Yamashita, H. Wille, S. Yura, Horibata, M. Ototake, *Appl. Phys. Lett.* 73, 422–423 (1995).
2. V.V. Zhirnof, E.I. Givargizov, and P.S. Plekhanov, *J. Vac. Sci. Technol. B* **13**, 418–421 (1995).
3. T.H. Her, R.J. Finlay, C. Wu, S. Deliwala, and E. Mazur, *Appl. Phys. Lett.* 73, 1673–1675.
4. T.H. Her, R.J. Finlay, C. Wu., and E. Mazur, *Appl. Phys. A* 70, 383–385 (2000).
5. S.E. Huq, C.H. Grayer, S.W. Moon, P.D. Prewett, *Materials Science and Engineering B* 51, 150–153 (1998).
6. C.W. Oh, C.G. Lee, B.G. Park, and J.D. Lee, *J. Vac. Sci. Technol. B* 16, 765–769 (1998).
7. R.H. Fowler, D.L. Nordheim, *Proc. R. Soc. London A* 119, 173 (1928).

SIONYX1403000027.0057

SAMSUNG EX. 1002 - 2595/4148

C1

Fabrication of Micrometer-Sized Conical Field Emitters Using Femtosecond Laser-Assisted Etching of Silicon

J.E. CAREY*, C.H. CROUCH*, R. YOUNKIN**, E. MAZUR**, M. SHEEHY***, C. FRIEND***
*Division of Engineering and Applied Sciences, Harvard University, Cambridge, MA
**Department of Physics, Harvard University, Cambridge, MA
***Department of Chemistry and Chemical Biology, Harvard University, Cambridge, MA

ABSTRACT

Arrays of sharp, conical microstructures were obtained by structuring the surface of a silicon wafer using femtosecond laser-assisted etching. Analysis of the arrays shows high, stable field emission without any further processing steps and turn-on fields as low as 1.3 V/μm.

INTRODUCTION

Field-emission arrays have been extensively investigated for device applications such as flat panel displays, electron multipliers and microelectronics. The use of silicon structures as emitters is especially attractive due to the low cost and availability of silicon. Because of the potential for efficient and inexpensive field emission, many fabrication techniques have been reported for making micron-sized silicon-tip arrays but they typically involve intricate processing and preparation such as multiple photolithography, etching, and oxidation steps [1,2]. Previously, our group reported the formation of sharp, micron-sized conical structures in quasi-ordered arrays after irradiating a silicon surface with hundreds of femtosecond-laser pulses in an atmosphere of SF_6 [3,4]. Figure 1 shows a scanning electron micrograph image of an array of microstructures formed in this manner. Emission currents suitable for applications and low turn-on fields are achieved with no further processing beyond the laser irradiation required to form our microstructures. We report on the field emission properties of these conical microstructures through analysis of the current-voltage characteristics and the Fowler-Nordheim relation[5].

EXPERIMENT

We irradiate a Si(111) surface with a train of 800 nm, 100 fs laser pulses in the presence of SF_6. The result of this irradiation is a quasi-ordered array of conical microstructures that form spontaneously, without the use of masks. The structures are 10-12 μm tall with a spacing of 4-6 μm and a tip with radius of curvature of about 250 nm. We formed microstructures over a 2×2 mm^2 area of an n-type silicon (800–1200 $\Omega \bullet$ cm) wafer. We then measure the current-voltage characteristics for an anode-cathode separation of 20 μm and applied voltages ranging from 0 to 1000 V.

RESULTS

The current-voltage characteristics are for potential differences up to 100 V are shown in Figure 2. The field required to produce an emission current density of 1 nA/mm^2, is 1.3 V/μm. We have obtained emission currents up to .5 mA/mm^2 at an applied field of 50 V/μm. The structures are robust and continue to produce field emission after being left in air for several weeks. Plots of the Fowler-Nordheim relation show two regions with linear behavior for potential differences of less than 100 V. Above 100 V the use of a series resistor in the protection circuit for the picoammeter results in an ohmic current-voltage relationship.

CONCLUSIONS

This novel method of creating silicon field emitters produced stable emitters with high emission currents and low-turn on fields without any further processing beyond laser irradiation. We plan to examine the effect of varying parameters such as microstructure height and substrate thickness in order to achieve lower turn-on fields and even higher emission currents. In addition, we are investigating to what degree the impurities and defects introduced during the microstructure formation are responsible for the high field emission observed.

ACKNOWLEDGEMENTS

We would like to acknowledge the NSF, the ARO, and the NDSEG for funding. We would also like to acknowledge Li Zhao of Fudan University, Shanghai, China for work in the early experiments.

REFERENCES

[1] S.E. Huq, C.H. Grayer, S.W. Moon, P.D. Prewett, *Materials Science and Engineering B* **51**, 150-153(1998)

[2] C.W. Oh, C.G. Lee, B.G. Park, and J.D. Lee, *J. Vac. Sci. Technol. B* **16**, 765-769(1998)

[3] T.H. Her, R.J. Finlay, C. Wu, S. Deliwala, and E. Mazur, *Appl. Phys. Lett.* **73**, 1673-1675

[4] T.H. Her, R.J. Finlay, C. Wu., and E. Mazur, *Appl. Phys. A* **70**, 383-385(2000)

[5] R.H. Fowler, D.L. Nordheim, *Proc. R. Soc. London A* **119**, 173 (1928)

Fig. 1 Scanning electron micrograph of conical microstructures

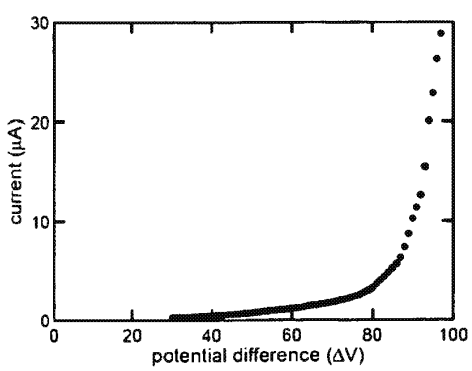

Fig. 2 Current-voltage characteristics for potential differences from 30-100 V and anode-cathode spacing of 20 μm. For potential differences above this region the use of a series resistor in the protection circuit results in ohmic behavior

Fabrication of micrometer-sized conical field emitters using femtosecond laser-assisted etching of silicon

Jim Carey
Eric Mazur
Catherine Crouch
Rebecca Younkin

IVMC 2001
UC Davis, 14 August 2001

SIONYX1403000027.0061
SAMSUNG EX. 1002 - 2599/4148

Introduction

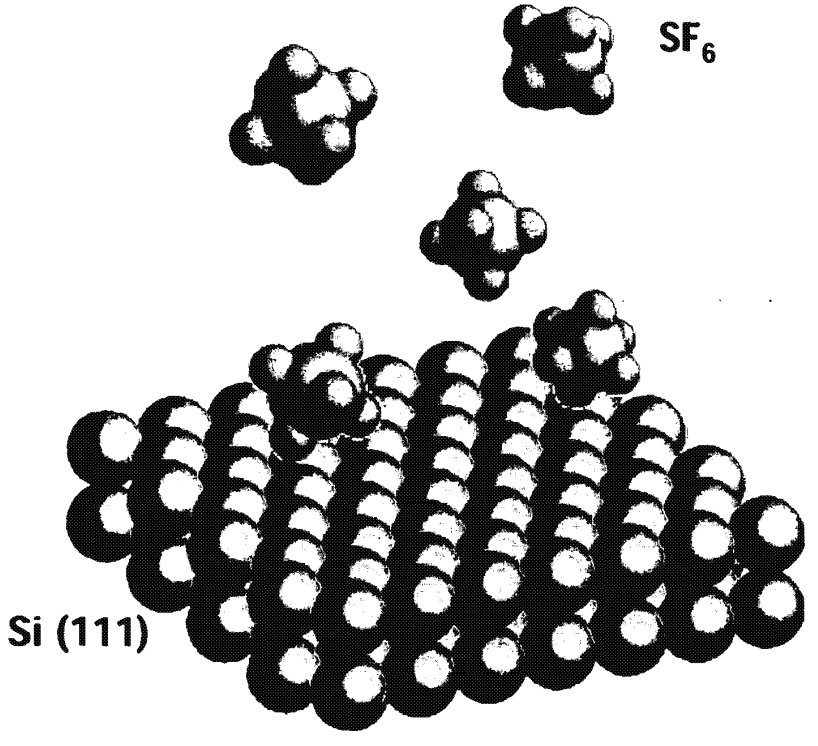

irradiate with 100-fs 10 kJ/m^2 pulses

SIONYX1403000027.0062

SAMSUNG EX. 1002 - 2600/4148

Introduction

5 mm

"black silicon"

SIONYX1403000027.0063

SAMSUNG EX. 1002 - 2601/4148

Introduction

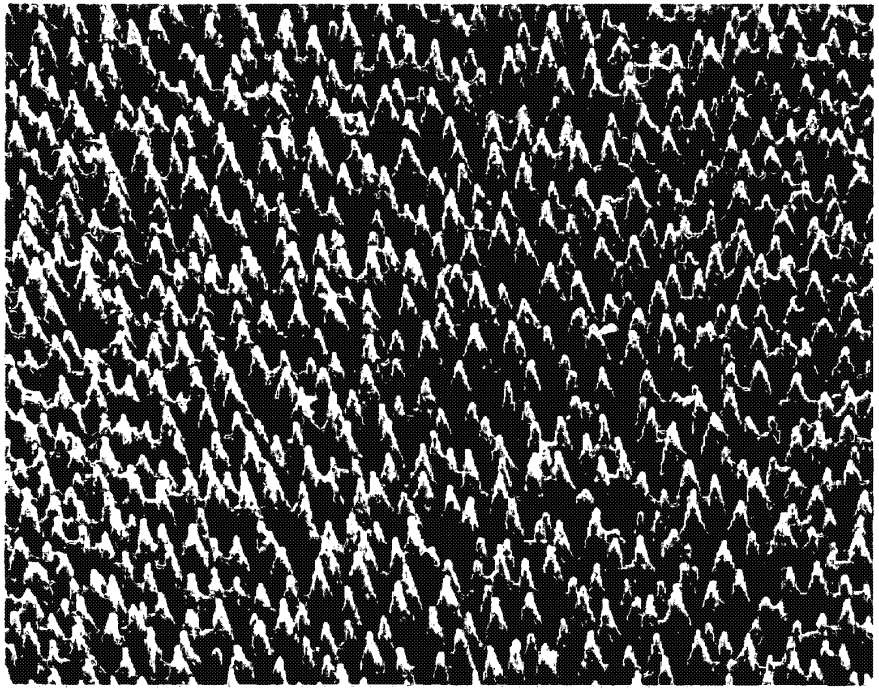

20 µm

SAMSUNG EX. 1002 - 2602/4148

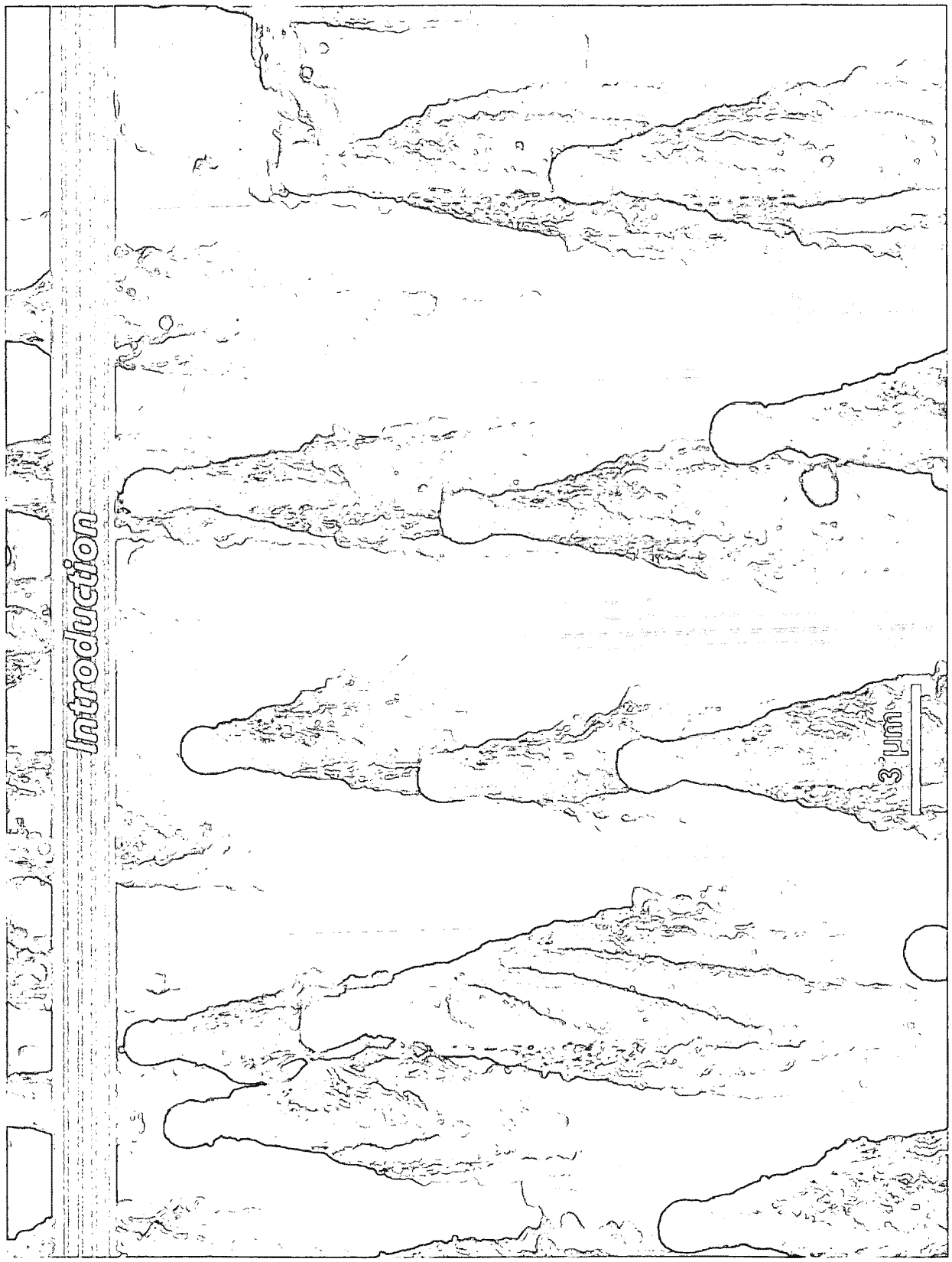
Introduction
3 μm

Introduction
10 μm

Outline

- Background
- Results
- Discussion

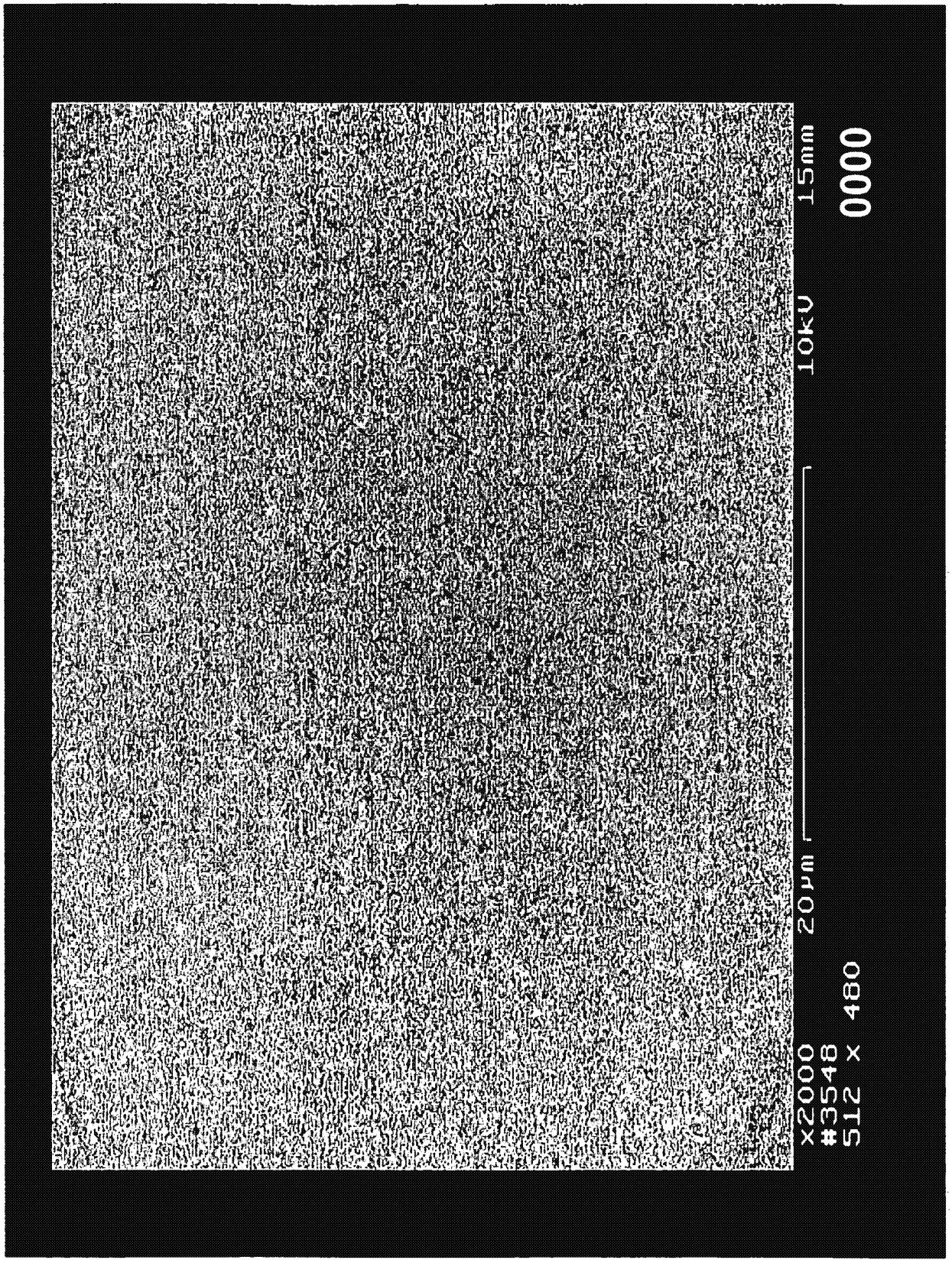
x2000
#3548
512 x 480
20μm
10kV
15mm
0000

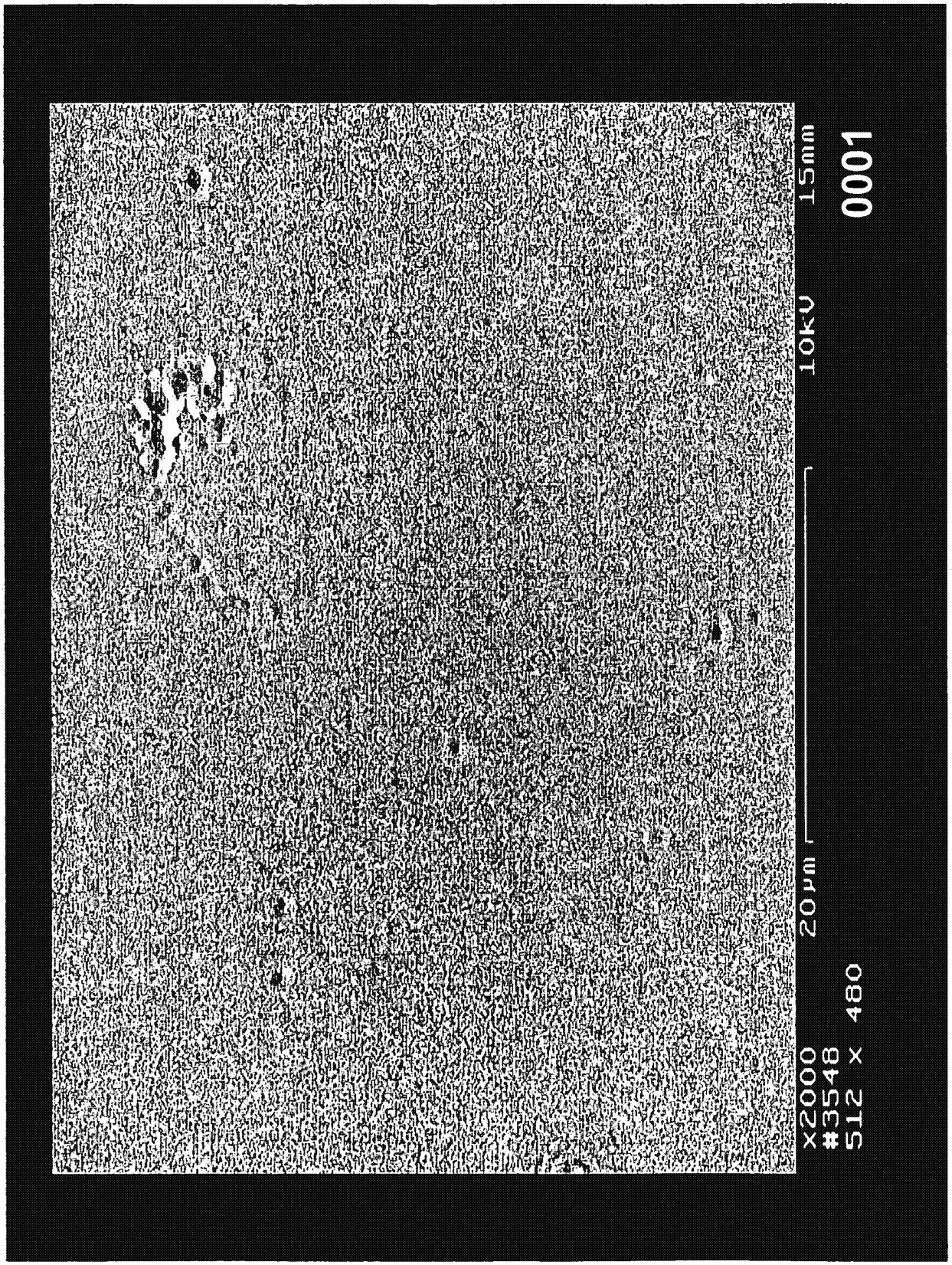
X2000
#3548
512 x 480
20μm
10kV
15mm
0001

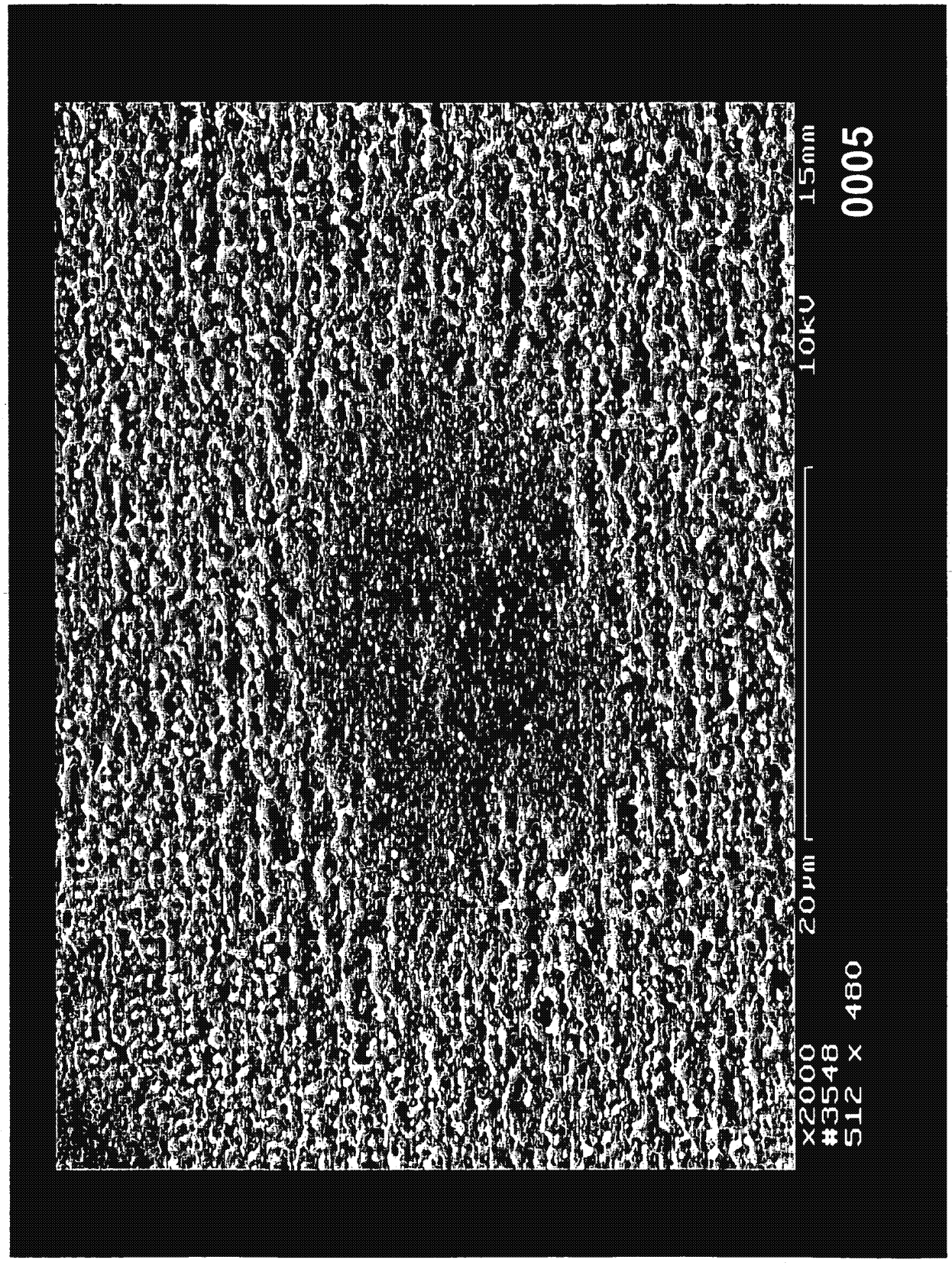
X2000
#3548
512 X 480
20μm
10kV
15mm
0005

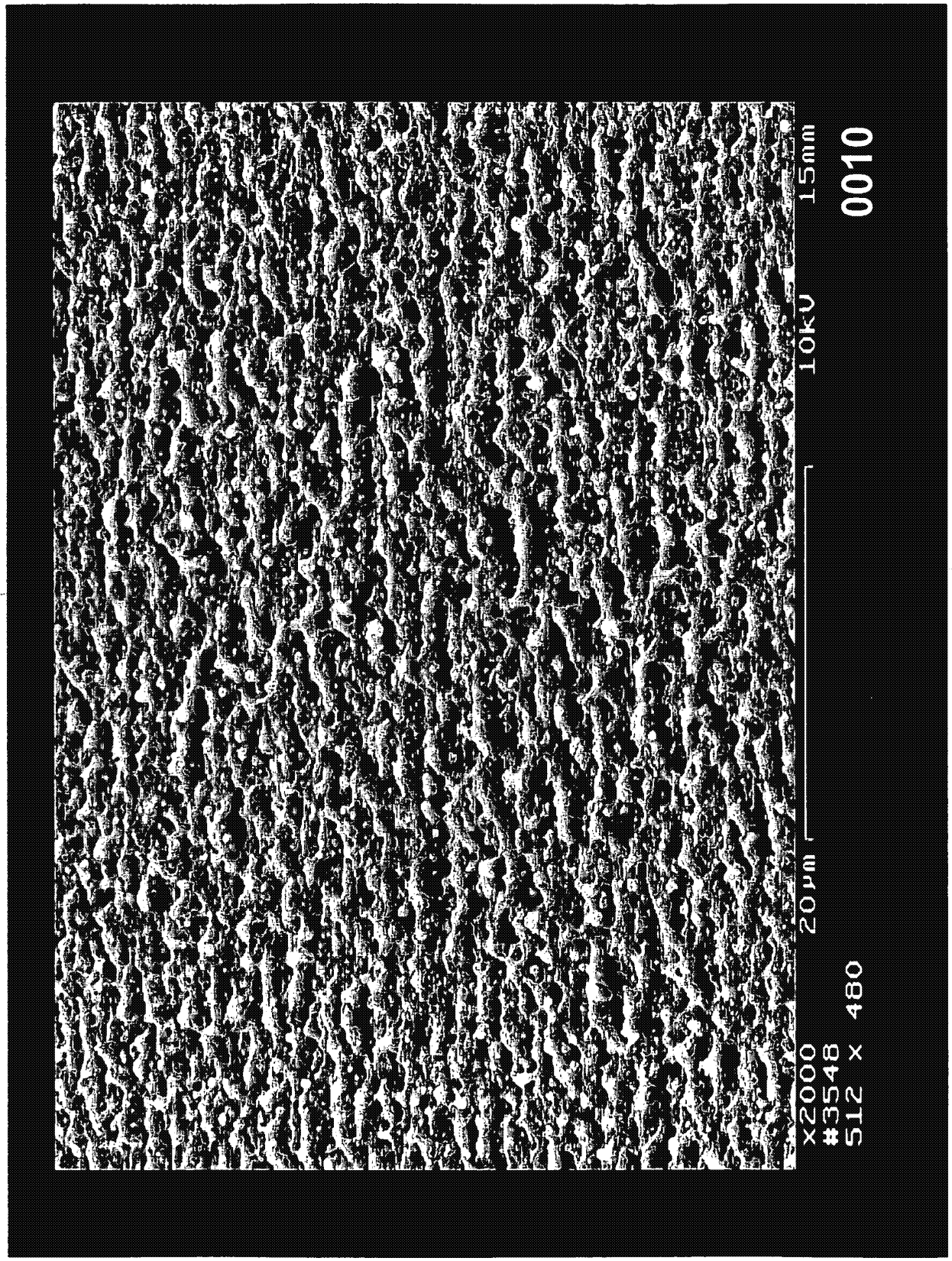
X2000
#3548
512 X 480
20μm
10kV
15mm
0010

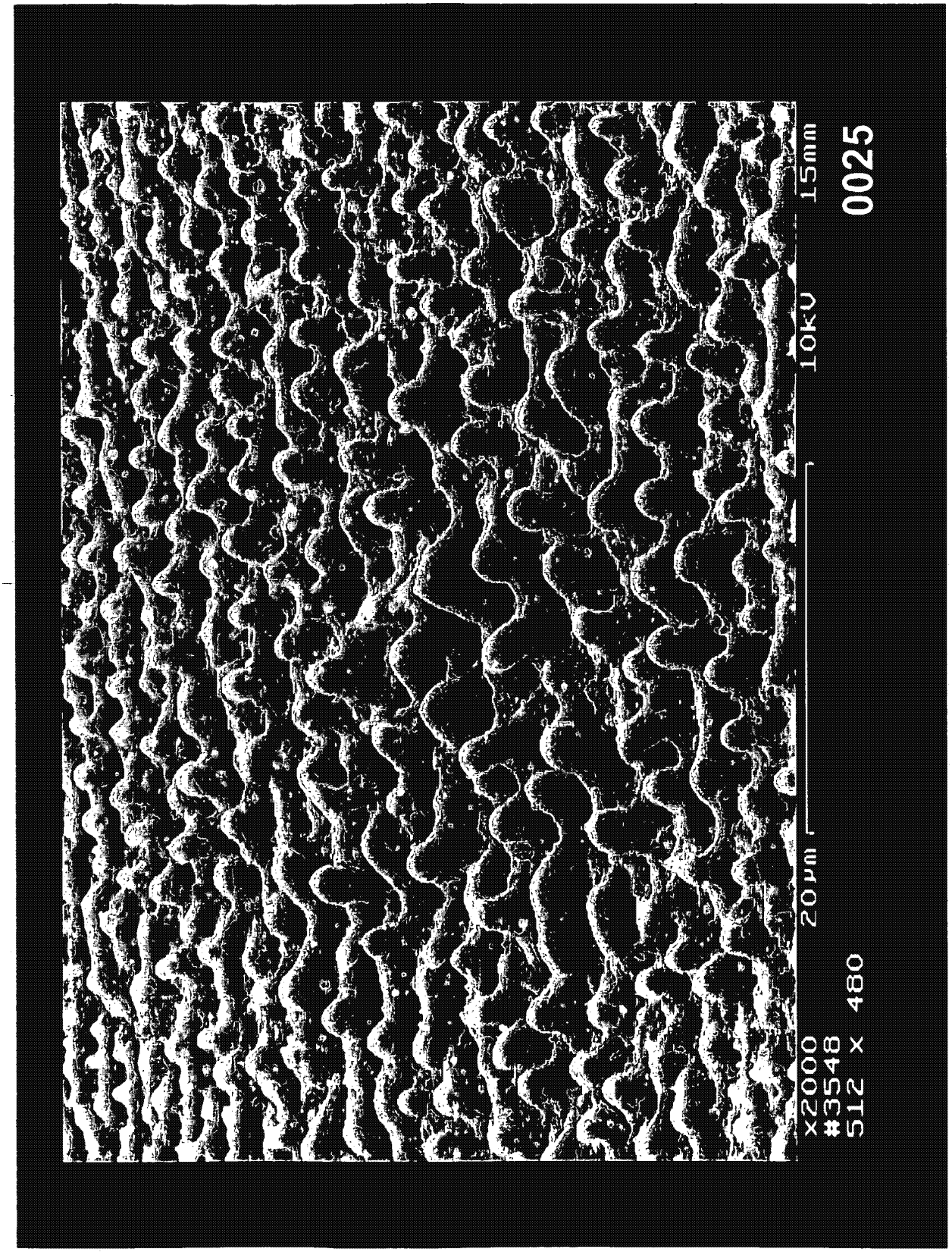

0025

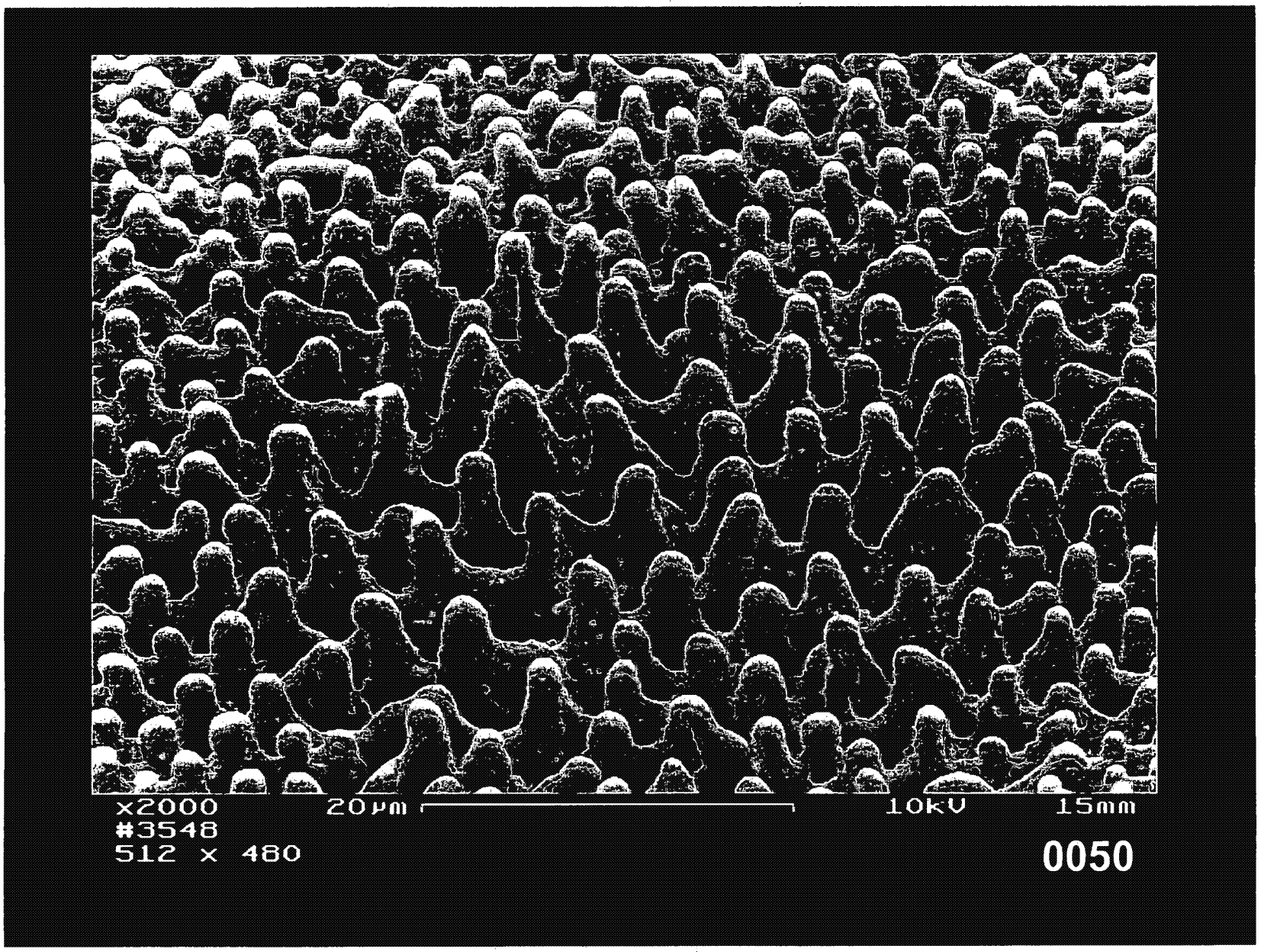
x2000
#3548
512 x 480
20μm
10kV
15mm
0050

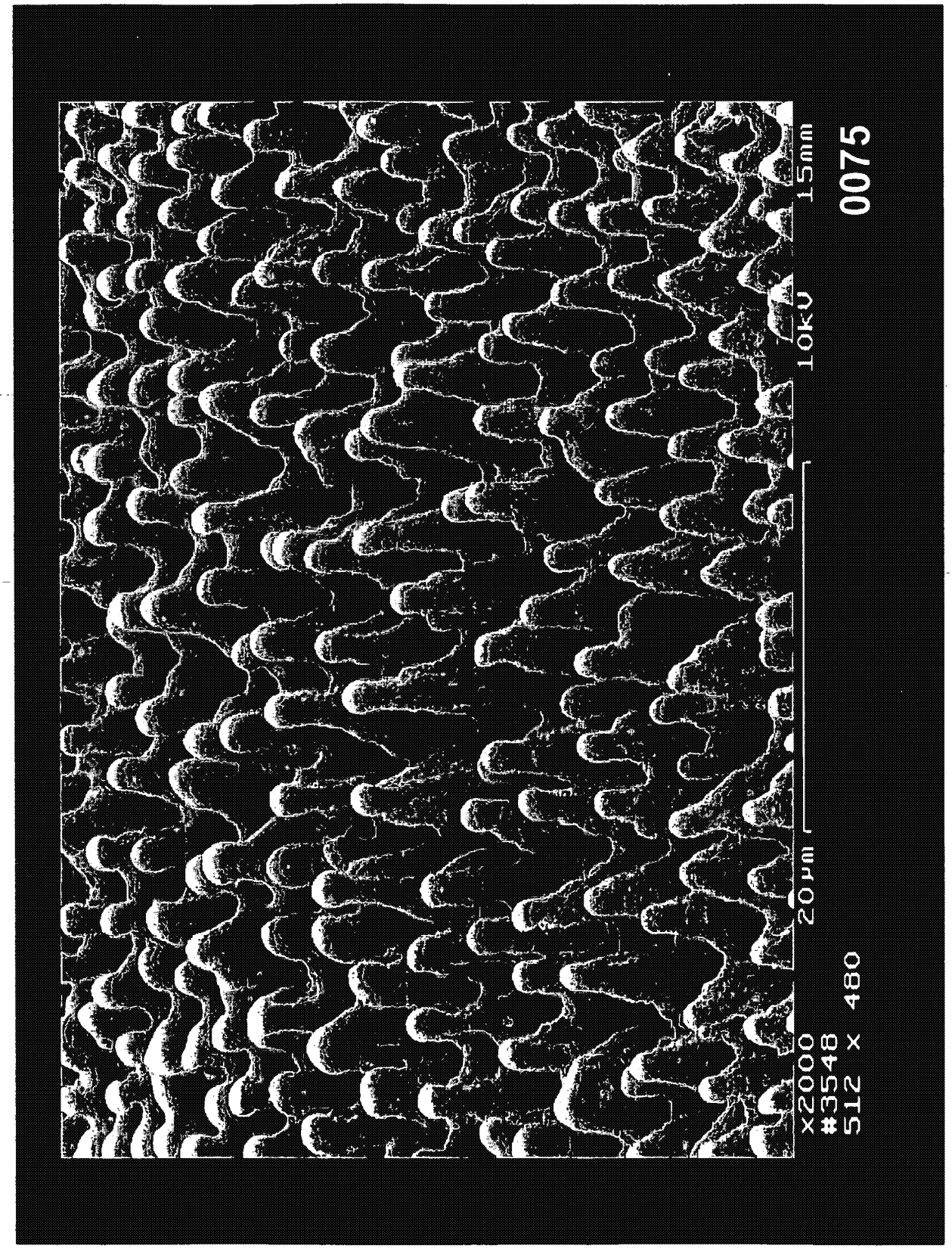

0075

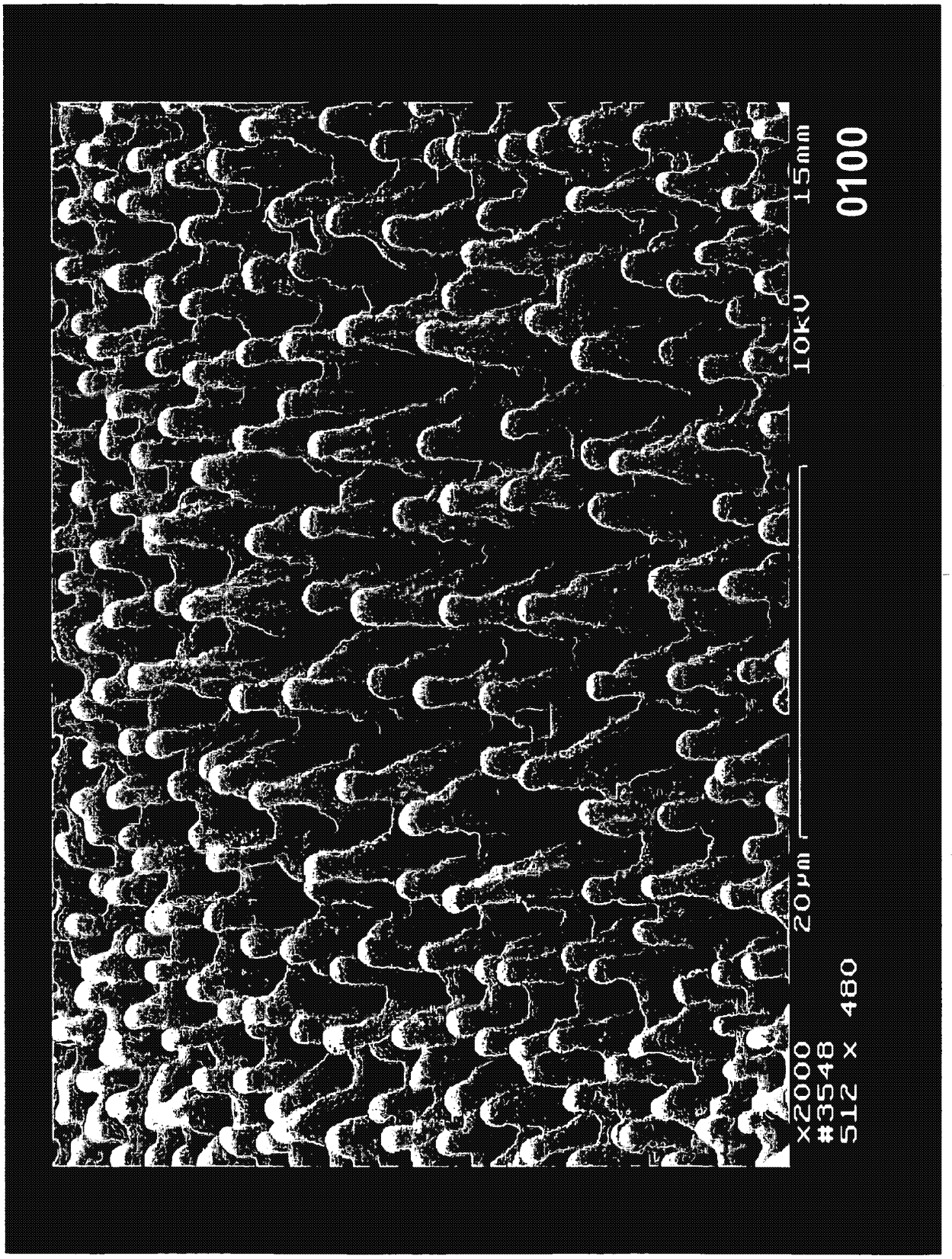
X2000
#3548
512 X 480
20μm
10kV
15mm
0100

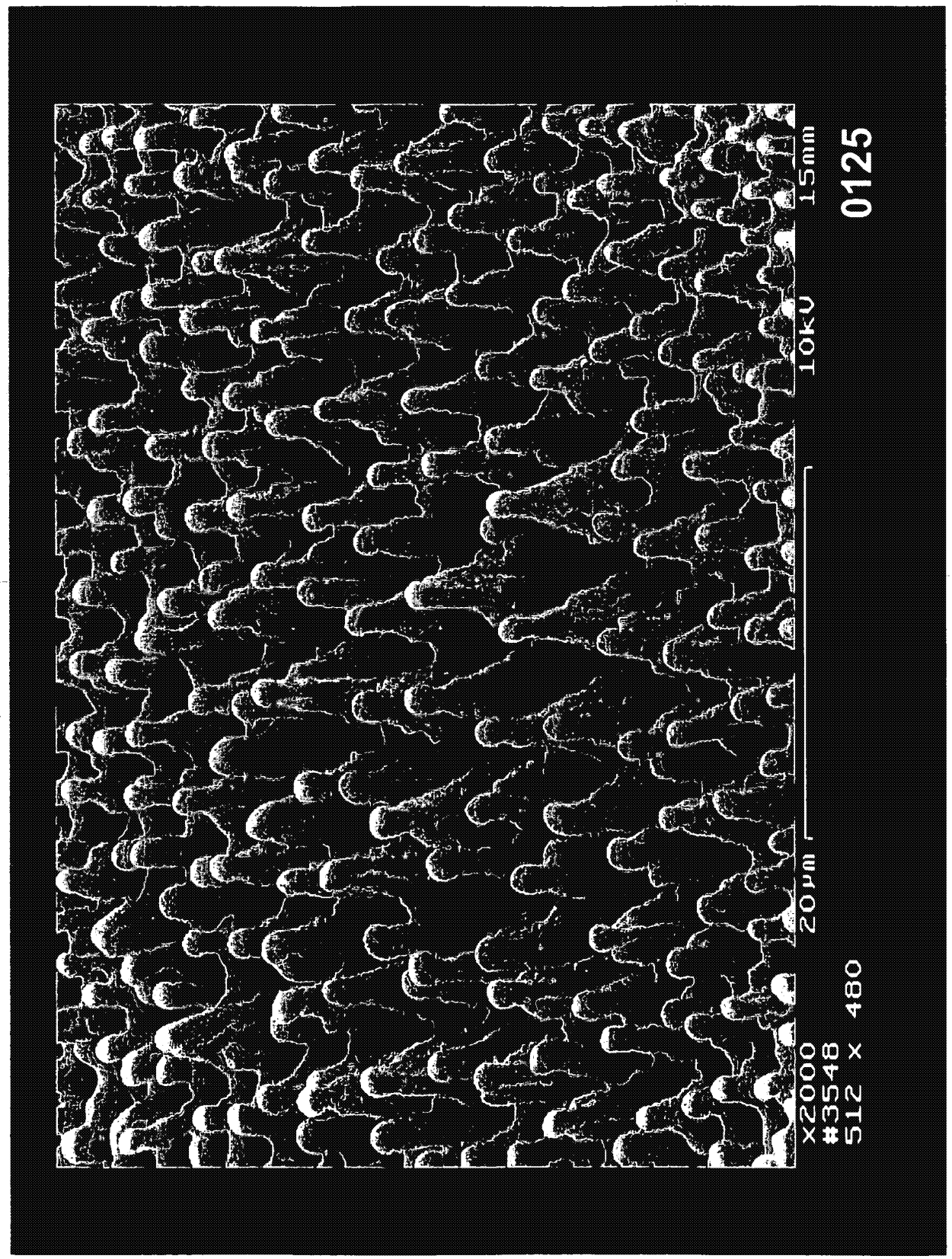

0125

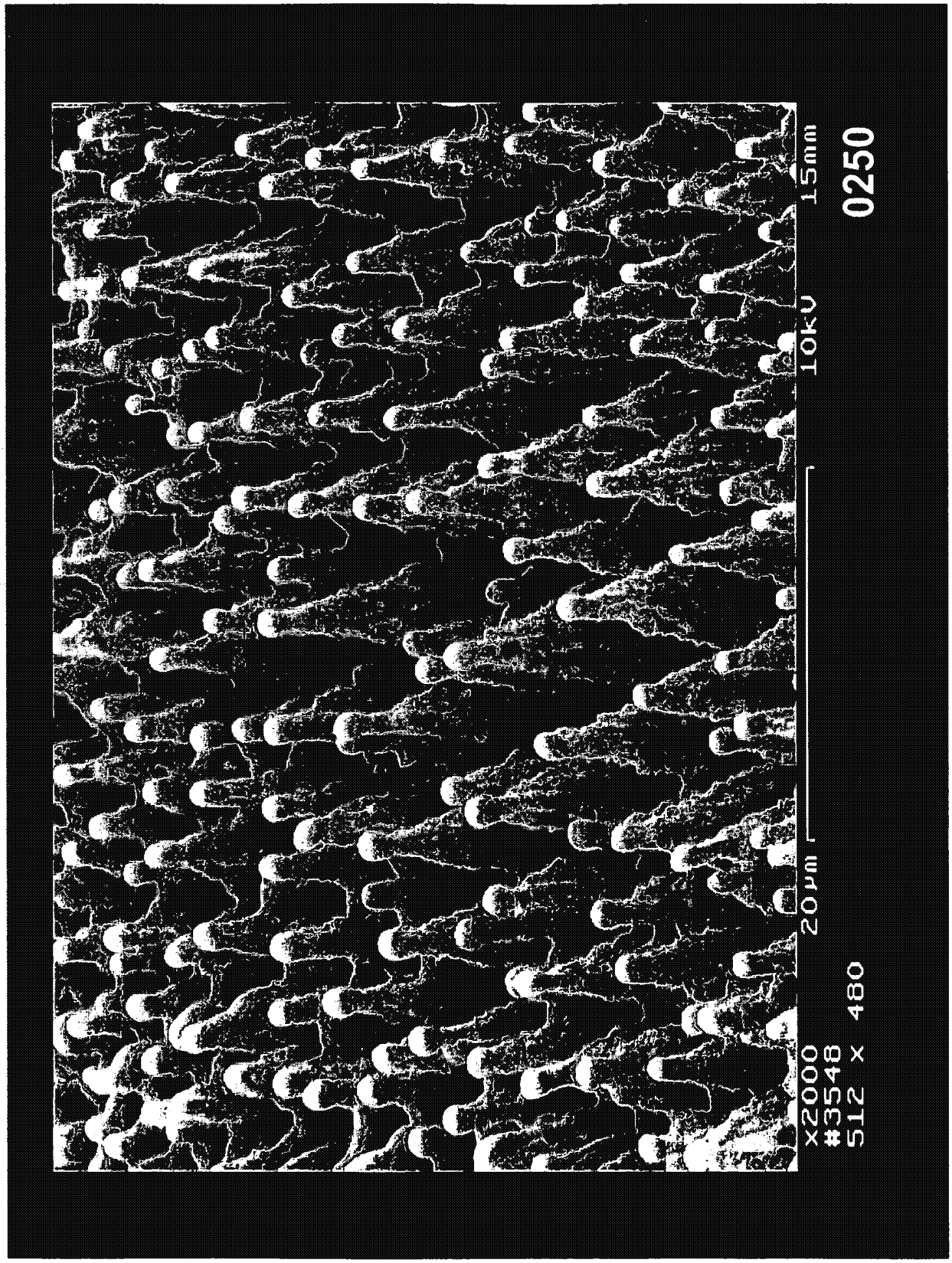
X2000
#3548
512 X 480
20μm
10kV
15mm
0250

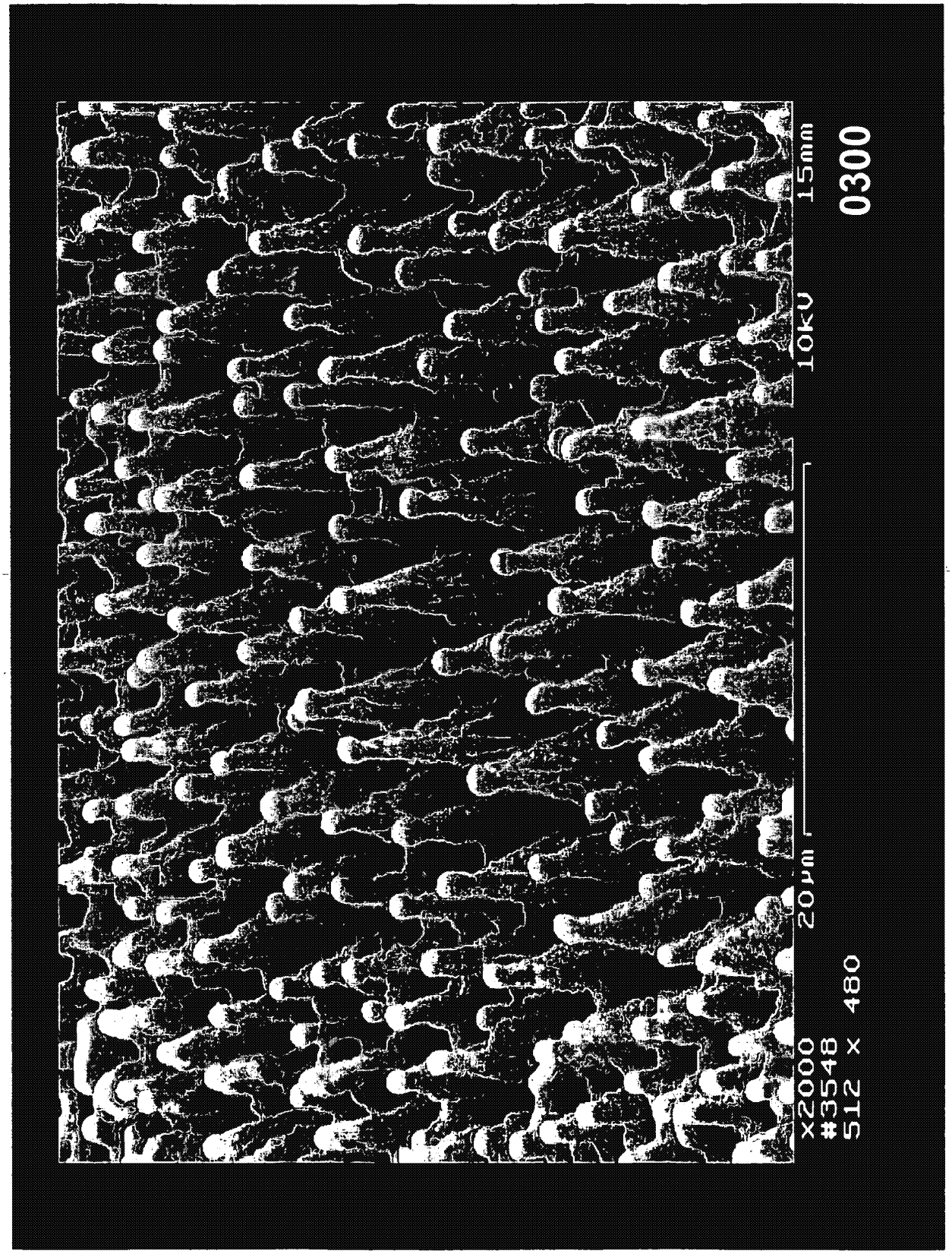
X2000
20 μm
#3548
512 X 480
10kV
15mm
0300

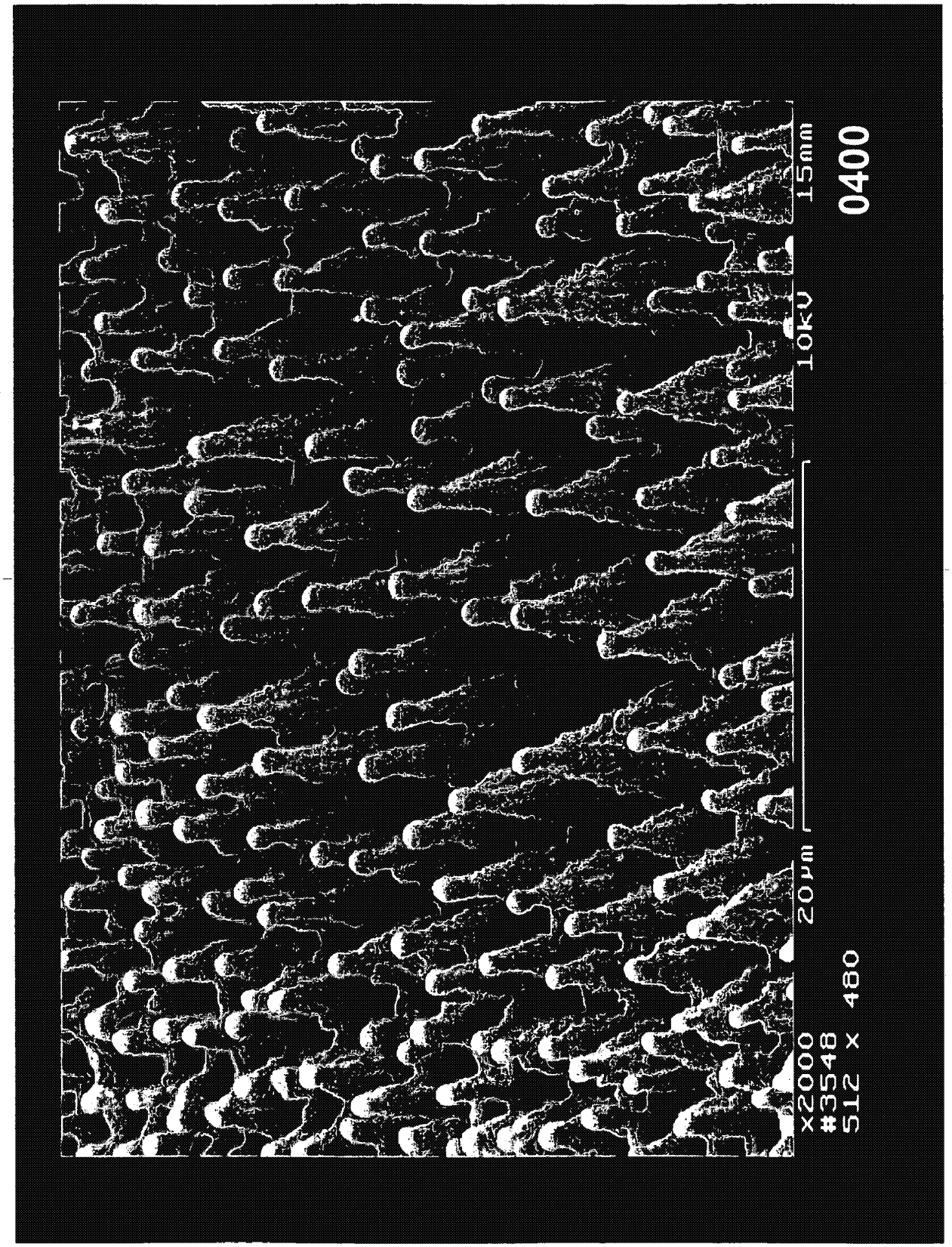
x2000
20μm
#3548
512 x 480
10kV
15mm
0400

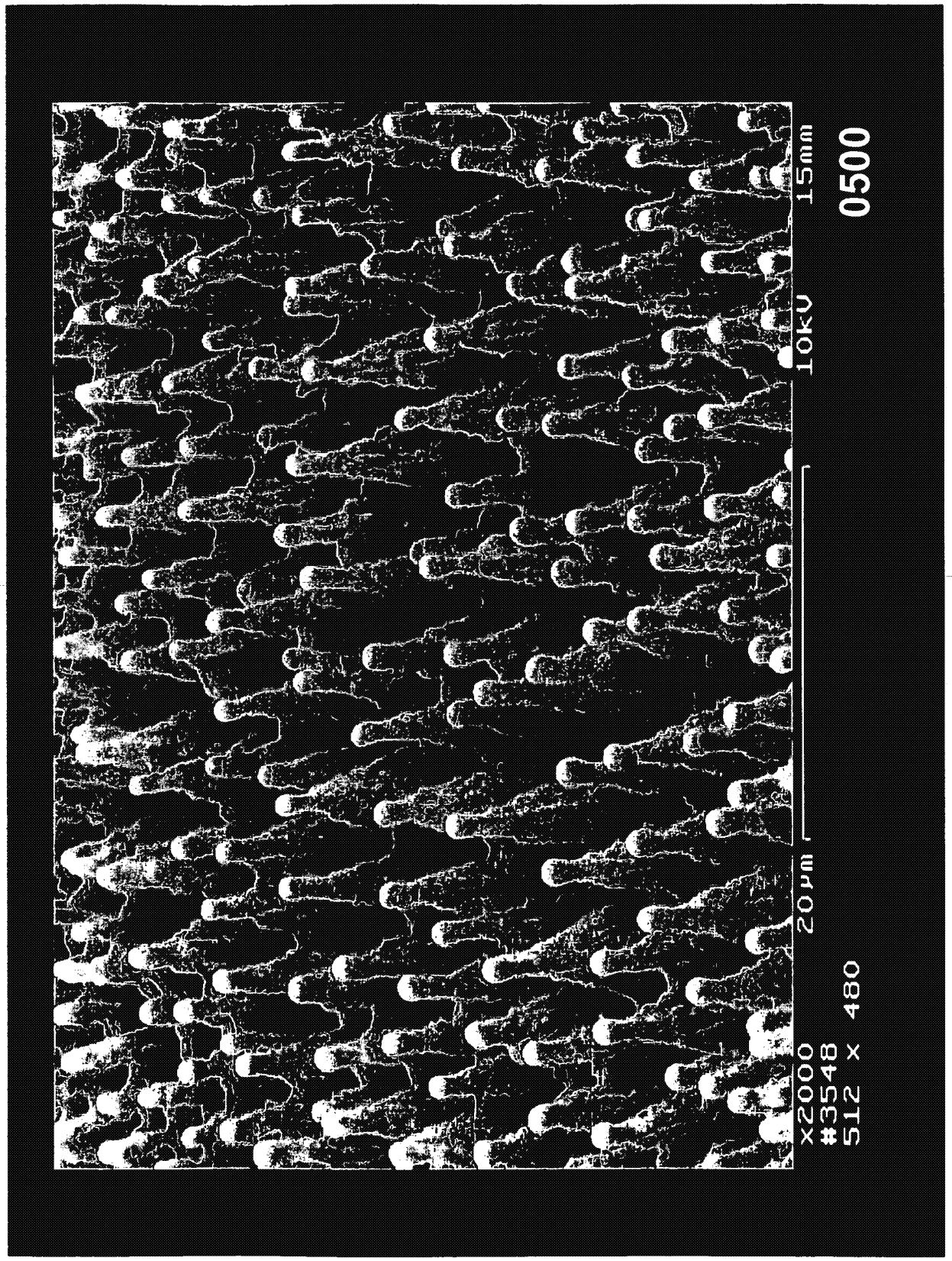
x2000
20μm
10kV
15mm
#3548
512 x 480
0500

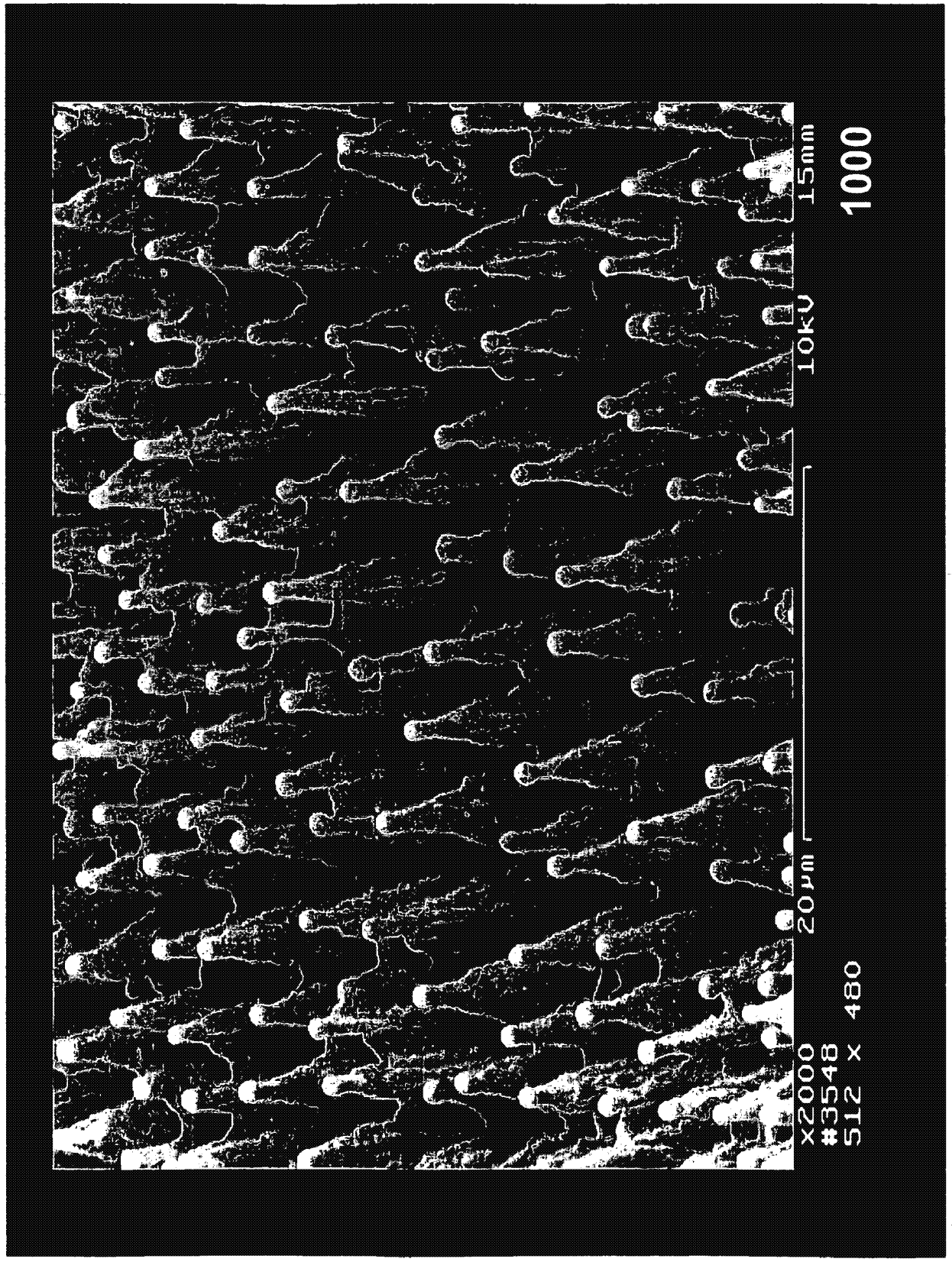
X2000
#3548
512 X 480
20μm
10kV
15mm
1000

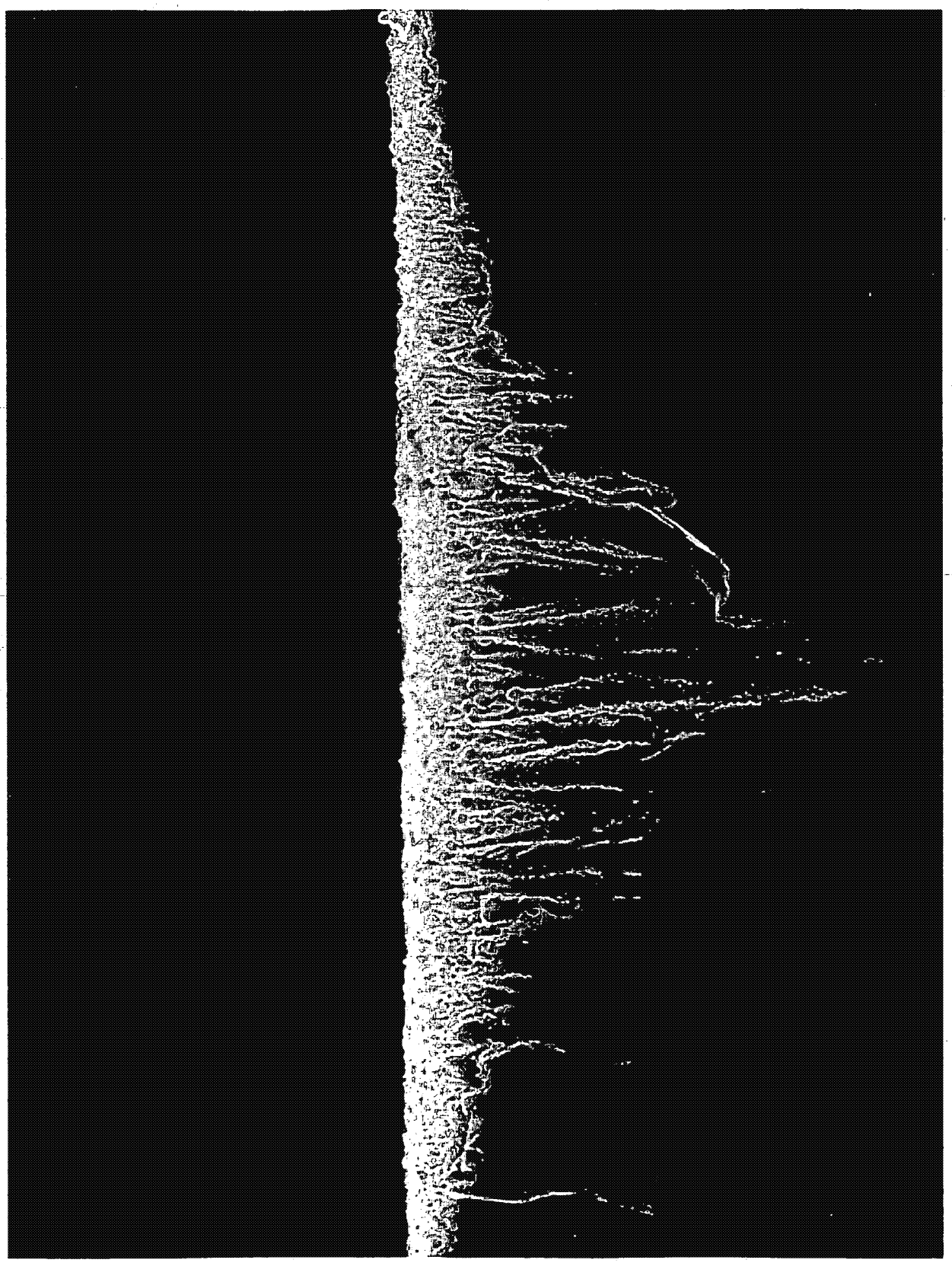

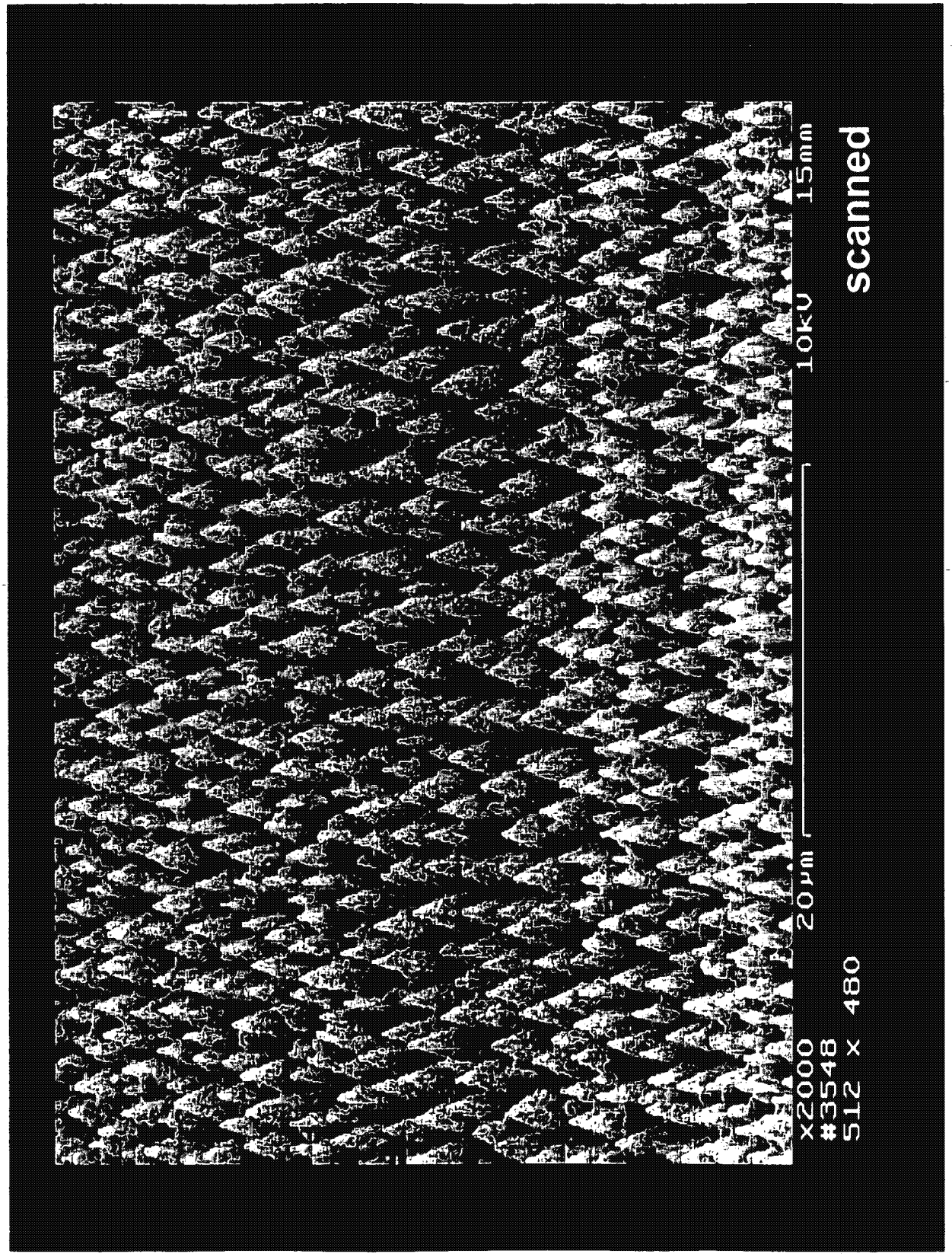
X2000
20μm
#3548
512 X 480
10kV
15mm
Scanned

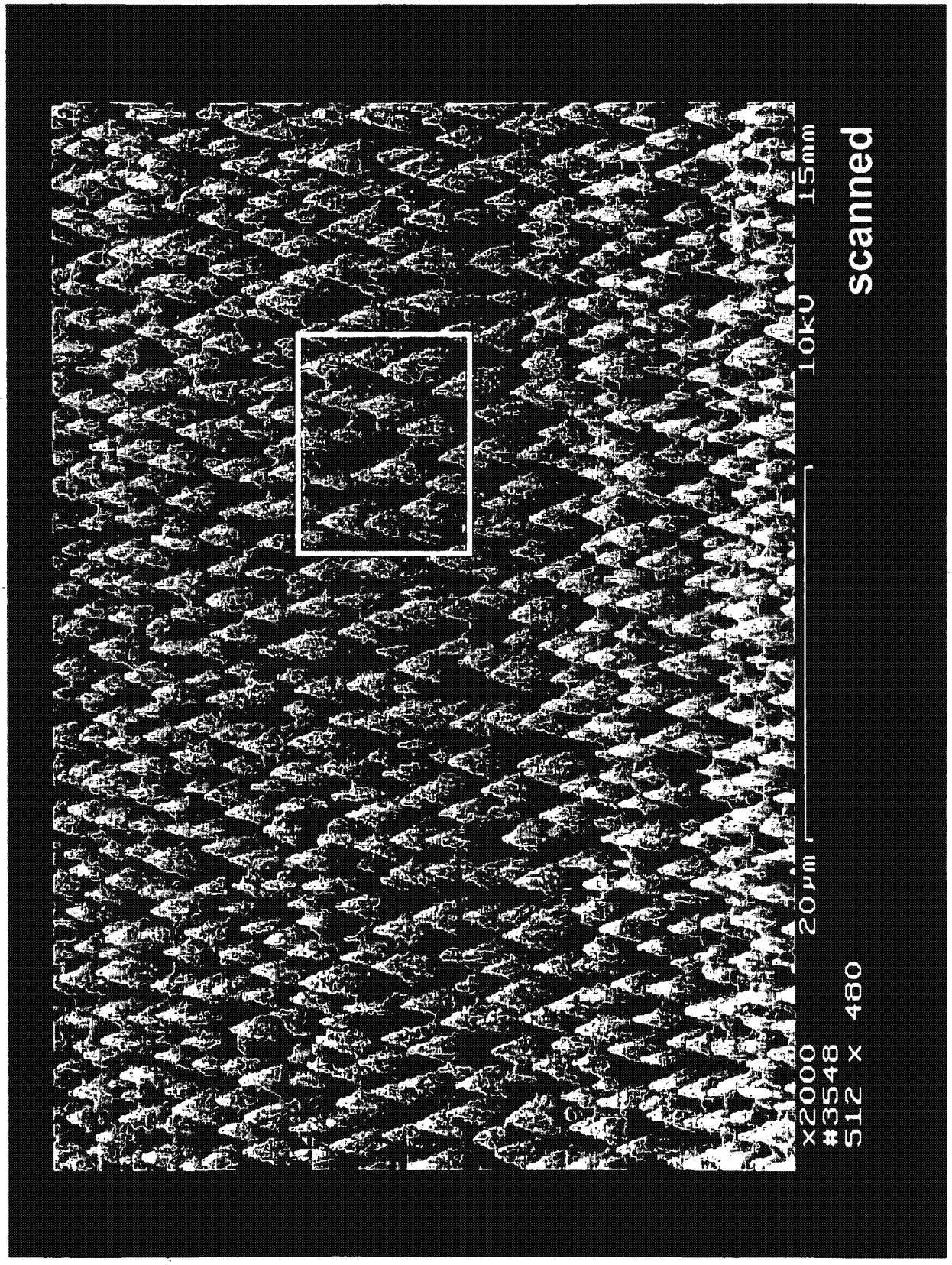
X2000
#3548
512 X 480
20μm
10kV
15mm
scanned

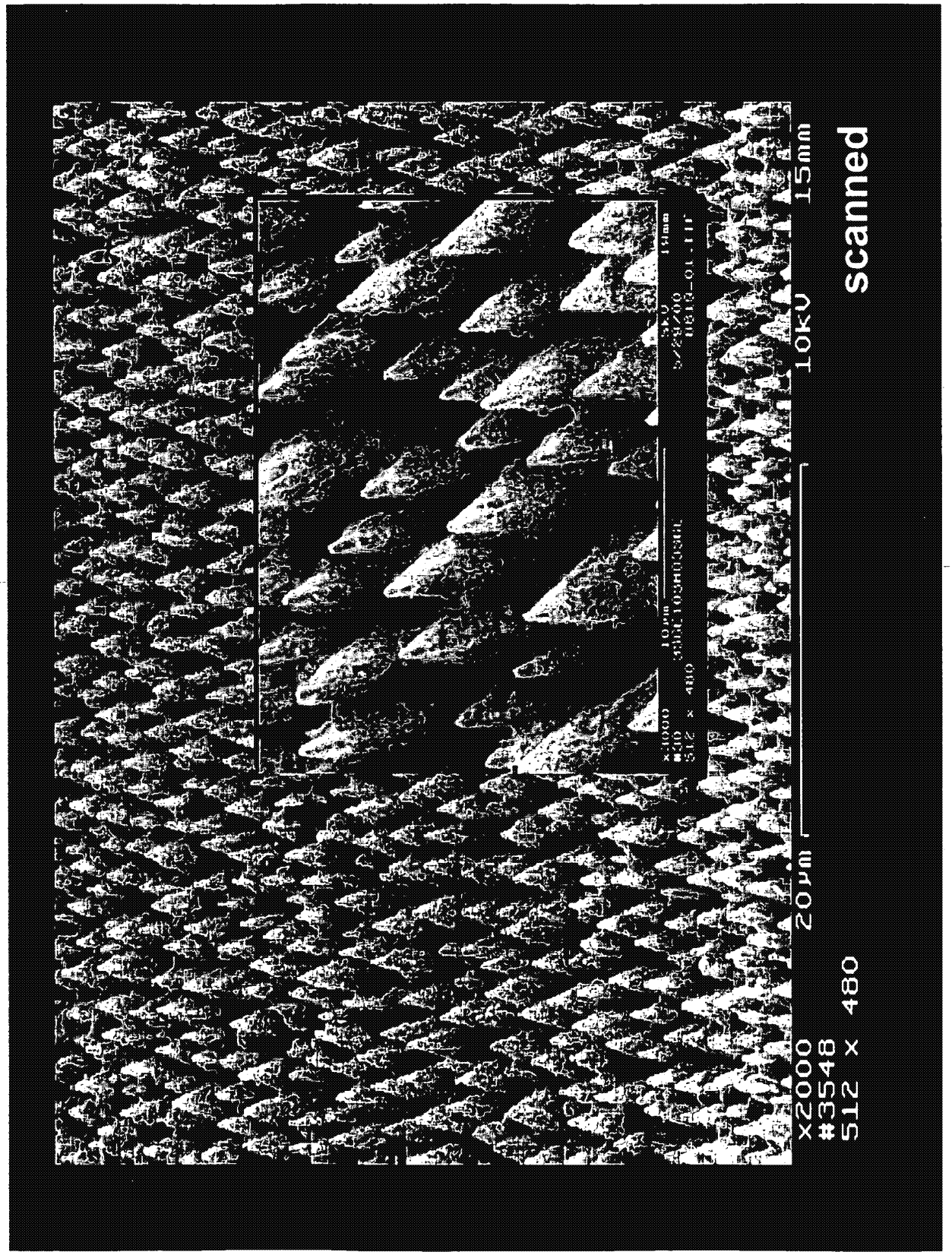
x2000
#3548
512 x 480
20μm
10kV
15mm
scanned

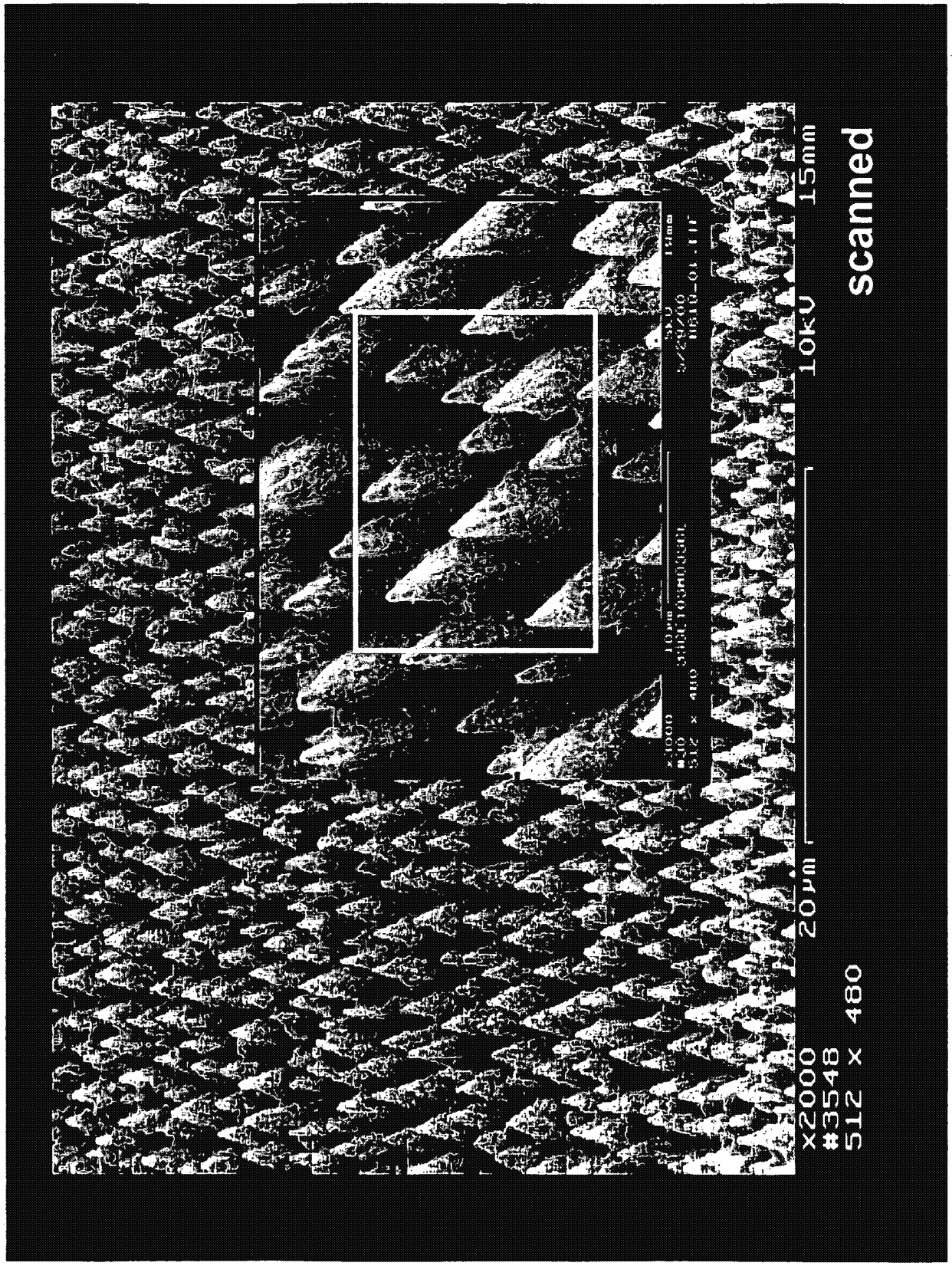
x2000
#3548
512 x 480
20μm
10kV
15mm
scanned

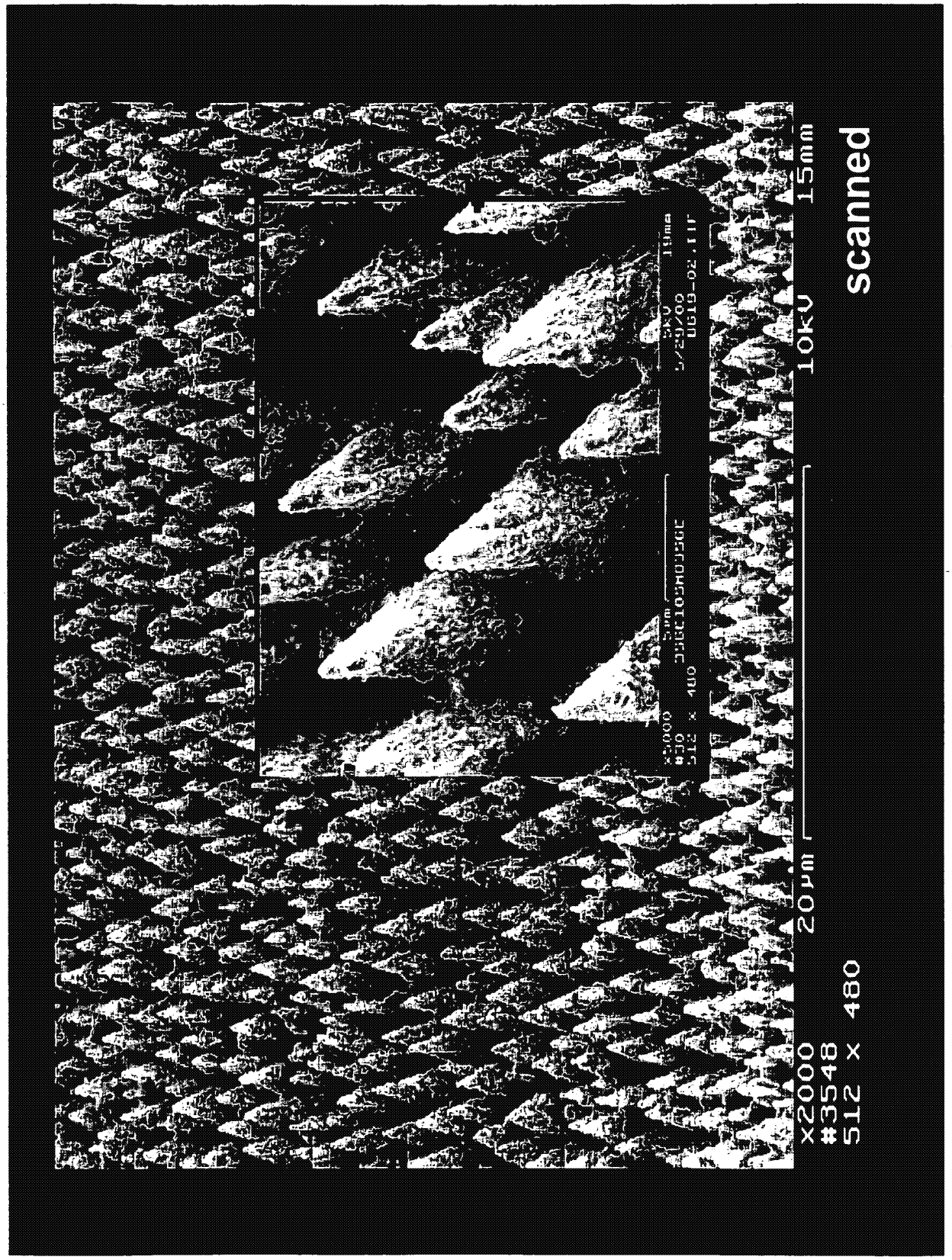
x2000
#3548
512 x 480
20μm
10kV
15mm
scanned

Background

absorptance

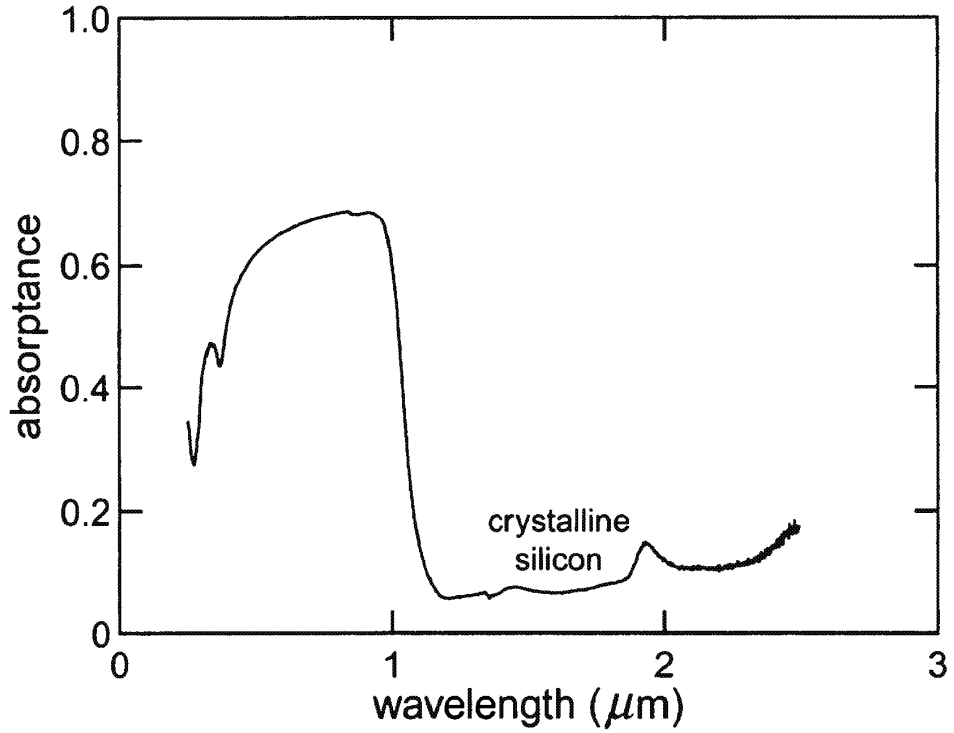

SIONYX1403000028.0014

SAMSUNG EX. 1002 - 2626/4148

Background

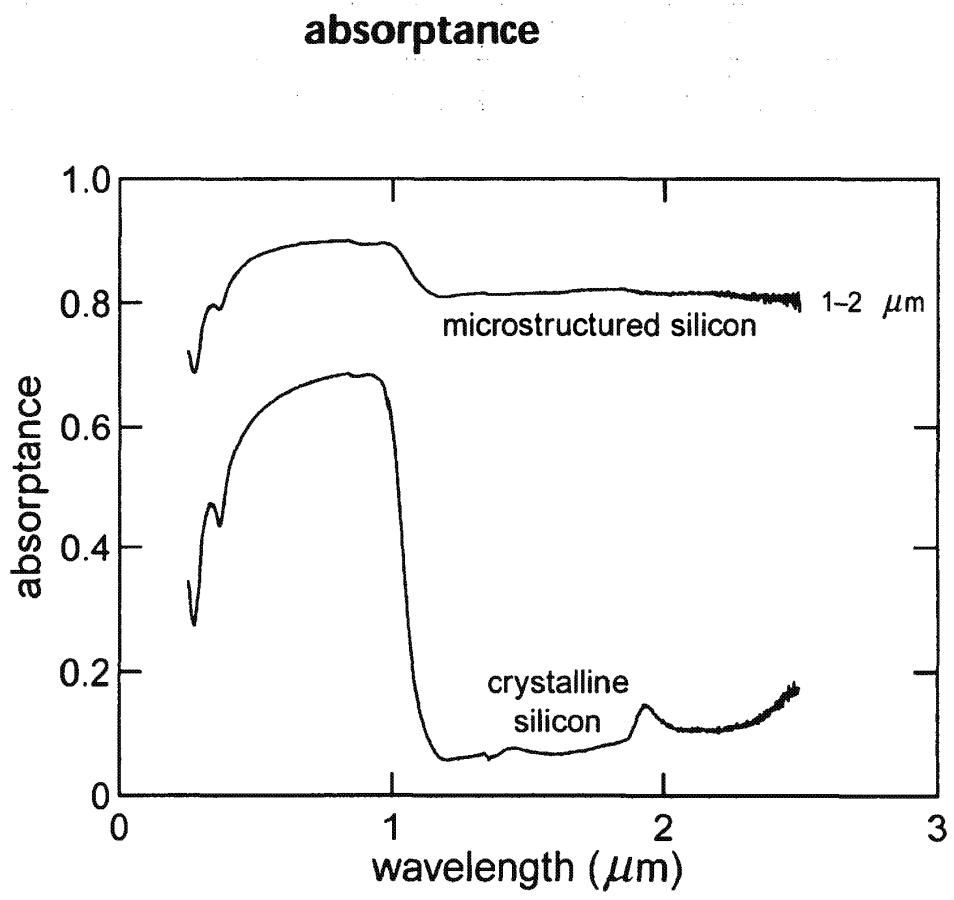

C. Wu, *et al.*, *Appl. Phys. Lett.* **78**, 1850 (2001)

SIONYX1403000028.0015
SAMSUNG EX. 1002 - 2627/4148

Background

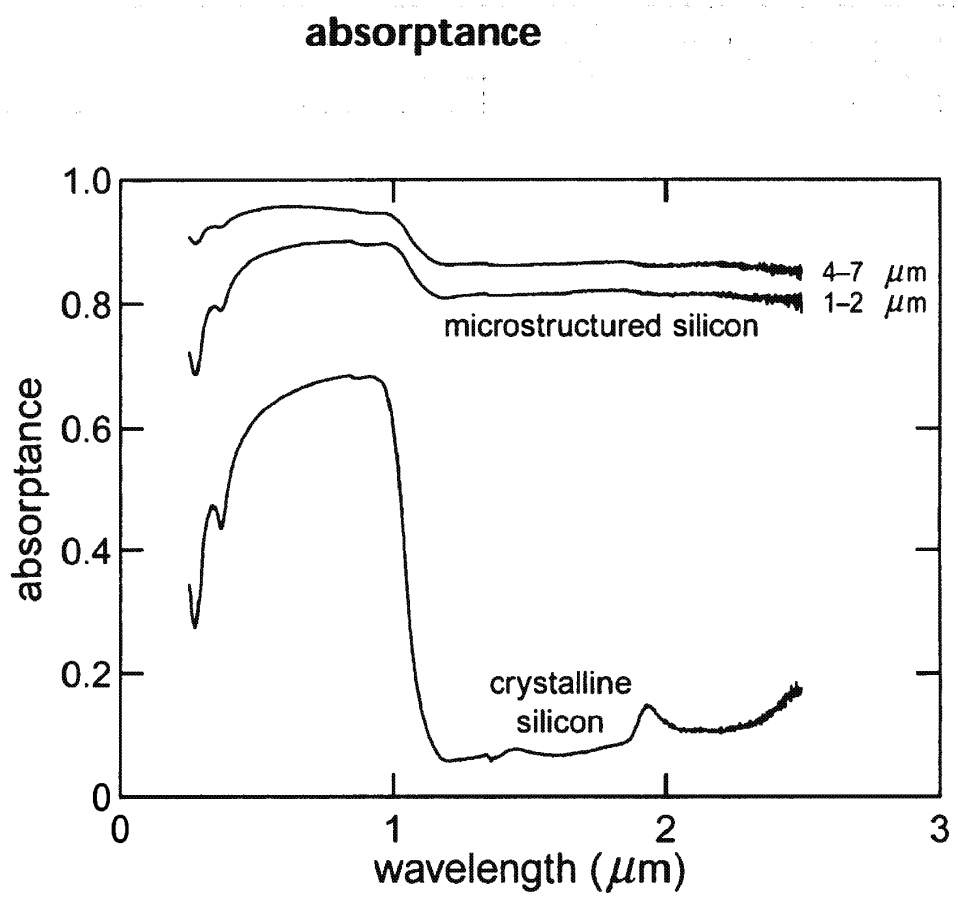

C. Wu, *et al.*, *Appl. Phys. Lett.* **78**, 1850 (2001)

SIONYX1403000028.0016
SAMSUNG EX. 1002 - 2628/4148

Background

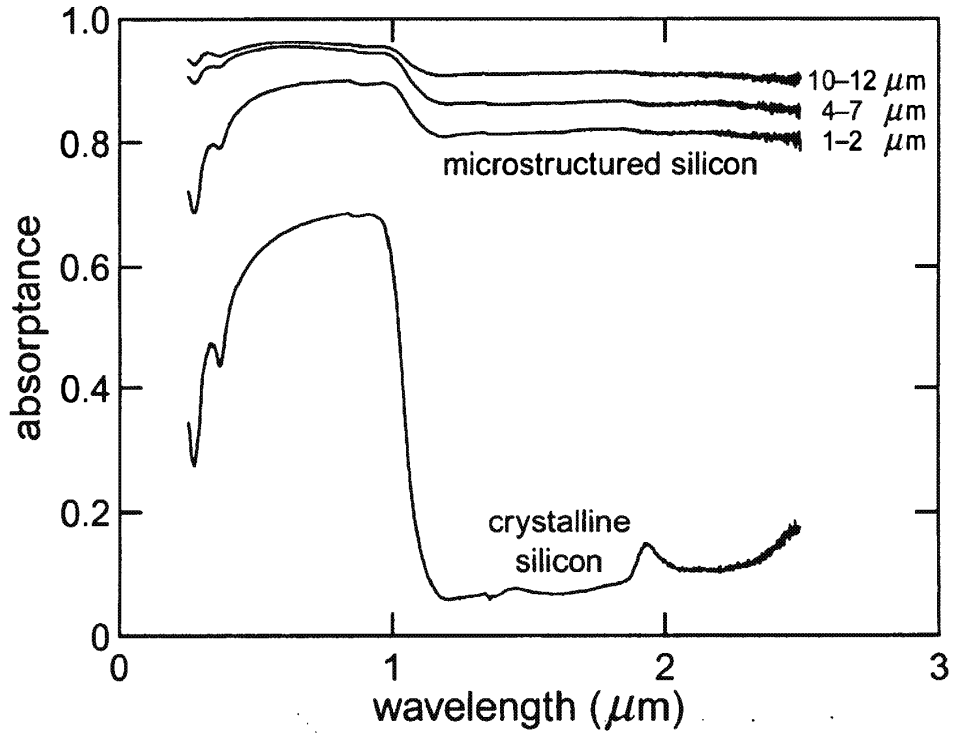

C. Wu, *et al.*, *Appl. Phys. Lett.* **78**, 1850 (2001)

SIONYX1403000028.0017
SAMSUNG EX. 1002 - 2629/4148

Background

Points to keep in mind:

- one-step, maskless process
- large area with uniform high density of spikes
- band structure change

Outline

- Background
- Results
- Discussion

Setup

Setup

gold coating

Setup

Setup

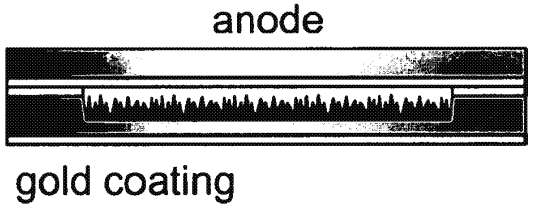

SAMSUNG EX. 1002 - 2635/4148

Setup

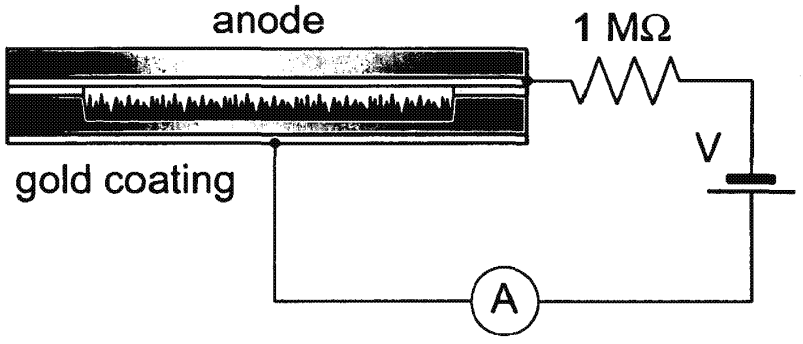

SAMSUNG EX. 1002 - 2636/4148

Results

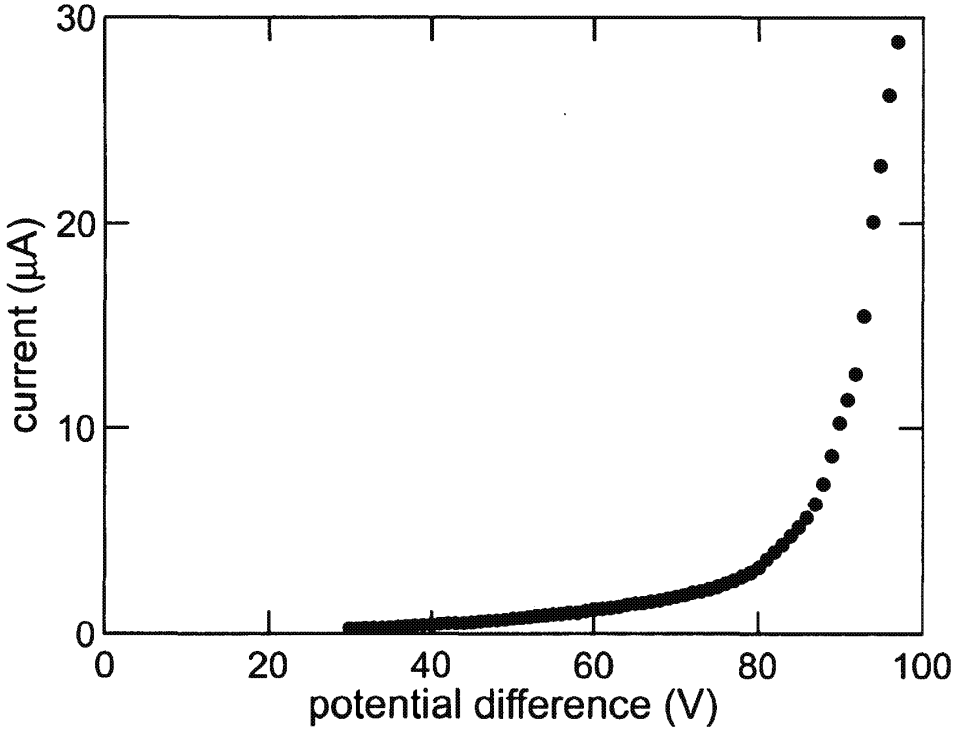

SAMSUNG EX. 1002 - 2637/4148

Results

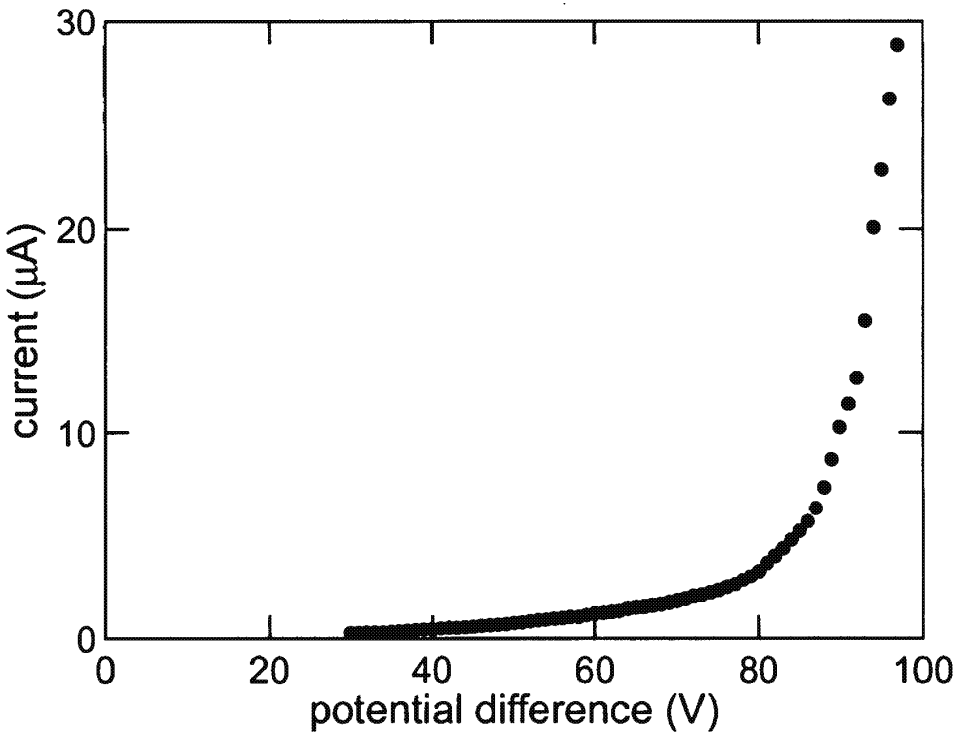

turn-on field (1 μA/cm^2): 1.2 V/μm

Results

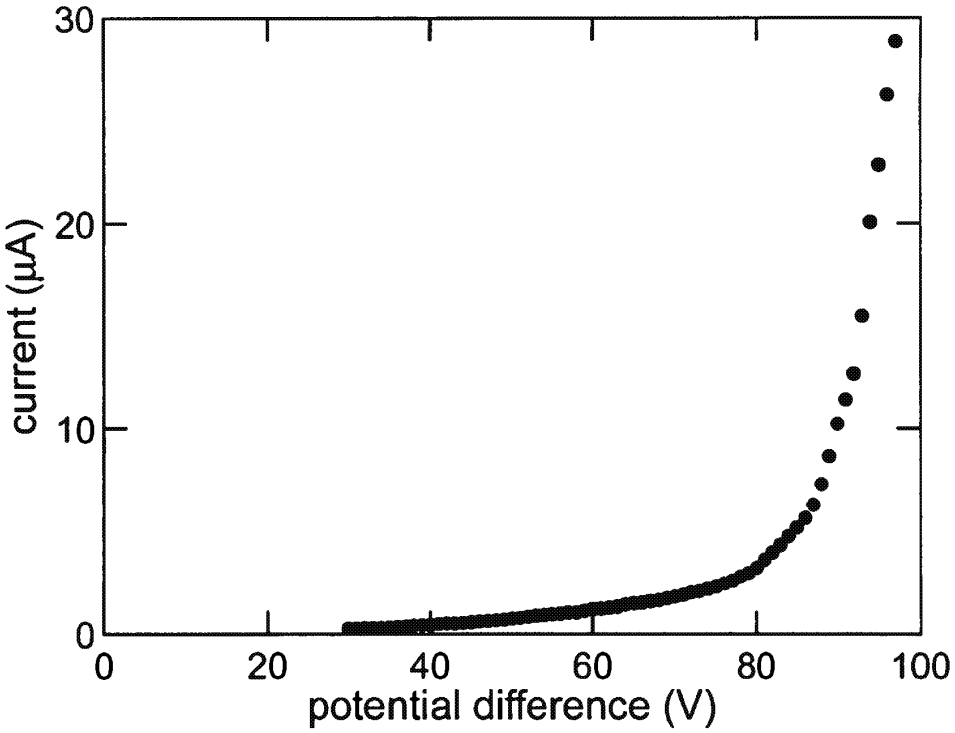

threshold field (10 μA/cm^2): 2.1 V/μm

SIONYX1403000028.0027

SAMSUNG EX. 1002 - 2639/4148

Results

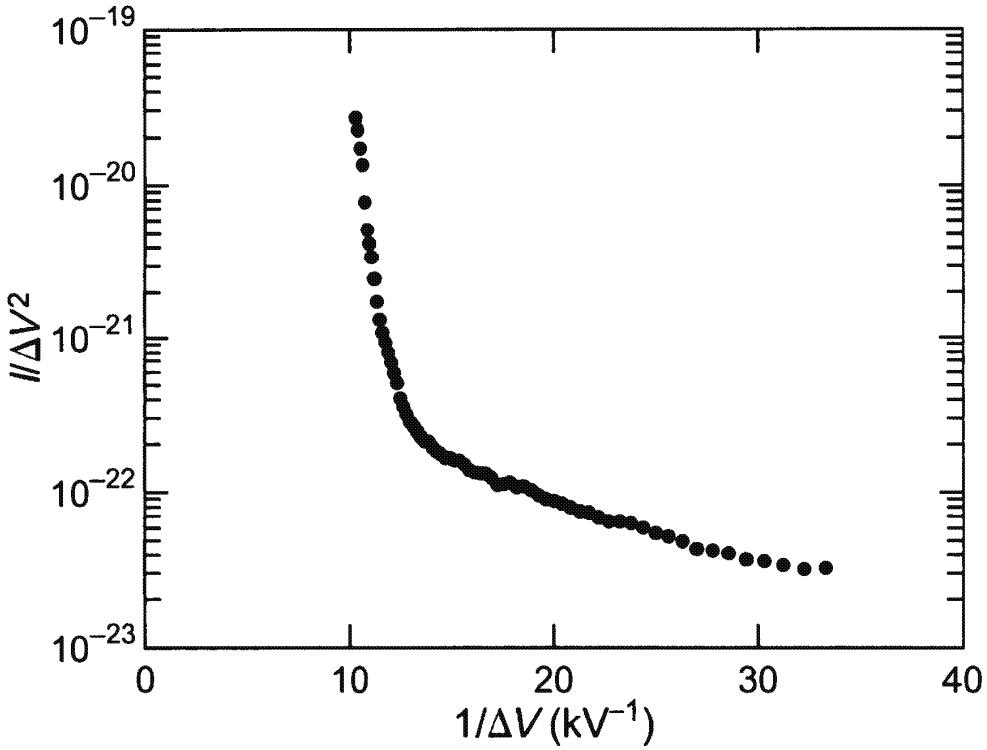

Results

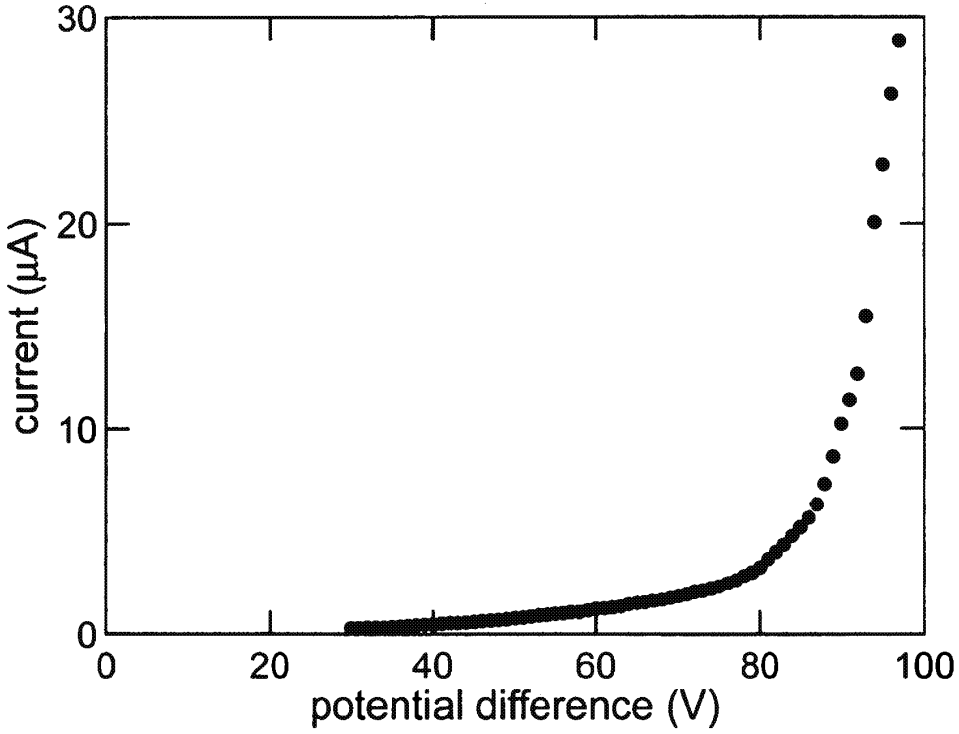

Results

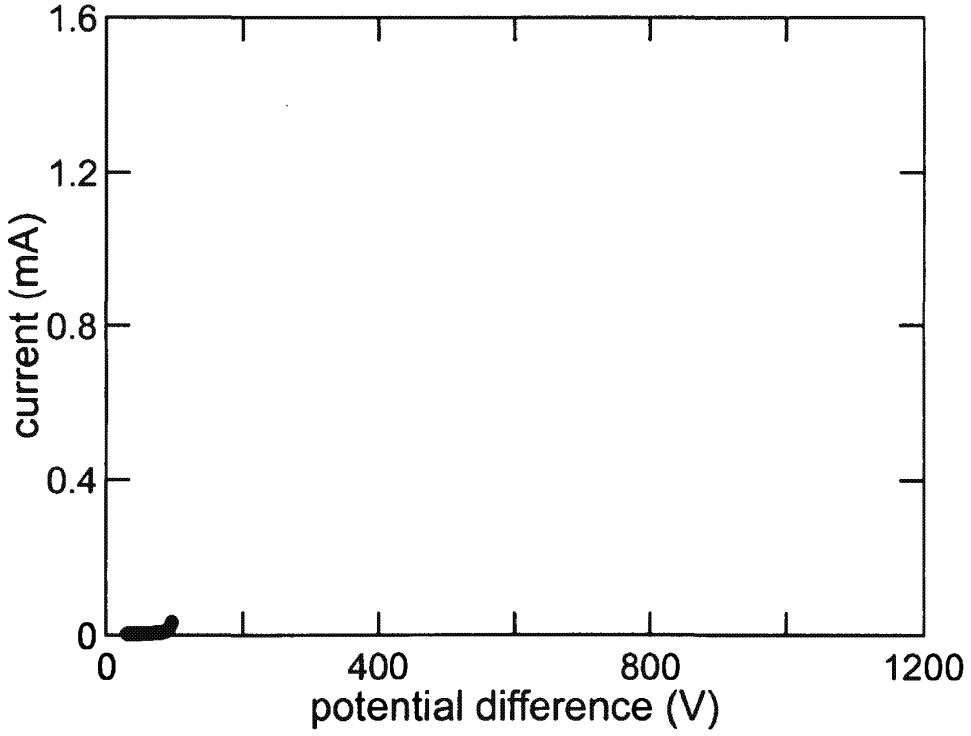

Results

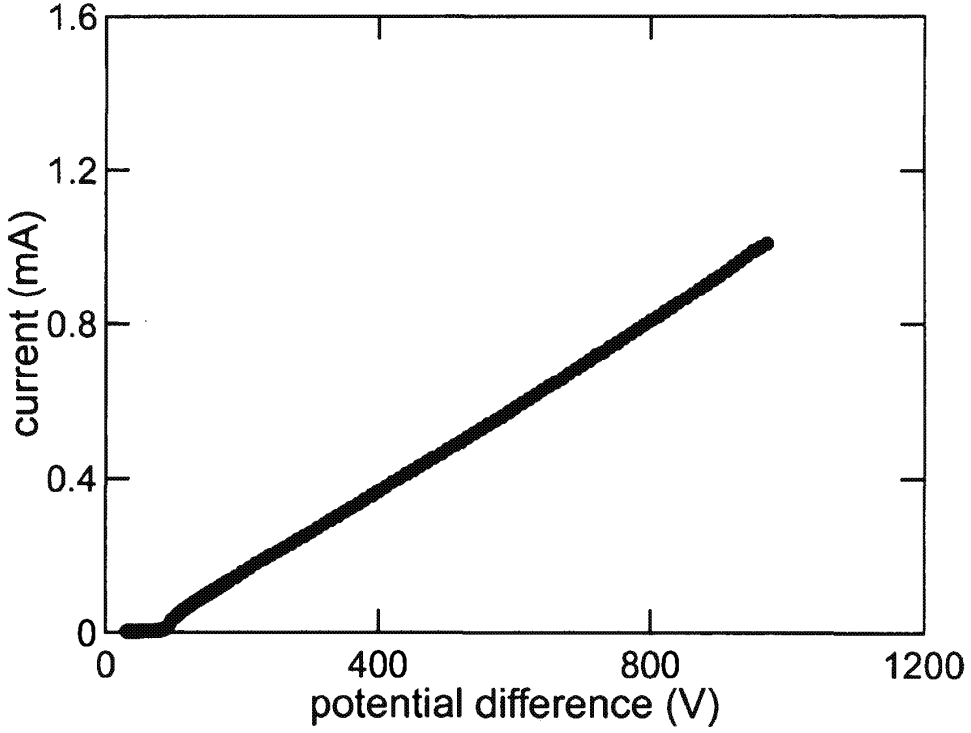

SAMSUNG EX. 1002 - 2643/4148

Results

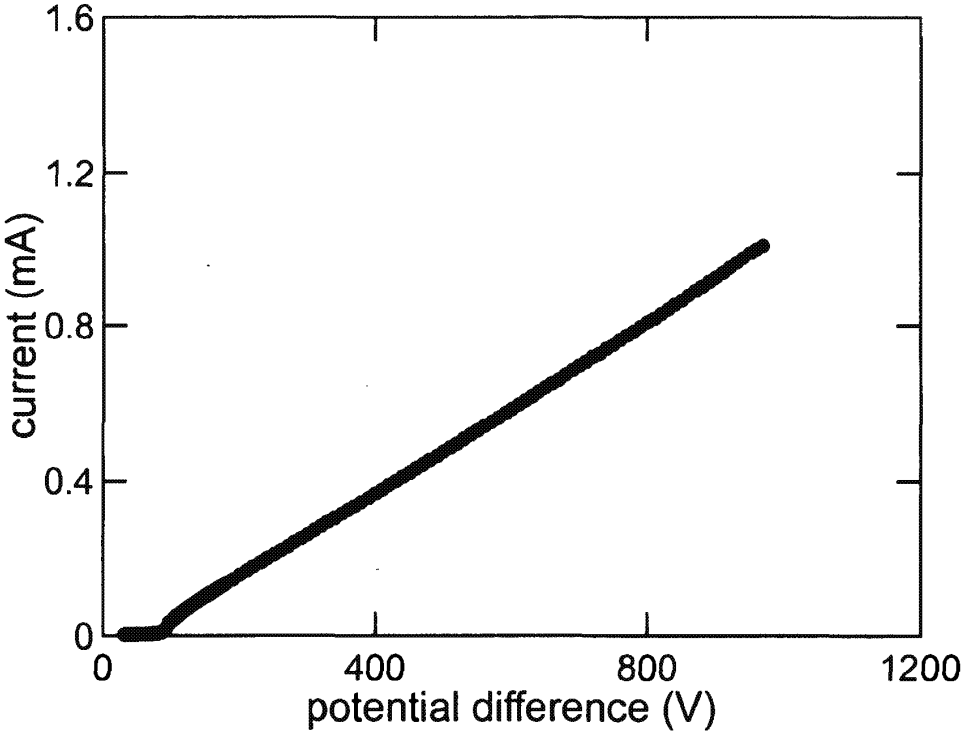

maximum current: 15 mA (4 mm^2 sample)

SIONYX1403000028.0032
SAMSUNG EX. 1002 - 2644/4148

Results

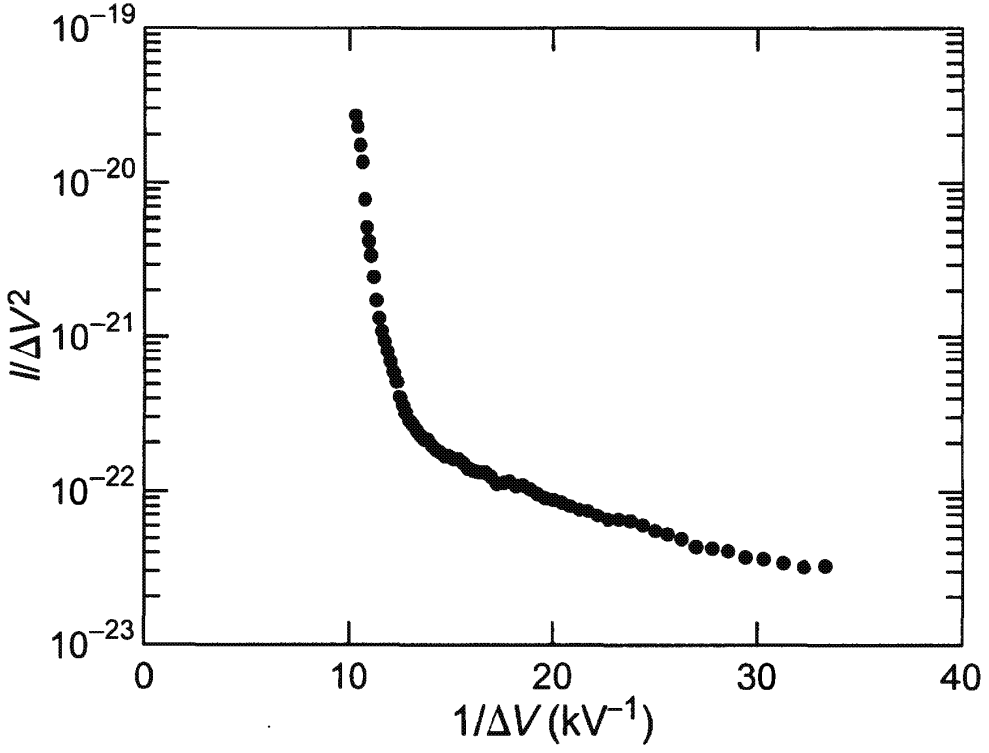

Results

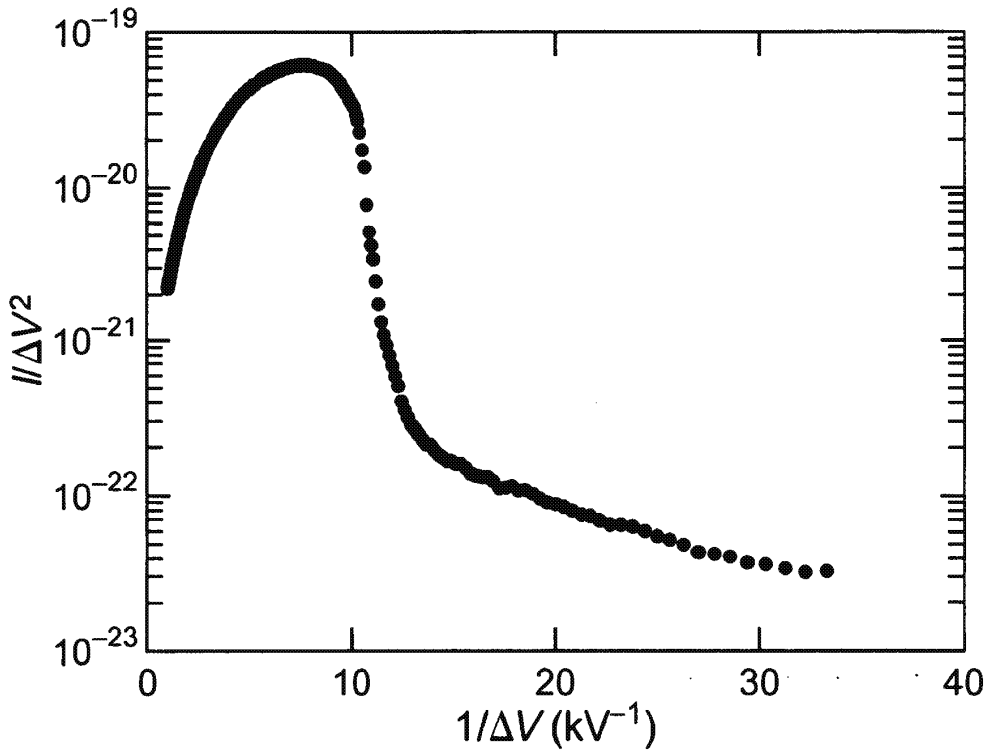

Outline

- Background
- Results
- Discussion

Discussion

Ion channeling and electron backscattering

- spikes retain crystalline order
- high density of defects

SAMSUNG EX. 1002 - 2648/4148

Discussion

Secondary ion mass spectrometry:

- 10^{20} cm^{-3} sulfur
- 10^{17} cm^{-3} fluorine

SAMSUNG EX. 1002 - 2649/4148

Discussion

VB

CB

Discussion

sulfur introduces states in the gap

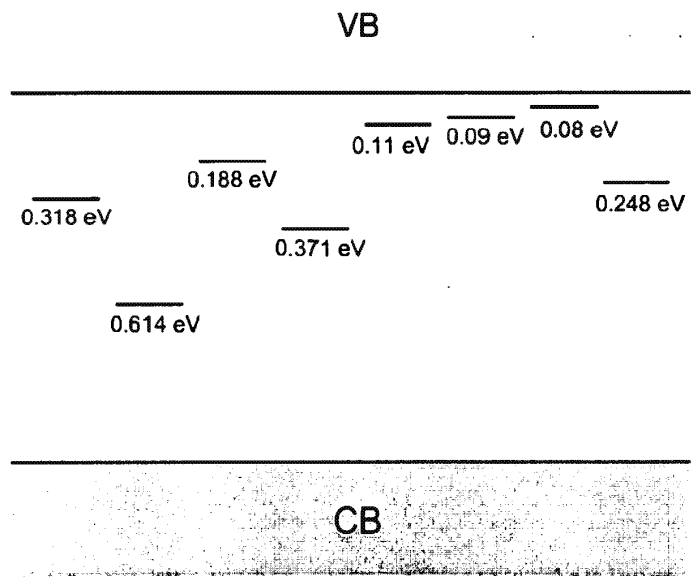

Janzén, *et al.*, *Phys. Rev. B* **29**,1907 (1984)

SIONYX1403000028.0039
SAMSUNG EX. 1002 - 2651/4148

Discussion

states broaden into a band

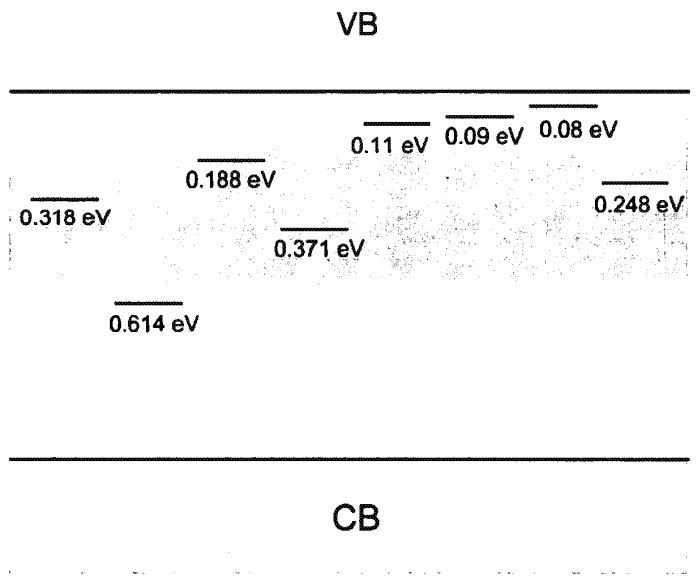

SIONYX1403000028.0040
SAMSUNG EX. 1002 - 2652/4148

Field emission

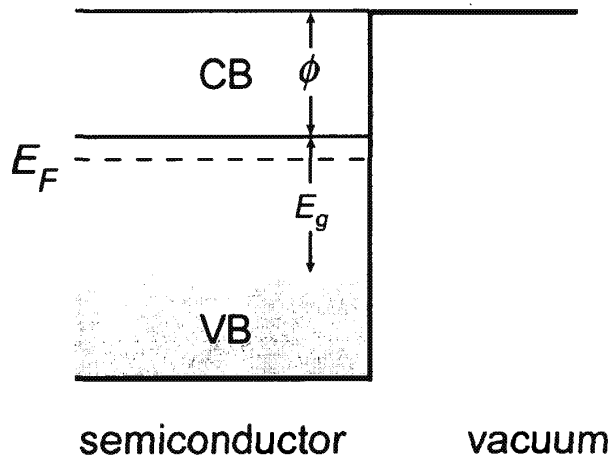

SIONYX1403000028.0041
SAMSUNG EX. 1002 - 2653/4148

Field emission

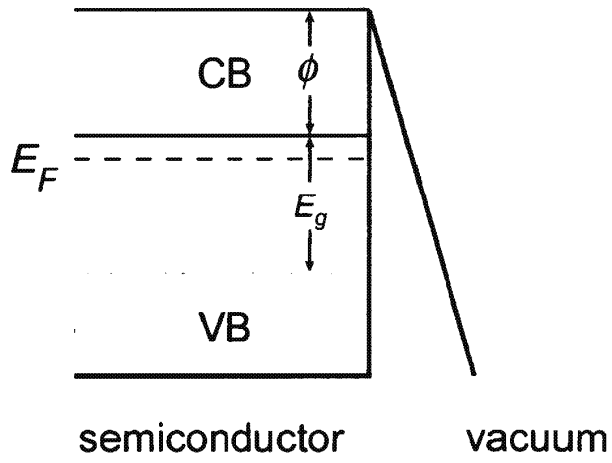

SIONYX1403000028.0042
SAMSUNG EX. 1002 - 2654/4148

Field emission

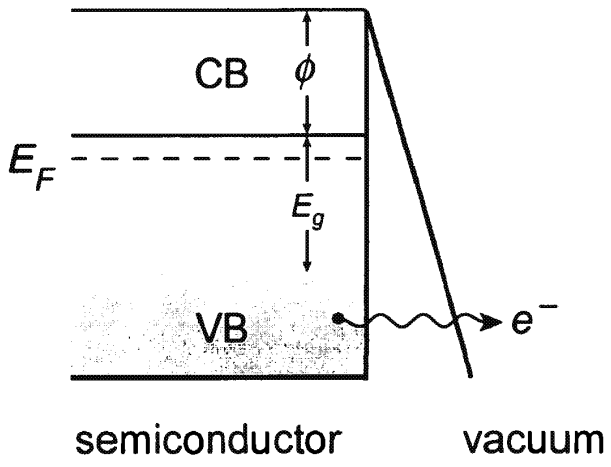

SIONYX1403000028.0043
SAMSUNG EX. 1002 - 2655/4148

Field emission

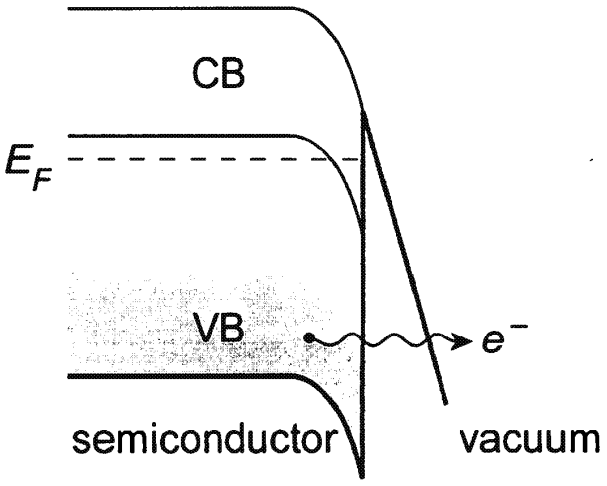

SIONYX1403000028.0044
SAMSUNG EX. 1002 - 2656/4148

Discussion

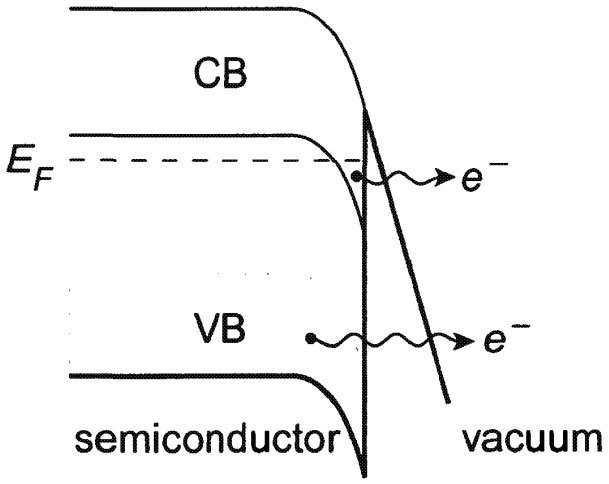

Discussion

sulfur band provides additional electrons

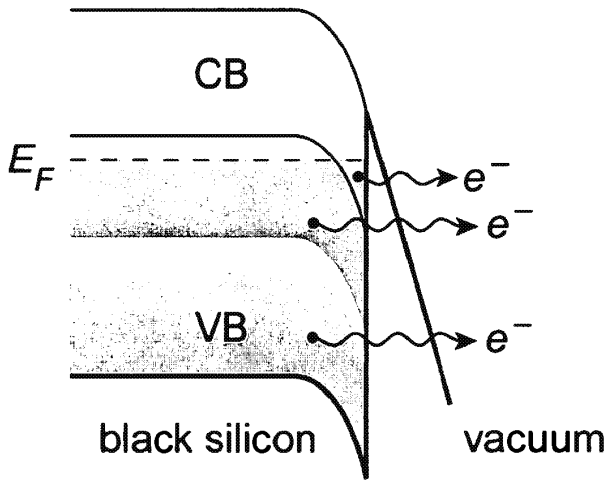

SAMSUNG EX. 1002 - 2658/4148

Summary

Microstructured silicon

- fabricated by simple, maskless process

Summary

Microstructured silicon

- fabricated by simple, maskless process
- can be integrated with microelectronics

SAMSUNG EX. 1002 - 2660/4148

Summary

Microstructured silicon

- fabricated by simple, maskless process
- can be integrated with microelectronics
- provides stable, high field-emission current

Summary

Microstructured silicon

- fabricated by simple, maskless process
- can be integrated with microelectronics
- provides stable, high field-emission current
- is durable

SIONYX1403000028.0050

SAMSUNG EX. 1002 - 2662/4148

Future Directions

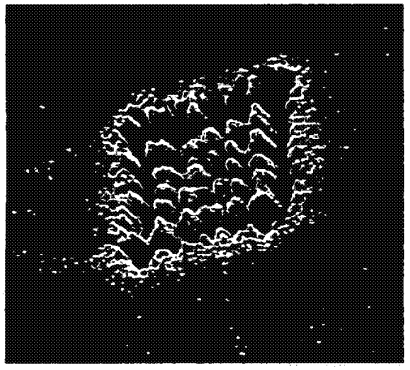

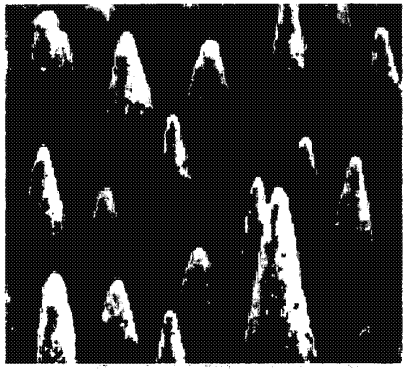

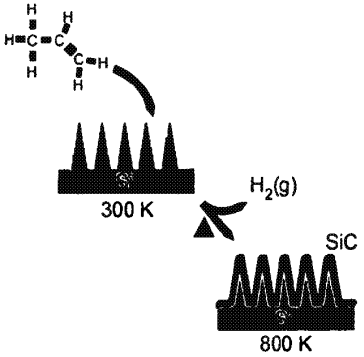

- Ordered arrays
- Other gases
- Functionalizing
- Emission mechanism

SIONYX1403000028.0051
SAMSUNG EX. 1002 - 2663/4148

Acknowledgements

Rebecca Younkin, Mike Sheehy, Catherine Crouch, Josh Levinson, and the Mazur group

Li Zhao, Fudan University, Shanghai, China

funding: ARO, NSF, NDSEG

http://mazur-www.harvard.edu

SIONYX1403000028.0052

SAMSUNG EX. 1002 - 2664/4148

C3

Femtosecond Laser-Assisted Microstructuring of Silicon for Novel Detector, Sensing and Display Technologies

James E. Carey and Eric Mazur
Harvard University, Department of Engineering and Applied Physics, 29 Oxford Street, Cambridge, MA 02138, Tel: +1 617-495-8729, Fax: +1 617-255-4622,
email: mazur@physics.harvard.edu

Arrays of sharp, conical microstructures are obtained by texturing the surface of a silicon wafer using femtosecond laser-assisted chemical etching. The one step, maskless texturing process drastically changes the optical, material and electronic properties of the original silicon wafer. These properties make microstructured silicon viable for use in a wide range of commercial devices including solar cells, infrared photodetectors, chemical and biological sensors, and field emission devices.

Previously, our group reported the formation of sharp, micrometer-sized conical structures in quasiordered arrays after irradiating a silicon surface with hundreds of femtosecond-laser pulses in an atmosphere of sulfur hexaflourite (SF_6) [1,2]. We irradiate a Si(111) surface with a 1-kHz train of 800 nm, 100 fs laser pulses in the presence of SF_6. The result of this irradiation is a quasi-ordered array of conical microstructures that form spontaneously, without the use of masks. Figure 1 shows a scanning electron micrograph of the microstuctured silicon surface at an angle of 45 degrees.

In addition to leaving the surface morphology altered, the irradiated region appears black to the eye unlike the silver mirror-like appearance of a flat wafer. The textured surface exhibits near-unity absorption of light from visible to infrared wavelengths [3]. Figure 2 shows the absorption versus wavelength for the textured silicon and a flat piece of silicon for the wavelength range of 250 nm to 2500 nm. This near-unity absorption offers opportunities for use in optically active devices such as solar cells and detectors. We have also demonstrated significant enhancement of below-band-gap photocurrent generation in textured avalanche photodiodes, as well as a 20 percent increase in the quantum efficiency of the avalanche photodiodes at 1064 nm. This enhancement could dramatically widen the wavelength sensitivity range of silicon photodetectors by making the infrared region above 1 μm detectable.

In addition to use in optical devices, we observed remarkable field emission characteristics have been measured. The rapidly growing field of field emission devices requires unique emitting materials that are robust, easily fabricated, and that have favorable emission characteristics. Figure 3 shows an I-V measurment for a 2 mm^2 area of textured silicon. The low turn-on fields and high current yields make the textured silicon ideal for use in field emission displays, ion thruster propulsion, and microwave amplification. Lastly, chemical functionalization of the increased surface area indicate great potential of the textured silicon for novel chemical and biological sensing applications.

This talk will cover the unique optical and electronic properties of microstructured silicon, discuss the formation process of the conical microstructures, and review the chemical and structural make-up of the surface that are responsible for the novel optoelectronic properties. We

will also discuss future directions for this technique including structuring of new materials, incorporation of new ambient gases, and better control over the position and density of the microstructures themselves (Figure 4).

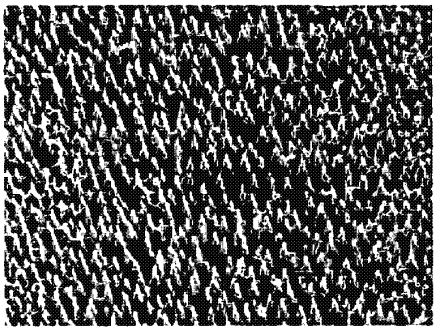

Figure 1: A scanning electron micrograph of silicon microstructures taken at a 45° angle and 3000x magnification.

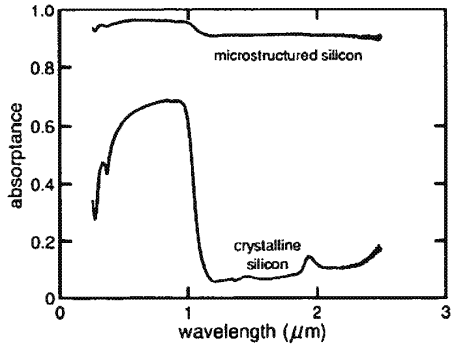

Figure 2: Absorptance vs. wavelength for crystalline and microstructured silicon.

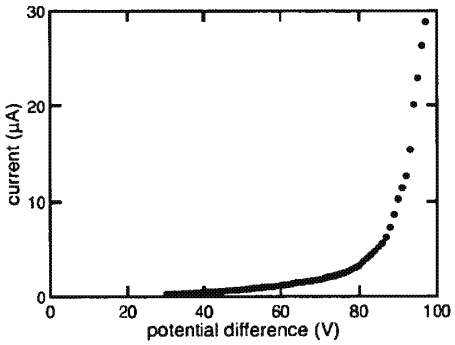

Figure 3: I-V curve for field emission from a 2-mm^2 surface of microstructured silicon. The anode-cathode used was 25 μm.

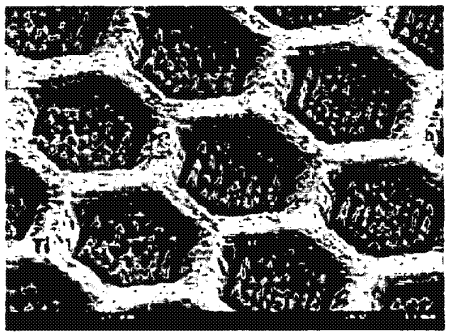

Figure 4: A scanning electron micrograph of structures made on Titanium using a spatial mask to control the organization of the structures.

[1] T.H. Her, R.J. Finlay, C. Wu, S. Deliwala, and E. Mazur, *Appl. Phys. Lett.* **73**, 1673-1675 (1998)

[2] T.H. Her, R.J. Finlay, C. Wu., and E. Mazur, *Appl. Phys. A* **70**, 383-385 (2000)

[3] C. Wu, C.H. Crouch, L. Zhao, J.E. Carey, R. Younkin, J.A. Lenvinson, R.M. Farrell, P. Gothoskar, A. Karger, and E. Mazur *Appl. Phys. Lett.* **78**, 1850-1852 (2001).

Femtosecond laser-assisted microstructuring of silicon for novel detector, sensing, and display technologies

Eric Mazur
Jim Carey
Mikey Sheehy
Catherine Crouch
Meng Yan Shen
Harvard University

LEOS 2002
Glasgow, UK, 11 November 2002

SIONYX1403000028.0055
SAMSUNG EX. 1002 - 2667/4148

Introduction

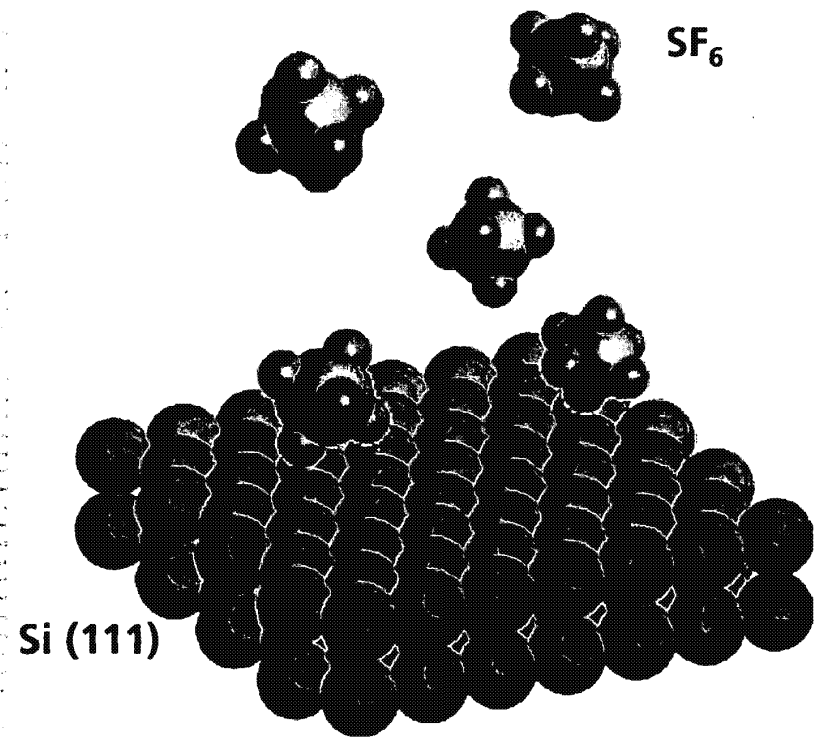

irradiate with 100-fs 10 kJ/m^2 pulses

Introduction

5 mm

"black silicon"

Introduction

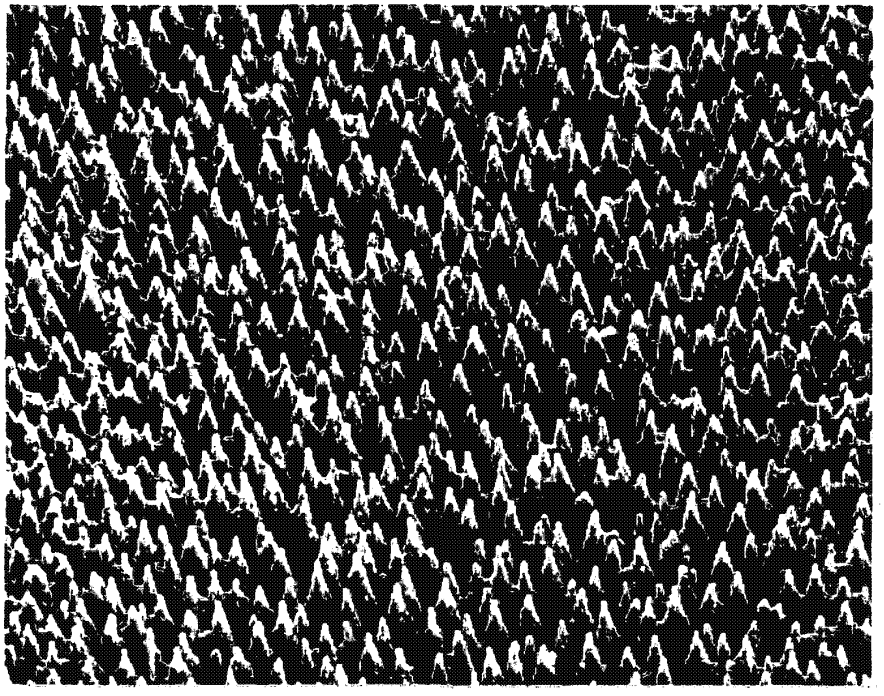

20 µm

Introduction
3 µm

Introduction

Introduction

Introduction

SAMSUNG EX. 1002 - 2674/4148

Introduction

- maskless etching process
- self-organized, tall, sharp structures
- nanoscale structure on spikes

Outline

- Properties
- Structural and chemical analysis
- Outlook

SAMSUNG EX. 1002 - 2676/4148

Properties

reflectance (integrating sphere)

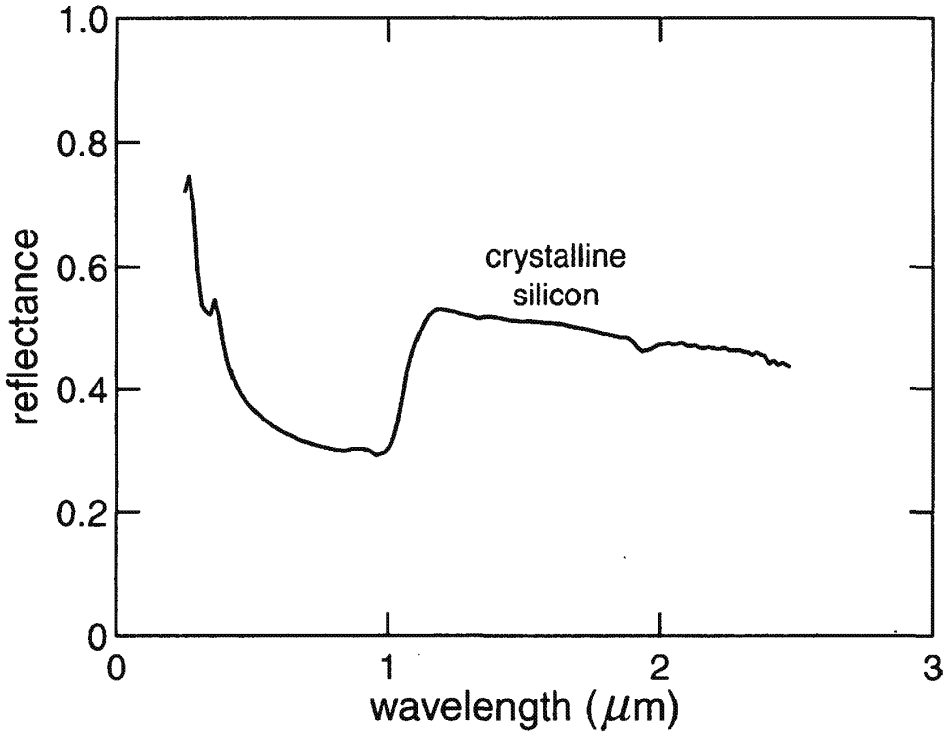

SIONYX1403000028.0065
SAMSUNG EX. 1002 - 2677/4148

Properties

reflectance (integrating sphere)

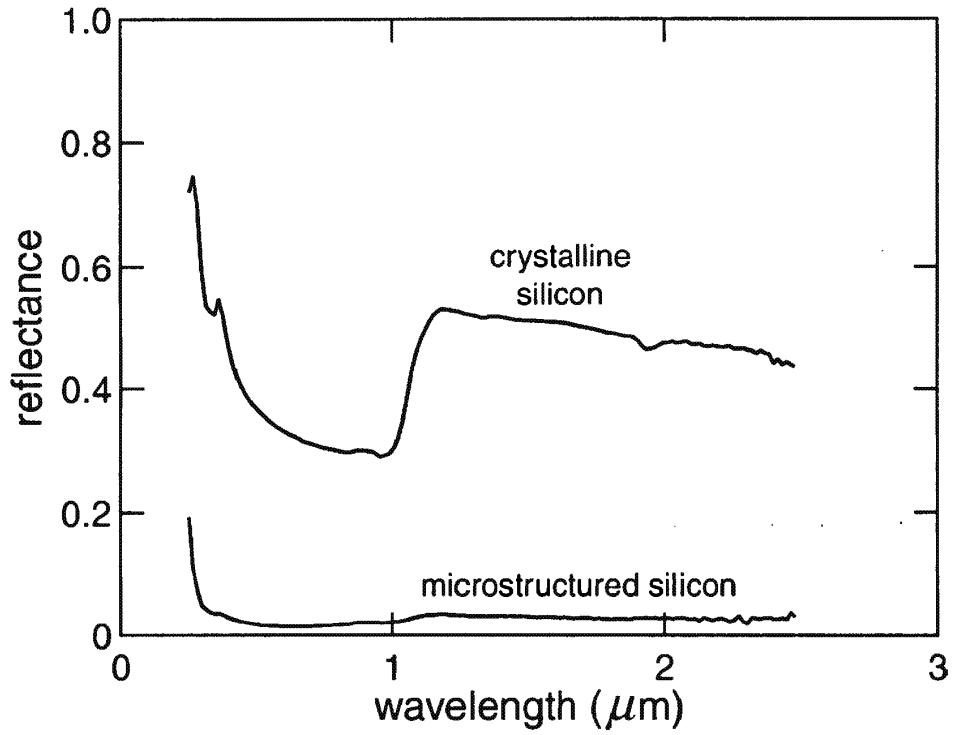

SIONYX1403000028.0066

SAMSUNG EX. 1002 - 2678/4148

Properties

transmittance (integrating sphere)

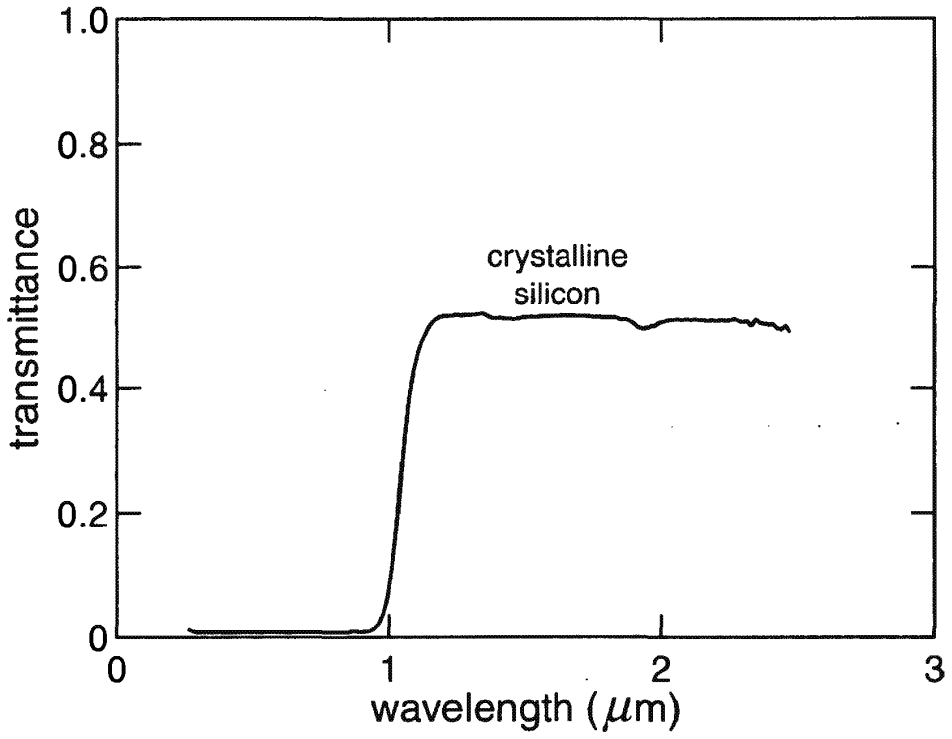

SIONYX1403000028.0067

SAMSUNG EX. 1002 - 2679/4148

Properties

transmittance (integrating sphere)

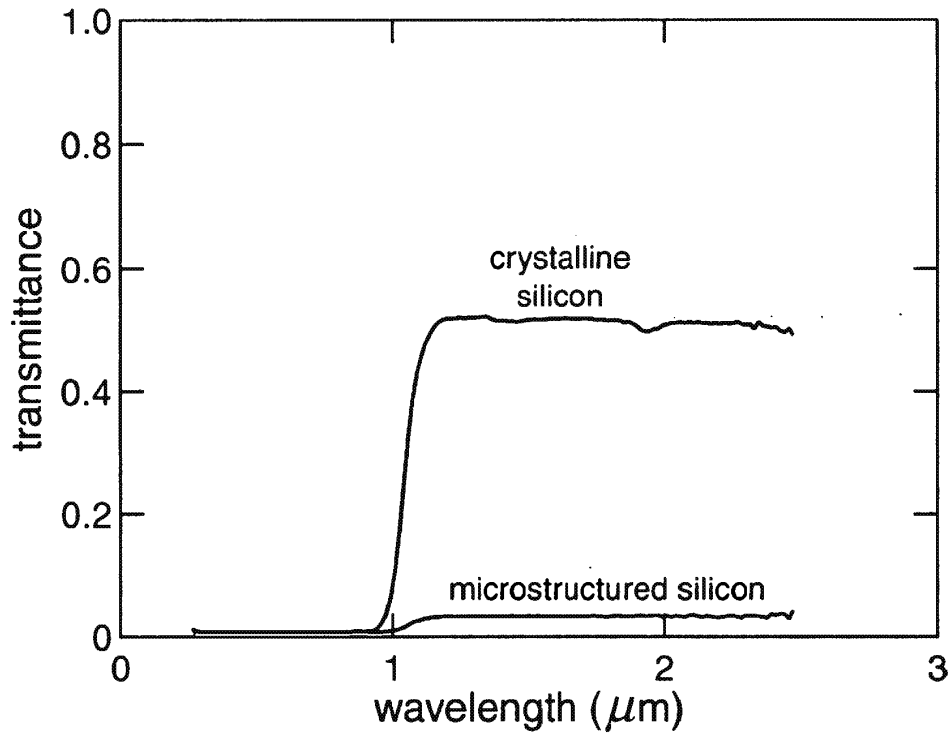

SIONYX1403000028.0068

SAMSUNG EX. 1002 - 2680/4148

Properties

absorptance (1 – *R* – *T*)

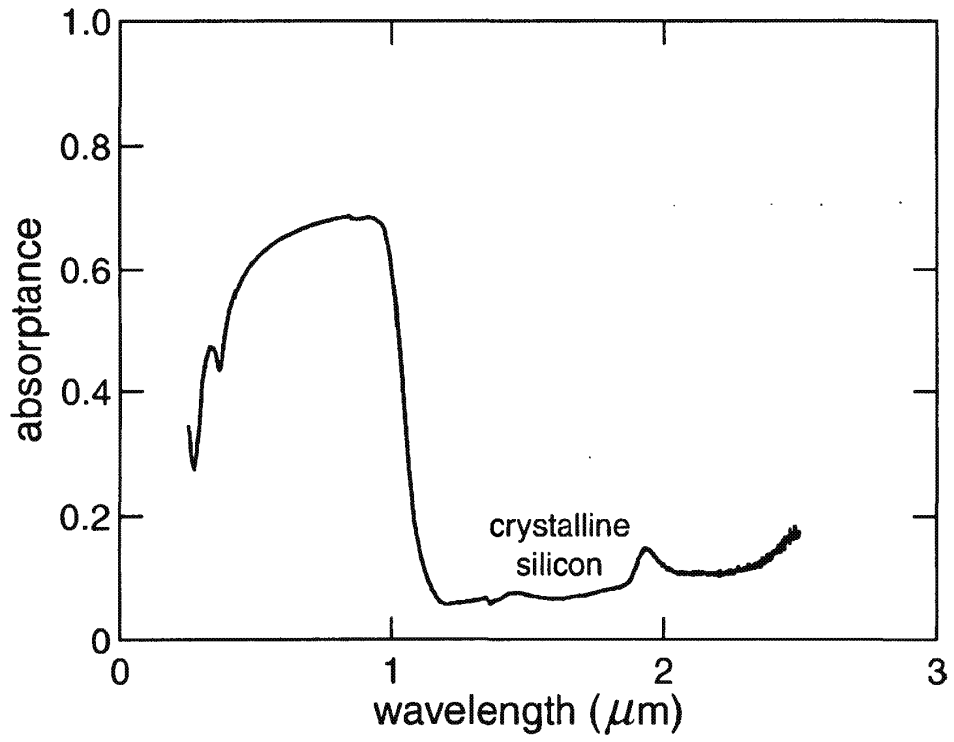

SIONYX1403000028.0069
SAMSUNG EX. 1002 - 2681/4148

Properties

absorptance (1 – *R* – *T*)

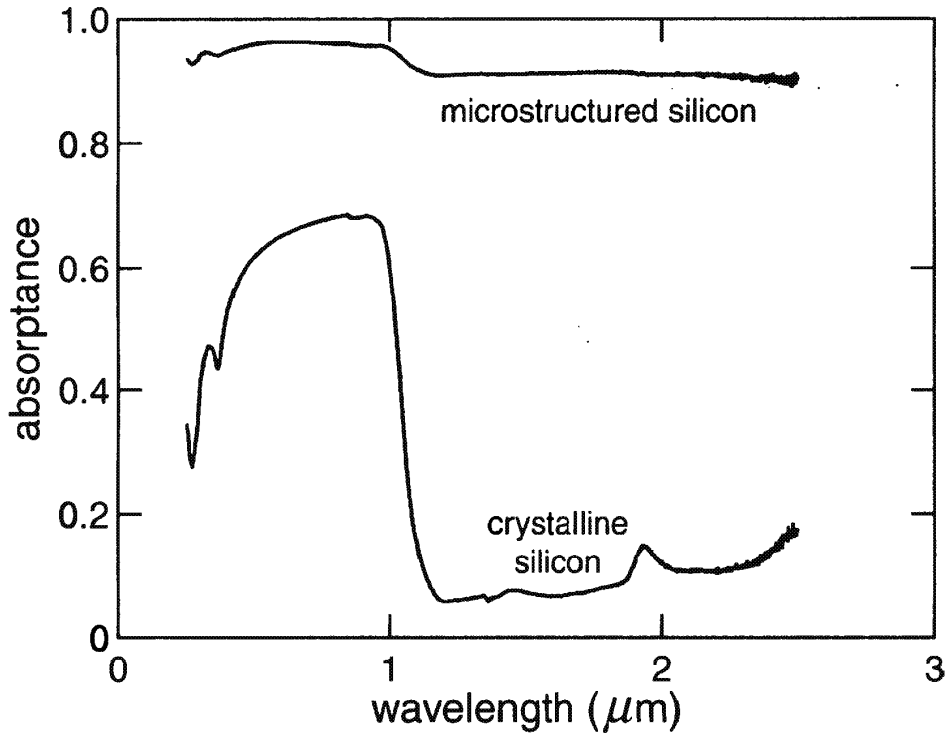

Appl. Phys. Lett. 78, 1850 (2001)

SIONYX1403000028.0070

SAMSUNG EX. 1002 - 2682/4148

Properties

absorptance ($1 - R - T$)

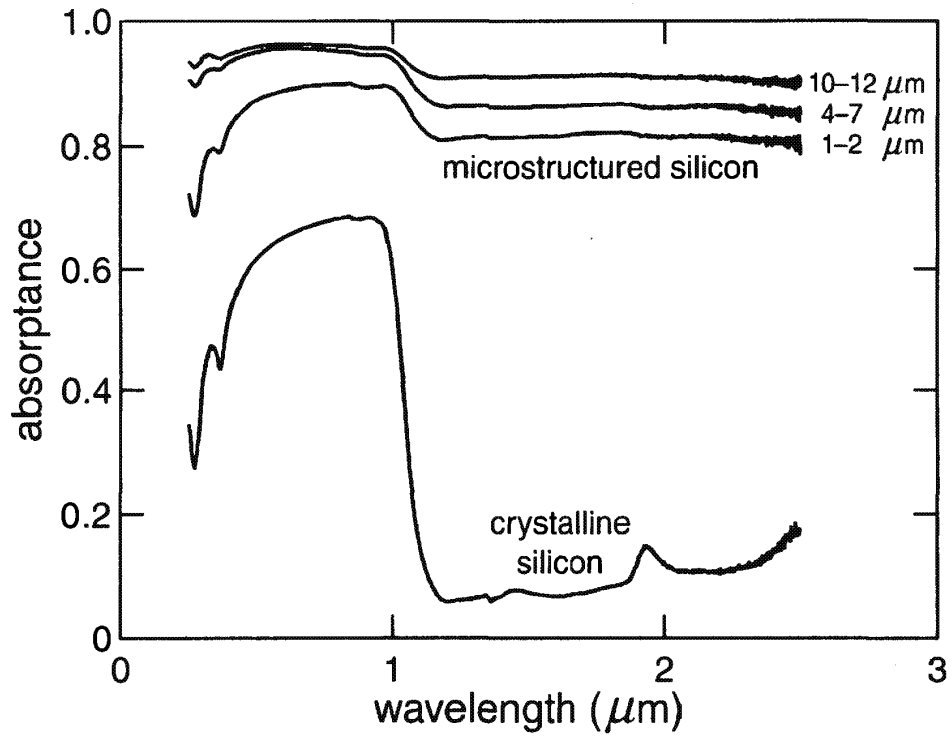

Appl. Phys. Lett. **78, 1850 (2001)**

SIONYX1403000028.0071

SAMSUNG EX. 1002 - 2683/4148

Properties

field emission setup

field emission setup

gold coating

Properties

field emission setup

Properties

field emission setup

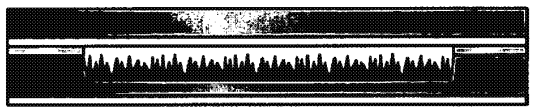

SAMSUNG EX. 1002 - 2687/4148

Properties

field emission setup

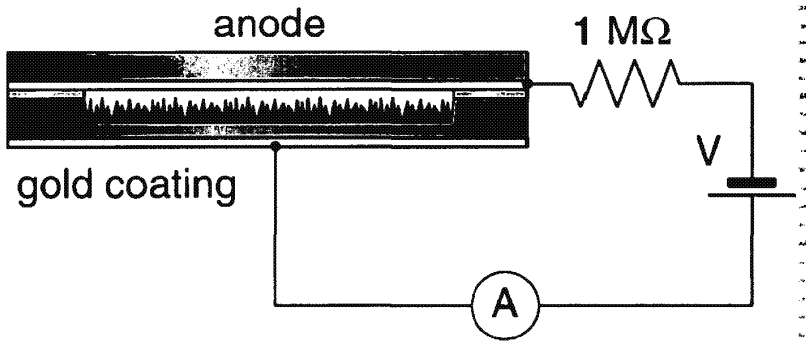

Properties

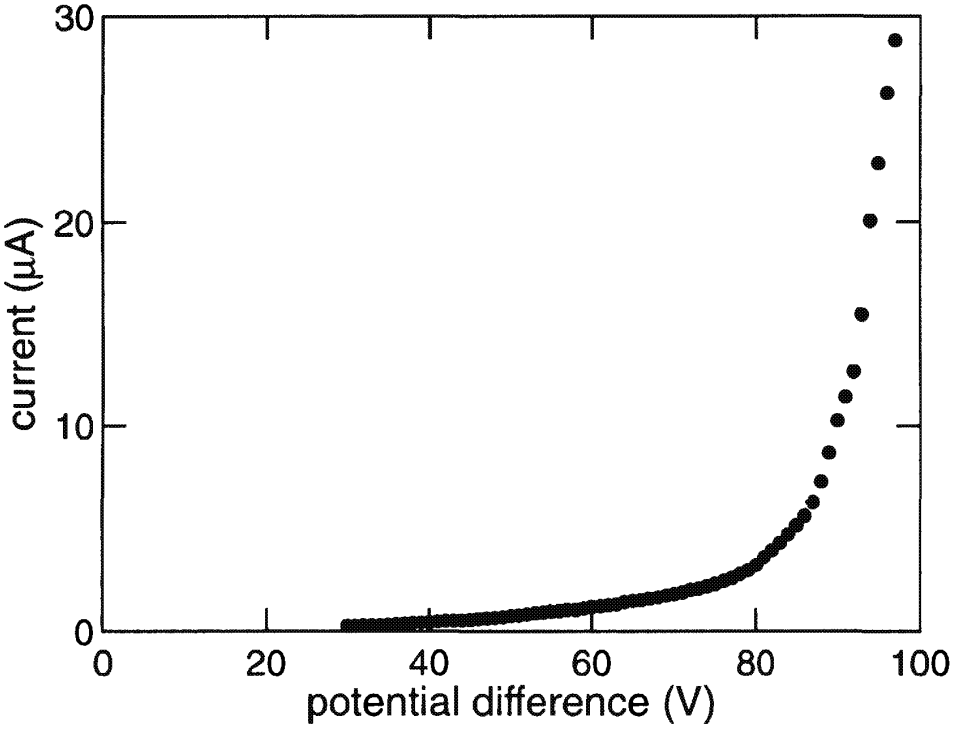

Properties

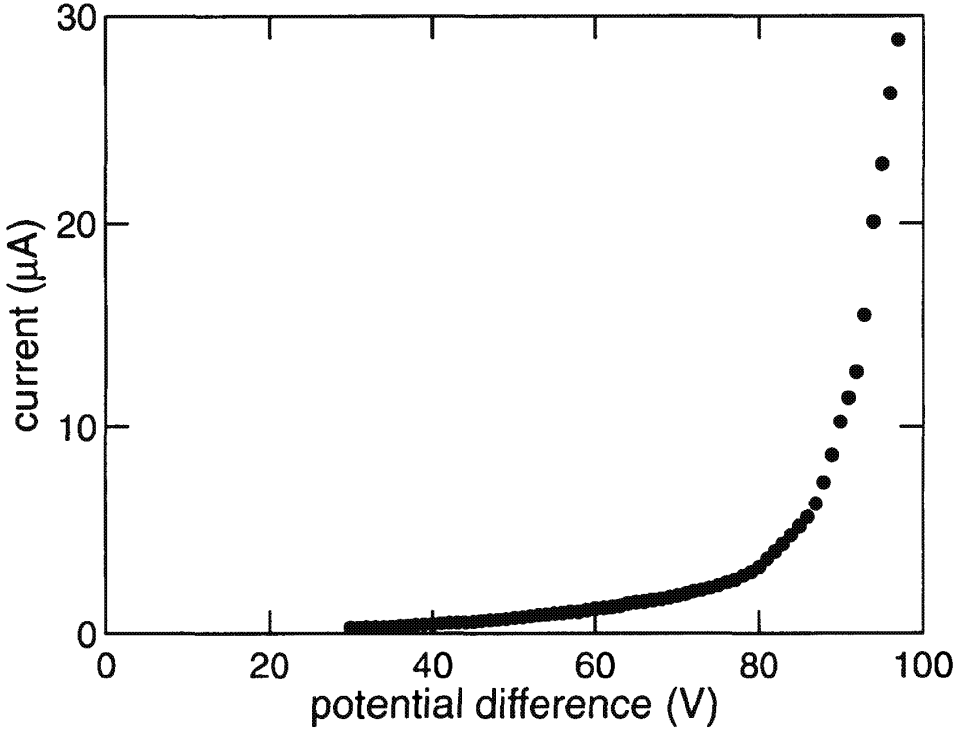

turn-on field (1 μA/cm^2): 1.2 V/μm

Properties

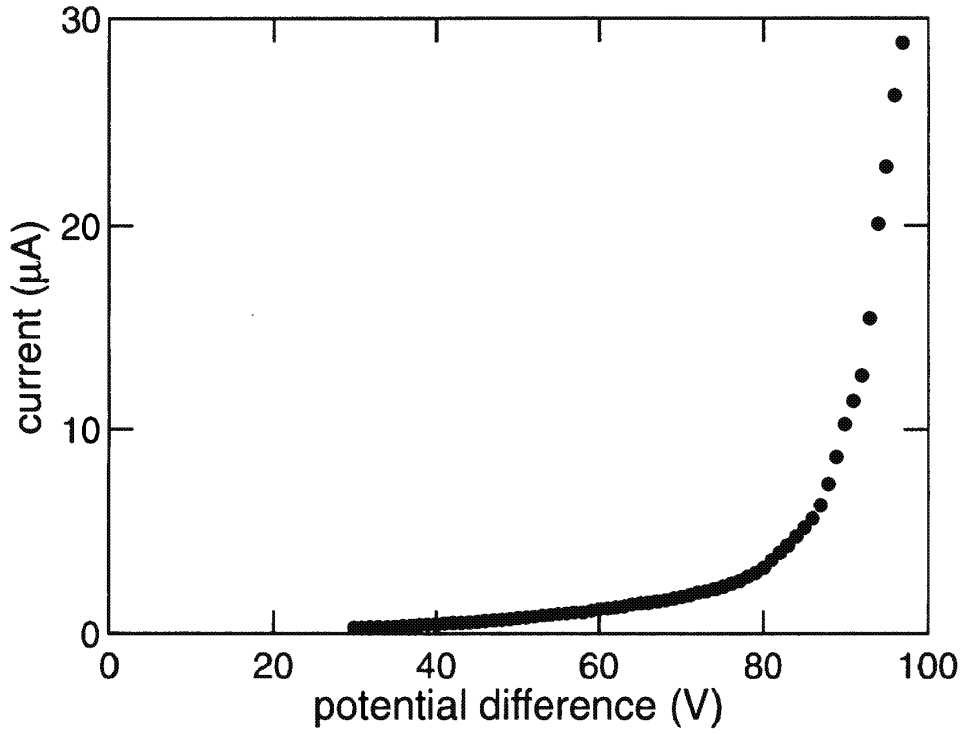

threshold field (10 $\mu A/cm^2$): 2.1 V/μm

Properties

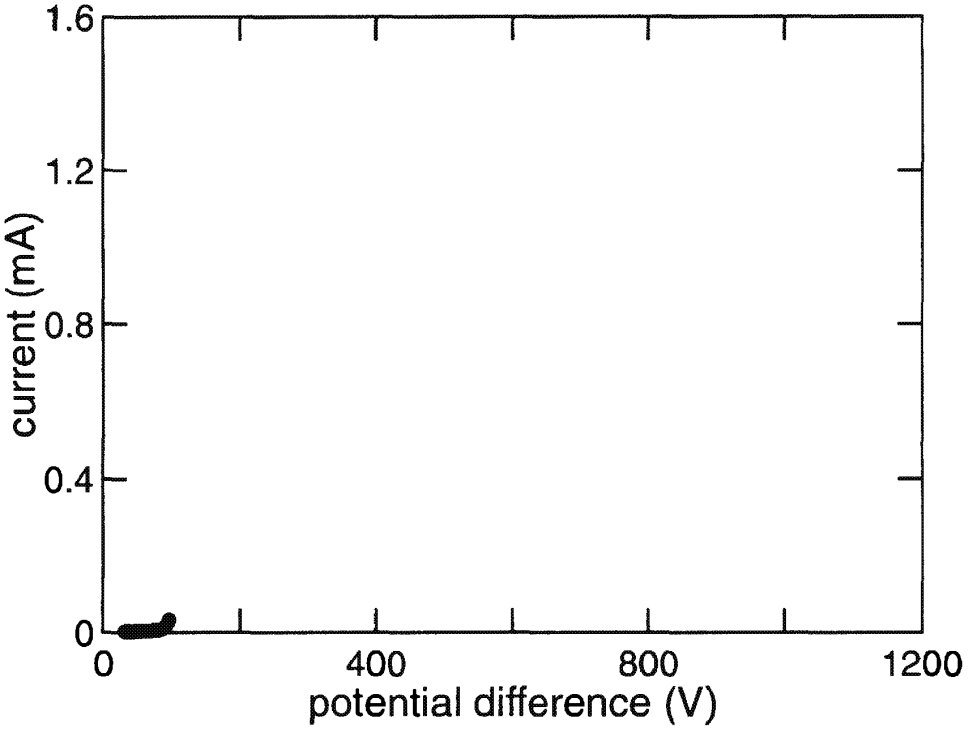

SAMSUNG EX. 1002 - 2692/4148

Properties

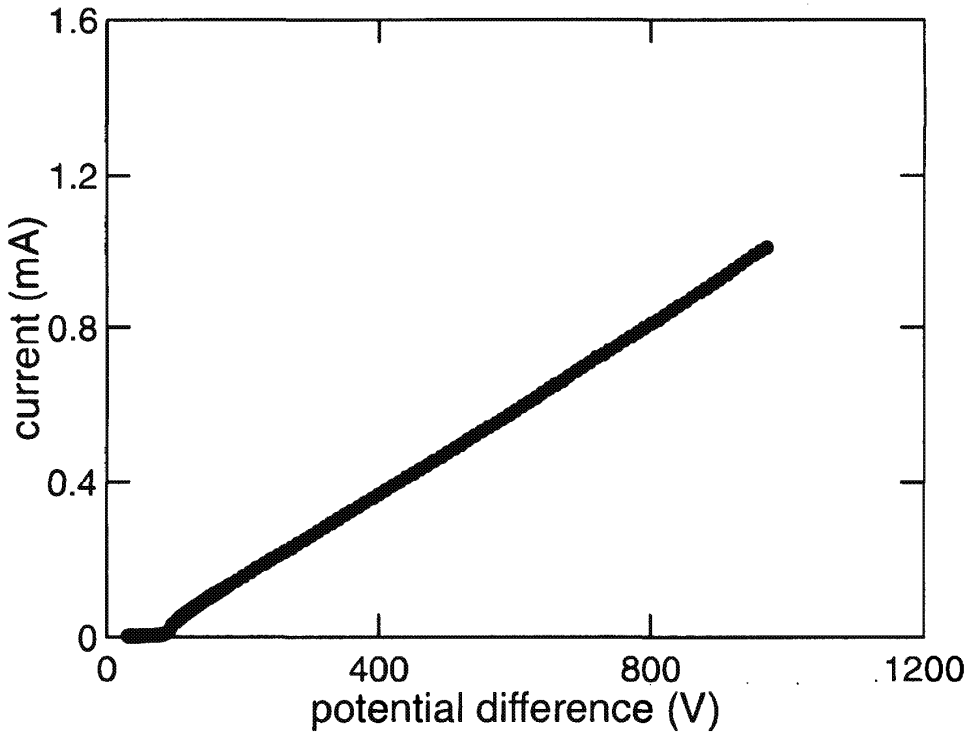

Properties

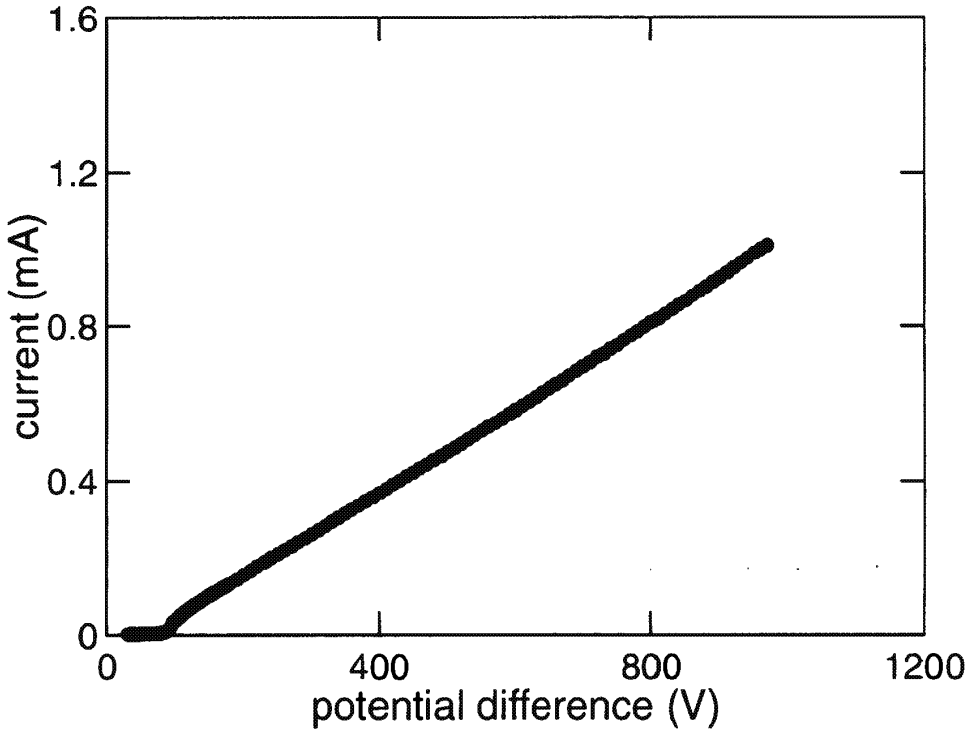

maximum current: 20 mA (4 mm^2 sample)

Properties

Points to keep in mind:

- near unity absorption
- sub-band gap absorption
- IR photoelectron generation
- high field emission at low fields

Outline

- Properties
- Structural and chemical analysis
- Outlook

SIONYX1403000028.0084

Structural and chemical analysis

- What causes these properties?
- Other gases?

SAMSUNG EX. 1002 - 2697/4148

Structural and chemical analysis

Secondary ion mass spectrometry:

- 10^{20} cm^{-3} sulfur
- 10^{17} cm^{-3} fluorine

SIONYX1403000028.0086

SAMSUNG EX. 1002 - 2698/4148

Structural and chemical analysis

Structural and chemical analysis

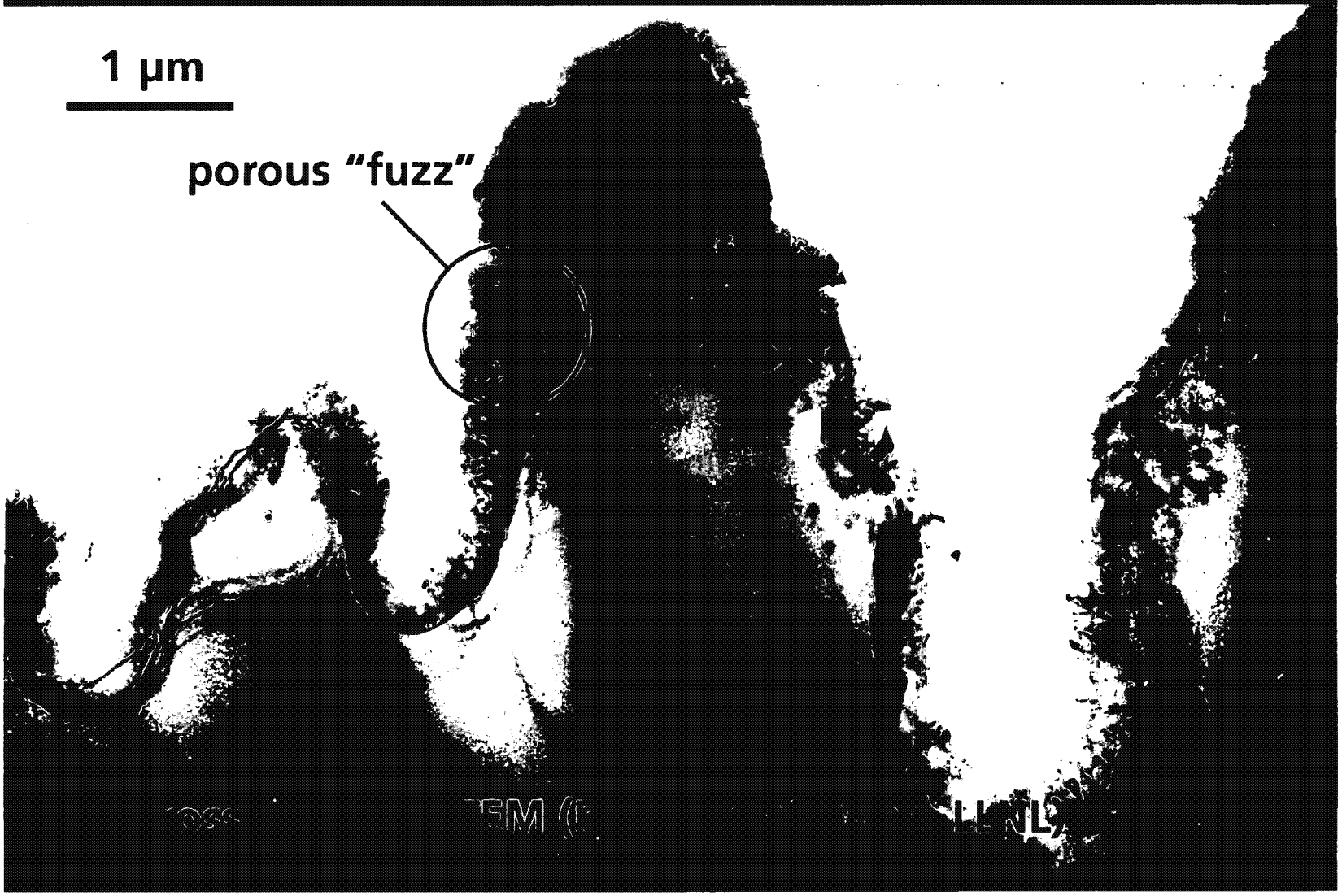

Structural and chemical analysis

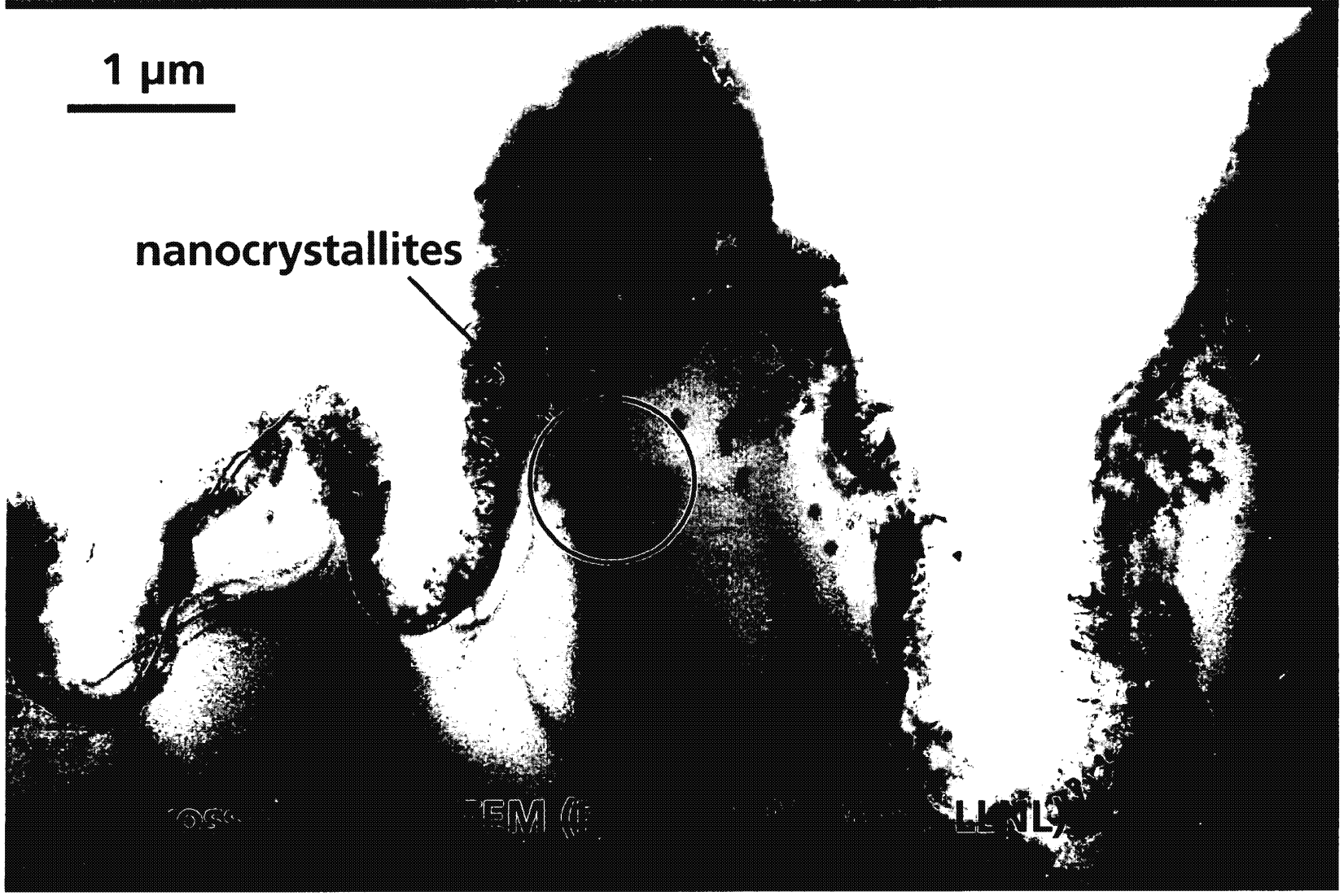

Structural and chemical analysis

Structural and chemical analysis

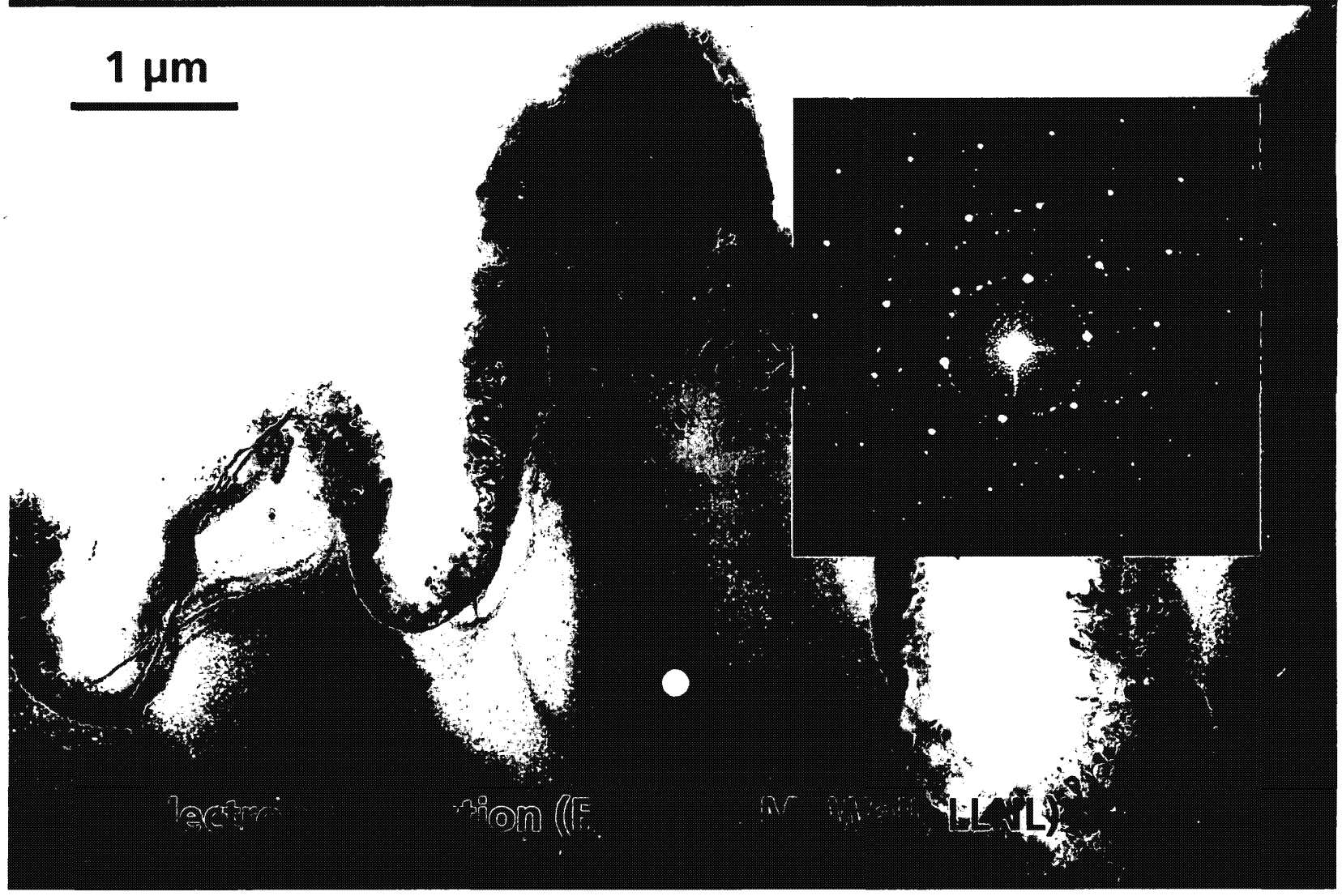

Structural and chemical analysis

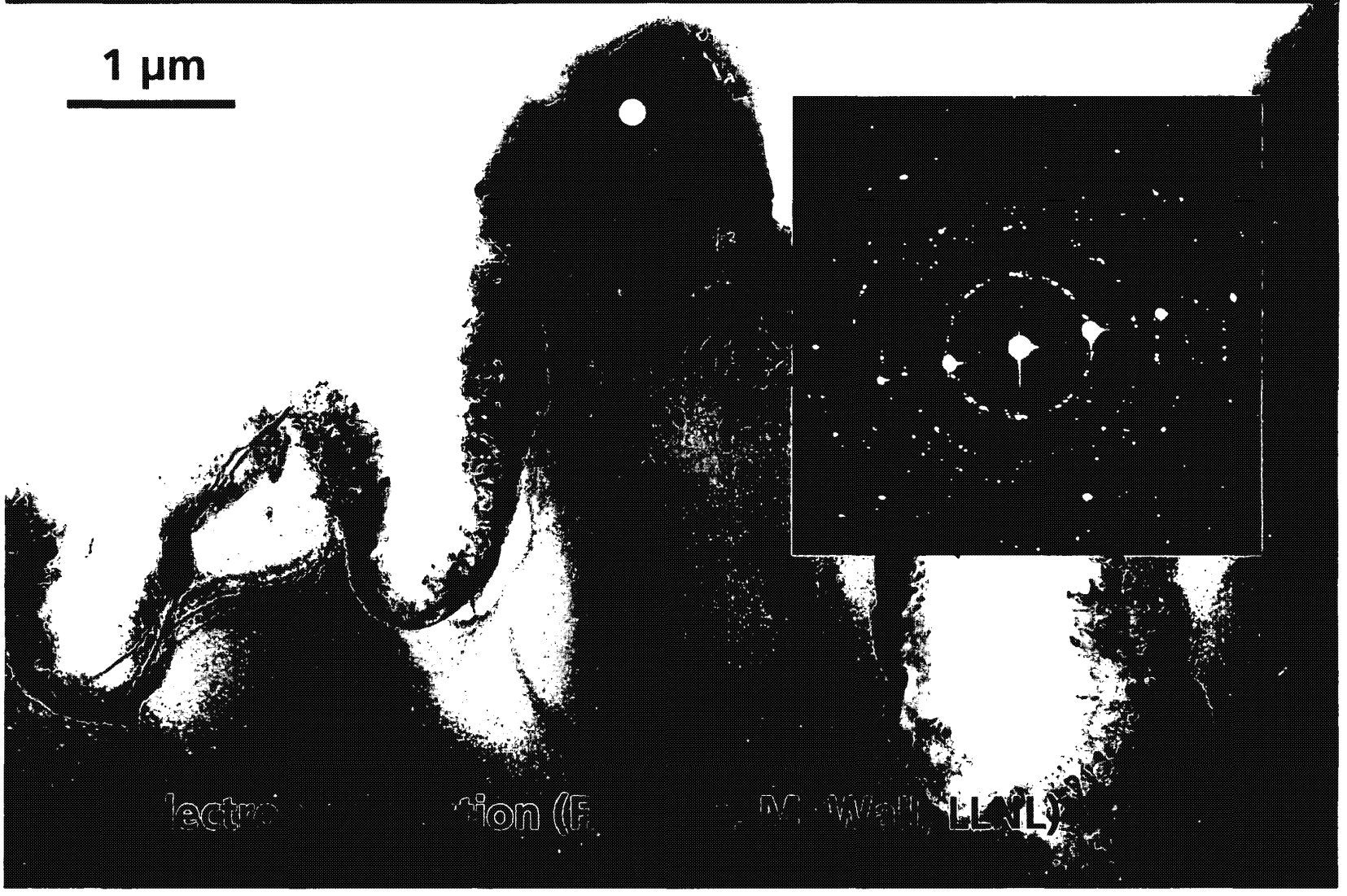

Structural and chemical analysis

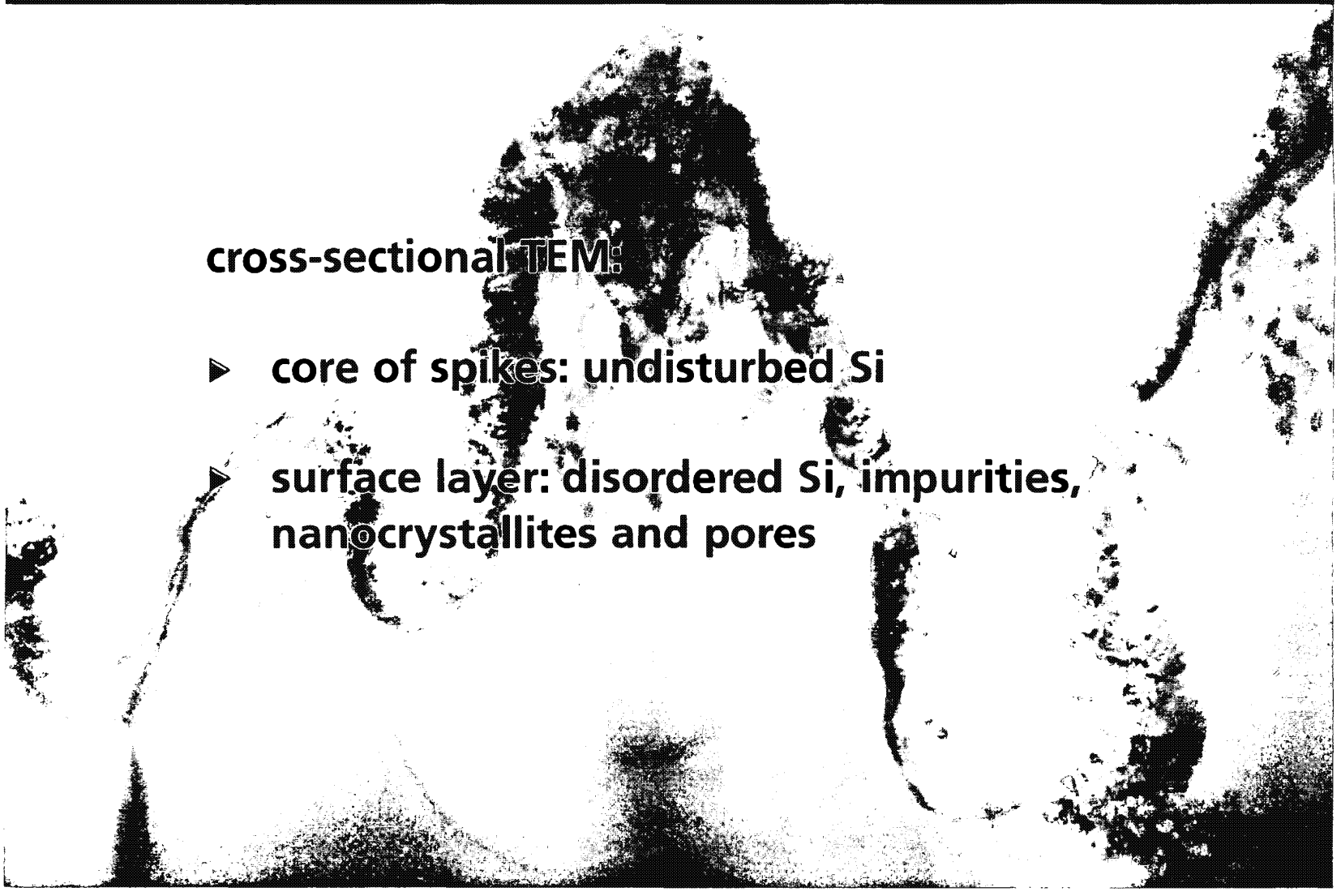

cross-sectional TEM:

- **core of spikes: undisturbed Si**
- **surface layer: disordered Si, impurities, nanocrystallites and pores**

SIONYX1403000028.0093

SAMSUNG EX. 1002 - 2705/4148

Structural and chemical analysis

anneal 4 hours at 1200 K

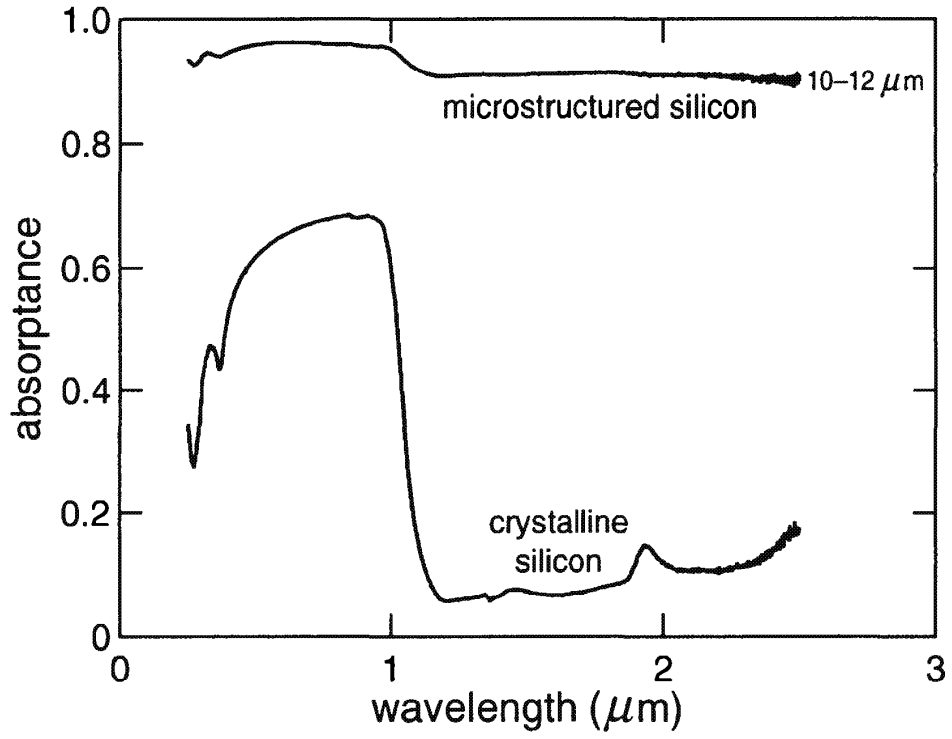

Appl. Phys. Lett. 78, 1850 (2001)

SIONYX1403000028.0094

SAMSUNG EX. 1002 - 2706/4148

Structural and chemical analysis

anneal 4 hours at 1200 K

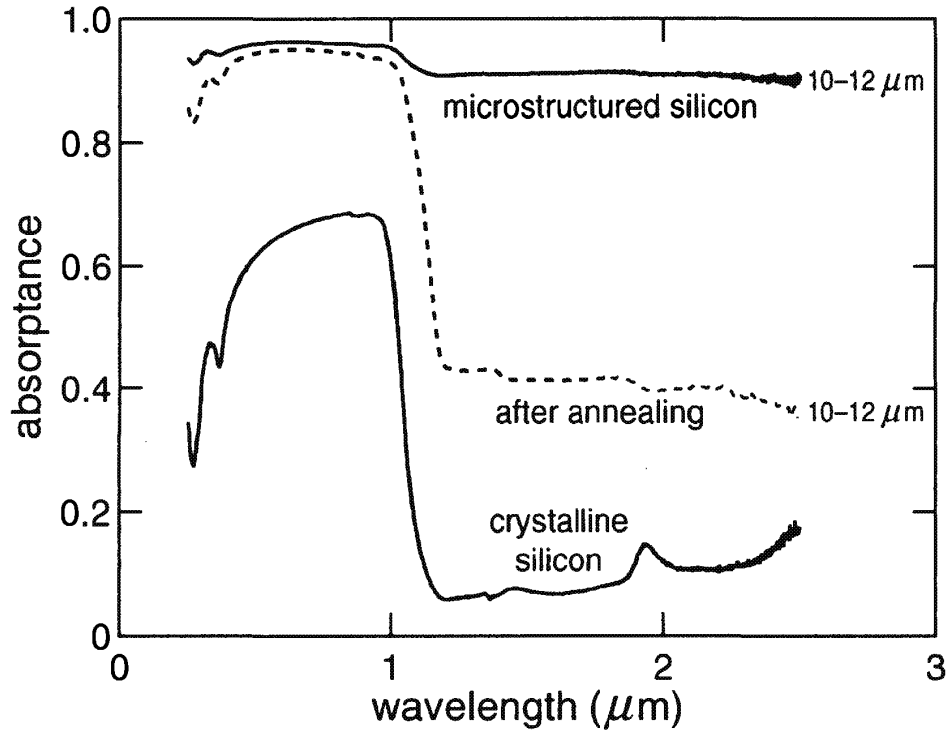

Appl. Phys. Lett. **78, 1850 (2001)**

SIONYX1403000028.0095

SAMSUNG EX. 1002 - 2707/4148

Structural and chemical analysis

anneal 4 hours at 1200 K

Appl. Phys. Lett. **78,** 1850 (2001)

SIONYX1403000028.0096

SAMSUNG EX. 1002 - 2708/4148

Structural and chemical analysis

anneal 4 hours at 1200 K

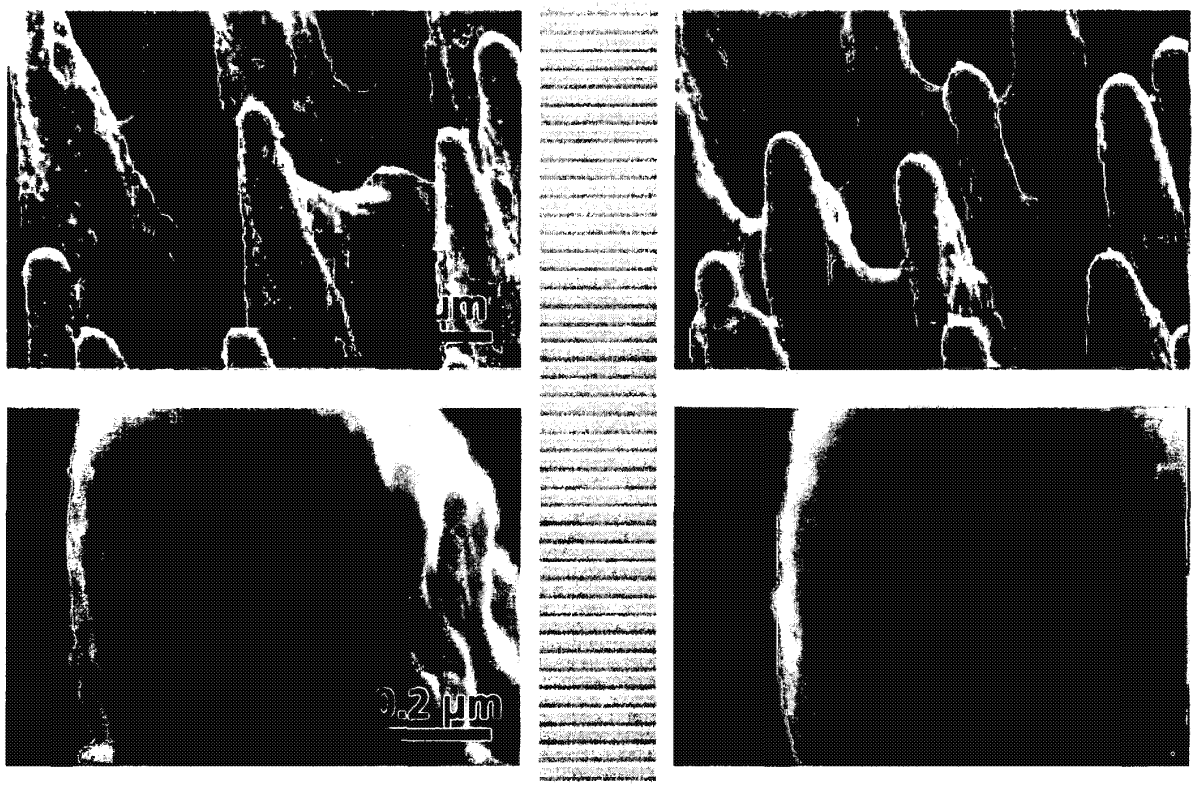

Appl. Phys. Lett. **78**, 1850 (2001)

SIONYX1403000028.0097

SAMSUNG EX. 1002 - 2709/4148

Structural and chemical analysis

Effects of annealing:

- **IR absorption: reduced twofold**
- **SEM: fewer surface nanostructures**
- **SIMS: sulfur content reduced twofold**

SIONYX1403000028.0098

SAMSUNG EX. 1002 - 2710/4148

Structural and chemical analysis

sulfur introduces states in the gap

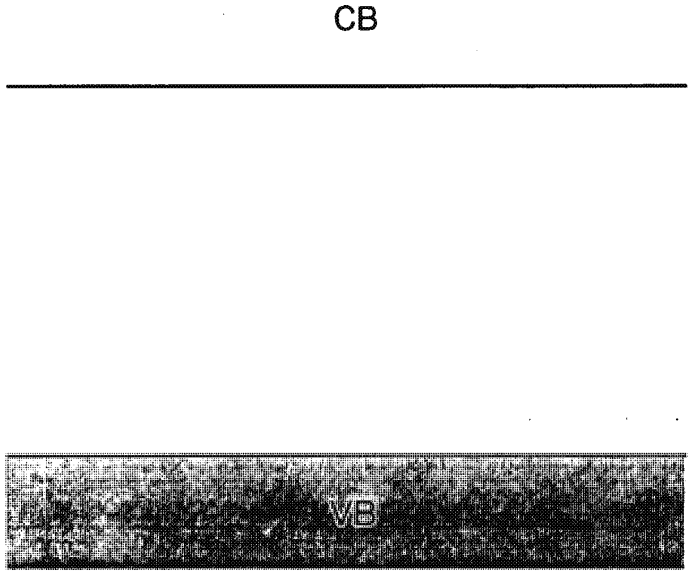

SIONYX1403000028.0099

SAMSUNG EX. 1002 - 2711/4148

Structural and chemical analysis

sulfur introduces states in the gap

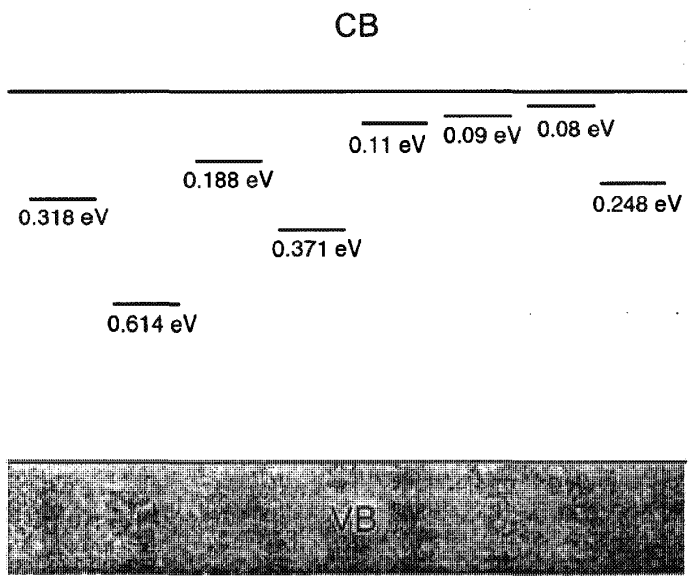

Janzén, *et al.*, *Phys. Rev. B* **29**, 1907 (1984)

SIONYX1403000028.0100
SAMSUNG EX. 1002 - 2712/4148

Structural and chemical analysis

states broaden into a band

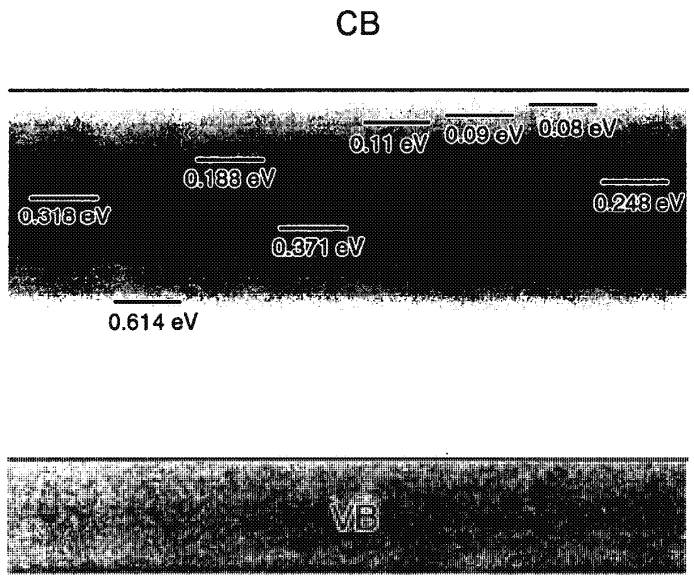

Structural and chemical analysis

effect of ambient gas on absorptance

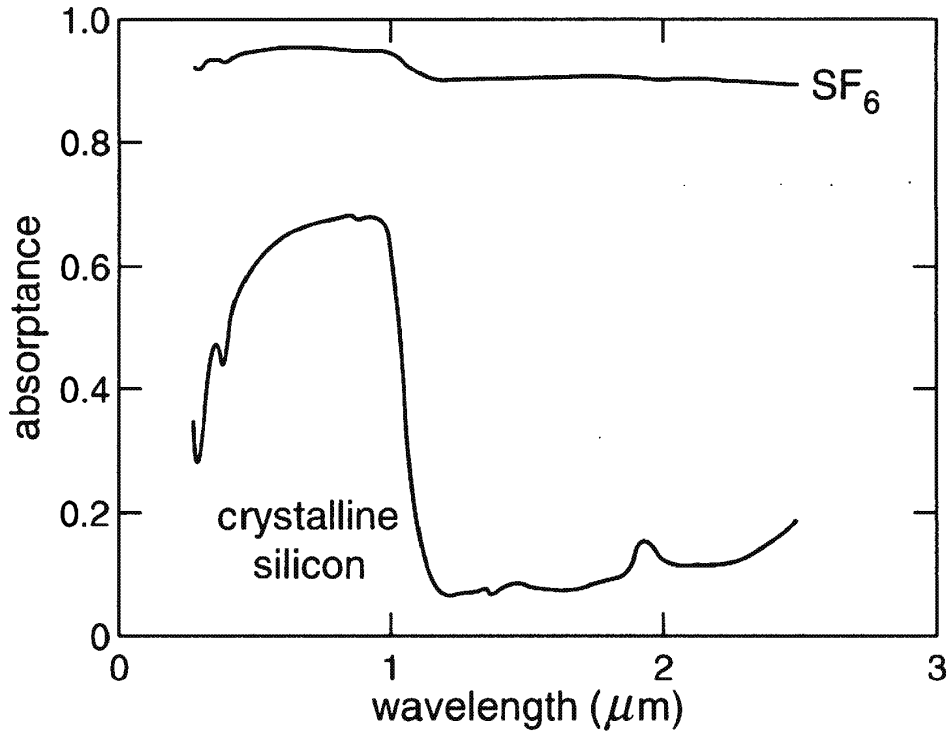

SIONYX1403000028.0102

SAMSUNG EX. 1002 - 2714/4148

Structural and chemical analysis

effect of ambient gas on absorptance

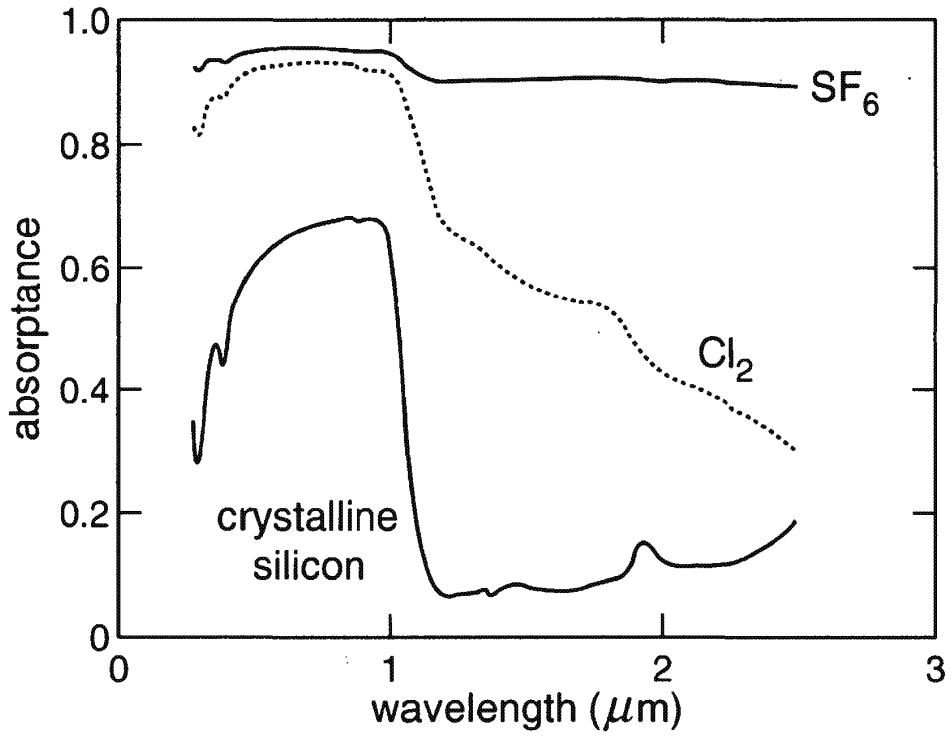

SIONYX1403000028.0103

SAMSUNG EX. 1002 - 2715/4148

Structural and chemical analysis

effect of ambient gas on absorptance

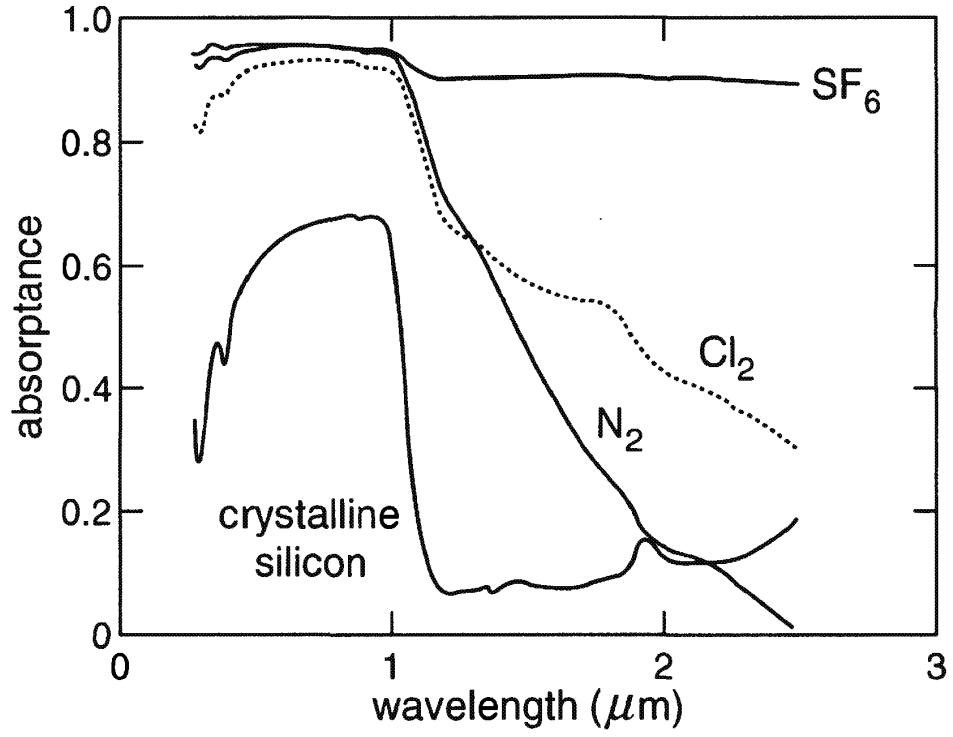

SIONYX1403000028.0104

SAMSUNG EX. 1002 - 2716/4148

Structural and chemical analysis

effect of ambient gas on absorptance

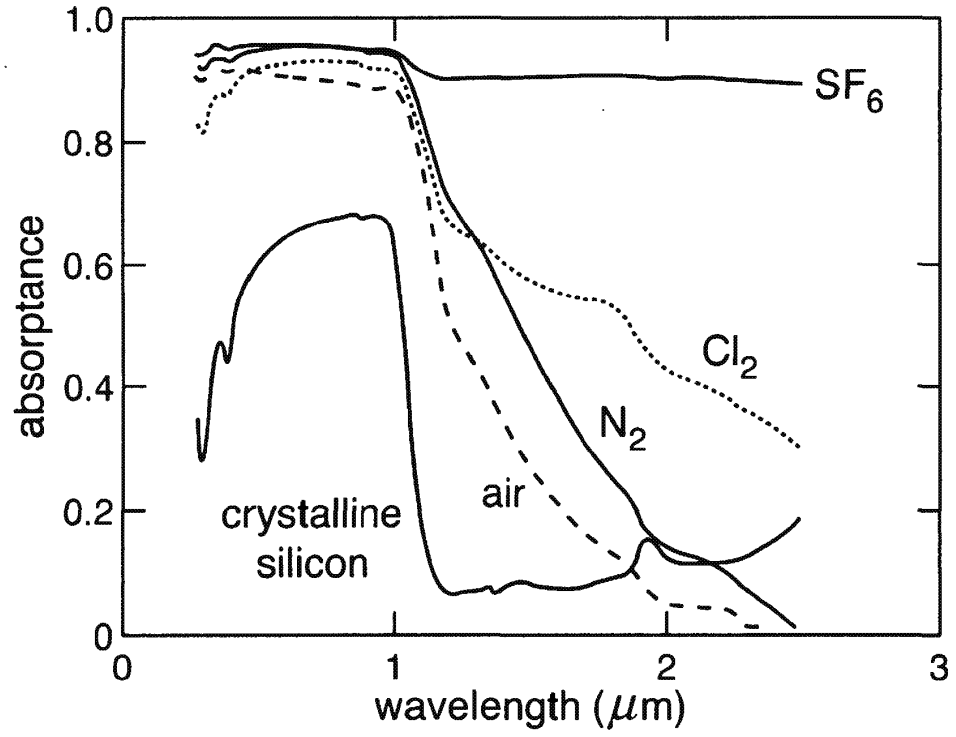

Structural and chemical analysis

effect of ambient gas on absorptance

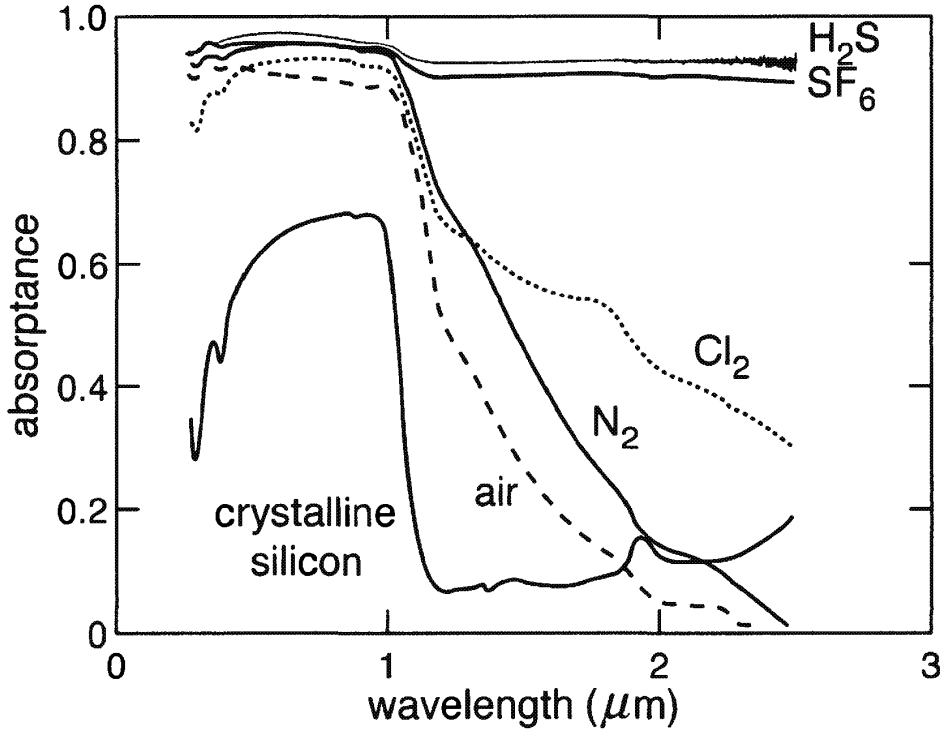

Structural and chemical analysis

effect of ambient gas on absorptance

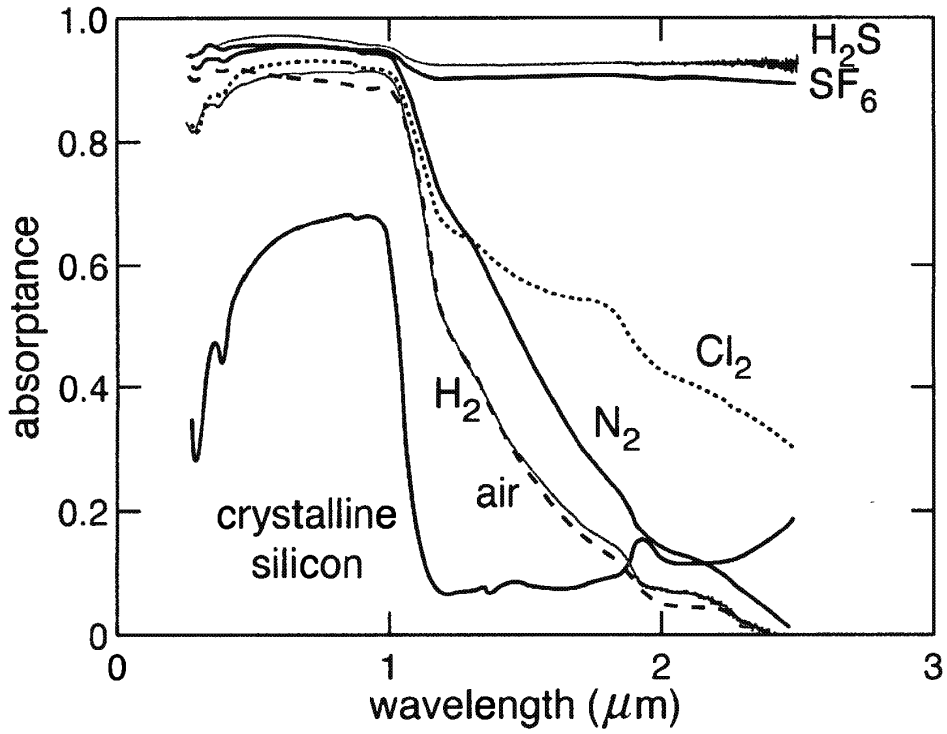

SIONYX1403000028.0107

SAMSUNG EX. 1002 - 2719/4148

Structural and chemical analysis

- significant incorporation of ambient species
- nanostructured surface layer
- sulfur content correlates with IR absorption

SAMSUNG EX. 1002 - 2720/4148

Outline

- Properties
- Structural and chemical analysis
- Outlook

New Scientist 13, 34 (2001)

A forest of silicon spikes could revolutionise solar cells and give you painless injections. **Bruce Schechter** peers into the mysterious world of black silicon

TALL, DARK AND STRANGER

WE ALL love stories of serendipity. They —m to hark back to a time when a fogged —tate or a filthy Petri dish —day, when

semiconductors with a powerful laser. In the early 1990s, Mazur's was the first academic lab in the world to get its hands on a femtosecond laser. This device —nates pulses of light that are hundreds —times brighter than the Sun —t extremely

around the laboratory," he claims.

Well, it was almost the only reason short laser pulse will break down into sulphur and fluorine radicals, v will attack a silicon substrate. "Hyd fluoride is used to etch silicon thought maybe the SF, would deco and then the fluorine would at the silicon," Mazur ex than

SIONYX1403000028.0110

SAMSUNG EX. 1002 - 2722/4148

Outlook

- **detector technology**

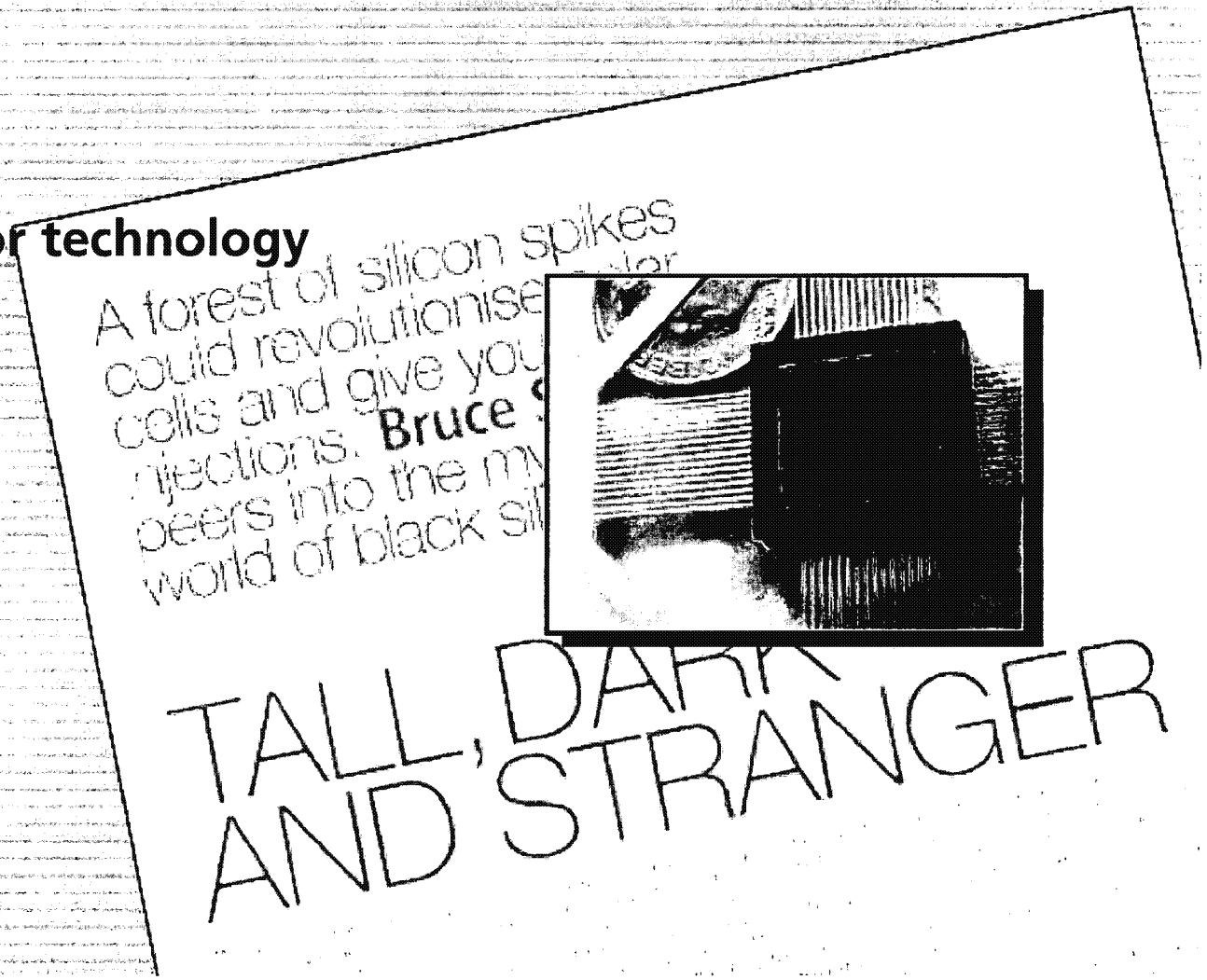

SIONYX1403000028.0111

SAMSUNG EX. 1002 - 2723/4148

Outlook

- detector technology
- solar cells

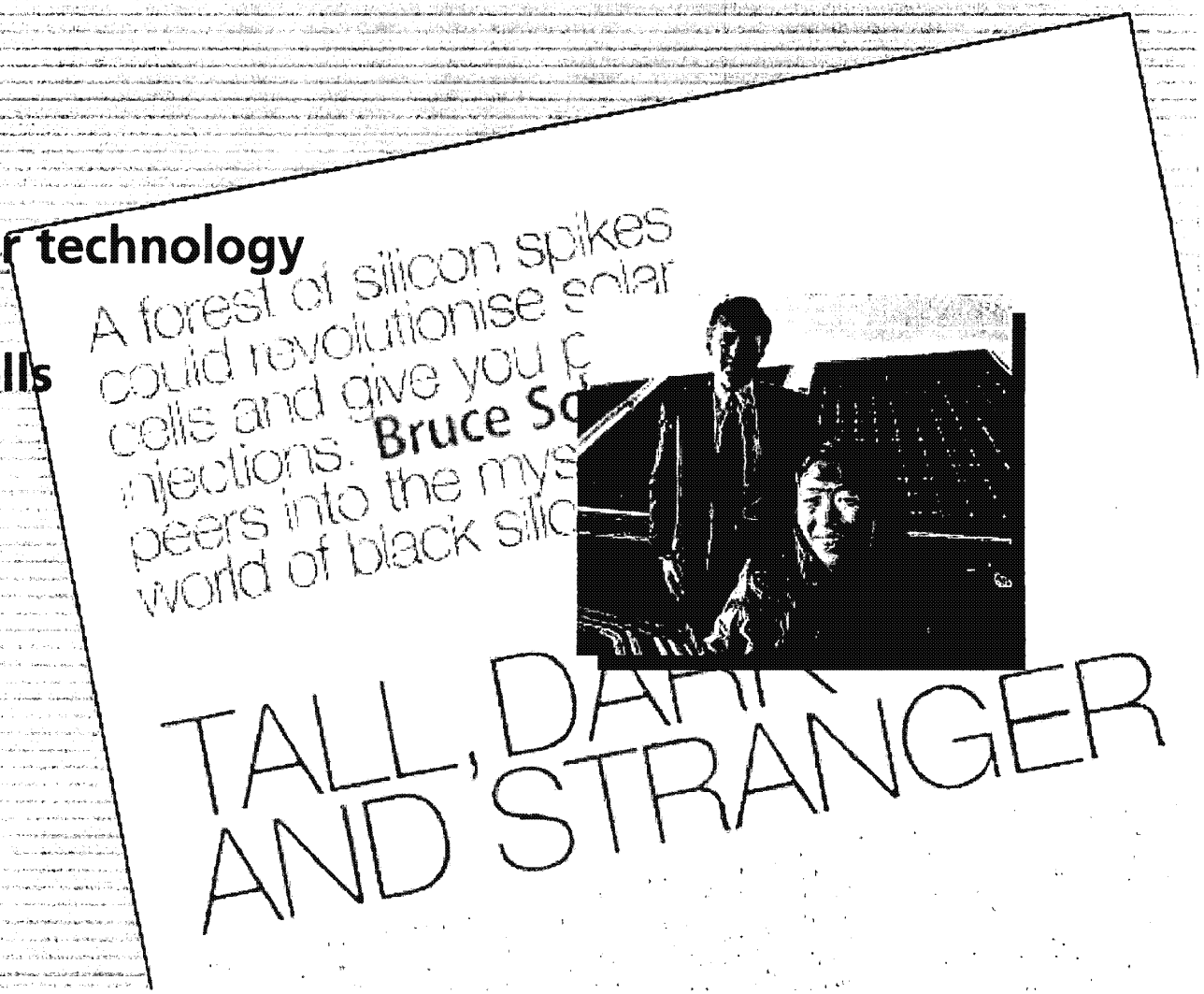

Outlook

- detector technology
- solar cells
- display technology

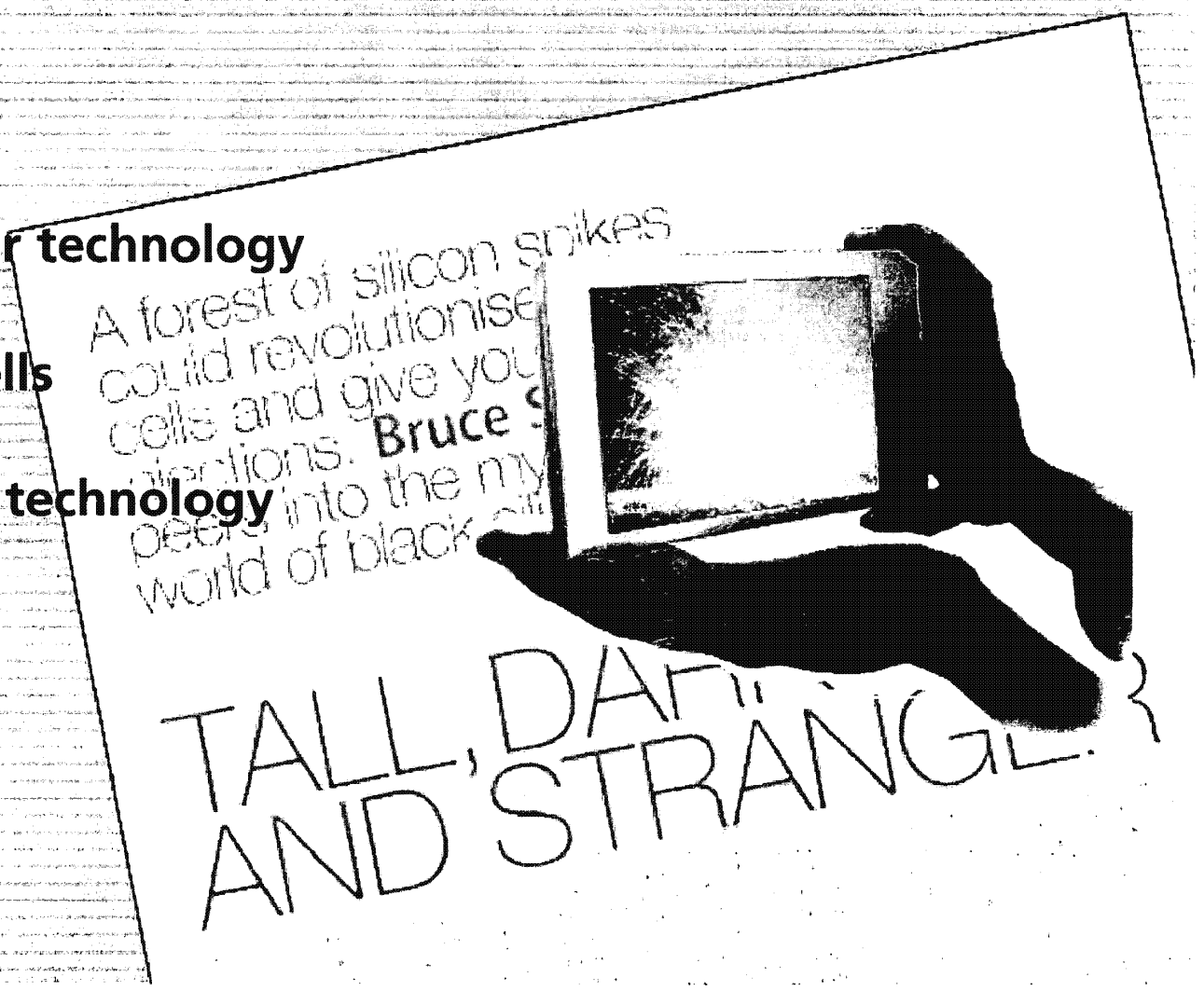

Outlook

- detector technology
- solar cells
- display technology
- sensors

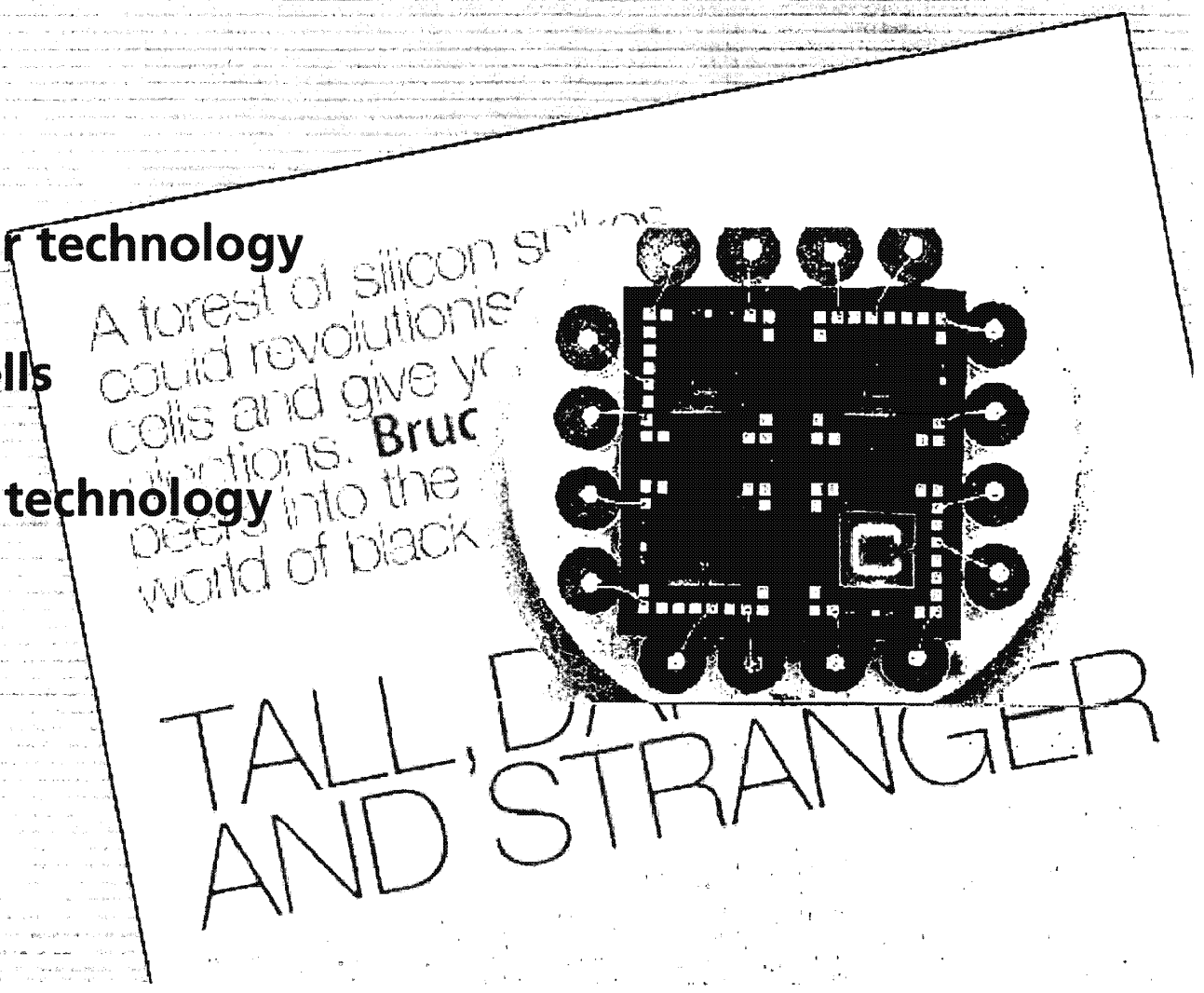

Outlook

- development of spikes
- spike formation through grids
- cell adhesion
- functionalization

SIONYX1403000028.0115

SAMSUNG EX. 1002 - 2727/4148

Outlook

can ordering of spikes be improved by using a grid?

SAMSUNG EX. 1002 - 2728/4148

Outlook

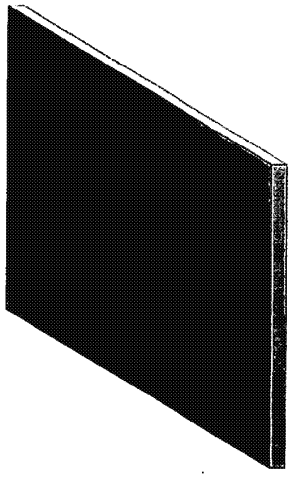

Si or Ti substrate

SIONYX1403000028.0117

SAMSUNG EX. 1002 - 2729/4148

Outlook

place grid in front of substrate

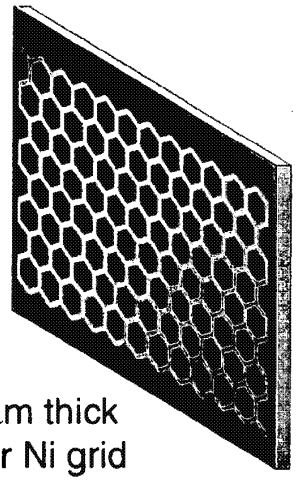

SAMSUNG EX. 1002 - 2730/4148

Outlook

scan laser beam

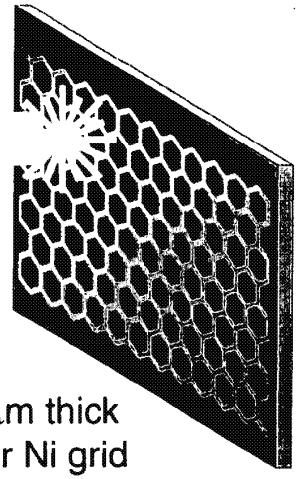

10 μm thick
Cu or Ni grid

Si or Ti substrate

SIONYX1403000028.0119

SAMSUNG EX. 1002 - 2731/4148

Outlook

scan laser beam

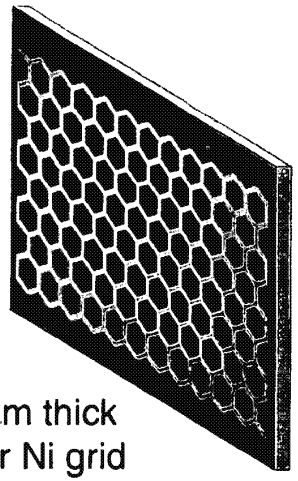

10 μm thick
Cu or Ni grid

Si or Ti substrate

Outlook

remove grid

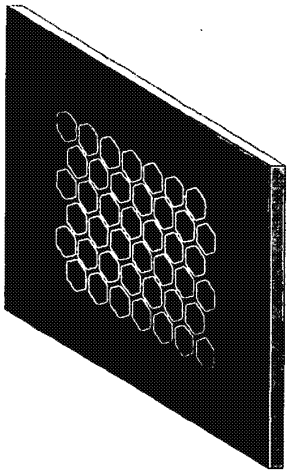

Si or Ti substrate

SIONYX1403000028.0121

SAMSUNG EX. 1002 - 2733/4148

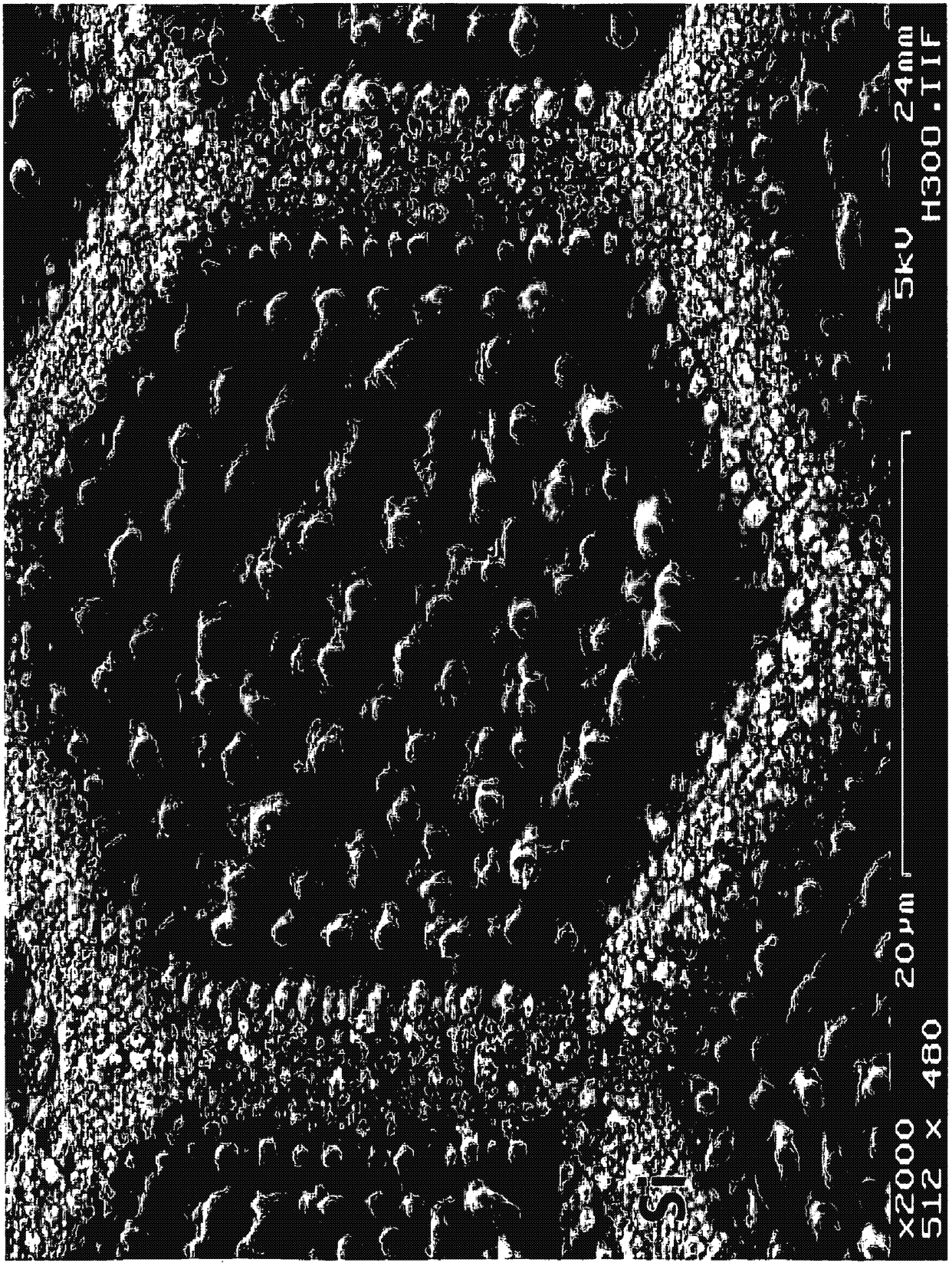
x2000
512 x 480
20μm
5kV
24mm
H300.TIF

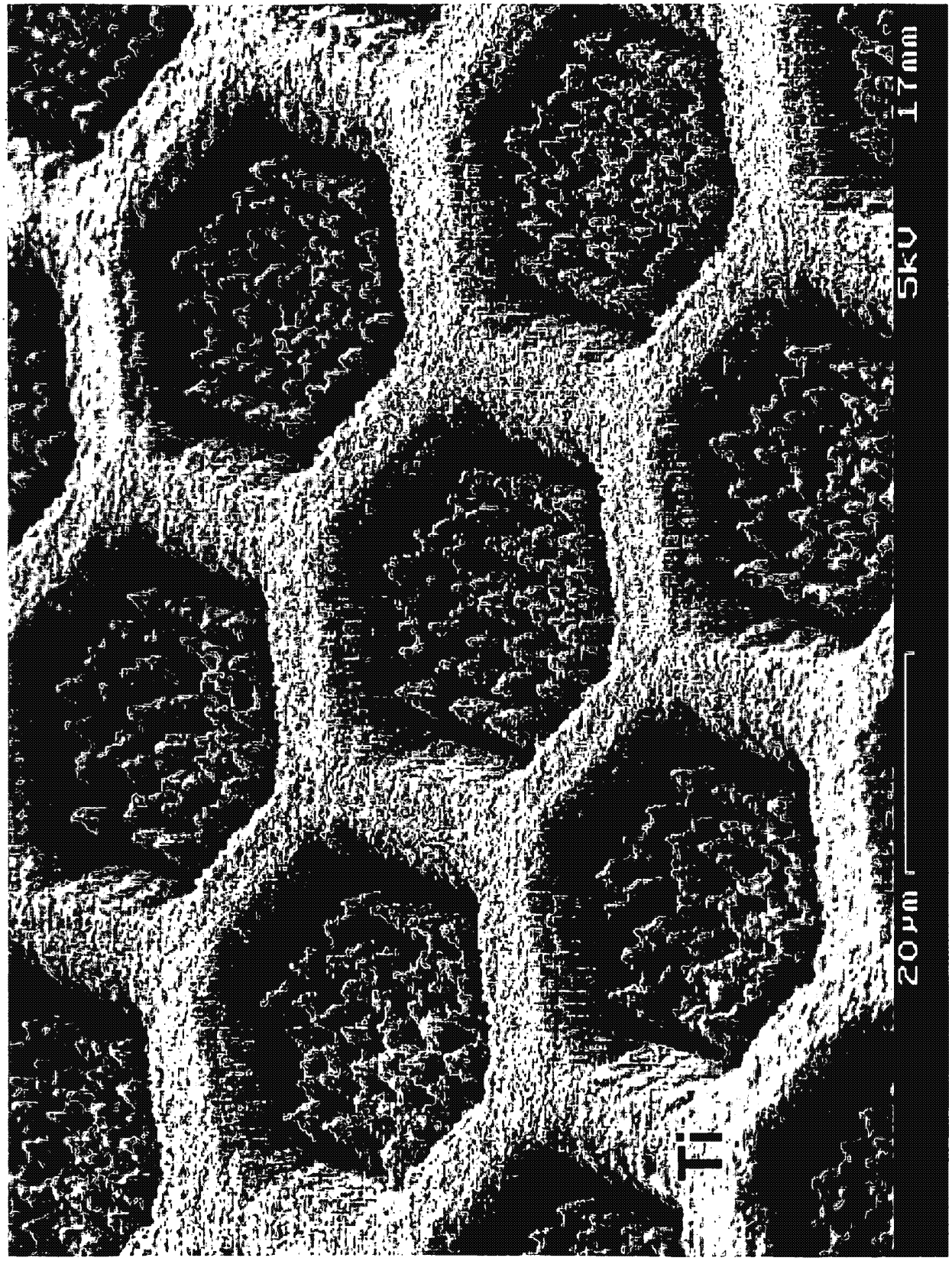

FIG. 1

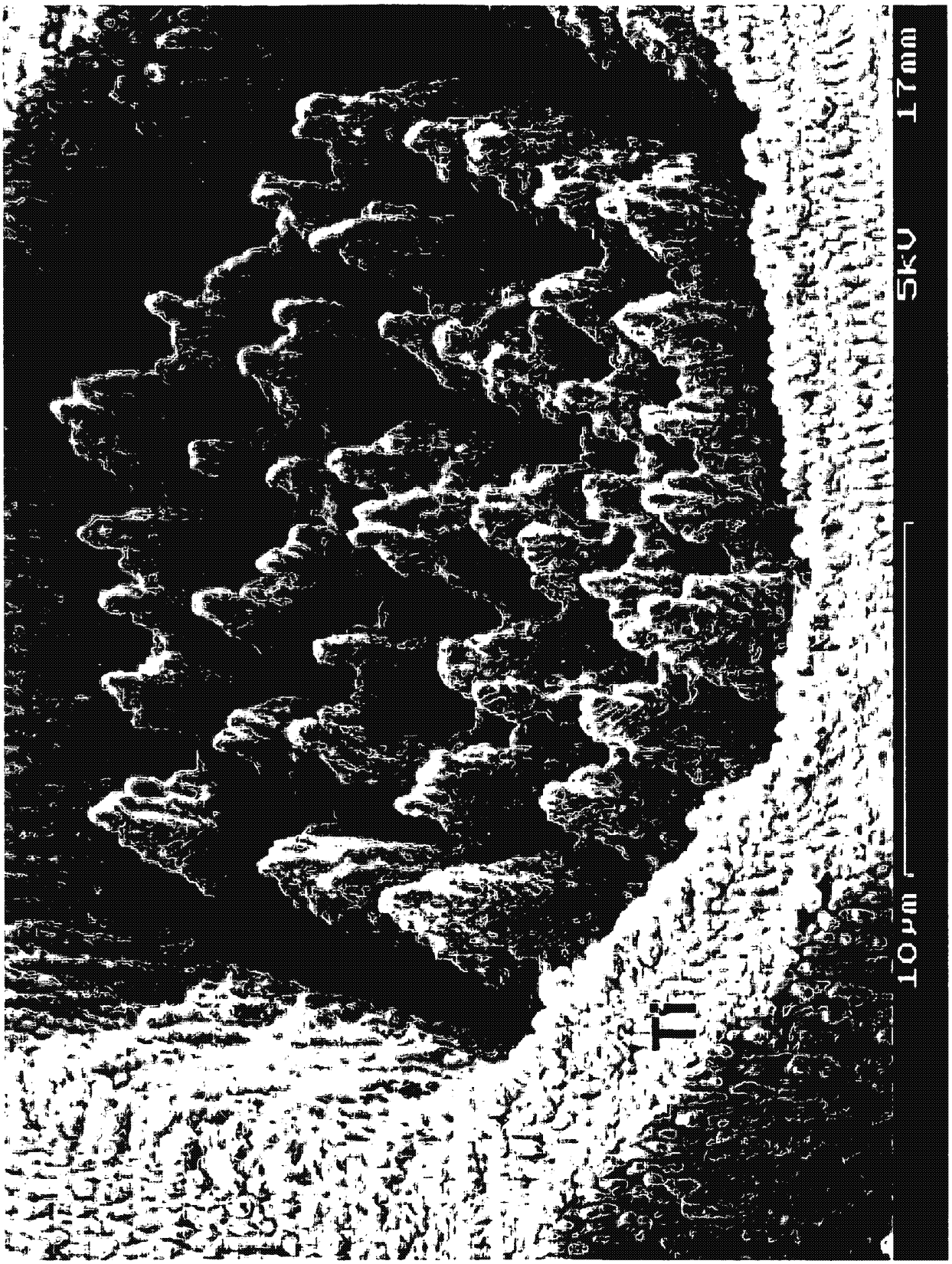
10 μm
5kV
17mm

Outlook

Summary

Microstructured silicon

- fabricated by simple, maskless process

SAMSUNG EX. 1002 - 2738/4148

Summary

Microstructured silicon

- fabricated by simple, maskless process
- can be integrated with microelectronics

SIONYX1403000029.0005

SAMSUNG EX. 1002 - 2739/4148

Summary

Microstructured silicon

- fabricated by simple, maskless process
- can be integrated with microelectronics
- generates IR photocurrent

SIONYX1403000029.0006

SAMSUNG EX. 1002 - 2740/4148

Summary

Microstructured silicon

- fabricated by simple, maskless process
- can be integrated with microelectronics
- generates IR photocurrent
- provides stable, high field emission current

Summary

Microstructured silicon
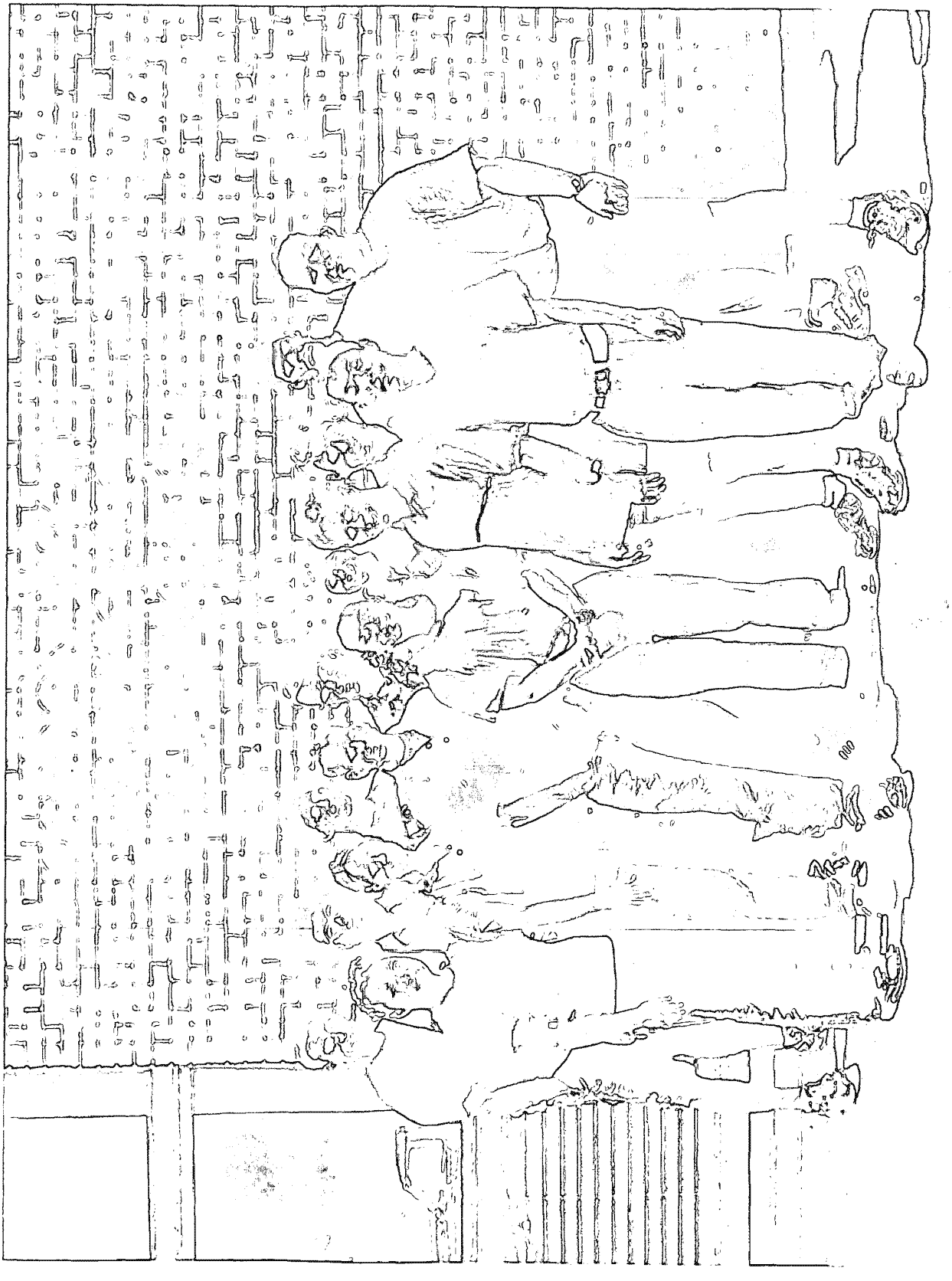
- fabricated by simple, maskless process
- can be integrated with microelectronics
- generates IR photocurrent
- provides stable, high field emission current
- is durable